Computational Investigation of Heusler compounds for Spintronics Application

---

A Dissertation

Presented to

the faculty of the School of Engineering and Applied Science

University of Virginia

---

in partial fulfillment
of the requirements for the degree

Doctor of Philosophy

by

Jianhua Ma

May 2019

APPROVAL SHEET

This Dissertation
is submitted in partial fulfillment of the requirements
for the degree of
Doctor of Philosophy

Author Signature: Jianhua Ma

This Dissertation has been read and approved by the examining committee:

Advisor: Avik Ghosh

Committee Member: Mona Zebarjadi

Committee Member: Sean R. Agnew

Committee Member: Joseph Poon

Committee Member: Joe C. Campbell

Committee Member: ______________________

Accepted for the School of Engineering and Applied Science:

Craig H. Benson, School of Engineering and Applied Science

May 2019

Abstract

Heusler compounds have become a large family of binary, ternary, and quaternary compounds that shows a variety of diverse properties and attracted tremendous scientific interest in the spintronics. The extensive tunability of the Heusler compounds through chemical substitutions makes the large potential for the family.

In this dissertation, we first present first-principles density functional calculations of the electronic structure, magnetism, and structural stability of 378 XYZ half-Heusler compounds (with $X =$ Cr, Mn, Fe, Co, Ni, Ru, Rh; $Y =$ Ti, V, Cr, Mn, Fe, Ni; $Z =$ Al, Ga, In, Si, Ge, Sn, P, As, Sb). We find that a "Slater-Pauling gap" in the density of states, (i.e. a gap or pseudogap after nine states in the three atom primitive cell) in at least one spin channel is a common feature in half-Heusler compounds. We find that the presence of such a gap at the Fermi energy in one or both spin channels contributes significantly to the stability of a half-Heusler compound. We calculate the formation energy of each compound and systematically investigate its stability against all other phases in the Open Quantum Materials Database (OQMD). We represent the thermodynamic phase stability of each compound as its distance from the convex hull of stable phases in the respective chemical space and show that the hull distance of a compound is a good measure of the likelihood of its experimental synthesis. We find low formation energies and mostly correspondingly low hull distances for compounds with $X =$ Co, Rh or Ni, $Y =$ Ti or V, and $Z =$ P, As, Sb or Si. We identify 26 18-electron semiconductors, 45 half-metals, and 34 near half-metals with negative formation energy, that follow the Slater-Pauling rule of three electrons per atom. Our calculations predict several new, as-yet unknown, thermodynamically stable phases which merit further experimental exploration — RuVAs, CoVGe, FeVAs in the half-Heusler structure, and NiScAs, RuVP, RhTiP in the orthorhombic MgSrSi-type structure. In addition, our calculations predict a number of hitherto unreported semiconducting (e.g., CoVSn, RhVGe), half-metallic (e.g., RhVSb), and near half-metallic (e.g., CoFeSb, CoVP) half-Heusler compounds to lie close to the respective convex hull of stable phases, and thus may be experimentally realized under suitable synthesis conditions, resulting in potential candidates for various semiconducting and spintronics applications.

The next set of systems studied was inverse-Heusler compounds. First-principles calculations of the electronic structure, magnetism and structural stability of 405 inverse-Heusler compounds with the chemical formula X_2YZ are presented and discussed with a goal of identifying compounds of interest for spintronics. Compounds for which the number of electrons per atom for Y exceed that for X and for which X and Y are each one of the $3d$ elements, Sc-Zn, and Z is one of the group IIIA-VA elements: Al, Ga, In, Si, Ge, Sn, P, As or Sb were considered. The formation energy per atom of each compound was calculated. By comparing our calculated formation energies to those calculated for phases in the Inorganic Crystal Structure Database (ICSD) of observed phases, we estimate that inverse-Heuslers with formation energies within 0.052 eV/atom of the calculated convex hull are reasonably likely to be synthesizable in equilibrium. The observed trends in the formation energy and relative structural stability as the X, Y and Z elements vary are described. In addition to the Slater-Pauling gap after 12 states per formula unit in one of the spin channels, inverse-Heusler phases often have gaps after 9 states or 14 states. We describe the origin and occurrence of these gaps. We identify 14 inverse-Heusler semiconductors, 51 half-metals and 50 near-half-metals with negative formation energy. In addition, our calculations predict 4 half-metals and 6 near-half-metals to lie close to the respective convex hull of stable phases, and thus may be experimentally realized under suitable synthesis conditions, resulting in potential candidates for future spintronics applications.

In the following the discovery, a series of half-metallic half-Heusler alloys are combined with MgO to create Heusler-MgO junctions. The electronic and magnetic properties of junctions are investigated. The strong oxidation between metal and oxygen atoms causes the systems with pure YY interfaces to be the most stable cases. We concluded that the uniaxial anisotropy can be induced in Heusler layers next to MgO. Type of interface layers determines the half-metallicity and the anisotropy (in-plane or perpendicular) in the Heusler-MgO junctions. The capacity to keep half-metallicity and perpendicular magnetic anisotropy (PMA) in NiMnSb/MgO and CoTiSn/MgO junction with MnMn interface layer makes it be potential candidates as electrode layers in Spin

Transfer Torque Random Access Memory (STT-RAM) devices.

Finally, using first-principles calculations of structural and magnetic properties, we identify several promising ferrimagnetic inverse Heusler half-metal/near half-metals can be the ideal candidate for hosting ultra-small, fast, and room temperature stable skyrmions.

Acknowledgments

The work presented in this document has been possible because of the support of many people. I want to express my gratitude to my supervisor, Professor Avik Ghosh, whose influence has guided me into the researcher I am today. He has taught me to think simple, to work hard, to make effective presentations and many more important skills to do research. Without his expert-level guidance I could have not achieved the present comfort in bringing this dissertation in its present format. I need to say a 'thank you' to him here, truly.

My gratitude also goes to Professor William H. Butler, who as the principal investigator of the DMREF project for Heusler compounds. As a world-famous expert in magnetic materials field, his intelligence and deeply love in science touched my heart greatly. I respect him as my second grandfather forever and I also dream to be a kindly, wise and merry old man as him, in one day.

I also want to thank the members of my committee, Professors Joe C. Campbell, Mona Zebarjadi and Sean R. Agnew specially Professors Joseph Poon for mentoring and guiding me along the magnetic skyrmion work.

I want to thank the members of my VINO research group for their friendship and all the innumerable enlightening meetings. I want to thank Yaohua Tan, Yunkun Xie, Kamaram Munira, Jingjie Zhang, Mirza M. Elahi, Sheikh Z. Ahmed and Carlos A. Polanco, for their time, interest and collaboration with first principles parameters. I also thank the new students, they given me the chance to share and pass along my research experience. I also need to thank my collaborators from University of Alabama, Northwest University, Southern Illinois University and Virginia Tech. Nariman, Vinay and Jiangang, they really help me so much and it is fortunate for me to work with such smart people.

I want to thank all my friends in Charlottesville. Bin Wang, Zan Gao, Yunya Zhang, Naiming

Liu, Chao Liu, Haoyi Liang, Puhan Zhang, Zhanyu Yang, Jiyuan Zheng, Keye Sun, Yuan Yuan, Qianhuan Yu and so on. Without your short but significant association, my Ph.D. life could not be filled with such many happiness.

I want to thank my beloved friend, Guangchuan "Craig" Yang. I still remember the day I met him for the first time back in 2006. We shared wonderful memories of senior high school together. Then during college and PhD years we stayed connected by WeChat, even half a globe away. It is this bromance that encourages, comforts, and supports me through this long and uneven journey. I believe we will continue to be there for each other in the days to come. Thank you, and love you.

Last but not least, I want to thank my father, mother and sister for their unconditional support. My discipline and self-drivability are qualities inherited from them. I thank my parents for their wise counsel and sympathetic ear all along my Ph.D. journey. You are the most important persons to me and I will be back with you in one day.

Contents

List of Tables

List of Figures

Chapter 1

Introduction

1.1 Spintronics Background and Heusler Compounds

As the channel length keeps on reducing, the conventional electronic logic transistors approach their physical limits and suffer from excessive leakage current [5]. To extend the life of Moore's Law, a series of novel techniques to reduce the off-chip power has been proposed and studied, such as fin-field effect transistor (FinFET), Si-nanowire MOSFET, Carbon nanotube field effect transistor (CNTFET) and other 2D materials-based FET [6–9]. Although they have presented high performance, transconductance and low power consumption, they are still at an early stage of feasibility study compared with conventional CMOS devices.

Another way which may allow the microelectronics industry go beyond Moore's Law is spintronics. Spintronics has emerged in the last two decades as a fertile research field based on the properties and usefulness of the spin degree of freedom of the electron. The studies of spintronics started in 1988 with the discovery of giant magetoresistant (GMR) effect in a multilayer structure composed of ferromagnets and a metallic spacer layer [10] , which laid the foundation for future success of hard disk drives (HDD), allowing for the significant increase in the area density due to the increasing sensitivity of the GMR read heads [11]. From 2001, with the advent of new tunneling insulator MgO, magnetic tunneling junction (MTJ) have now become mature enough to become commercial magnetoresistive random access memory (MRAM) products [12, 13]. Not only in data storage application, exploiting spintronics for logic computation is also a topic of growing interest due to the non-volatility, which could give computing systems zero static power and instant ON-OFF

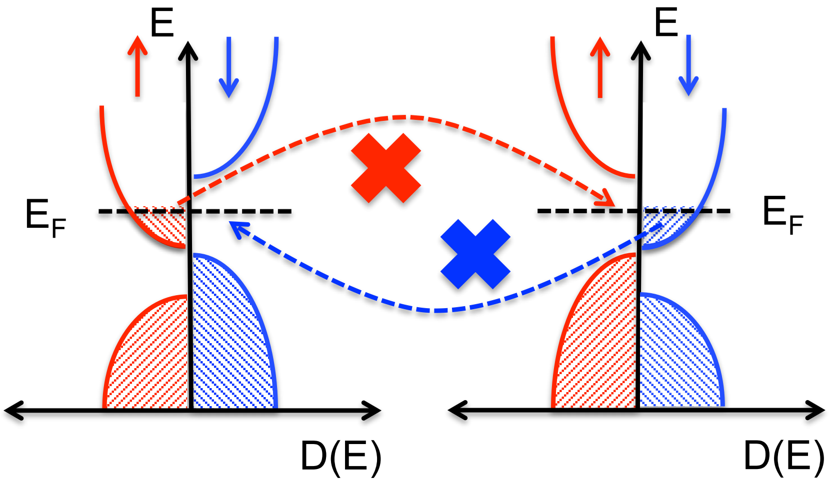

Figure 1.1: Electron tunneling in a MTJ using half-metallic electrodes in the anti-parallel magnetization configuration. The left and right represent two schematic density of states $D(E_F)$ for half-metals. The occupied states are indicated by filled areas. The arrows indicate the majority (↑) and minority (↓) states.

features [14, 15]. Both spin memory and spin logic devices require high spin polarization material to generate high magnetoresistance and spin current to encode logic 1 and logic 0. So efficient generation of a spin-polarized current, which consists of motion of electrons with ordered spins, is an essential issue in spintronics.

The spin polarization at Fermi level E_F is usually defined theoretically by the below given relation:

$$\mathcal{P}(E_F) = \frac{N_{\uparrow}(E_F) - N_{\downarrow}(E_F)}{N_{\uparrow}(E_F) + N_{\downarrow}(E_F)} \tag{1.1}$$

where $N_{\uparrow}$ and $N_{\downarrow}$ are the density of states for majority (spin-up) and minority (spin-down) electrons, respectively. The current method to generate polarized spin current is using conventional ferromagnetic materials, e.g., Fe, Co, Ni, and Gd. But these conventional ferromagnets only contain a spin polarization of $\leq 50\%$ [16], so they cannot inject a strongly polarized current into the non-magnetic spacer. Therefore, a highly spin-polarized ferromagnet is necessary as junction electrode and spin injector in spin memory and spin logic device, respectively.

If $N_{\downarrow} = 0; \mathcal{P} = 1$ in this case only majority spins are there and the spin polarization is 100%. Such materials are known as half-metal. As shown in Fig. 1.1, in the half-metal, the majority spin channel shows the typical metallic behavior, and the minority spin channel exhibits a semiconducting behavior with a band gap at the Fermi level, resulting in 100% spin polarization at the Fermi level and thus a fully spin-polarized current should be feasible in this material. There are a series of half-metals have been studied theoretically and experimentally. M. Bowen et al. studied the spin-conserving process of tunneling between $La_{0.7}Sr_{0.3}MnO_3$ half-metallic electrodes across an ultrathin $SrTiO_3$ insulator [17]. This experiment demonstrated that the class of half-metals indeed exists at non-zero temperatures, even at interfaces. Other known half-metals except for $La_{0.7}Sr_{0.3}MnO_3$ are some oxides (e.g. CrO_2) [18], the double perovskites (e.g. Sr_2FeReO_6) [19], and the pyrites (e.g. CoS_2) [20] and the transition metal chalcogenides (e.g. CrSe) [21]. Although thin films of CrO_2 and $La_{0.7}Sr_{0.3}MnO_3$ have been verified to present practically 100% spin polarization at the Fermi level at low temperatures, they haven't been observed to keep the half-metallicity at room temperature and suffer from their relative low Curie temperature [21–25].

The Heusler compounds hold the greatest potential to realize half-metallicity at room temperature due to their relatively high Curie temperature compared to previous half-metallic materials, lattice constant matching with major spacers (such as III-V semiconductors and MgO) [26, 27]. The family of Heusler compounds has three subfamilies, full-Heuslers(X_2YZ), half-Heuslers(XYZ), and inverse-Heuslers(X_2YZ), and their crystal structures are presented in Fig. 1.2 c, d and e, respectively. The three subfamilies are most easily visualized by beginning with a bcc lattice represented by the familiar cubic cell shown in Figure 1.2a with all X-type atoms. If the center atom is made different from the atoms at the corners, the structure becomes the B2 structure with composition XY (Figure 1.2b). If, in addition, alternate atoms at the corners are made different, (shown in the larger cell of Figure 1.2c) the structure becomes the full-Heusler or $L2_1$ structure with composition X_2YZ. The half-Heusler structure or $C1_b$(composition XYZ) can be visualized by removing half of the X atoms as shown in Figure 1.2d. The inverse-Heusler structure or XA structure (composition X_2YZ) is obtained by switching an X atom with a Y or Z as shown in Figure 1.2e. The X and Y atoms are typically transition metals (at least for the systems that are potential half-metals), while the Z atom is typically an s-p metal.

This large compound family exhibits diverse magnetic phenomena like itinerant and localized magnetism, antiferromagnetism, helimagnetism, Pauli paramagnetism or heavy-fermionic behavior [26,28,29]. Especially, the most famous half-metal, half-Heusler NiMnSb, was uncovered in 1983 by de Groot and collaborators [30]. Although the half-metallicity in the NiMnSb film was lost in experiment due to the segregation of Sb and Mn in the surface [31], it also sparked a heat wave to search other

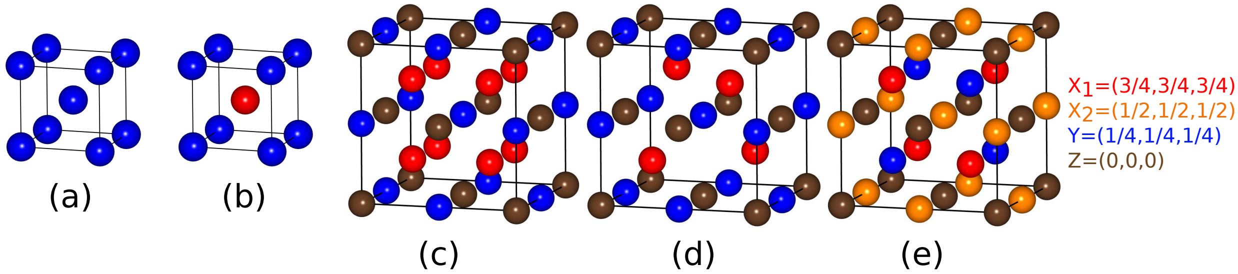

Figure 1.2: Schematic representation of full-Heusler $L2_1$ structure, half-Heusler $C1_b$ structure and inverse-Heusler XA structure. (a) The BCC body-center cubic structure. (b) The B2 cubic structure. (c) The $L2_1$ structure consists of four interpenetrating fcc sublattices with atomic sites X_1 $\left(\frac{3}{4}, \frac{3}{4}, \frac{3}{4}\right)$, X_2 $\left(\frac{1}{4}, \frac{1}{4}, \frac{1}{4}\right)$, Y $\left(\frac{1}{2}, \frac{1}{2}, \frac{1}{2}\right)$, and Z (0, 0, 0). (d) The $C1_b$ structure consists of three interpenetrating fcc sublattices with atomic sites X $\left(\frac{1}{4}, \frac{1}{4}, \frac{1}{4}\right)$, Y $\left(\frac{1}{2}, \frac{1}{2}, \frac{1}{2}\right)$, and Z (0, 0, 0). (e) The XA structure consists of four interpenetrating fcc sublattices with atomic sites X_1 $\left(\frac{3}{4}, \frac{3}{4}, \frac{3}{4}\right)$, X_2 $\left(\frac{1}{2}, \frac{1}{2}, \frac{1}{2}\right)$, Y $\left(\frac{1}{4}, \frac{1}{4}, \frac{1}{4}\right)$, and Z (0, 0, 0). In the XA structure, X_1 and X_2 have the same transition metal elements and their valence smaller than Y.

novel half-metals in Heusler compound family. So far, numerous full-Heusler, half-Heusler and inverse-Heusler compounds have been predicted to be half-metallic by first-principles calculations [32–42]. Many experimentalists have fabricated a series of Heulser compounds successfully, and a 100% spin polarization for bulk Heusler compound, such as NiMnSb, was confirmed by polarized positron annihilation experiments and inverse photoemission [43–45]. The surfaces and interfaces, however, do not show half-metallicity, which can partly be explained by the disorder, defects, and vacancies at the interfaces [31, 46, 47]. The highest surface $\mathcal{P}$ value is obtained with 93% for Co_2MnSi, which is less than predicted 100% [48, 49]. Fortunately, a magnetic tunneling junction can still achieve impressive Tunnel magnetoresistance(TMR) ratio based on Heusler compounds. The highest record of TMR ratio around 2610% at 4.2K and 429% at room temperature was obtained by quaternary Heusler compound thin films of Co_2(Mn,Fe)Si [50]. Similar TMR ratios were also gained in the Co_2FeAl-based MJT device with 360% at room temperature and 785% at 10K [51], and in the Co_2MnSi-based MTJ device with 1995% at 4.2K and 354% at room temperature [52, 53]. All the experimental results of MTJs based on Heusler compounds are summarized in Fig.1.3.

Those results proved that Heusler compounds still have the potential to be the electrode material as spintronic devices, and searching out more effective Heusler compounds for spintronics application is significant and necessary. Although numerous Heusler compounds have been predicted to be half-metallic by first-principles calculations [32–36], a comprehensive study of the structural, electronic and magnetic properties of the Heusler family is useful, because it is not clear which of the many

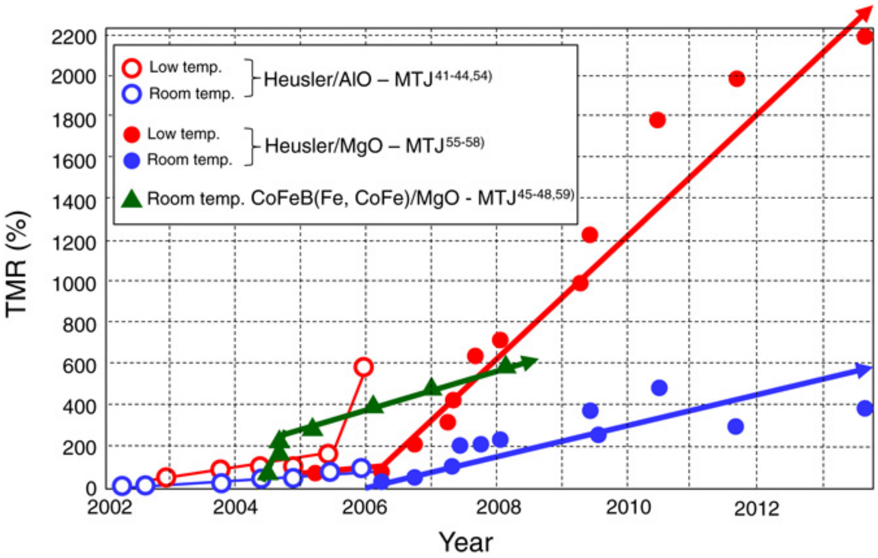

Figure 1.3: Change in TMR ratio. Annual changes in the TMR ratio at low and room temperatures are shown for devices with different compositions of the ferromagnet and insulator [1].

half-metallic Heuslers that can be imagined, are stable. Thus, a systematic study of structural stability of the half- ($C1_b$) and inverse-Heusler (XA) family should provide guidance for future experiments. We will also estimate the basic current-voltage characteristics for the Heusler/MgO magnetic tunnel junction in this dissertation.

Recent development in understanding various topological excitations has spurred great interests in exploiting the topology of materials for spintronics applications that could potentially lead to better devices. Magnetic Skyrmion is one interesting system for future spintronics. Magnetic skyrmions are topological excitations that can be used as the information carrier. Magnetic skyrmions share similar properties as magnetic domains: they can be nucleated, annihilated, and driven by various mechanisms. Magnetic skyrmions can stabilize in smaller sizes and are essential zero- dimensional objects compared to their counterpart, which could mean higher packing density and other advantages. The potential Heusler compounds to manipulate ultrasmall and fast skyrmion will be exploited in this dissertation.

1.2 Dissertation Organization

In the remainder of this dissertation, we will discuss the DFT calculation results for the half-Heusler compounds, inverse-Heusler compounds, the half-Heusler/MgO junctions, and ideal inverse-Heusler candidates for magnetic skyrmion. The basic and most used theoretical methods are outlined in chapter 2. In chapter 3, we will start by describing how to design a half-metal based on the tight-binding toy model. Then we will describe the process of ground state structure determination for half-Heusler compounds and the phase stability concept. Following that, we use formation energy and hull distance to discuss how to estimate the structural stability of half-Heusler compounds. The semiconductors, half-metals and near half-metals in half-Heusler will be listed successively. In chapter 4, the similar analysis flow about structural stability and magnetism for inverse-Heusler will be represented. The stable novel near half-metals in inverse-Heusler family will be listed out. In chapter 5, we extend our discussion to the interface properties and I-V behavior of the half-Heusler/MgO junction. For magnetic skyrmion (chapter 6), we will look for the exchange coupling, Neel temperature and Gilbert damping parameters for the selected 9 inverse-Heusler compounds to demonstrate they are ideal material candidates to manipulate ultrasmall and fast skyrmion. The final conclusion will be summarized in chapter 7

Chapter 2

Theoretical Background

Investigating ground state properties of quantum mechanical systems is a challenging task. Where the hydrogen atom as a two-body problem can be solved analytically, this is very difficult for helium. Numerically, small quantum systems can be solved, e.g., via matrix diagonalization. However, as the dimension of the underlying parameter space scales exponentially with the system size, computational limits are reached very quickly. Walter Kohn, one of the founders of the density functional theory (DFT), estimated in his Nobel prize lecture: The parameter space required for a system of 100 interacting particles would already severely exceed the number of baryons in the universe. He called this fact the "exponential wall" [54].

Therefore, complex many-body system like solids require different methods to solve. One of the most well-known approaches is DFT. In this chapter, a simple introduction to DFT is given in Sec. 2.1 followed by a brief review of the two implementations used in this work in Sec.2.2. A pathway to estimate Curie Temperature of magnetic materials based on the results from DFT is discussed in Sec. 2.3. Finally, the linear response formalism to calculate the Gilbert damping is described in Sec.2.4. We need to point out that almost all the equations in this chapter are programmed in the commercial tools, not developed and solved by ourselves.

2.1 Density Functional Theory (DFT)

Density functional theory as formulated by Hohenberg and Kohn in 1964 [55] is an exact theory of an interacting electron gas in an external potential. In the case of a solid or a molecule, the external potential is the Coulomb potential of the nuclei, which are assumed as fixed (Born-Oppenheimer-Approximation). The Hamiltonian of the many-electron system can be written as

$$\hat{H} = -\frac{1}{2}\sum_i \nabla_i^2 + \frac{1}{2}\sum_{i \neq j} \frac{1}{|\boldsymbol{r}_i - \boldsymbol{r}_j|} + \sum_i V_{ext}(\boldsymbol{r}_i) + E_{nn} \tag{2.1}$$

in which the first term is the kinetic energy, the second term is the Coulombic repulsion between electron pairs, and the third term represents the energy of the electrons in the external potential. E_{nn} is the classical interaction of the nuclei and also contains all other contributions to the energy that do not influence the electrons. The stationary solution of the N-electron Schrödinger equation has the form $\Psi(\boldsymbol{r}_1, \ldots, \boldsymbol{r}_N)$. The electron density $n(\boldsymbol{r})$ is given by expectation value of the density operator $\hat{n}(\boldsymbol{r}) = \sum_{i=1}^{N} \delta(\boldsymbol{r} - \boldsymbol{r}_i)$:

$$n(\boldsymbol{r}) = \frac{\langle \Psi | \hat{n}(\boldsymbol{r}) | \Psi \rangle}{\langle \Psi | \Psi \rangle} \tag{2.2}$$

The total energy is the expectation value of the Hamiltonian:

$$E = \left\langle \hat{H} \right\rangle := \frac{\left\langle \Psi \middle| \hat{H} \middle| \Psi \right\rangle}{\langle \Psi | \Psi \rangle} \tag{2.3}$$

2.1.1 The Hohenberg-kohn Theorems

Hohenberg and Kohn proved the following two theorems [55]:

1. Theorem I: For any system of interacting particles in an external potential $V_{ext}(\boldsymbol{r})$, this potential is determined uniquely up to an additive constant by the ground state particle density $n_0(\boldsymbol{r})$. Since the Hamiltonian is thus fully determined up to a constant shift of the energy, it follows that the many-electron wavefunctions are determined. Therefore all properties of the system are completely determined by the ground state density $n_0(\boldsymbol{r})$.

2. Theorem II: A universal functional for the energy $E[n]$ in terms of the density $n(\boldsymbol{r})$ can be defined, valid for any external potential $V_{ext}(\boldsymbol{r})$. For any particular $V_{ext}(\boldsymbol{r})$, the exact ground state energy of the system is the global minimum value of this functional, and the density $n(\boldsymbol{r})$ that minimizes the functional is the exact ground state density $n_0(\boldsymbol{r})$. The functional $E[n]$ alone is sufficient to determine the exact ground state energy and density.

In brief, the Hohenberg-Kohn theorems state that there is a one-to-one correspondence between the ground-state density and the ground-state potential. So the ground-state density is the global minimum of the energy function $E[n]$. Thus, the energy minima can be determined from a variational calculation.

Similar with the many-body Hamiltonian (2.1), the Hohenberg-Kohn total energy functional $E_{HK}(n)$ is:

$$E_{HK}[n] = T[n] + E_{int}[n] + \int V_{ext}(\boldsymbol{r})n(\boldsymbol{r})d\boldsymbol{r} + E_{nn} \tag{2.4}$$

where $T[n]$ is the electron kinetic energy and $E_{int}[n]$ is the interaction energy among the electrons. These terms can be gathered in a universal functional of the density, i.e., one that is the same for all electrons systems:

$$F_{HK}[n] \coloneqq T[n] + E_{int}[n] \tag{2.5}$$

If this functional was known, one could find the ground state by minimizing the total energy with respect to the density $n(\boldsymbol{r})$.

A generalization to spin-polarized systems is easily possible. A zeeman term is added to the Hamiltonian, which is different for spin up and down electrons in the presence of a magnetic field. In this case, two densities, one for each spin, are defined and satisfy the Hohenberg-Kokn-Theorems individually. So the density is $n(\boldsymbol{r}) = n(\boldsymbol{r}, \uparrow) + n(\boldsymbol{r}, \downarrow)$, and the spin density is given by $s(\boldsymbol{r}) = n(\boldsymbol{r}, \uparrow) - n(\boldsymbol{r}, \downarrow)$.

2.1.2 The Kohn-Sham Ansatz

The density functional theory as formulated by Hohenberg and Kohn lacks two central points: First, the functional $F_{HK}[n]$ is unknown in general. Therefore, a simple variational approach to find the ground density is impossible. Second, although there is a unique correspondence between the ground state density and properties of the solid, there is no way known how to extract them from the density.

Kohn and Sham proposed in 1965 to replace the full interacting many-body problem with a simpler, non-interacting auxiliary problem [56]. Their ansatz rests on the assumption that the ground state density of the interacting system can be expressed by the ground state density of a properly chosen non- nteracting system. The key idea is to reintroduce orbitals for non-interacting electrons and put the many-body problem into an exchange-correlation functional of the density. This way, the Hohenberg-Kohn functional $F_{HK}[n]$ becomes simply the kinetic energy of the non-interacting ficticious electrons.

The auxiliary Kohn-Sham Hamiltonian, replacing Eq.2.1, is defined by

$$H^{\sigma}_{KS} = -\frac{1}{2}\nabla^2 + V^{\sigma}_{KS}(\boldsymbol{r}) \tag{2.6}$$

where σ denotes the spin-index. The $N = N_{\uparrow} + N_{\downarrow}$ electrons occupy orbitals $\psi^{\sigma}_i(\boldsymbol{r})$ with the lowest eigenvalues determined by the Schrödinger-like Kohn-Sham equations:

$$(H^{\sigma}_{KS} - \epsilon^{\sigma}_i)\psi^{\sigma}_i(\boldsymbol{r}) = 0 \tag{2.7}$$

where ϵ_i are the corresponding Kohn-Sham eigenvalues. The density of the Kohn-Sham system is given by:

$$n(\boldsymbol{r}) = \sum_{\sigma}\sum_{i=1}^{N^{\sigma}} |\psi^{\sigma}_i(\boldsymbol{r})|^2 \tag{2.8}$$

and the Kohn-Sham kinetic energy is

$$T_s = \frac{1}{2}\sum_{\sigma}\sum_{i=1}^{N^{\sigma}} |\nabla\psi^{\sigma}_i(\boldsymbol{r})|^2 \tag{2.9}$$

The classical Coulomb interaction energy of the electron density with itself is given by the Hartree energy

$$E_{Hartree}[n] = \frac{1}{2}\int \frac{n(\boldsymbol{r})n(\boldsymbol{r}')}{|\boldsymbol{r}-\boldsymbol{r}'|} d\boldsymbol{r} d\boldsymbol{r}' \tag{2.10}$$

With these ingredients, the Hohenberg-Kohn total energy functional (3.4) can be rewritten as

$$E_{KS}[n] = T_s[n] + E_{Hartree}[n] + \int V_{ext}(\boldsymbol{r})n(\boldsymbol{r})d\boldsymbol{r} + E_{nn} + E_{xc}[n] \tag{2.11}$$

where all unknown contributions due to interaction and correlation are merged in the so called exchange-correlation functional $E_{xc}[n]$. Simply spoken, $E_{xc}[n]$ contains all errors introduced by the reduction to a non-interacting system except the classical Coulomb interaction between the electrons.

The Kohn-Sham potential $V_{KS}^{\sigma}(r)$ can be expressed in terms of variations with respect to the density as

$$V_{KS}^{\sigma}(\boldsymbol{r}) = V_{ext}(\boldsymbol{r}) + \frac{\delta E_{Hartree}}{\delta n(\boldsymbol{r},\sigma)} + \frac{\delta E_{xc}}{\delta n(\boldsymbol{r},\sigma)} =: V_{ext}(\boldsymbol{r}) + V_{Hartree}(\boldsymbol{r}) + V_{xc}^{\sigma}(\boldsymbol{r}) \tag{2.12}$$

As Eq.2.12 depends on the density computed from the solution of Eq.2.7, one has to iterate the equations to self-consistency, starting from an initial guess (from, *e.g.*, a superposition of atomic densities).

2.1.3 The Exchange-Correlation Function

The Kohn-Sham ansatz is an exact way to find the exact ground-state density and total energy, no approximations have been made yet. Unfortunately, the exchange-correlation functional is not known. The major obstacle of solving the full many-body problem has been reformulated with the Kohn-Sham equations, so that most of the total energy of the electron system is calculated correctly. Only a small fraction of the total energy, the exchange-correlation energy, has to be approximated. Two different paradigms for the derivation of the approximations can be distinguished: empirical and non-empirical. While empirical functions are constructed to match experimental datasets as good as possible, non-empirical functions are constructed based on known physical constraints, which the functional has to obey.

Local Density Approximation (LDA)

The major remaining task is to find a suitable approximation for the exchange-correlation (xc) functional $E_{xc}[n]$. Historically, the most important approximation is based on the homogeneous electron gas (HEG), where electrons are considered to move on a positive background charge distribution created by the nuclei. The xc functional can now be written in the simple form

$$E_{xc}^{LDA}[n] = \int n(\boldsymbol{r}) e_{xc}^{HEG}(n(\boldsymbol{r})) d\boldsymbol{r} \tag{2.13}$$

Here, e_{xc}^{HEG} is the energy density of the HEG. In this case E_{xc} only depends on the local value of the density, so the approximation is called local density approximation (LDA). As the exchange contribution is known analytically, the energy density can be split into exchange and correlation parts:

$$e_{xc}^{HEG}(n(\boldsymbol{r})) = e_{x}^{HEG}(n(\boldsymbol{r})) + e_{c}^{HEG}(n(\boldsymbol{r})) \tag{2.14}$$

The explicit expression for the correlation part is unknown, hence its determination remains subject to an approximation. First, approximations based on perturbation theory have been developed [57, 58]. Modern expressions are parameterized using data of quantum Monte Carlo simulations of the HEG [59]. As the HEG resembles a perfect metal, the LDA is well suited, *e.g.*, for metallic solids. Moreover, it also works surprisingly well for other systems like molecules, as it incorporates a systematic error cancellation [60]. Nevertheless, LDA tends to overestimate binding energies resulting in too short bond lengths. Examples for LDA xc functionals are implementations of Vosko, Wilk, and Nusair (VWN) [61] or Perdew and Wang (PW) [62].

Generalized Gradient Approximation (GGA)

In real systems the electron density is in general inhomogeneous, so non-vanishing density gradients occur. The LDA can be considered as a zeroth-order approximation of a general expansion in terms of the density and its derivatives. Hence, an extension to LDA are functions which not only depend on the local value, but also on density gradients. So called gradient expansion approximations tried to include higher-order corrections in terms of $|\nabla n(\boldsymbol{r})|$, $\left|\nabla^2 n(\boldsymbol{r})\right|$ etc., but almost always failed to improve the results. A breakthrough was made by introducing a more general functional of $n(\boldsymbol{r})$ and $\nabla n(\boldsymbol{r})$, the generalized gradient approximation (GGA), instead of a power series like expansion. Such a GGA functional takes the form

$$E_{xc}^{GGA}[n] = \int f(n(\boldsymbol{r}), \nabla n(\boldsymbol{r})) d\boldsymbol{r} \tag{2.15}$$

where there are generally no restrictions for the functional f . The GGA functions are especially useful for systems with a significant inhomogeneous electron density. Regarding applicability, they can behave quite differently due to their choice of f. One of the most used GGA functions in solid state physics is the implementation of Perdew, Burke and Ernzerhof (PBE) [62]. The PBE function corrects the overestimation of binding energies in the LDA, but systematically overestimates the bond lengths slightly.

Many functions such as the PBE function are non-empirical, i.e., not based on any experimentally measured values. This is the essence of *ab initio* calculations, as they are only based on fundamental physics without the use of any empirical values. However, empirical functions supported by experimental data also exist, which aim to reproduce this data well.

2.1.4 Periodic Boundary Conditions

In solid state physics we deal with crystals, i.e. ideal - at least in theory - periodic systems. Here, the nuclei are perfectly ordered on a periodic lattice, thus the potential the electrons are moving in is periodic as well. Consequently, the whole problem becomes periodic and allows us to apply periodic boundary conditions. Hence, we are able to deduce bulk properties from a primitive unit cell of the crystal containing only a few atoms. For a periodic potential $V(\boldsymbol{r}) = V(\boldsymbol{r} + \boldsymbol{R})$, where $\boldsymbol{R} = n_1\boldsymbol{a}_1 + n_2\boldsymbol{a}_2 + n_3\boldsymbol{a}_3 (n_j = 0, 1, 2 \ldots)$ is an arbitrary translation along the lattice vectors $\boldsymbol{a}_j$, the *Bloch theorem* states that solutions of the Schrödinger equation take the general form

$$\psi_{\boldsymbol{k}}(\boldsymbol{r}) = \exp(i\boldsymbol{k} \cdot \boldsymbol{R}) u_{\boldsymbol{k}}(\boldsymbol{r}) \tag{2.16}$$

where $u_{\boldsymbol{k}}(\boldsymbol{r} + \boldsymbol{R}) = u_{\boldsymbol{k}}(\boldsymbol{r})$ has the same periodicity as the crystal lattice (and thus $V(\boldsymbol{r})$). Therefore, except for a phase factor, the wave functions are periodic as well:

$$\psi_{\boldsymbol{k}}(\boldsymbol{r} + \boldsymbol{R}) = \exp(i\boldsymbol{k} \cdot \boldsymbol{R}) \psi_{\boldsymbol{k}}(\boldsymbol{r}) \tag{2.17}$$

From this it follows that the probability distribution and thus the electron density is also periodic. The Kohn-Sham equations can be separately solved for each $\boldsymbol{k}$ of the first Brillouin zone in the reciprocal space, leading to a band structure of energy eigenvalues. In principle we would need to integrate over the whole Brillouin zone. However, in practice, this integration can be approximated by a weighted summation, as the wave functions vary slowly with $\boldsymbol{k}$. The electron density is therefore calculated by

$$n(\boldsymbol{r}) = \frac{1}{N_k} \sum_{\boldsymbol{k}} n_{\boldsymbol{k}}(\boldsymbol{k}) \tag{2.18}$$

where $n_{\mathbf{k}}(\mathbf{r})$ is the electron density for a given $\mathbf{k}$ and N_k the number of k-points. The numerical results crucially depend on an adequate choice of N_k. Fortunately, it is possible to exploit symmetries of the crystal lattice. The summation over the Brillouin zone can be reduced to an irreducible wedge, and the result extended to the whole Brillouin zone via symmetry operations. Nevertheless, convergence regarding the chosen k-point mesh has to be ensured for each system separately to obtain consistent results.

2.2 DFT Implementations

In the following sections we will briefly discuss the DFT implementations and codes used in this work. Fundamental investigations are done using the Vienna *Ab Initio* Simulation Package (VASP) [63,64]. In order to determine Curie temperatures and damping parameters for magnetic materials, exchange parameters and are calculated using the Munich spin-polarized relativistic Korringa-Kohn-Rostoker (SPR-KKR) package [65].

A very convenient choice to write down the periodic part of the wave function is an expansion in terms of plane waves, where the expansion is cut off at a certain wave vector. Plane waves are solutions of the free electron Schrödinger equation, so this is a reasonable choice while dealing with metal-type materials, where the free electron assumption approximately applies. Furthermore, the implementation of the Hamiltonian as well as the calculation of energies is trivial. However, due to the deep Coulomb potential in close vicinity to the nuclei, the orthogonal wave functions are rapidly varying. An adequate expansion would require an enormous set of plane waves.

There are different approaches facing this problem. The augmented plane waves (APW) method divides the space into nuclei centered non-overlapping augmentation spheres and an interstitial region. Within the augmentation spheres, the wave functions are augmented by various approaches such as atomic orbitals. For this method, a matching of the APWs with the plane wave expansion in the interstitial region at the sphere boundary is necessary.

Another approach uses pseudopotentials. Electrons are usually divided into core and valence electrons. The first ones are localized close to the nucleus, e.g. $1s$, $2s$, $2p$ states and so on, and their states are assumed not to change in different environments. Further away from the nuclei only the valence electron states are non-zero resulting in much smoother wave functions. Pseudopotentials for isolated atoms then are created by pre-calculating an effective potential of the nuclei in conjunction with the core electrons. The resulting potential leads to smoother wave functions significantly reducing the necessary size of the plane wave basis set. The Kohn-Sham equations are then only solved for the valence electrons. An all-electron wave function is lost, and corresponding information about core-related quantities, e.g., hyperfine fields, cannot be obtained.

2.2.1 Vienna Ab Initio Simulation Package (VASP)

Besides the pseudopotential method, VASP supports the projector augmented wave (PAW) method invented by Peter Blöchl in 1994 [66]. It provides special advantages compared to APW or pseudopotential methods, hence it is used for most of the calculation presented in this work. A brief introduction to the method follows based on two introductory papers by Blöchl [67].

In principle, the PAW method is a merging of the ideas behind APW and pseudopotentials. In fact, APW methods can be obtained as a special case and the pseudopotential method by a well-defined approximation of the PAW method [66]. The idea is to define a transformation $\hat{T}$ by

$$|\Psi\rangle = \hat{T}\,|\tilde{\Psi}\rangle \tag{2.19}$$

which transforms an auxiliary smooth wave function $|\tilde{\Psi}\rangle$, solution of the single-particle Kohn-Sham equation Eq.2.7. In the following, original, untransformed functions are referred to as all-electron (AE) functions, whereas transformed functions, marked with a tilde, are referred to as pseudo (PS) functions. For the sake of clarity, we drop any index and deal with a single wave function only. As the wave functions are naturally smooth in the valence region, a transformation is only required within a certain distance to the nucleus. A radius r_c^a defines an augmentation region Ω, similar to APW methods, around the atom a at position $\mathbf{R}^a$, where $|\mathbf{r} - \mathbf{R}^a| \leq r_c^a$. Requiring $\hat{T}$ to affect the wave function only within these non-overlapping augmentation regions, we can write it in a site-wise form

$$\hat{T} = 1 + \sum_a \hat{T}_a \tag{2.20}$$

The sum runs over all atoms a with the atom-centered transformations $\hat{T}_a$. Within the Ω_a regions we expand the PS wave function $|\tilde{\Psi}\rangle$ into partial waves $|\tilde{\Phi}_j^a\rangle$

$$|\tilde{\Psi}\rangle = \sum_j |\tilde{\Phi}_j^a\rangle \, c_j^a \text{ within } \Omega_a \tag{2.21}$$

where c_j^a are the expansion coefficients for atom a and the index j refers to quantum numbers of the partial waves. Each of the PS partial waves corresponds an AE partial wave Φ_j^a, which is the result of the transformation:

$$|\Phi_j^a\rangle = \hat{T} \, |\tilde{\Phi}_j^a\rangle = (1 + \hat{T}_a) \, |\tilde{\Phi}_j^a\rangle \text{ within } \Omega_a \tag{2.22}$$

Therefore, as in the region Ω_a only $\hat{T}_a$ has an effect, this defines the atom-centered transformations $\hat{T}_a$ by

$$\hat{T}_a \, |\tilde{\Phi}_j^a\rangle = |\Phi_j^a\rangle - |\tilde{\Phi}_j^a\rangle \tag{2.23}$$

so the transformation adds the difference between the PS partial waves and the AE partial waves. As by definition the transformation $\hat{T}_a$ has no effect outside the augmentation region, the PS and AE partial waves are equal beyond the distance r_c^a to the nucleus:

$$|\Phi_j^a\rangle = |\tilde{\Phi}_j^a\rangle \text{ for } |\mathbf{r} - \mathbf{R}^a| > r_c^a \tag{2.24}$$

We write the AE wave function by applying the transformation

$$|\Psi\rangle = \hat{T} \, |\tilde{\Psi}\rangle = \sum_j |\tilde{\Phi}_j^a\rangle \, c_j^a \text{ within } \Omega_a \tag{2.25}$$

and see that the expansion has the same expansion coefficients as the PS wave function. As the transformation $\hat{T}$ is linear, the coefficients must be linear functionals of the PS wave function $|\tilde{\Psi}\rangle$. Therefore, the coefficients are obtained by a scalar product

$$c_j^a = \langle \hat{p}_j^a | \hat{\Psi} \rangle \tag{2.26}$$

with the name-giving smooth projector functions $|p_j^a\rangle$. Without overlap of the augmentation regions, by inserting Eq.2.25 into Eq.2.21, we can deduce the completeness relation

$$\sum_j |\tilde{\Phi}_j^a\rangle \langle \tilde{p}_j^a| = 1 \tag{2.27}$$

This also implies the orthogonality $\langle \hat{p}_j^a | \tilde{\Phi}_j^a \rangle = \delta_{ij}$, where δ_{ij} is the Kronecker-Delta. Multiplying the atom-centered transformation $\hat{T}_a$ with the identity Eq.2.27 and inserting the result of Eq.2.24 we obtain the representation

$$\hat{T}_a = \sum_j \hat{T}_a |\tilde{\Phi}_j^a\rangle \langle \tilde{p}_j^a| = \sum_j (|\Phi_j^a\rangle - |\tilde{\Phi}_j^a\rangle) \langle \tilde{p}_j^a| \tag{2.28}$$

Using this, the full transformation takes the form

$$\hat{T} = 1 + \sum_a \sum_j (|\Phi_j^a\rangle - |\tilde{\Phi}_j^a\rangle) |\tilde{p}_j^a\rangle \tag{2.29}$$

Furthermore, with knowledge of the AE and PS partial waves, and the projector functions, we are able to obtain the exact AE wave function from the PS wave function by

$$|\Psi\rangle = |\tilde{\Psi}\rangle - \sum_a \underbrace{\sum_j |\tilde{\Phi}_j^a\rangle \langle \tilde{p}_j^a | \tilde{\Psi}\rangle}_{|\tilde{\Psi}^a\rangle} + \sum_a \underbrace{\sum_j |\Phi_j^a\rangle \langle \tilde{p}_j^a | \tilde{\Psi}\rangle}_{|\Psi^a\rangle} \tag{2.30}$$

This equation shows the nature of the transformation: In the first term, the smooth, pseudo part in the augmentation region is removed, and in the second term replaced by the all-electron part. By construction $|\tilde{\Psi}\rangle$ is smooth everywhere, hence much more easy to handle numerically than the original Kohn-Sham AE wave function. Inserting the transformation into the Kohn-Sham equation we get the transformed Kohn-Sham equation

$$\hat{\tilde{H}} \, |\tilde{\Psi}_n\rangle = \epsilon_n \hat{\tilde{S}} \, |\tilde{\Psi}_n\rangle \tag{2.31}$$

with the transformation Hamiltonian $\hat{\tilde{H}} = \hat{T}^\dagger \hat{H} \hat{T}$ and the overlap operator $\hat{\tilde{S}} = \hat{T}^\dagger \hat{T}$. The variational quantity for this equation is now the smooth pseudo wave function $|\tilde{\Psi}_n\rangle$. Finding the self-consistent solution for this trans- formed problem is much more feasible. No information is lost as the complete all-electron wave function of the original Kohn-Sham problem can be reconstructed. However, PAW data sets (partial wave expansions, projector functions, etc.) for each element need to be constructed in advance. This is done by highly accurate atomic DFT calculations on isolated atoms. Details about a reasonable choice for partial wave functions as well as construction of the projector functions can be found in Ref. [67]. The VASP code provides PAW data sets for all elements, which are ready to use; their construction is not part of this work.

The electronic structure of the isolated atoms is often used as a starting configuration in PAW calculations. Usually the frozen-core approximation is used, where the core states are considered well localized within the augmentation regions, and are not affected by changes of the atomic environment. In the DFT calculation, only the valence electrons will be calculated. This is equivalent to the pseudopotential approach, however, due to the PAW transformation all correlated information can be restored.

2.2.2 Munich SPR-KKR Package

A different approach to find the electronic ground state is proposed by Korringa [68], Kohn and Rostoker [69] (KKR) by means of multiple scattering theory (MST). The problem is formulated as electrons scattered by the nuclear potential. The total potential is separated into scattering centers located at each nuclei. First, the scattering properties of these centers are calculated individually. Second, the solution of the Schrödinger equation is determined by the requirement that an incident wave at one center is the sum of the outgoing waves from all other centers. Due to the formulation in multiple scattering the KKR method is not restricted to periodic systems like solids, and can be easily applied to finite systems like molecules.

In this section the fundamental considerations implemented in the Munich SPR-KKR package as of the publication by Ebert et al. [65], the authors of the code, are outlined. A very detailed introduction as well as explicit forms of quantities and functions dealt with can be found in this reference as well as in the one by Mavropoulos and Papanikolaou [70]. The KKR theory is an approach of determining the electronic structure equivalent to the usual DFT way. Instead of using the electron density, the Green's function $G(\mathbf{r}, \mathbf{r}', E)$ is introduced, which is defined by

$$(E - H)G(\mathbf{r}, \mathbf{r}', E) = \delta(\mathbf{r} - \mathbf{r}') \tag{2.32}$$

The Hamilton operator $H = H_0 + V$ is decomposed into a "free" part H_0, for which solutions $\Psi^0(\mathbf{r}, E)$ are known, and a perturbation part V. This allows us to write the Schrödinger equation in an integral form, the *Lippmann-Schwinger equation*

$$\Psi(\mathbf{r}, E) = \Psi^0(\mathbf{r}, E) + \int G^0(\mathbf{r}, \mathbf{r}', E)V(\mathbf{r})\Psi(\mathbf{r}, E)d\mathbf{r}' \tag{2.33}$$

where $G^0(\mathbf{r}, \mathbf{r_0}, E)$ is the Green's function of the unperturbed system. The Green's function in its spectral representation is

$$G^+(\mathbf{r}, \mathbf{r}', E) = \lim_{\epsilon \to +0} \sum_j \frac{\psi_j(\mathbf{r})\psi_j^*(\mathbf{r}')}{E - E_j + i\epsilon} \tag{2.34}$$

with the eigenfunctions $\psi_j(\mathbf{r})$ and the eigenvalues E_j. Poles of the Green's function indicate the eigenvalues, so the limit avoids divergencies. Using the Dirac identity $\lim_{\epsilon\to 0} \Im(x + i\epsilon)^{-1} = -\pi\delta(x)$ we can relate the Green's function to the density of states $\rho(E)$, the charge density $n(\mathbf{r})$ and the expectation value of an operator A by:

$$\rho(E) = -\frac{1}{\pi}\Im \int G^+(\mathbf{r}, \mathbf{r}', E)d\mathbf{r} \tag{2.35}$$

$$n(\mathbf{r}) = -\frac{1}{\pi}\Im \int^{E_F} G^+(\mathbf{r}, \mathbf{r}', E)dE \tag{2.36}$$

$$\left\langle \hat{A} \right\rangle = -\frac{1}{\pi}\Im \int \int^{E_F} \hat{A}G^+(\mathbf{r}, \mathbf{r}', E)dEd\mathbf{r} \tag{2.37}$$

where E_F is the Fermi energy. With the expressions above we are able to calculate all ground state properties of the system without the explicit use of the eigenfunctions. Thus, the Green's function contains all information about the system just as the ground state electron density.

The calculation of the Greens function as follows is split into a (single-site) potential and a geometrical part. For this purpose, in the full potential mode the system is split into Wigner-Seitz polyhedra centered at each nucleus, and the potential is split accordingly into non-overlapping single-site parts $V = \sum_n V^n$ within these polyhedra. The full potential in the polyhedra is expressed in an angular momentum expansion using spherical harmonics.

Now the solutions of the single-site problems are calculated, where the scattering solutions $n(\mathbf{r}, E)$ could be obtained from the Lippmann-Schwinger equation2.33. However, a major, appealing benefit of the Green's function formalism is the use of the Dyson equation, which provides an alternative approach. It allows us to write the Green's function G for a system $\hat{H} = \hat{H}^{ref} + \hat{H}^{pert}$ in terms of a Green's function $\hat{H}^{pert}$ for a simpler reference system $\hat{H}^{ref}$ with a perturbation $\hat{H}^{pert}$. The Dyson equation here in operator form is:

$$\hat{G} = \hat{G}^{ref} + \hat{G}^{ref}\hat{H}^{pert}\hat{G} \tag{2.38}$$

Interpreting the single-site problem as a free electron scattered at the potential V^n, we can write the Dyson equation for the single-site scattering problem as

$$\hat{G}^n(E) = \hat{G}^0(E) + \hat{G}^0(E)\hat{V}^n(E)\hat{G}^n(E) \tag{2.39}$$

with the perturbation V^n, where n is the site index. The free electron Green's function of the reference system corresponding to $\hat{G}^0$ is

$$G^0(\mathbf{r}, \mathbf{r}', E) = -\frac{\exp(-i\sqrt{E}\,|\mathbf{r} - \mathbf{r}'|)}{4\pi\,|\mathbf{r} - \mathbf{r}'|} \tag{2.40}$$

We remember the Lippmann-Schwinger equation in order to solve the Dyson equation. In Dirac notation, it reads $|\Psi\rangle = \left|\Psi^0\right\rangle + \hat{G}^0\hat{V}\,|\Psi\rangle$. We define a transition matrix $\hat{T}$ by

$$\hat{V}\,|\Psi\rangle = \hat{T}\left|\Psi^0\right\rangle \tag{2.41}$$

This transition matrix relates the eigenfunctions of the perturbed Hamiltonian to the eigenfunctions of the unperturbed system. It has the general form

$$\hat{T} = \hat{V} + \hat{V}\hat{G}^0\hat{T} = \hat{V}(1 - \hat{G}^0\hat{V})^{-1} \tag{2.42}$$

and can be expanded into a Born series by iterative insertion. The Dyson equation using a single-site *t-matrix* $\hat{t}^n$, which transforms the incoming wave of an electron into a scattered wave, is

$$\hat{G} = \hat{G}^0(E) + \hat{G}^0(E)\hat{t}^n(E)\hat{G}^0(E) \tag{2.43}$$

When dealing with multiple scatters we find an analogous equation for the complete problem:

$$\hat{G}(E) = \hat{G}^0(E) + \hat{G}^0(E)\hat{V}\hat{G}(E) = \hat{G}^0(E) + \hat{G}^0(E)\hat{T}\hat{G}^0(E) \tag{2.44}$$

All scattering processes can be decomposed into a series of single-site scattering events characterized by $\hat{t}^n$ and free propagation in between.Hence,the multiple scattering $\hat{T}$-matrix operator is

$$\hat{T}(E) = \sum_{nn'} \hat{\tau}^{nn'}(E) \tag{2.45}$$

using the scattering path operator $\hat{\tau}^{nn'}(E)$, which translates a wave incoming at site n' to an outgoing wave at site n. The operator takes all possible scattering events in between into consideration. The equation of motion for this operator in an angular momentum basis is

$$\underline{\tau}^{nn'}(E) = \underline{t}^n(E)\delta_{nn'} + \underline{t}^n(E)\sum_{m\neq n} G^{0nm}(E)\underline{\tau}^{mn'}(E) \tag{2.46}$$

where we note the adoption in an angular momentum basis by the underlines. Solving this problem for a finite system is done via matrix inversion by

$$\underline{\underline{\tau}}(E) = [\underline{\underline{t}}(E)^{-1} - \underline{\underline{G}}^0(E)]^{-1} \tag{2.47}$$

where double underlines include site and angular momentum indices, so in this case $[\underline{\underline{\tau}}]_{nn'} = \underline{\tau}^{nn'}$, $[\underline{\underline{G}}^0]_{nn'} = \underline{G}^{0nn'}$ and $[\underline{\underline{t}}]_{nn'} = \underline{t}^n\delta_{nn'}$. Commonly, the matrix $[\underline{\underline{t}}^{-1} - \underline{\underline{G}}^0] = \underline{\underline{M}}$ is called real-space KKR matrix. The dimension of these matrices is determined by the number of scatterers N and the angular momentum expansion, which is usually cut off at a certain maximum l_{max}. The resulting dimension is $D = N(l_{max} + 1)^2$. Hence, l_{max} crucially affects the numerical effort. Usually, a value of $l_{max} = 3$ or 4 is sufficient. This finite cutoff introduces systematic errors in the charge density resulting in a miscalculation of the Fermi energy. Lloyd proposed an analytical expression (Lloyds formula) [71] to solve this problem by an accurate charge density normalization.

For a periodic system like solids, the solution is found by a Fourier transformation of Eq into

$$\underline{\tau}^{nn'}(E) = \frac{1}{\Omega_{BZ}} \int_{\Omega_{BZ}} [\underline{t}(E)^{-1} - \underline{G}^0(\mathbf{k}, E)]^{-1} \exp[i\mathbf{k} \cdot (\mathbf{R_n} - \mathbf{R}_{n'})] d\mathbf{k} \tag{2.48}$$

where Ω_{BZ} is the Brillouin zone volume, $\mathbf{R}_n$ the positions of the nuclei and $\underline{G}^0(\mathbf{k}, E)$ the so-called reciprocal space structure constant matrix.

Similar to other DFT codes, the core electrons, which are well localized within the constructed Wigner-Seitz polyhedra, are not considered within the multiple scattering calculation. They are treated separately in a relativistic way by the Dirac equation. The problem then is solved only for the valence electrons, where the SPR-KKR package supports either a scalar-relativistic way neglecting spin-orbit coupling or a full relativistic calculation.

2.3 Calculation of Curie Temperature

One of the most important properties of magnetic materials is their transition temperature, above which no spontaneous ordering is found anymore. For ferromagnets and ferrimagnets, this temperature is the Curie temperature T_C. As these kinds of magnetism are of collective origin, a straight forward calculation from a primitive unit cell is not directly possible. Total energy differences between ferromagnetic and ferrimagnetic configurations can provide information of the interaction strength, but the estimation is typically not very accurate. The SPR-KKR package ships with an implementation of the theory by Liechtenstein et al. [72] to directly calculate the interaction between spins, the exchange coupling parameters. As this is the origin of collective magnetic ordering, we can deduce transition temperatures from the exchange parameters.

2.3.1 Exchange Coupling Interactions

An effective Hamiltonian describing the exchange interaction is the Heisenberg Hamiltonian

$$\hat{H}_{Heis} = -\sum_{i,j} \hat{\mathbf{S}}_i \mathbf{J} \hat{\mathbf{S}}_j \tag{2.49}$$

where $\hat{\mathbf{S}}_i$ is the spin operator for site i. $\mathbf{J}$ contains the interaction and can be in general a complex matrix. In a first order approximation, the spins i and j interact directly only via a single exchange coupling parameter J_{ij} . In a classical Heisenberg model, which has proven to work well [73], the spins are able to orient arbitrarily in space. The Hamiltonian consists of the unit vectors e_i pointing in the direction of the magnetic moment at site i:

$$\hat{H} = -\sum_{i,j} J_{ij} \mathbf{e}_i \cdot \mathbf{e}_j \tag{2.50}$$

To calculate these exchange parameters from an ab-initio calculation, the energy difference δE induced by a small deviation from the magnetic configuration in the ground state is calculated. This is done by rotating a pair of spins i and j by an angle $\pm\theta/2$ in real space. This requires localized magnetic moments which do not change in magnitude dependent on the spin configuration. The resulting energy difference is $\delta E_{ij} = J_{ij}(1 - \cos\theta)$. Using the local force theorem of Andersen [74] this energy difference can be expressed as

$$\delta E = \int^{E_F} E \delta\rho(E) dE = -\int^{E_F} \delta N(E) dE \tag{2.51}$$

where $\rho = dN/dE$ is the density of states. In this way,the energy difference can be calculated in the KKR Greens function formalism. Mapped to the classical Heisenberg Hamiltonian we have:

$$J_{ij} = \frac{1}{4\pi} \int^{E_F} dE \Im \mathrm{Tr}(\hat{t}^{-1}_{i\uparrow} - \hat{t}^{-1}_{i\downarrow}) \hat{\tau}^{ij}_{\uparrow} (\hat{t}^{-1}_{j\uparrow} - \hat{t}^{-1}_{j\downarrow}) \hat{\tau}^{ji}_{\downarrow} \tag{2.52}$$

The arrows denote the spin-up and spin-down operators. This Liechtenstein formula is proposed by Liechtenstein et al. in 1987 [72]. The exchange parameters J_{ij} are only calculated up to a certain cluster radius r, where sites i and j are separated by less than r.

2.3.2 Mean Field Approximation

With the atomistic pair-wise exchange coupling, we can obtain the Neel temperature from the mean field approximation:

$$\frac{3}{2}k_B T_C^{MFA} = J_0 = \sum_j J_{0j} \tag{2.53}$$

Since Heusler compounds have four sublattices, we have to solve the coupled equation:

$$\begin{aligned} \frac{3}{2}k_B T_C^{MFA} \left\langle e^{\mu} \right\rangle &= \sum_{\nu} J_0^{\mu\nu} \left\langle e^{\nu} \right\rangle \\ J_0^{\mu\nu} &= \sum_{\boldsymbol{r}\neq 0} J_{0\boldsymbol{r}}^{\mu\nu} \end{aligned} \tag{2.54}$$

where $\langle e^{\mu} \rangle$ is the average z component of the unit vector $e_{\boldsymbol{r}}^{\nu}$ in the direction of magnetic moment at site $(\nu, \boldsymbol{r})$. The coupled equation can be rewritten as eigenvalue equation:

$$\begin{aligned} (\Theta - \boldsymbol{T}\boldsymbol{I})\boldsymbol{E} &= 0 \\ \frac{3}{2}k_B \Theta_{\mu\nu} &= J_0^{\mu\nu} \end{aligned} \tag{2.55}$$

with a unit matrix $\boldsymbol{I}$ and the vector $\boldsymbol{E}^{\nu} = \langle e^{\nu} \rangle$. The Neel temperature can be calculated from the largest eigenvalue J_{max} of the Θ matrix [75, 76].

2.4 Calculation of Gilbert Damping

The Gilbert damping is calculated by the linear response formalism [77]. The approach derives from the electronic structure represented by the Green function $G^{+}(E)$. $G^{+}(E)$ is determined by means of the multiple scattering formalism [78]. The diagonal elements $\mu = x, y, z$ of the Gilbert damping tensor can be written as:

$$\alpha^{\mu\mu} = \frac{g}{\pi m_{tot}} \sum_j Tr \left\langle \mathcal{T}_0^{\mu} \tilde{\tau_{0j}} \mathcal{T}_j^{\mu} \tilde{\tau_{j0}} \right\rangle_c \tag{2.56}$$

where the effective g factor $g = 2(1 + m_{\text{orb}}/m_{\text{spin}})$ and the total magnetic moment $m_{\text{tot}} = m_{\text{spin}} + m_{\text{orb}}$ is the sum of the spin and orbital moments m_{spin} and m_{orb} ascribed to a unit cell. Eq. 2.56 gives $a^{\mu\mu}$ for the atomic cell at lattice site 0 and implies a summation over contributions from all sites indexed by j, including $j = 0$. $\tilde{\tau_{ij}}$ is given by the imaginary part of the multiple scattering operator that is evaluated at the Fermi energy E_F. $\mathcal{T}_i^{\mu}$ is represented by the matrix elements of the torque operator $\hat{\mathcal{T}}^{\mu} = \beta(\overrightarrow{\sigma} \times \hat{m}_z)_{\mu} B_{xc}(\overrightarrow{r})$ [79]. The notation $\langle \cdots \rangle$ represents the configurational average including the vertex corrections [80] derived by Bulter [81]. The configurational average accounts for finite temperature using the alloy analogy model within coherent potential approximation (CPA) [82].

Chapter 3

Screening for Novel Half-Heusler Compounds

3.1 Introduction

Although numerous half-Heusler compounds have been predicted to be half-metallic by first-principles calculations [32–36], a comprehensive study of the structural, electronic and magnetic properties of the half-Heusler family is useful, because it is not clear which of the many half-metallic half-Heuslers that can be imagined, are stable. Thus, a systematic study of the structural stability of the half-Heusler ($C1_b$) family should provide guidance for future experiments.

In this chapter, we describe a computational investigation covering 378 half-Heusler compounds using first-principles methods. We have constructed a database of their electronic, magnetic and structural properties [83], which enables us to identify potentially useful electrode/spacer materials for future spintronics applications. In Sec. 3.3 we present the details of our computational method. The techniques, codes and parameters used in our DFT calculations are described in Sec. 3.3.1. In Sec. 3.3.2 we discuss how we determine the structure with the lowest energy for each compound, and deal with the multiple solutions in energy and magnetic configuration that occur for some of these compounds. Sec. 3.3.3 describes our approach to investigating the stability of these compounds through the calculation of their formation energies and the comparison of these calculated energies to the calculated energies of other possible phases and combinations of phases.

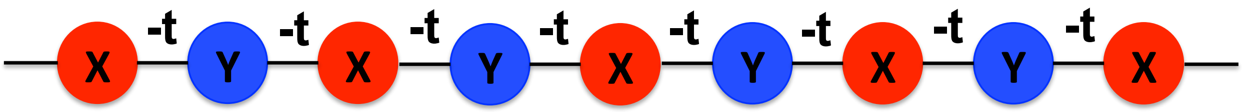

Figure 3.1: 1D atomic system with two sub lattices, type X atom sits on one sub-lattice and type Y atom sits on the other. There is only nearest neighbor interaction and the interaction is represented by the hopping parameter $-t$

In Sec. 3.4 we discuss the trends in (and the factors influencing) the formation energy and thermodynamic stability of these compounds across the periodic table. In Sec. 3.5 we list some 18-electron Slater-Pauling half-Heusler semiconductors and analyze their electronic structures and chemical bonding characteristics. In Sec. 3.6, we discuss the possibility and implications of zero-moment half-metallic Slater-Pauling half-Heusler compounds. In Sec. 3.7, we present some half-metallic and near half-metallic ferromagnets that result from our calculations in terms of the Slater-Pauling rule. For all the half-Heusler compounds presented in this chapter, we systematically discuss their thermodynamic stability relative to other competing phases in the respective chemical space. Finally, we summarize our results and conclusions in Sec. 3.8.

3.2 How to design a half-metal

To explain the origin of half-metals in the Heusler family, we need to start from a 1D atomic system with two different atoms, X and Y, as shown in Fig.3.1. We assume different on-site energies of the orbitals for X sites and Y sites, E_X and E_Y ($E_X < E_Y$), respectively. If we only consider the first-nearest-neighbor interaction, the 1D atomic chain can be described by the tight-binding Hamiltonian for the periodic array of dimers:

$$\begin{gathered} E\{\psi\}_n = [\alpha]\{\psi\}_n - [\beta]\{\psi\}_{n+1} - [\beta]^{\dagger}\{\psi\}_{n-1} \\ [\alpha] = \begin{bmatrix} E_X & -t \\ -t & E_Y \end{bmatrix}, [\beta] = \begin{bmatrix} 0 & 0 \\ t & 0 \end{bmatrix} \end{gathered} \tag{3.1}$$

where $-t$ is the coupling between nearest neighbor atoms.

Assuming periodic boundary conditions and invoking a plane wave solution (Bloch's theorem) $\psi_n \sim e^{ikna}$, we can get a band gap extending from E_X to E_Y with bandgap $E_g = E_Y - E_X$. This gap is independent of the hopping term, $-t$, letting us easily extend the 1D chain to 3D body-center cubic B2 structures [84, 85]. B2 structure can be viewed as alternate atomic layers along (001) direction only with nearest neighbor interactions (As shown in Fig. 1.2(b)), but there are no intra-layer interactions. This means that the wave vector perpendicular to the (001) plane, $k_\perp$, generates an $E - k$ expression identical to the 1-D dimer $E - k$ expression above, resulting in a gap between E_X and E_Y. Since the gap between E_X and E_Y is not dependent on $k_\parallel$, the gap will remain after integration over $k_\parallel$.

In order to create half-metallic ferromagnets, we can select different transition metal elements with $d-$orbitals on the X and Y sites. As long as the interactions are restricted to nearest neighbors, we can predict that there is still a gap between the onsite energy for the X sites and the onsite energy for the Y sites for a B2 structure.

If we assume the onsite energy is determined primarily by the onsite electron number, then we see that the system can lower its energy if it enhances the size of the gap by increasing the difference in the number of electrons for X and Y atoms, so that the Fermi energy falls inside the gap. The outermost electronic states that participate in hybridization in B2 compounds are a single $4s$ and five $3d$ orbitals, so we have nearly six bonding states below the Fermi energy. In other words, there are a total of six electrons in the gapped spin channel. We thus end up with an approximate thumb rule for these compounds: in the gapped spin channel, the approximate electron count on alternate atoms X and Y must be four and two (the '4-2' rule) [85]. If the total valence electron number is twelve, it is easy then to create a semiconductor since each spin channel has six electrons. By making the total valence electron number larger (or smaller) than 12, the majority (or minority) spin channel will now be 'doped' to be metallic, while the other spin channel remains semiconducting since the Fermi energy falls in the gap.

While the above design rule seems compelling, first principles calculations indicate that the B2 structure only achieves a pseudogap instead of a true gap. This is because of residual next nearest neighbor (NNN) interactions [85] that were not included in our consideration so far. To reduce the NNN interactions, we can replace one transition Y atom with a main group Z atom without any d-states, acting as a 'spacer' - resulting in the full-Heusler family of compounds X_2YZ (Fig.1.2 c). Furthermore, We can delete half of the X atoms to generate half-Heusler compounds XYZ with a 'cleaner' gap (Fig.1.2 d). We can also exchange the position of Y atoms and X atoms to generate

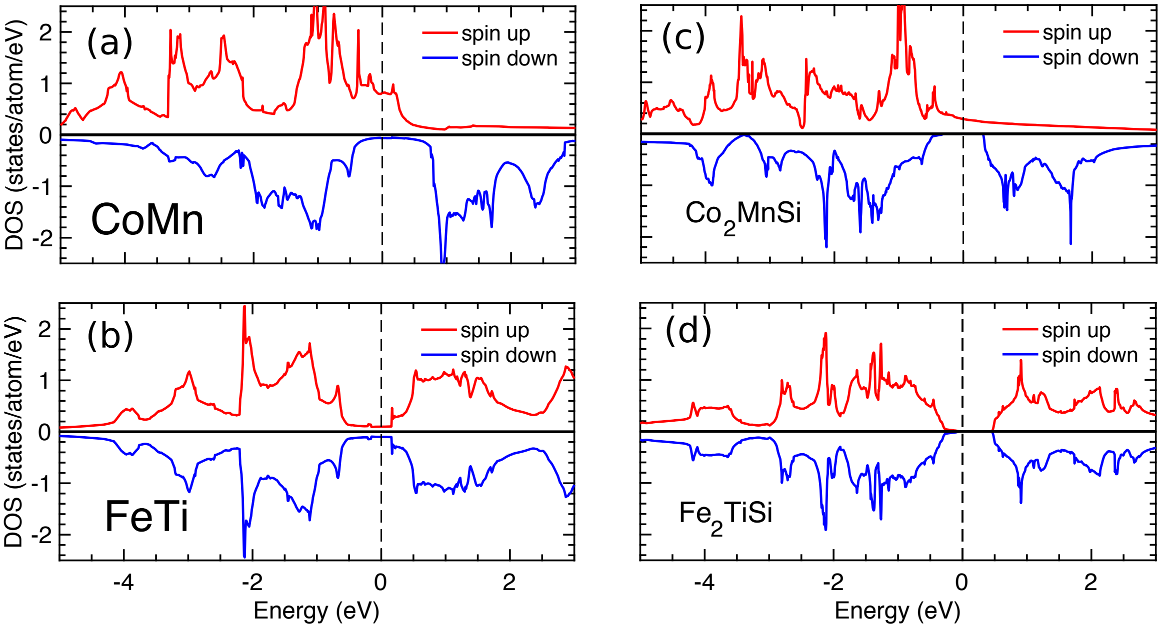

Figure 3.2: Density of States (DOS) for (a) CoMn, (b) FeTi, (c) Co_2MnSi, and (d) Fe_2TiSi. The blue color is for the majority spin channel and the red color is for the minority spin channel.

inverse-Heusler compounds X_2YZ (Fig.1.2 d). In all cases, the decreased NNN interactions will narrow the bands and prevent the density of states from tailing into the gap.

To confirm this rational design approach, We performed all calculations using Density-Functional Theory (DFT) as implemented in the Vienna Ab-initio Simulation Package (VASP) [86] to calculate the density of states for CoMn and FeTi in the B2 phase. Rather than a gap, we find a deep, wide minimum in the minority spin density of states at half-filling which we refer to as a pseudogap, with 3 electrons per atom under the Fermi energy. For the pseudogapped channel, the 4-2 rule forces X atoms (Fe or Co) to hold 4 electrons and Y atoms hold 2 electrons. As we replace one Mn or Ti with a Si spacer, the pseudogaps in B2 systems turn into real gaps, resulting in the half-metal Co_2MnSi and semiconducting Fe_2TiSi. For these two full-Heusler compounds, the spacer Si atom also holds 2 electrons in the gapped channels to sustain the '4-2' rule. We can thus create half-metals by turning B2 compounds into Heusler compounds.

Based on this idea, a large number of layered half-metallic structures can be obtained in full-Heusler, half-Heusler, and inverse-Heusler family. Let us discuss half-Heusler compounds in this section.

3.3 Computational Methods

In this study, (a) X is one of 7 elements – Cr, Mn, Fe, Co, Ni, Ru, or Rh, (b) Y is one of 6 elements – Ti, V, Cr, Mn, Fe, or Ni, and (c) Z is one of 9 elements – Al, Ga, In, Si, Ge, Sn, P, As, or Sb. In addition to these 378 ($7 \times 6 \times 9$) XYZ systems, we also perform some calculations with $Y = \mathrm{Sc}$ in order to study additional examples of half-metallic and semiconducting half-Heusler compounds. For each of the 378 potential half-Heusler compounds, we calculate its electronic and magnetic structure, stability against structural distortion, formation energy, and thermodynamic phase stability.

3.3.1 Density functional theory calculations

We perform all calculations using density-functional theory (DFT) as implemented in the Vienna Ab-initio Simulation Package (VASP) [86] with a plane wave basis set and projector-augmented wave (PAW) potentials [66]. The set of PAW potentials for all elements and the plane wave energy cutoff of 520 eV for all calculations were both chosen for consistency with the Open Quantum Materials Database (OQMD) [87, 88]. The Perdew-Burke-Ernzerhof (PBE) version of the generalized gradient approximation (GGA) to the exchange-correlation functional was adopted [89]. The integrations over the irreducible Brillouin zone (IBZ) used the automatic mesh generation scheme within VASP with the mesh parameter (the number of k-points per Å^{-1} along each reciprocal lattice vector) set to 50, which usually generated a $15 \times 15 \times 15$ Γ-centered Monkhorst-Pack grid [90], resulting in 288 k-points in the IBZ. The integrations employed the linear tetrahedron method with Blöchl corrections [91]. To achieve a higher accuracy with respect to the magnetic moment, the interpolation formula of Vosko, Wilk, and Nusair [61] was used in all calculations. Finally, during ionic relaxations, the convergence criterion for structural optimization was an energy change of less than 1×10^{-5} eV between successive ionic steps.

3.3.2 Determination of the Relaxed Structure

We explain our procedure for obtaining the relaxed structures in some detail in order to make clear that the $C1_b$ structure is not guaranteed to minimize the energy of a particular equiatomic XYZ system and that the possibility of multiple solutions to the DFT equations must be be considered when there is more than one magnetic species in the unit cell. We calculate the formation energy

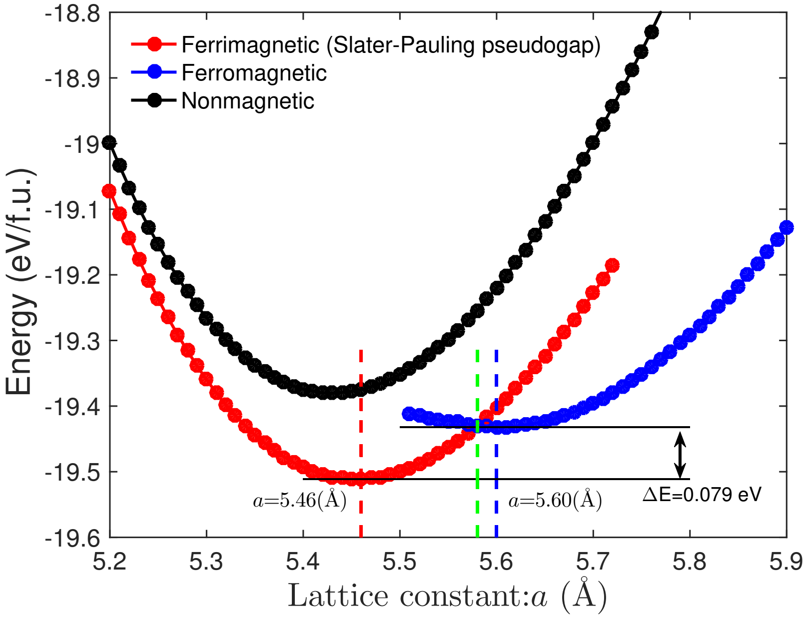

Figure 3.3: Calculated total energies of CoMnAl in the half-Heusler $C1_b$ structure as a function of the lattice constant a in ferrimagnetic, ferromagnetic, and nonmagnetic states.

using the pseudopotentials and convergence parameters consistent with the OQMD [88] so that the calculated formation energies of the half-Heusler compounds can be directly compared to those of many other phases in the OQMD.

We performed full ionic relaxations within a 6-atom tetragonal cell for all of the 378 potential half-Heusler compounds. All relaxations started from the $C1_b$ structure with small displacements to avoid vanishing of the net force on each atom due to symmetry. 300 of these compounds were found to remain in the $C1_b$ structure, 6 relaxed to a tetragonal structure ($|c/a - 1| > 0.01$), while 72 compounds relaxed to a distorted structure that was neither cubic nor tetragonal.

For all systems, we performed DFT calculations using multiple initial magnetic configurations to start the iterative process that (usually) leads to a fixed point that minimizes the energy for a given set of atoms and atomic coordinates. As we shall see, a fixed point may be a local rather than a global energy minimum. Use of multiple initial magnetic configurations including moment configurations in which the X and Y moments were parallel and anti-parallel increased our chances of finding the global minimum.

To clarify this point, we provide a few examples of XYZ systems, for which we found multiple DFT solutions with different magnetic configurations at the same or similar lattice constants. An

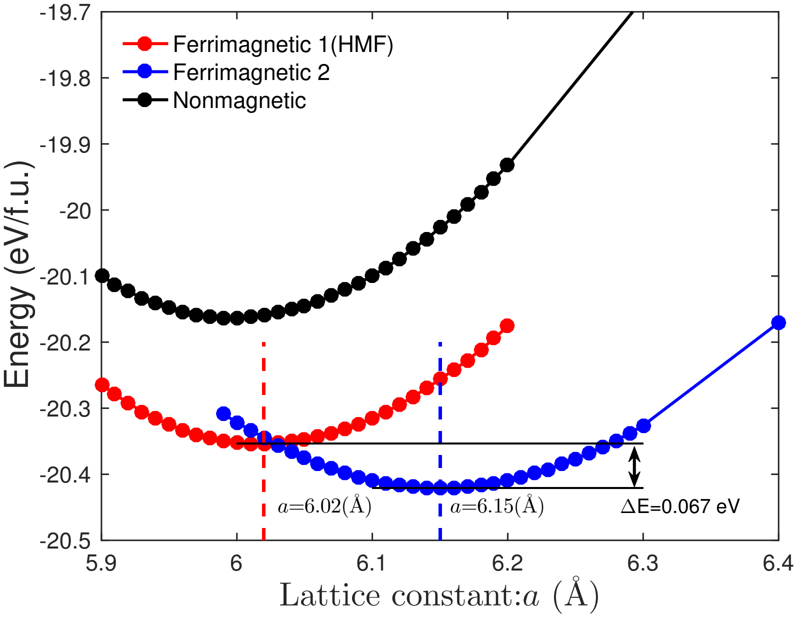

Figure 3.4: Calculated total energies of RhCrSn in the half-Heusler $C1_b$ structure as a function of the lattice constant a in two different ferrimagnetic and the nonmagnetic states.

example of competition between a ferrimagnetic phase and a ferromagnetic phase is shown in Fig. 3.3 which displays the total energy as a function of the lattice parameter for CoMnAl in the $C1_b$ structure. Two energy minima occur at $a = 5.46$ and $a = 5.60$ Å. For $a = 5.46$ Å, the moments within spheres of radius 1.45 Å surrounding each atom are 1.38 for Mn, -0.25 for Co and -0.10 μ_B for Al, which indicates a ferrimagnetic state. For $a = 5.60$ Å, the compound has a total magnetic moment of 3.60 μ_B per formula unit (f.u.) and the magnetic configuration is ferromagnetic in the sense that Mn and Co have parallel moments. The moments within the 1.45 Å spheres in this case are 3.20, 0.46 and -0.09 μ_B for Mn, Co, and Al, respectively. The ferromagnetic solution has an energy 0.079 eV/f.u. higher than the ferrimagnetic solution. The lower-energy ferrimagnetic solution is a "Slater-Pauling solution", and the electronic density of states (DOS) shows a pseudogap near the Fermi energy that becomes a gap for slightly larger lattice constants.

RhCrSn provides an example of competition between two different ferrimagnetic states as shown in Fig. 3.4. In this case, the energy minima at $a = 6.02$ and 6.15 Å correspond to ferrimagnetic states with different atomic magnetic moments (see Table 3.1). The $a = 6.02$ Å solution is half-metallic while the $a = 6.15$ Å solution is metallic. The metallic solution has a lower energy than the half-metallic solution by 0.067 eV/f.u.

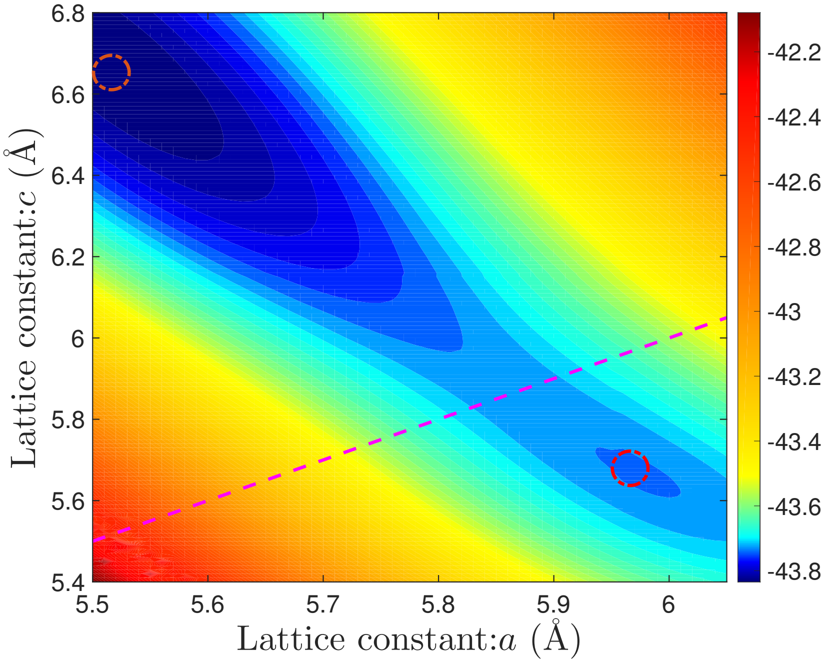

Figure 3.5: Calculated total energies of tetragonal distorted CrTiAs as a function of two lattice constants a and c. There are two half-metallic energy minima corresponding to two different tetragonal phases, labelled by dashed circles, at $(a, c) = (5.52, 6.66)$ Å and $(a, c) = (5.97, 5.67)$ Å. They differ in energy by 0.051 eV/f.u. The pink dashed line corresponds to cubic structures.

A few systems showed multiple local energy minima in a tetragonal structure, e.g., CrTiAs. Fig. 3.5 presents the total energy as a function of the two lattice constants a and c for ordered CrTiAs. There are two energy minima (labeled by the dashed circles) with tetragonality (c/a) less than and larger than 1 respectively. One local minimum is $(a, c) = (5.97, 5.67)$ Å, with tetragonality $c/a = 0.95$. The other local minimum with a lower energy is $(a, c) = (5.52, 6.66)$ Å, with tetragonality $c/a = 1.21$. Both energy minima have total magnetic moments of 3 μ_B per f.u. and display half-metallicity. The energy difference between them is 0.051 eV/f.u. In fact, CrTiAs displays half-metallicity in almost the entire blue region of Fig. 3.5. We found a few other compounds that behave similar to CrTiAs; these will be discussed in Sec. 3.7.

We list the total and partial magnetic moments for CoMnAl, RhCrSn and CrTiAs at different local energy minima in Table 3.1 for comparison. These compounds might have interesting properties if they can be synthesized. CrTiAs is particularly interesting because it is unusual to find two metastable half-metallic phases so close in energy. Tetragonal half-metallic phases are also rare and might be interesting for applications that require uniaxial magnetic anisotropy.

Table 3.1: Calculated total (M_{tot}) and X-, Y-, Z-site-projected partial spin magnetic moments (m) of CoMnAl, RhCrSn, and CrTiAs in different local minima of energy. All magnetic moment values listed are in units of μ_B. (PG = pseudogap, HM = half-metal)

Compound	Magnetic state	Structure	M_{tot}	$m(X)$	$m(Y)$	$m(Z)$
CoMnAl	Ferrimagnetic (PG)	$C1_b$	1.04	−0.25	1.38	−0.10
CoMnAl	Ferromagnetic	$C1_b$	3.60	0.46	3.20	−0.09
RhCrSn	Ferrimagnetic 1 (HM)	$C1_b$	1.00	−0.22	1.36	−0.09
RhCrSn	Ferrimagnetic 2	$C1_b$	3.25	−0.10	3.29	−0.06
CrTiAs	Ferromagnetic (HM)	Tetragonal	3.00	2.35	0.48	−0.01
CrTiAs	Ferromagnetic (HM)	Tetragonal	3.00	2.46	0.38	−0.01

3.3.3 phase stability

We explain our procedure for obtaining the relaxed structures in some detail in order to make clear that the $C1_b$ structure is not guaranteed to minimize the energy of a particular equiatomic XYZ system and that the possibility of multiple solutions to the DFT equations must be be considered when there is more than one magnetic species in the unit cell. We calculate the formation energy using the pseudopotentials and convergence parameters consistent with the OQMD [88] so that the calculated formation energies of the half-Heusler compounds can be directly compared to those of many other phases in the OQMD.

We performed full ionic relaxations within a 6-atom tetragonal cell for all of the 378 potential half-Heusler compounds. All relaxations started from the $C1_b$ structure with small displacements to avoid vanishing of the net force on each atom due to symmetry. 300 of these compounds were found to remain in the $C1_b$ structure, 6 relaxed to a tetragonal structure ($|c/a - 1| > 0.01$), while 72 compounds relaxed to a distorted structure that was neither cubic nor tetragonal.

For all systems, we performed DFT calculations using multiple initial magnetic configurations to start the iterative process that (usually) leads to a fixed point that minimizes the energy for a given set of atoms and atomic coordinates. As we shall see, a fixed point may be a local rather than a global energy minimum. Use of multiple initial magnetic configurations including moment configurations in which the X and Y moments were parallel and anti-parallel increased our chances of finding the global minimum.

After the relaxed structure is determined, we will calculate the formation energy and hull distance to analyze the phase stability.

Formation Energy

The formation energy of a half-Heusler compound XYZ is defined as

$$\Delta E_f\left(XYZ\right) = E\left(XYZ\right) - \frac{1}{3}\left(\mu_X + \mu_Y + \mu_Z\right) \tag{3.2}$$

where $E(XYZ)$ is the total energy per atom of the half-Heusler compound, and μ_i is the reference chemical potential of element i, chosen to be consistent with those used in the OQMD (See Ref. [88] for details). A negative value of ΔE_f indicates that at zero temperature, the half-Heusler compound is more stable than its constituent elements. It is a *necessary but not sufficient* condition for ground state thermodynamic stability. It does not, for example, guarantee the stability of a half-Heusler phase over another competing phase or mixture of phases.

Distance from the Convex Hull

A measure of the thermodynamic stability of a phase is its distance from the convex hull. In other words, the farther away a phase is from the convex hull, higher is the thermodynamic driving force for it to transform or decompose into another phase or combination of phases. The distance from the convex hull ΔE_{HD} for a phase with formation energy ΔE_f can be calculated as

$$\Delta E_{\mathrm{HD}} = \Delta E_f - E_{hull} \tag{3.3}$$

where E_{hull} is the energy of the convex hull at the composition of the phase. We utilize the formation energy data from OQMD to do the phase competing analysis [88,92,93].

Let's give two examples to present the hull distance calculation. In Fig.3.6 (a), the hull distance ΔE_{HD} for cubic FeMnAs is the formation energy difference between the cubic phase and the orthorhombic phase, which has the lowest formation energy at that chemical composition. In Fig.3.6 (b), although we don't have available the formation energy of other phases at that chemical composition, we can still estimate stability using the hull distance ΔE_{HD} for cubic FeMnP by defining the hull energy ($E_{hull}(FeMnP)$) as a linear combination of formation energies of nearby phases Mn_2P and Fe_2P.

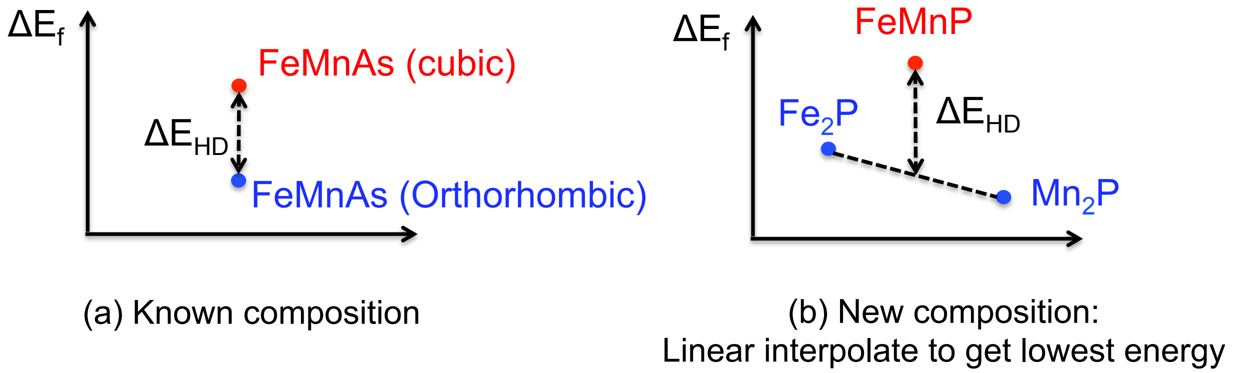

Figure 3.6: (a) Hull distance ΔE_{HD} for half-Heusler FeMnAs (b) Hull distance ΔE_{HD} for half-Heusler FeMnP

Obviously, the hull distance E_{HD} for a phase on the convex hull (hence thermodynamically stable) is 0, i.e., there is no other phase or linear combination of phases lower in energy than the phase at that composition. We note here that the distance from the convex hull of a phase depends on the completeness of the set of phases considered in the construction of the convex hull. Ideally, for calculating the convex hull of a system X–Y–Z, one would investigate all possible compounds that can be formed from elements X, Y, and Z (no matter how large or complex their structure), which is not feasible. A practical approach is to construct the convex hull using all the currently reported compounds in the X–Y–Z phase space. Here, we have limited our universe of considered phases to those in the OQMD, which includes all of the binary and ternary phases that have been reported in the ICSD, and ∼350,000 hypothetical compounds based on common structural prototypes. Thus, the calculated formation energy of each XYZ half-Heusler compound is compared against the calculated formation energies of all phases and all linear combinations of phases with total composition XYZ in the OQMD database.

Further, as we will demonstrate in Sec. 3.4, the distance of a phase from the convex hull (or simply "hull distance") ΔE_{HD}, apart from being a measure of its thermodynamic stability, is an indicator of the likelihood of its synthesis in experiments. We also note that since we use 0 K DFT energetics in our analysis, a phase that is above the convex hull may be either actually metastable or stabilized (i.e., moved onto the convex hull, and thus become experimentally accessible) due to (a) finite temperature contributions to the free energy such as phonons, magnons, configurational entropy, and/or (b) other external conditions such as pressure. Thus, while a phase that is above the convex hull may be experimentally realizable under carefully controlled conditions, we assert that the hull distance is still a good measure available of the *likelihood* of its experimental synthesis (see Sec. 3.4 for further discussion).

3.4 Energetics: Formation Energy and Distance from the Convex Hull

In this section, we systematically investigate the energetics of 378 half-Heusler compounds in the $C1_b$ structure. For each XYZ half-Heusler compound, we calculate its formation energy ΔE_f using Eq. 4.1 and distance from the convex hull ΔE_{HD} using Eq. 4.2. We explore the relationship between formation energy and hull distance of compounds at the compositions considered in this work (focusing on experimentally reported compounds and half-Heuslers, in particular), followed by an analysis of the trends in energetic quantities with composition.

For each composition XYZ considered here, in an effort to identify all the compounds experimentally synthesized at the composition, we begin by compiling a list of all compounds reported (if any) in the Inorganic Crystal Structure Database (not limited to the half-Heusler $C1_b$ structure), and tabulate their formation energies and hull distances as calculated in the OQMD — a total of 110 compounds (with 98 distinct compositions) and corresponding energies. The above sets of formation energies and hull distances are displayed in Fig. 3.7. The experimentally reported half-Heuslers are shown as blue circles. Other experimentally reported XYZ phases are shown as green diamonds. (The yellow circles, red pentagons and blue-green squares will be discussed later.) From Fig. 3.7, it is clear that the vast majority of the reported compounds that have been experimentally synthesized (blue circles and green diamonds) lie on or close to the calculated convex hull — 37 compounds are on the convex hull (i.e., a hull distance of 0 eV/atom) and an additional 52 lie relatively close to it (i.e., a hull distance less than about 0.1 eV/atom).

The red pentagons represent XYZ phases that have been reported to exist at high pressure or high temperature. The blue-green squares represent experimentally reported XYZ phases with partial site occupancies e.g., RhFeAs is reported to have occupancies of (0.75 Fe, 0.25 Rh) on the $3f$, and (0.25 Fe, 0.75 Rh) on the $3g$ Wyckoff positions in the $P\overline{6}2m$ Fe_2P structure [94], whereas the calculation in the OQMD corresponds to a structure in which $3f$ and $3g$ are respectively completely occupied by Fe and Rh). Finally, the yellow circles represent phases that have not been experimentally synthesized, but have been sourced into the ICSD from previous first-principles calculations.

The only two exceptions to the above observation that experimentally reported XYZ compounds (stoichiometric and ordered, at ambient conditions) have a hull distance less than about 0.1 eV/atom, are FeFeSn (at $\Delta E_f = 0.156$ eV/atom) and MnTiAs (at $\Delta E_f = -0.408$ eV/atom). Both of these compounds have a calculated hull distance of about 0.2 eV/atom. There appears to be some ambiguity about the exact composition of the former compound: FeFeSn in the $P63/mmc$ Ni_2In structure. The phase has been reported twice, once with the Fe_2Sn stoichiometry [95], and more recently with an Fe off-stoichiometry ($Fe_{1.68}Sn$) [96]. MnTiAs has been reported in the $P\overline{6}2m$ Fe_2P structure, synthesized using a sealed-silica tube technique followed by annealing [97, 98]. Since only its energy in a ferromagnetic configuration has been calculated in the OQMD, it is possible that other magnetic configurations may be energetically more favorable.

Overall, we find that most experimentally reported compounds in the XYZ compositions considered here (90 of 99) have a hull distance less than about 0.1 eV/atom. Thus, even though a larger hull distance does not preclude the experimental realization of a compound, the likelihood of its synthesis and stability at ambient conditions is low.

We reiterate that while all the experimentally observed phases (blue circles and green diamonds in Fig. 3.7) might ideally be expected to lie on the calculated convex hull (i.e., with $\Delta E_{\mathrm{HD}} = 0$), in practice, we find some as much as 0.1 eV/atom above it. As mentioned in Sec. 3.3.3, the reasons for this include inaccuracies in DFT, actual metastability, and finite temperature effects. We speculate that the latter may be very important because most of the phases in Fig. 3.7 were synthesized at high temperatures, typically by arc melting or solid state diffusion followed by annealing. Even when properties are measured at low temperatures, if synthesis and processing are done at high temperatures, atomic positions and structures corresponding to the processing temperature may be "frozen-in" for periods long compared to laboratory time scales. Thus although the free energy at the processing temperature may be more relevant for determining relative phase stability we find empirically that the total energy as determined by DFT is a reasonable substitute with an uncertainty of about 0.1 eV/atom.

Overall, it is clear from Fig. 3.7 that the distance of a phase from the DFT-calculated zero

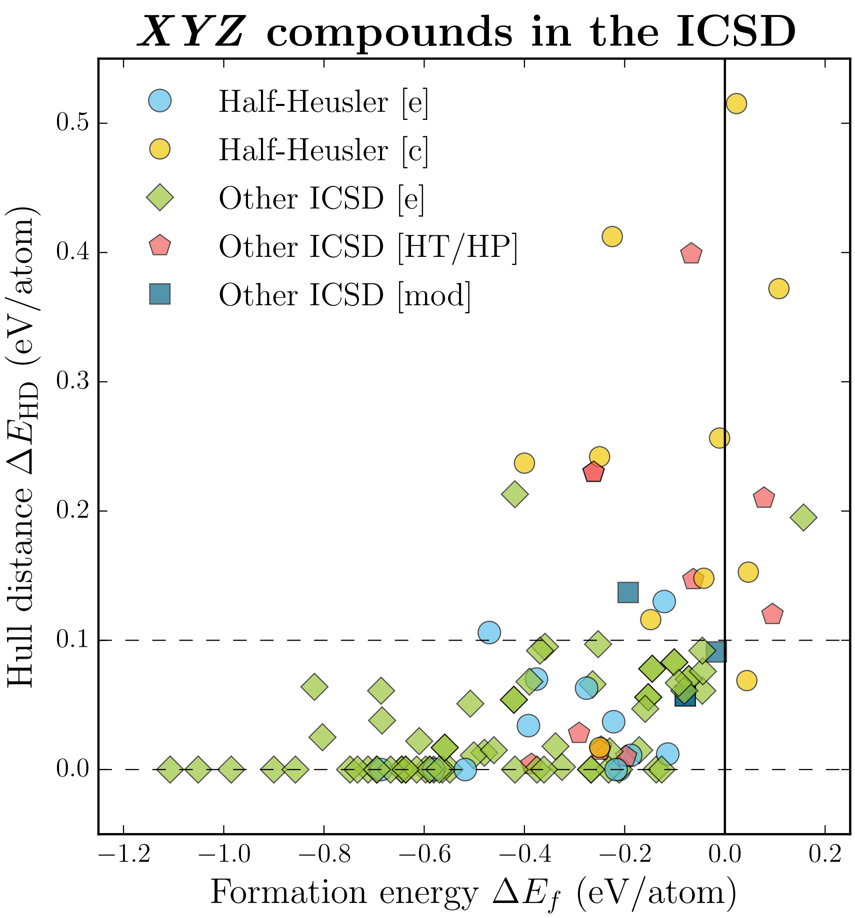

Figure 3.7: DFT-calculated formation energy vs. hull distance of all compounds reported in the ICSD in the XYZ compositions considered in this work. A hull distance $\Delta E_{\mathrm{HD}} = 0$ indicates a stable ground state compound on the convex hull. Blue circles indicate half-Heuslers in the ICSD that have been experimentally synthesized. Green diamonds indicate XYZ phases other than C1_b that have been experimentally synthesized. Red pentagons indicate XYZ phases experimentally reported to be stable at high temperature or pressure. Blue-green squares indicate reported XYZ phases with site occupations that differ from the OQMD calculation. Yellow circles indicate C1_b phases sourced into ICSD from electronic structure calculations rather than from experiment.

temperature convex hull ΔE_{HD} is a good indicator of the likelihood of its synthesis in experiments. This insight has important implications for the potential application of half-Heusler compounds. We expect that the further a compound lies from the convex hull, the less likely will be its successful synthesis, especially if the synthesis is limited to equilibrium processing.

We extend the comparison of formation energies and hull distances to all the 378 half-Heusler compounds considered in this work (see Fig. 3.8), and find that: (a) There is a large variation in formation energy of the half-Heusler compounds, ranging from −1.1 to 0.7 eV/atom, with a large number (197) possessing a negative formation energy indicating stability against decomposition into constituent elements. (b) There is a relatively small number (24) of the half-Heusler compounds considered in this work that are reported in the ICSD. (c) As observed previously, of the half-Heusler compounds reported in the ICSD, almost all the experimentally synthesized ones (green squares, labeled "In ICSD [e]") lie on or close to the convex hull, with hull distances between 0.0 and about 0.1 eV/atom. (d) In contrast, most of the half-Heusler compounds in the ICSD sourced from previous calculations (red diamonds, labeled "In ICSD [c]") lie above the convex hull, with hull distances up to 0.5 eV/atom. Overall, consistent with our previous observations for all compounds reported in the ICSD, we find that *the distance of a half-Heusler compound from the convex hull is a good measure of the likelihood of its experimental synthesis*, and a hull distance of less than $\sim$0.1 eV/atom seems to be the corresponding approximate threshold. Our calculations predict about 50 (out of 378) half-Heusler compounds to be within the empirical threshold of a hull distance of $\sim$0.1 eV/atom, of which about 35 have not been previously reported. Further, we calculate 16 half-Heusler compounds considered in this work to lie on the convex hull ($E_{\mathrm{HD}} = 0$ eV/atom) of which (a) 6 have been reported in the $C1_b$ structure, (b) 6 have been reported in other structures ($Pnma$ and $P\overline{6}2m$ structures), and (c) 4 (RhTiP, RuVAs, CoVAs, CoTiAs) do not have any reported compounds at the composition in the ICSD. Thus, *our calculations predict a number of new, hitherto unknown, potential half-Heusler compounds for further experimental investigation.* We discuss the properties of these predicted compounds in relevant later sections, Sec. 3.5–3.7.

We now analyze the variation in formation energies and hull distances with composition of all the 378 half-Heusler compounds in the $C1_b$ structure. All the formation energies are represented in a 3-dimensional plot in Fig. 3.9, and the corresponding hull distances are plotted in Fig. 3.10. It can be seen from the darker blue colors that compounds with X = (Ni, Co, Rh), Y = (V, Ti) and Z = (group 5 elements P, As, Sb) tend to have lower formation energies and lie closer to or on the convex hull. This is largely consistent with known empirical rules for the stability of half-Heusler compounds, with the most electronegative (e.g., P, As, Sb) and the most electropositive elements (e.g., Ti) forming the NaCl-like sublattice, and the intermediate electronegative element (e.g., Co, Ni) occupying alternate tetrahedral sites [99]. To better illustrate the relation between structural stability and composition, we arranged the formation energy and hull distance data according to X, Y, and Z element respectively in Figs. 4.5–4.7.

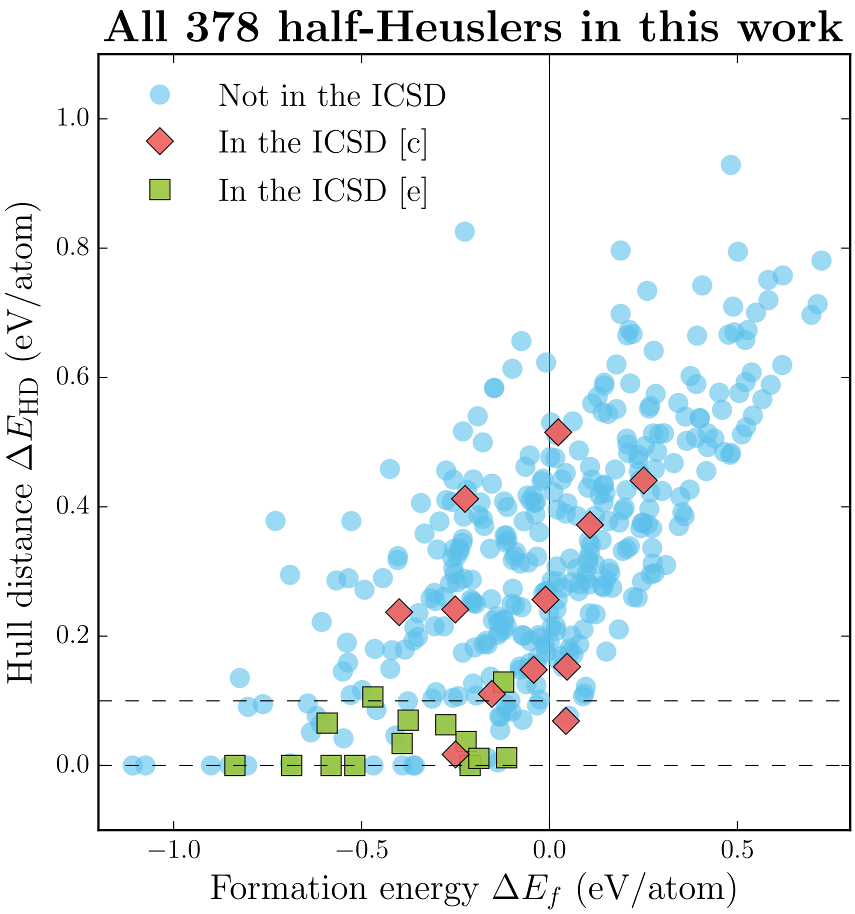

Figure 3.8: DFT-calculated formation energy vs. hull distance of all the 378 XYZ half-Heusler compounds considered in this work. A hull distance $\Delta E_{\mathrm{HD}} = 0$ indicates a stable ground state compound on the convex hull. Almost all the experimentally reported half-Heusler compounds (green squares, "In ICSD [e]") have a hull distance less than ∼0.1 eV/atom (the window represented by the two horizontal dashed lines); half-Heusler compounds sourced into the ICSD from previous computational work are represented by red diamonds (labeled "In ICSD [c]").

From Fig. 4.5, we see that Co, Rh, and Ni on the X-site form more compounds with negative formation energy (and more compounds with smaller hull distances) than other elements on the X-site. From Fig. 4.6, it can be seen that Ti and V on the Y-site form more compounds with negative formation energies and smaller hull distances than other elements. Similarly, when the compounds are ordered by the element on the Z-site as shown in Fig. 4.7, one can see that there is a trend for formation energy to decrease and stability to increase with group number, i.e., compounds with group 5 elements on the Z-site are in general more stable than those with group 4 elements which are more stable than those with group 3 elements on the Z-site. For a fixed number of valence electrons on the Z atom, i.e. 3, 4 or 5, the formation energy is typically lower for the smaller atom,

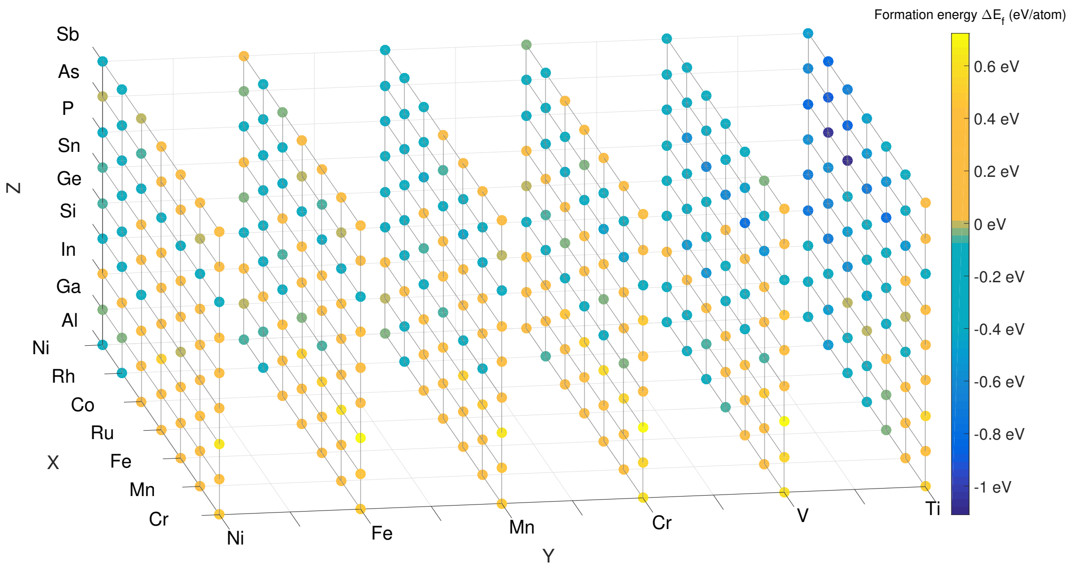

Figure 3.9: DFT formation energies per atom for the 378 half-Heusler compounds considered in this work (colors represent the formation energy; blue and yellow = increasingly negative and positive formation energies respectively). The 3 coordinates represent the X, Y, and Z species of the corresponding XYZ compound.

(i.e. Al, Si, P). However, the trend is different for the hull distance with the larger atoms, especially Sn and Sb leading to greater stability relative to other phases. The large number of compounds with very low formation energies with Z = P is striking in Fig. 4.7, but can also be observed in Figs. 4.5 and 4.6 as the periodic pattern of low formation energy compounds, i.e., compounds 7, 16, 25, 34, etc. for fixed X in Fig. 4.5 or fixed Y in Fig. 4.6. Although the Z = P compounds have lower formation energies, there are more compounds with Z = (As, Sb) that lie on or closer to the convex hull (hull distance close to 0 eV/atom).

We speculate that the smaller Z atom allows for smaller interatomic distances increasing the binding and reducing the total energy, however the relatively open structure of the $C1_b$ phase means that there are fewer nearest neighbor bonds, so that the $\mathrm{C1}_b$ phase is at a disadvantage compared to more closely packed phases. Thus, while low formation energies sometimes correspond to low hull distances, a low formation energy is not sufficient to ensure the thermodynamic stability of a compound, which further depends on other competing phases in the chemical space.

We also observed that group 3 elements (Al, Ga, In) on the Z-site yield many compounds with distorted structures lower in energy than the cubic or tetragonal structures. For Z = Al, Ga, and In, the corresponding numbers of compounds with a lower-energy distorted structure are 19, 18,

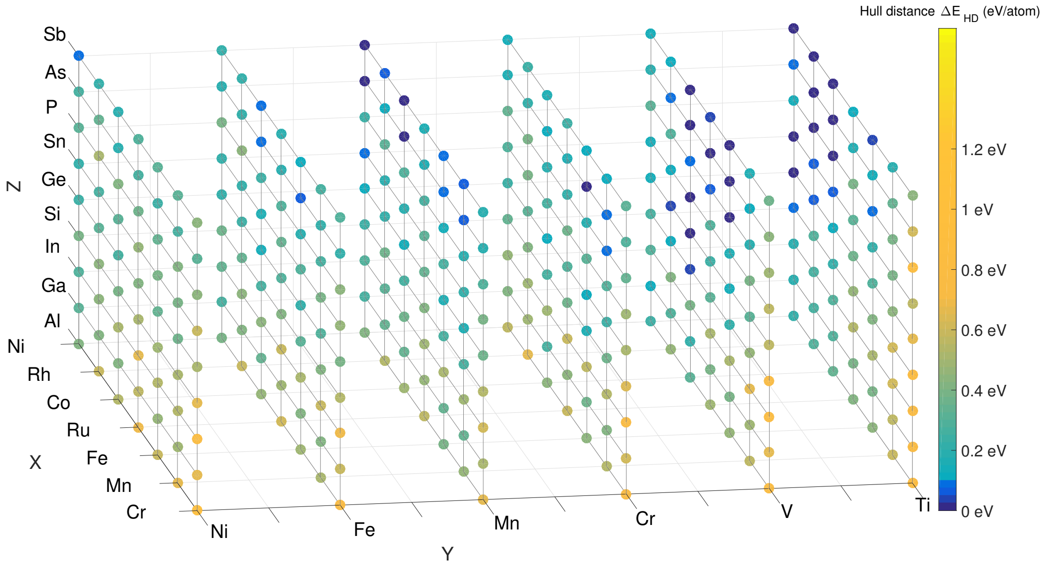

Figure 3.10: DFT-calculated distances from the convex hull for the 378 half-Heusler compounds considered in this work (colors represent the hull distance; blue and yellow = increasingly close to and away from the convex hull respectively. All shades of blue represent hull distances $\Delta E_{\mathrm{HD}} \leq$ 0.1 eV/atom). The 3 coordinates represent the X, Y, and Z species of the corresponding XYZ compound.

and 22 respectively. Thus, most of the 72 compounds that relaxed to a distorted phase had a group 3 element on the Z-site.

Prompted by the trend of decreasing formation energy with decreasing the atomic number of the element on the Y-site in Fig. 4.6, we investigated Y = Sc and found three additional semiconductors (NiScP, NiScAs, and NiScSb) with a negative formation energy (listed in Table 4.1 but not included in Figs. 4.5–4.7). The NiSc(P,As,Sb) compounds have lower formation energies than the corresponding CoTi(P,As,Sb) compounds. We also found two additional $C1_b$ half-metals (CrScAs and CrScSb) with a negative formation energy. These are listed in Table 3.5 but not included in Figs. 4.5–4.7).

Another interesting trend among the half-Heusler compounds is the preference for the transition metal with the larger atomic number to occupy the X-site $(\frac{1}{4},\frac{1}{4},\frac{1}{4})$ in an XYZ Heusler compound. Our calculations included formation energies for CrMnZ, CrFeZ, CrNiZ, and MnFeZ, which can be compared directly with the formation energies calculated for MnCrZ, FeCrZ, NiCrZ, and FeMnZ where Z represents one of 9 non-transition metal atoms considered. Of these 36 pairs we found no exceptions to the rule that the energy is lower if the atomic number of the element on the X-site is larger than that of the element on the Y-site. Of course, this rule may be violated if structures

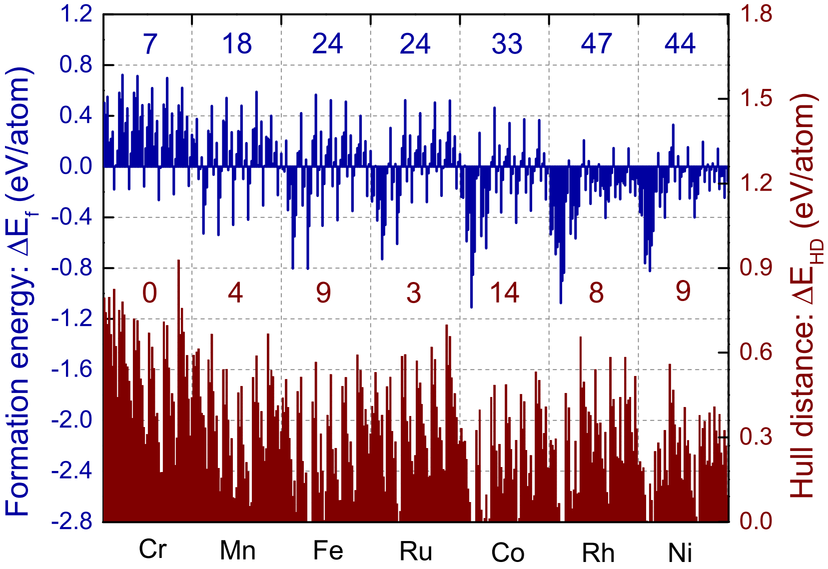

Figure 3.11: DFT formation energies and hull distances for potential half-Heusler compounds grouped by the element on the X-site. The numbers near the top (in blue) and center (in brown) of each column denote the number of compounds with negative formation energy ΔE_f and hull distance $\Delta E_{\mathrm{HD}} \leq 0.1$ eV/atom, respectively, in the corresponding Z-element group. Within a given X-element column, the compounds are ordered first by the element on the Y-site (same order as in Fig. 4.6) and then by the element on the Z-site (same order as in Fig. 4.7), i.e., Z varies more rapidly than Y.

other than $C1_b$ are considered. For example, CrNiAl and CrNiIn had lower formation energies than NiCrAl and NiCrIn, respectively, because the lowest energy relaxed structures for CrNiAl and CrNiIn were distorted triclinic cells. If comparisons are restricted to all compounds in the $\mathrm{C}1_b$ structure, then the above observation of lower formation energy corresponding to the transition metal atom with the larger atomic number occupying the X-site is consistently true (at least for the 36 pairs we considered).

In addition, the formation of band gaps plays an important role in structural stability. From Figs. 4.5–4.7, it can be seen that there are five compounds (CoTiP, RhTiP, CoTiAs, RhTiAs, RhTiSb) with formation energies less than −0.83 eV/atom. All of them have Co or Rh on the X-site, Ti on the Y-site, and P, As or Sb on the Z-site, consistent with previous observations in this section, but another common characteristic of these five compounds is that they are all 18-electron Slater-Pauling semiconductors, with 3 electrons per atom in both spin channels. We speculate that a gap in one spin channel at the Fermi energy contributes to the stability of the compound, and

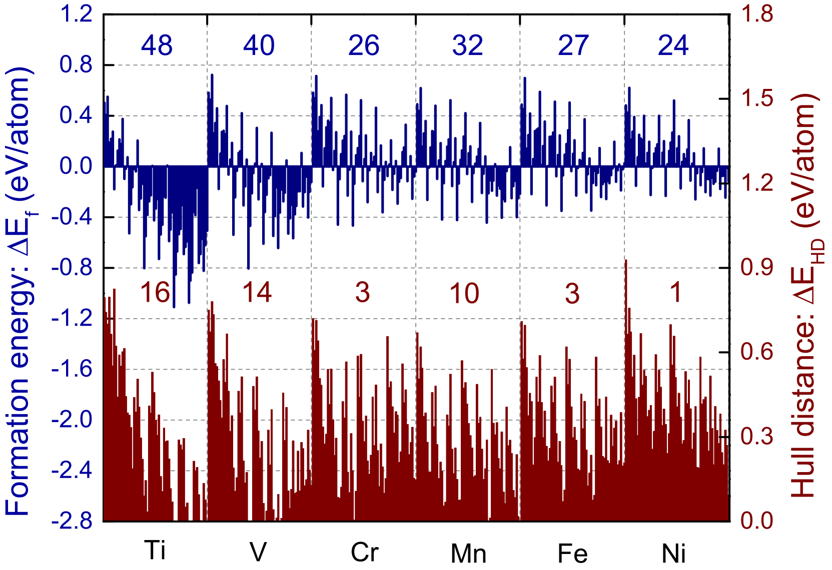

Figure 3.12: DFT formation energies and hull distances for potential half-Heusler compounds grouped by the element on the Y-site. The numbers near the top (in blue) and center (in brown) of each column denote the number of compounds with negative formation energy ΔE_f and hull distance $\Delta E_{\mathrm{HD}} \leq 0.1$ eV/atom, respectively, in the corresponding Y-element group. Within a given Y-element column, the compounds are ordered first by the element on the X-site (same order as in Fig. 4.5) and then by the element on the Z-site (same order as in Fig. 4.7), i.e., Z varies more rapidly than X.

that gaps in both spin channels contribute even more to stability, resulting in the compounds with the lowest formation energies in our database.

The next 18 compounds in the order of increasing formation energy have Co, Rh, Ru, Fe or Ni on the X-site, Ti (13 out of 18) or V on the Y-site, and a group 5 element (P, As, Sb) or group 4 element (Si or Ge) on the Z-site. All except four (RuTiP, RhTiSi, RhVP, CoTiSi, which have competing lower-energy $Pnma$ or $P\overline{6}2m$ phases) lie on or close to the convex hull with hull distances lower than ~0.1 eV/atom. Of the 18 compounds, 7 (FeVP, NiTiSi, NiTiGe, NiTiSn, CoTiSb, RuVP, CoVSi) are also 18-electron Slater-Pauling semiconductors and are listed in Table 4.1.

We calculated the electronic structure of each compound and obtained its spin polarization $\mathcal{P}$ at Fermi level E_F using:

$$\mathcal{P}(E_F) = \frac{N_\uparrow(E_F) - N_\downarrow(E_F)}{N_\uparrow(E_F) + N_\downarrow(E_F)} \tag{3.4}$$

where $N_\uparrow$ and $N_\downarrow$ are the densities of states for majority (spin-up) and minority (spin-down) electrons, respectively. The distribution of spin polarization $\mathcal{P}(E_F)$ of the 378 half-Heusler compounds

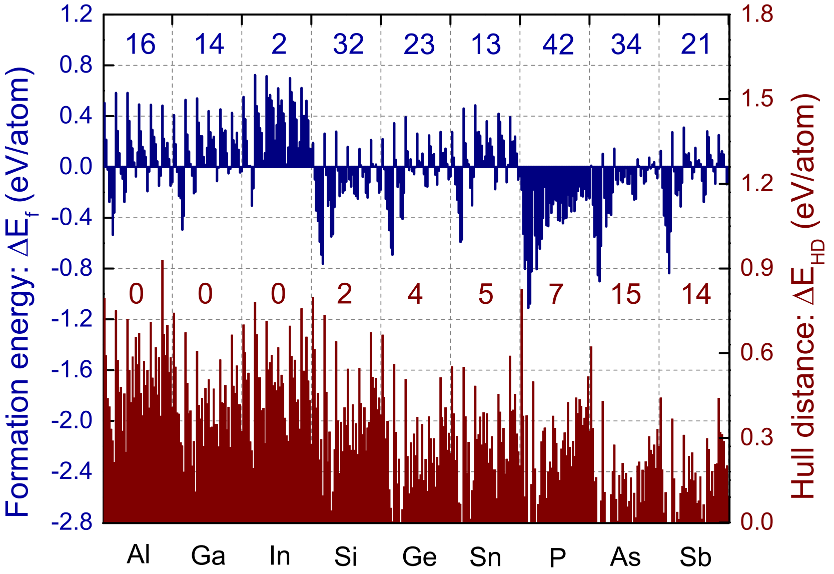

Figure 3.13: DFT formation energies and hull distances for potential half-Heusler compounds grouped by the element on the Z-site. The numbers near the top (in blue) and center (in brown) of each column denote the number of compounds with negative formation energy ΔE_f and hull distance $\Delta E_{\mathrm{HD}} \leq 0.1$ eV/atom, respectively, in the corresponding Z-element group. Within a given Z-element column, the compounds are ordered first by the element on the X-site (same order as in Fig. 4.5) and then by the element on the Y-site (same order as in Fig. 4.6), i.e., Y varies more rapidly than X.

separated into those with positive and negative formation energies (and similarly, with hull distances greater than and less than ~0.1 eV/atom) is shown in Figs. 4.8 and 4.9. A correlation between a negative formation energy and gaps at the Fermi energy is apparent. In particular, we have separated on the left in Fig. 4.8 24 compounds with exactly zero polarization that are semiconductors. Only one of these has a positive formation energy. We have also separated on the right, 72 compounds that are fully spin polarized, i.e., they are half-metals. The majority (42) of these half-metals have negative formation energies. In fact, a majority of the near half-metals also have negative formation energies. The contribution of gaps at Fermi energy to stability of a compound is even more striking in Fig. 4.9. Almost all the half-Heusler compounds that are on or close to the convex hull (within ~0.1 eV/atom of it) are either semiconductors (or near semiconductors with close to $\mathcal{P}(E_F) = 0$), or half-metals (or near half-metals with close to $\mathcal{P}(E_F) = 1$). In other words, having a gap (or even almost a gap) at the Fermi energy in one or both spin channels seems to contribute greatly to the stability of a compound, consistent with our previous observations.

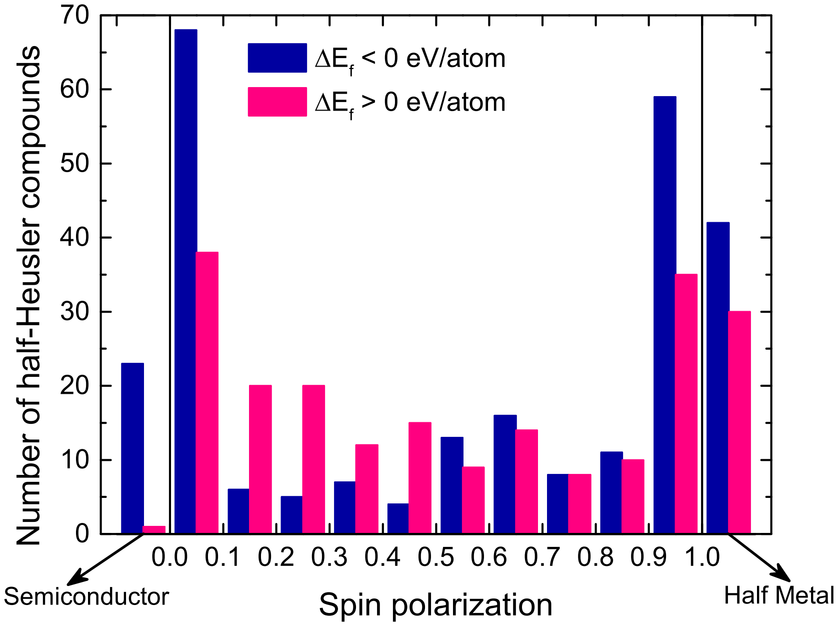

Figure 3.14: The distribution of half-Heusler compounds with negative ($\Delta E_f < 0$ eV/atom) and positive ($\Delta E_f > 0$ eV/atom) formation energies as a function of spin polarization $\mathcal{P}(E_F)$ (given by Eq. 4.3). In the central region, we show the number of half-Heusler compounds grouped by 10 percentage points of spin polarization. In an additional region to the left, we show the 24 semiconductors, including 23 compounds with a negative formation energy and 1 with a positive formation energy. In the additional region on the right, we show 72 half-metals, including 42 and 30 with negative and positive formation energies respectively.

Among the half-Heusler compounds considered in this work, we identify a total of 27 18-electron semiconductors and 45 half-metals with negative formation energies. We discuss semiconductors in Sec. 3.5 and half-metals in Secs. 3.6 and 3.7.

3.5 Slater-Pauling Semiconductors

Table 3.2 lists the 60 half-Heuslers in our database with 18 valence electrons per formula unit. The row labels give the X atoms and their number of valence electrons. The column labels give the Y atoms and their number of valence electrons. Each entry in the table represents 3 compounds. Thus CoV4 represents CoVSi, CoVGe, or CoVSn. Note that the final number (e.g., the 4 in CoV4) is actually redundant since the total number of valence electrons is 18.

For the 27 18-electron half-Heusler compounds that are Slater-Pauling semiconductors, we tabulate the DFT-calculated properties such as lattice constant, band gap, gap type, formation

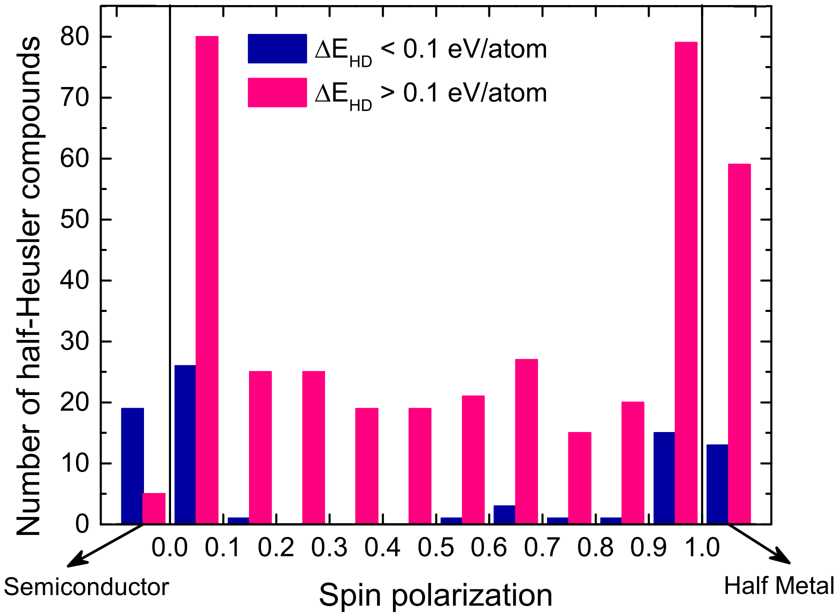

Figure 3.15: The distribution of half-Heusler compounds that lie on or close to ($\Delta E_{\mathrm{HD}} <$ 0.1 eV/atom) and far away ($\Delta E_{\mathrm{HD}} >$ 0.1 eV/atom) from the convex hull, as a function of spin polarization $\mathcal{P}(E_F)$ (given by Eq. 4.3). In the central region, we show the number of half-Heusler compounds grouped by 10 percentage points of spin polarization. We show the 24 semiconductors (of which 19 compounds have $E_{\mathrm{HD}} <$ 0.1 eV/atom) in the additional region to the left, and show the 72 half-metals (of which 15 compounds have $E_{\mathrm{HD}} >$ 0.1 eV/atom). Clearly, the existence of a gap at the Fermi level in one or both spin channels contributes to the stability of a half-Heusler compound.

Table 3.2: List of the 60 18-electron half-Heusler compounds considered in this work. Row and column labels indicate the atom on the X- and Y-sites respectively. Compounds in bold (and underlined) are Slater-Pauling semiconductors with no moment on any atom. $Z = 5$ means $Z =$ P, As, or Sb; $Z = 4$ means $Z =$ Si, Ge, or Sn; $Z = 3$ means $Z =$ Al, Ga, or In.

X/Y	3Sc	4Ti	5V	6Cr	7Mn	8Fe
10Ni	**NiSc5**	**NiTi4**	**NiV3**			
9Co		**CoTi5**	**CoV4**	CoCr3		
9Rh		**RhTi5**	**RhV4**	RhCr3		
8Fe			**FeV5**	FeCr4	FeMn3	
8Ru			**RuV5**	RuCr4	RuMn3	
7Mn				MnCr5	MnMn4	MnFe3
6Cr					CrMn5	CrFe4

energy, and hull distance in Table 4.1. Remarkably all of the 27 systems with Sc, Ti, or V as on the Y-site have similar electronic structure in that they are in Slater-Pauling states with zero magnetic moment on all atoms and are therefore semiconductors (band gaps are given in Table 4.1). It is also remarkable that the decrease in energy due to the creation of the gaps in both spin channels associated with the Slater-Pauling state is sufficient to eliminate the magnetic moment on all atoms including those that are usually found to be magnetic (e.g., Ni, Co, Fe).

We suggest that the absence of moments in these materials results from the atoms on the Y-site (Sc, Ti, and V) being difficult to magnetically polarize. Since the total moment in the Slater-Pauling state for an 18-electron half-Heusler must be zero, zero moment on the atoms on the Y-site (due to the broad, high-lying $d-$states of Sc, Ti, and V) and the Z-site (which is even more difficult to polarize than the atom on the Y-site) implies zero moment on the atom on the X-site. Another important factor in their stability may be that the large difference in the number of d-electrons in the atoms on the X- and Y-sites leads to a large difference in the on-site energies of the d-states, which in turn contributes to relatively large energy gaps. Slater and Koster showed in 1954 that for X-Y compounds with only nearest-neighbor interactions involving d-states, there will be no states between the d-onsite energies of the atoms on the X- and Y-sites [84].

If our entire dataset of 384 $C1_b$ half-Heusler compounds is ordered by calculated formation energies (see Table 4.1), the "lowest-formation energy" list is dominated by 18-electron semiconductors. A low formation energy does not, however, guarantee stability against other phases with still lower energy. The experimental literature suggests that the most common competing phase for the 18-electron half-Heusler semiconductors is the orthorhombic MgSrSi-type $Pnma$ phase with 4 formula units per cell. We calculate the formation energies for these competing $Pnma$ phases, list them in Table 4.1 for comparison with the formation energy of the corresponding $C1_b$ phases, and include them in the construction of the respective convex hulls. Interesting patterns can be observed in the formation energies of the $C1_b$ semiconductors and those of the competing $Pnma$ compounds: As one proceeds from left to right and top to bottom in Table 3.2 (or alternatively as the difference in the number of valence electrons of the atoms on the X- and Y- sites decreases) the formation energies tend to increase (stability against decomposition into elements decreases) for both $C1_b$ and $Pnma$ phases. In addition, for a given X and Y, the formation energies increase as the size of the atom on the Z-site increases, thus the formation energy increases from XYP to XYAs to XYSb, and from XYSi to XYGe to XYSn. This increase in formation energy is faster for the $Pnma$ compounds than for the $C1_b$ semiconductors so that in most cases, for a given X and Y, the $Pnma$ compound has the lower energy for $Z =$ P or Si. When $Z =$ As or Ge, the formation energies are similar, and when $Z =$ Sb or Sn, the $C1_b$ semiconductor has the lower energy.

Table 3.3: For each of the 27 18-electron XYZ half-Heusler compounds that are Slater-Pauling semiconductors, we list the calculated lattice constant a, band gap E_g within DFT, the type of gap, the formation energy of the compound in the $C1_b$ and $Pnma$ structures, distance from the convex hull for the $C1_b$ phase $\Delta E_{\mathrm{HD}}^{C1_b}$, previous experimental reports, whether or not a full-Heusler X_2YZ phase (in the $L2_1$ structure) has been observed, and the formation energy of the observed full-Heusler $L2_1$ phase where applicable. ([Legend] Gap type: D = direct, I = indirect band gap.)

XYZ	a	E_g	Gap	$\Delta E_f^{C1_b}$	ΔE_f^{Pnma}	$\Delta E_{\mathrm{HD}}^{C1_b}$	Experimental	X_2YZ	$E_f^{L2_1}$
	(Å)	(eV)	type		(eV/atom)		reports	reports	(eV/atom)
NiScP	5.67	0.57	D	−1.139	−1.308	0.169	$Pnma$ [100]		
NiScAs	5.82	0.46	D	−0.994	−1.029	0.035			
NiScSb	6.10	0.25	D	−0.911	−0.773	0	$F\bar{4}3m$ [101,102]		
NiTiSi	5.56	0.74	I	−0.762	−0.846	0.084	$Pnma$ [103,104]		
NiTiGe	5.65	0.62	I	−0.691	−0.684	0	$Pnma$ [105]		
NiTiSn	5.93	0.44	I	−0.571	−0.392	0	$F\bar{4}3m$ [106–108]	[108,109]	−0.473
CoTiP	5.43	1.39	I	−1.109	−1.245	0.136	$Pnma$ [110]		
CoTiAs	5.61	1.29	I	−0.852	−0.804	0	$Pnma$ [111]		
CoTiSb	5.88	1.06	I	−0.670	−0.415	0	$F\bar{4}3m$ [112,113]		
RhTiP	5.74	0.87	I	−1.075	−1.258	0.183			
RhTiAs	5.87	0.85	I	−0.901	−0.890	0	$Pnma$ [114]		
RhTiSb	6.12	0.75	I	−0.837	−0.621	0	$F\bar{4}3m$ [115]		
NiVAl	5.57	0.10	D	−0.196	−0.164	0.230		[116]	−0.389
NiVGa	5.55	0.30	D	−0.195	−0.270	0.108		[117]	−0.287
NiVIn	5.84	0.26	D	0.106	0.078	0.280			
CoVSi	5.41	0.55	I	−0.548	−0.584	0.036	$Pnma$ [103,118]	[119]	−0.424
CoVGe	5.50	0.68	I	−0.391	−0.300	0	$Pnma$ [120]		
CoVSn	5.79	0.65	I	−0.164	0.046	0.012		[109,121]	−0.092
RhVSi	5.69	0.31	I	−0.529	−0.657	0.109			
RhVGe	5.77	0.43	I	−0.410	−0.391	0.046			
RhVSn	6.04	0.39	I	−0.302	−0.244	0.113		[122]	−0.349
FeVP	5.31	0.32	I	−0.804	−0.907	0.103	$Pnma$ [98]		
FeVAs	5.49	0.37	I	−0.468	−0.357	0	$P\bar{6}2m$ [98]		
FeVSb	5.78	0.38	I	−0.211	0.083	0	$F\bar{4}3m$ [123,124] $P6_3/mmc$ [125,126]		
RuVP	5.62	0.19	I	−0.609	−0.767	0.158			
RuVAs	5.76	0.24	I	−0.358	−0.295	0			
RuVSb	6.02	0.20	I	−0.222	−0.031	0.037	$F\bar{4}3m$ [126]		

The NiV(Al,Ga,In) sequence is an exception to the above pattern due to the relatively high formation energies of both phases ($C1_b$ and $Pnma$) and the low formation energy of the Ga phases relative to the Al phases. Our calculated formation energies indicate that neither of the $C1_b$ or $Pnma$ compounds would be an equilibrium phase at low temperature due to the very low formation energy of competing binary phases – NiAl ($B2$), Ni_2Ga_3 and Ni_2In_3 (Al_3Ni_2 structure type), respectively. In fact, we predict NiVIn to have a positive formation energy in both the $Pnma$ and semiconducting $C1_b$ phases. NiVIn is the only one of the 27 semiconducting $C1_b$ compounds that we find to have a positive formation energy.

The trend of the formation energy of the $Pnma$ phase being lower than that of the $C1_b$ phase for the smaller Z atoms, and vice versa for the larger Z atoms, may be explained by the atomic size of the Z atom and its effect on the lattice constant. For the $C1_b$ phase, the X atom has 4 nearest neighbors that are Z atoms and 4 that are Y atoms, all at the same distance. The X–Z distances in the $Pnma$ structure are smaller than in the $C1_b$ structure for small Z atoms, but about the same for the larger ones. However, for the large Z atoms, the X–Y distances in the $C1_b$ structure are significantly smaller than in the $Pnma$ structure. Thus, in the case of large Z atoms, the smaller X–Y distances in the $C1_b$ structure seem to result in stronger interatomic binding when compared to the corresponding $Pnma$ phase, leading to lower formation energies.

The hull distance is determined by the energy differences of the $\mathrm{C1}_b$ and $Pnma$ phases for most of these systems. Exeptions are the NiV3 and RhV4 systems for which OQMD predicts that both the $\mathrm{C1}_b$ and Pnma phases are undercut by a mixture of binaries (NiAl+V for the case of NiVAl). For CoVSn and RuVSb, the $\mathrm{C1}_b$ phase is almost degenerate with a mixture of binaries.

Overall, there is good agreement between theory and experiment displayed in Table 4.1. First, all the six half-Heusler compounds that have been experimentally synthesized (NiScSb, NiTiSn, CoTiSb, RhTiSb, FeVSb, and RuVSb) are predicted to lie on or close to the convex hull, with the energy of the $C1_b$ structure correctly predicted to be lower than that of the $Pnma$ structure in all cases. Of the six compounds, all except RuVSb are predicted to lie *on* the convex hull. RuVSb is predicted to have a small hull distance $E_{\mathrm{HD}} = 0.037$ eV/atom with a linear combination of binaries (RuV_3–RuV–$RuSb_2$) in the OQMD predicted to be lower in energy. Second, of the systems for which the calculated formation energy of the $Pnma$ phase is lower than that of the $C1_b$ phase, most (five, i.e., NiScP, NiTiSi, CoTiP, CoVSi, and FeVP) are experimentally observed in the $Pnma$ structure. In two cases (NiTiGe, CoTiAs) the difference between the energies of the two structures is very small ($\Delta E^{Pnma-C1_b} = 0.007$ and 0.011 eV/atom, respectively), and both have been experimentally observed in the $Pnma$ structure. The two cases for which the calculated formation energy of the $C1_b$ phase is considerably lower than the $Pnma$ phase while experimental reports of the $Pnma$

phase exist are CoTiAs and CoVGe, with $\Delta E^{Pnma-C1_b} = 0.048$ and 0.091 eV/atom, respectively. The source of these discrepancies is not clear, though errors in DFT, unusual magnetic ordering, and finite temperature contributions to the free energy are the usual suspects (see Sec. 3.4).

In all the above cases discussed, the lower energy phase ($C1_b$ or $Pnma$) is predicted to lie on the convex hull. In particular, according to our calculations, the formation energy of CoVGe in the $C1_b$ structure is considerably lower than that of the experimentally reported $Pnma$ structure by 0.091 eV/atom. Similarly, FeVAs has been experimentally observed in the Fe_2P $P\overline{6}2m$ structure but our calculations indicate that the $C1_b$ structure is lower in energy than the $P\overline{6}2m$ structure by 0.143 eV/atom. In both the above cases, the calculated difference in formation energies is sufficiently large that efforts to fabricate the corresponding $C1_b$ phases are justified.

The 18-electron semiconductors in Table 4.1 for which we did not find experimental reports are NiScAs, RhTiP, NiV(Al,Ga,In), CoVSn, RhV(Si,Ge,Sn), RuVP, and RuVAs. Based on our calculations and the phases in the OQMD for each of those systems, we predict the following compounds to be thermodynamically stable in the corresponding structures: NiScAs ($Pnma$), RhTiP ($Pnma$), RuVP ($Pnma$) and RuVAs ($C1_b$). CoVSn in the $C1_b$ structure is predicted to be only just above the convex hull with $\Delta E_{\mathrm{HD}} = 0.012$ eV/atom. In all other cases, we find a linear combination of other phases in the OQMD, usually binaries, to have a lower energy than both the XYZ $C1_b$ and $Pnma$ phases, with ΔE_{HD} ranging from 0.037 eV/atom (RuVSb) to 0.280 eV/atom (NiVIn). As discussed in Sec. 3.4, we expect that the further a compound lies from the convex hull, the less likely will be its successful synthesis.

For several of the XYZ 18-electron $C1_b$ semiconductors in Table 4.1, there are reports of a corresponding $L2_1$ (full-Heusler) phase at the X_2YZ composition (namely, Ni_2TiSn, Ni_2VAl, Ni_2VGa, Co_2VSi, Co_2VSn, and Rh_2VSn). We include these reports in the table (see the rightmost columns in Table 4.1 for references to the reports and corresponding calculated formation energies) for completeness, and because it is sometimes difficult to distinguish between the $L2_1$ and $C1_b$ phases during experimental characterization. However, our calculated formation energies for these reported $L2_1$ phases predict all of them to lie above the convex hull, with a linear combination of other phases having a lower energy in each case: (a) Ni_2TiSn: NiTiSn–Ni_3Ti–Ni_3Sn_2 (lower in energy by $\Delta E_{\mathrm{HD}} = 0.029$ eV/atom), (b) Ni_2VAl: Ni_2V–NiAl–NiV_3 ($\Delta E_{\mathrm{HD}} = 0.050$ eV/atom), (c) Ni_2VGa: Ni_2V–NiV_3–$Ni_{13}Ga_9$ ($\Delta E_{\mathrm{HD}} = 0.025$ eV/atom), (d) Co_2VSi: CoVSi–Co_3V–Co_2Si

($\Delta E_{\mathrm{HD}} = 0.031$ eV/atom), (e) Co_2VSn: CoSn–Co_3V–CoV_3 ($\Delta E_{\mathrm{HD}} = 0.079$ eV/atom), and (f) Rh_2VSn: RhSn–RhV ($\Delta E_{\mathrm{HD}} = 0.016$ eV/atom). The calculated hull distances ΔE_{HD} of all the $L2_1$ phases are small – all except Co_2VSn are within 0.050 eV/atom (possible reasons for experimentally observed phases being predicted to lie above the convex hull are discussed in Sec. 3.4). We note that the Rh_2VSn phase was observed to occur in a tetragonally-distorted structure (space group $P4_2/ncm$, $c/a = 1.27$) in slowly cooled samples, and in a two-phase mixture of $L2_1$ and tetragonal phases in quenched samples [122]. Thus, the $L2_1$ structure seems to be stable only at high temperatures. Similarly, Ni_2VAl was experimentally observed in a two-phase mixture, with XRD data insufficient to distinguish between the $C1_b$ and CsCl structure types [116]. Further, the experimentally reported lattice parameter $a = 6.33$ Å is not only ∼12% larger than the DFT-calculated value but also ∼8% larger than that of Ni_2VGa. Since a Ga atom is larger than an Al atom, one would expect the lattice constant of Ni_2VGa to be similar or larger than that of Ni_2VAl. Thus, we conclude that the reported lattice constant of Ni_2VAl is unreasonable and call for careful recharacterization of the phase.

We now briefly discuss the bonding and electronic structure of these 18-electron Slater-Pauling semiconductors. Several authors (see for example Ref. [35] and references therein) have suggested that these 18-electron semiconductors can be viewed as covalently bonded XZ negative ions forming a zincblende lattice "stuffed" with positive Y ions. In this picture, for instance, NiSc5 (5 = P, As, Sb) compounds would be viewed as a covalently bonded $(\mathrm{Ni5})^{3-}$ zincblende lattice stuffed with Sc^{3+} ions. We investigated the electronic structure of CoTiP, RhTiP, CoTiSb, RhTiSb, FeVSb and RuVSb in more detail to test these ideas. The atom-projected density of states (DOS) of RhTiP is presented in Fig. 3.16. The 27 semiconducting 18-electron half-Heuslers have a similar electronic structure. The nearest neighbor interactions are between the X and Z atoms (Rh and P in this case) and between the X and Y atoms (Rh and Ti). As mentioned previously, a lattice having only the X-Z atoms or only the X-Y atoms would have the zincblende crystal structure.

As can be seen from Fig. 3.16, the energy ordering of the atomic orbitals is Z-s (in this case forming a narrow band more than 10 eV below the Fermi level and not shown in the figure), followed by Z-p, followed by X-d and finally Y-d. The Z-p–Y-d interaction generates a hybridization gap well below the Fermi energy, while the Y-d–X-d interaction generates a hybridization gap (the Slater-Pauling gap) at the Fermi energy. The electronic structure of the other 18 electron

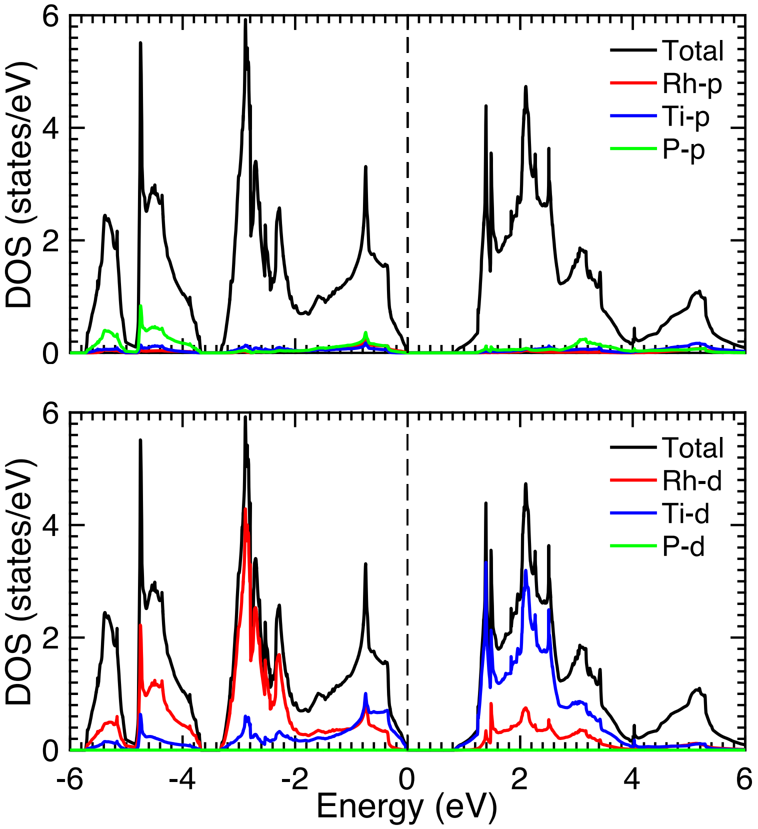

Figure 3.16: Density of electronic states (DOS) of the 18-electron half-Heusler semiconductor RhTiP. The upper panel presents the total DOS (black) and the DOS projected on the *p*-orbitals of Rh (red), Ti (blue) and P (green).The lower panel presents the contribution from the corresponding *d*-orbitals of each atom. Zero energy corresponds to the Fermi level.

semiconductors is similar except that the Z-s states are somewhat higher (≈ -7 to -8 eV) for group 4 Z elements and higher still (≈ -5 to -7 eV) for group 3 Z elements. Additionally, the hybridization gap between the X-d and the Z-p states is not fully formed in the systems with group 3 and 4 Z elements. The DOS can be interpreted in terms of a more covalent bond between the X and Z atoms and a more ionic bond between the X and Y atoms. This picture is supported by plots of the charge density shown in Fig. 3.17. These show a much larger charge density between the X and Z atoms than between the X and Y atoms. We also calculate the net charge within spheres of radius 1.45 Å. These are difficult to interpret in terms of "ionic charges" because of well-known ambiguities in how one partitions space among atoms in a solid. Nevertheless, all of the spheres are calculated to have net positive charges, with the positive charges on the Y atoms larger than those on the X or Z atoms.

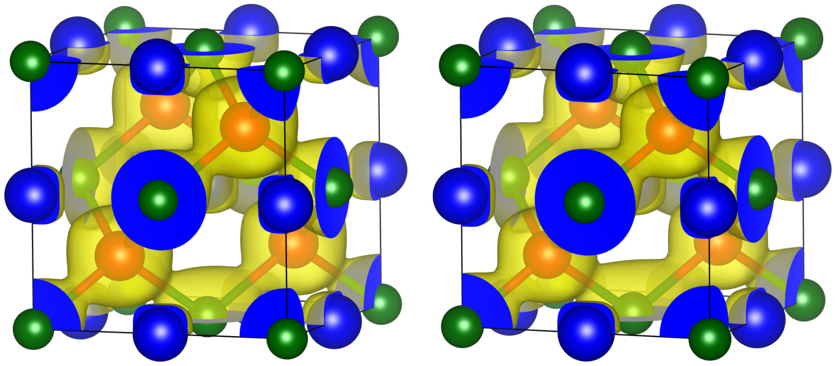

(a) RhTiP charge (b) CoTiP charge

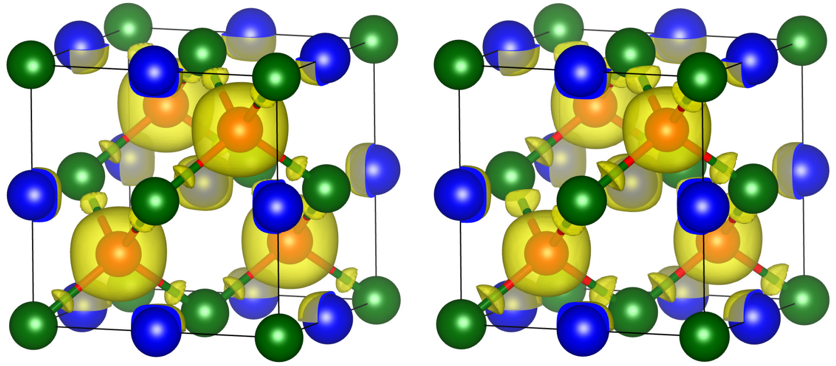

(c) RhTiSb charge (d) CoTiSb charge

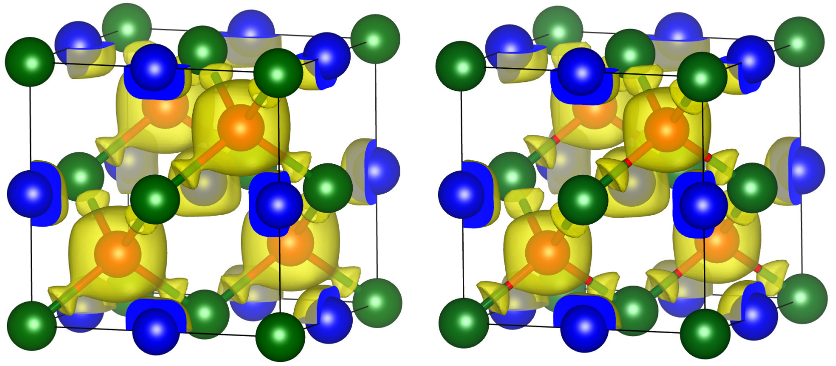

(e) RuVSb charge (f) FeVSb charge

Figure 3.17: Charge densities for (a) RhTiP, (b) CoTiP, (c) RhTiSb, (d) CoTiSb, (e) RuVSb, and (f) FeVSb, for an isovalue of 0.405 $e \cdot \text{Å}^{-3}$, respectively. The figures were generated using Visualization for Electronic and Structural Analysis (VESTA) [2].

3.6 Zero-Moment Half-Metals

Even more interesting than the non-magnetic 18-electron half-Heusler semiconductors discussed in the previous section are those 18-electron half-Heuslers that may be ferrimagnetic zero-moment Slater-Pauling half-metals. In contrast to an XYZ half-Heusler with Y = Ti or V, one with Y = Cr, Mn, or Fe (see columns 6Cr, 7Mn and 8Fe of Table 3.2) may have a ground state with a moment on the Y atom. If such a system is in a Slater-Pauling state, we expect it to have zero net moment per f.u. so any moment on the Y atom should be approximately balanced by an equal and opposite moment on the X atom. The word, "approximately", is needed in the last sentence because the magnetization density cannot be unambiguously partitioned among the atoms, and because there may be a small moment on the Z atom. This type of system should not be confused with an antiferromagnet because, even if the total magnetic moment is zero, it will have, unlike the typical antiferromagnet, different electronic structures for the two spin channels.

A zero-moment half-metal would be interesting since it would not respond to magnetic fields (assuming the internal exchange fields are sufficiently strong) but its transport currents would be nominally fully spin polarized. Another interesting feature would be that any magnetic anisotropy might lead to a potentially infinite magnetic anisotropy field, H_K, since $H_K = 2K/\mu_0 M_s$ where K is the magnetic anisotropy energy density, and M_s is the saturation magnetization. This anisotropy field would be associated with an extremely high (nominally infinite) ferromagnetic resonance (FMR) frequency. Robust materials of this type, if they can be fabricated, might offer the potential for magnetoelectronics that is competitive in terms of switching speed with traditional semiconductor electronics [127].

We investigate the electronic structure and formation energies of the 18-electron half-Heuslers in columns 6Cr, 7Mn and 8Fe of Table 3.2. The calculated properties for these systems – lattice constants, formation energies, magnetic moments, gap types – are summarized in Table 3.4. Many of these compounds have positive formation energies but the earlier observed trends of formation energies of the XYZ half-Heusler compounds decreasing with the group number of the Z element, and increasing with the size of the Z-element are still evident.

Many of these compounds are predicted to be nonmagnetic at the equilibrium lattice constant. The total moment per f.u. and the moments within spheres of radius 1.45 Å surrounding the atoms are listed in Table 3.4. All of the 33 compounds develop magnetic moments when the lattice is artificially expanded. The approximate lattice constant associated with the onset of magnetic moments is listed in the rightmost column of the table. If the 33 18-electron systems are sorted by "groups" having a common X and Y but different Z element, we find that the onset of magnetism occurs at approximately the same lattice constant for the three members of the same "group".

The lattice constant associated with the onset of magnetism varies between groups roughly according to our notion of the tendency of the various atoms to magnetically polarize. Thus, groups with Mn and Cr as the X and Y elements tend to become magnetic at smaller lattice constants. One interesting feature is that groups for which the atomic number of Y exceeds that of X polarize at a smaller lattice constant. That is, CrMn5, MnFe3, and CrFe4 polarize at smaller lattice constants than MnCr5, FeMn3, and FeCr4 respectively. Another interesting feature is that the moment on the Y atom (within the 1.45 Å sphere) always exceeds that on the X atom. This is true even when X and Y are interchanged (e.g., FeMn4 and MnFe4). The reason for this may be that X has a full complement of 8 nearest neighbors at a distance of $a\frac{\sqrt{3}}{4}$, while Y only has 4 at this distance, and thus has, in a sense, "more space". This notion of more space for the Y atom also helps explain the onset of magnetism at smaller lattice constants for CrFe4 compared to FeCr4, for MnFe3 compared to FeMn3, and CrMn5 compared to MnCr5, especially if the transition to the Slater-Pauling state is determined by the magnetic polarization of the atom on the X-site, i.e., the one with less space. In other words, Mn is easier to polarize than Cr which is easier to polarize than Fe. Remember that a magnetic Slater-Pauling state for an 18-electron half-Heusler requires that the X atom have a moment that is approximately equal in magnitude and opposite in sign to the moment on the Y atom.

For the CoCr3, RhCr3 and RuCr4 groups, the magnetic states form with a much larger moment on the Cr than on the Co, Rh or Ru atoms. Although these magnetic states are ferrimagnetic in the sense that the small Co, Rh, or Ru moments align oppositely to the larger Cr moments, their different magnitudes lead to a non-zero moment per formula unit precluding the Slater-Pauling state which would have zero moment. We speculate that the reason for this behaviour is that the Cr atom forms a large moment (especially as a Y atom with only four nearest neighbors) more easily when compared to Co, Rh, and Ru atoms. The density of electronic states (DOS) for systems with Y = Cr typically shows pseudogaps rather than gaps at the Fermi energy for the equilibrium lattice constant [83]. We speculate that the reason for this is that there is insufficient contrast between the $d-$onsite energies of the Co, Rh or Ru atoms and the Cr atom to support a gap. On (artificial) expansion of the lattice, a large magnetic moment forms on the Cr atoms, the minority $d-$onsite energy of the Cr atoms shifts upward significantly while the minority Co, Rh or Ru $d-$onsite energy shifts down slightly, creating a large difference between the minority $d-$onsite energies and a

Slater-Pauling gap. However, this gap is not at the Fermi energy because the X and Y moments are *not* approximately equal and opposite, so the system is not a half-metal even with an expanded lattice.

The RuMn3 compounds behave similarly to the three groups described in the previous two paragraphs, with the interesting exception that at a lattice constant of approximately 6.1 Å, these three compounds form a non-Slater-Pauling (non-SP) half-metallic state with a moment of 4 μ_B. In this state, the moment is largely on the Mn site with a small parallel moment on the Ru site. This non-SP half-metal actually seems to be the equilibrium state for $C1_b$ RuMnIn; however, the gap is very small and the formation energy is significantly greater than zero. The reason these compounds do not form in the Slater-Pauling state even for an expanded lattice is the same as that for the CoCr3, RhCr3, and RuCr4 groups of compounds: the X element cannot match the moment of the more easily polarizable Y element.

The 7 other groups in Table 3.4, show an interesting competition between the Slater-Pauling state at larger lattice constants and a nonmagnetic state with a pseudogap near the Fermi energy for smaller lattice constants. As the lattice is expanded, these compounds undergo a transition into a Slater-Pauling state with zero total moment, as opposite and approximately equal moments form on the X and Y atoms. If the moment on the X atom is taken to be positive, the gap is in the majority channel. Surprisingly, this result seems to be independent of whether the X or the Y atom has the larger number of valence electrons. Thus for MnCr5, as one expands the lattice, the Mn and Cr atoms acquire moments around $a = 5.5$ Å. In this case, the moment enhances the contrast between the atomic potentials in one channel and decreases it in the other. The gap forms in the channel with the increased contrast, i.e., since Mn has more electrons than Cr, a positive moment on the Mn and a negative moment on the Cr will increase the contrast in the majority channel and lead to a gap in the majority channel. More explicitly, neglecting charge transfer, Mn without a moment has 3.5 valence electrons/atom in each spin channel. Similarly, Cr without a magnetic moment has 3 valence electrons/atom in each spin channel. If Mn atoms gain a moment of 1.5 μ_B and Cr atoms gain a moment of -1.5 μ_B, then one spin channel will contain 4.25 electrons on Mn and 2.25 electrons on Cr, whereas the other spin channel will have 2.75 electrons/atom on Mn and 3.75 electrons/atom on Cr atoms. Thus, the contrast between the atoms in the two spin channels *increases* in one spin channel from 0.5 electrons/atom to 2 electrons/atom and in the other from 0.5 electrons/atom to 1 electron/atom. It is not surprising that the gap is in the channel with the larger contrast, i.e., the majority channel if Mn is assumed to have a positive moment. It is surprising however that for CrMn5, CrFe4, and MnFe3, the gap is also in the majority channel if the sign of the moment on the X atom is taken to be positive. For these compounds, the moments increase rapidly, even discontinuously, as the lattice is expanded. The moments are generally larger, sufficiently large in fact to cause large contrast in the majority channel and support a gap in that channel. Of course, the contrast in the number of electrons per atom is even larger for the minority channel, without inducing a gap. It is clear that, at least in this case, the contrast in the number of electrons/atom/spin channel is not the only factor controlling the origin of the gap.

According to our calculations, many of these compounds that are non-magnetic with pseudogaps could be converted to half-metals if the lattice could be expanded. One way to expand the lattice is to insert a larger atom on the Z-site. Unfortunately, from the point of view of fabricating a zero-moment half-metal, as one substitutes larger Z elements to increase the lattice constant, the formation energy also appears to increase. It is also possible to make the lattice constant too large for the Slater-Pauling zero net-moment half-metallic state. In this case the gap continues to be large as the lattice expands and the moments increase in magnitude, but the Fermi energy moves below the Slater-Pauling gap. An example of this effect is MnCrSb which has a gap, but it lies above the Fermi level, whereas MnCrAs with a smaller lattice constant and smaller moments is a half-metal.

Although a number of zero net-moment half-Heusler half-metals are listed in Table 3.4, only two (MnCrAs and CrMnAs) have negative formation energies. However, both are predicted to lie above the convex hull with hull distances $\Delta E_{\mathrm{HD}} = 0.083$ and 0.175 eV/atom respectively, due to a low-energy competing binary phase MnAs (MnP structure type, space group *Pnma*). Non-equilibrium processing techniques such as epitaxial growth would likely be needed to synthesize the $C1_b$ phases.

3.7 Half-metallic ferromagnets

Considering our entire database of 384 $C1_b$ systems rather than just the 18-electron systems, we find 75 half-metals of which 45 are calculated to have negative formation energy. In addition we find 34 half-Heusler compounds that are *near* half-metals with negative formation energy. In this section, we will focus on these compounds which are listed with their properties – number of valence electrons, spin magnetic moments, formation energy, hull distance, band gap, spin polarization – in Tables 3.5 and 3.7, respectively.

Although we restrict our attention to the systems with negative values of the calculated formation energy, our results to not conclusively exclude the existence of $C1_b$ systems with a calculated positive formation energy. Apart from limitations of DFT, there may be significant contributions to the entropy and free energy from several types of thermal disorder. In particular, the open structure of the half-Heuslers may be conducive to soft-phonon modes which may reduce its free energy relative to competing phases. This is a complex phenomenon because the magnetic and vibrational excitations may be coupled. There is also the possibility of configurational entropy arising from substitutional disorder, especially due to off-stoichiometry, i.e., excess X in the vacant sublattice, vacancies in the Y, Z sublattices, etc., but this is beyond the scope of our current work.

When we tested for stability against tetragonal distortions, only one of the 45 half-metallic half-Heusler compounds in Table 3.5 was calculated to have a lower energy in a tetragonal structure, CrTiAs. The total energy landscape for CrTiAs as a function of lattice constants a and c was discussed in Sec. 3.3.2, where it was shown to have two local minima, one with $c/a > 1$ and another at a slightly higher energy with $c/a < 1$. CrScP, CrScAs, CrScSb, CrTiP, and CrTiSb behave similarly to CrTiAs with the exception that the $Z =$ Sb compounds have a single global energy minimum. The $Z =$ (P, As) compounds have two energy minima that lie along a line describing volume conserving distortions. The calculated energy difference between these minima is extremely small, especially for the $Y =$ Sc compounds. If any of these phases can be fabricated, they would be expected to have anomalous properties.

Table 3.6 shows the lattice constants corresponding to the local energy minima for CrSc(P,As,Sb) and CrTi(P,As,Sb), the calculated magnetic spin moments at each minimum and the energy difference between the minima. CrScP appears in Table 3.7 and not in Table 3.5 because it is a near half-metal at its global minimum, but there is a nearly cubic local minimum that is only 2 meV higher in energy which is calculated to be half-metallic. For CrTiP, neither of the solutions is half-metallic although the one for $a > c$ comes close. Its energy, however is significantly higher than the phase with $c > a$. CrTiP is not included in Table 3.7 because its Fermi energy falls rather far from the gap ($M_{tot} = 2.53\ \mu_B$ rather than 3.00 μ_B per f.u.). CrScSb and CrTiSb are both predicted to be half-metallic and have only small tetragonal distortions. Although CrTiSb is predicted to be a half-metal in its ground state, it is omitted from Table 3.5 because its formation energy is calculated to be positive.

It may be important to note that these anomalous energy landscapes would imply soft long-wavelength phonons which would impact several physical properties, possibly including enhanced stability of these phases because of the associated contributions to the entropy and free energy. Observation of these anomalous phases may, unfortunately, be difficult because of the very low formation energy of the competing $B1$ Sc(P,As,Sb) and orthorhombic $P6_3/mmc$ Ti(P,As, Sb) binary phases.

If we consider up to NNN interactions, the nearest-neighbor couplings will only occur between $Y-X$ and $Z-X$ atoms. Since the four $s-p$ orbitals from the main group element Z hybridize with a lower energy level, the origin of the gap in the gapped spin channel comes from the hybridization between the five $3d$ states of the higher valence and the lower valence transition metal atoms X and Y. As the Fermi energy falls in the gap, there are a total of $4+5=9$ states being filled in this spin channel (as shown in Fig.3.18). Since the spin moment per atom is just the difference in the number of up and down electrons per atom ($M = N^{\uparrow} - N^{\downarrow}$), and since $N = N^{\uparrow} + N^{\downarrow}$, with 9 states fully occupied in the gapped channel ($N^{\downarrow} = 9$) we get the simple ‘rule of 18 for half-metallicity in half-Heusler compounds:

$$M_{tot} = N_V - 18 \tag{3.5}$$

where M_{tot} is the total magnetic moment and N_V is the total number of valence electrons per XYZ formula unit. If the total valence electron number is 18, the system will tend to be semiconducting with 9 electrons under the Fermi energy per spin channel. If the total valence electron number is not equal to be 18, one spin channel may be ’doped’ to be metallic while the other spin channel remains semiconducting, resulting in a half-metal. We find from our computational results that all the semiconductors and half-metals in the half-Heusler family do follow this simple Slater-Pauling rule precisely with integer total moments.

In Fig. 3.19, we summarize the calculated total magnetic moments as a function of the total number of valence electrons for all the investigated half-Heusler compounds (including the 6 additional compounds with $Y=$ Sc) with negative formation energy (203 of the 384 compounds

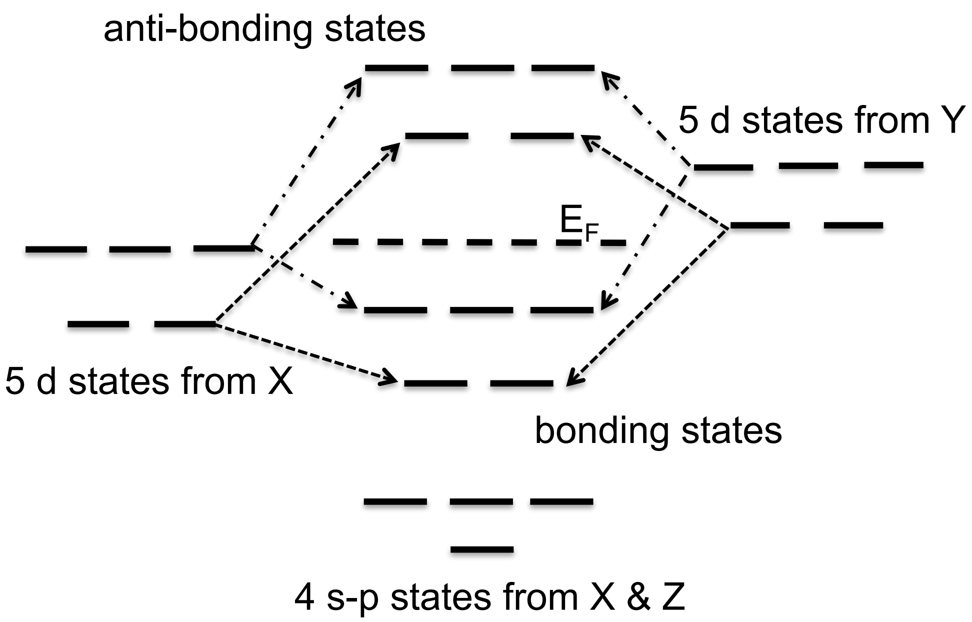

Figure 3.18: Schematic illustration of hybridization in the gapped channel of the half-Heusler compounds: The energy levels of the energetically lower lying bonding *d* states are separated from the energy levels of the anti-bonding *d* states by a gap, such that only the 5 bonding *d* states are occupied. The lowest occupied 4 $s-p$ states come from the hybridization between X and Z elements.

considered in this work). From our calculations, we discovered 26 semiconductors and 45 half-metals with negative formation energy. All the half-metals (listed in boxes and square symbols in the green ovals surrounding the dashed lines) and semiconductors (triangles in the gray circle at the base of the dashed lines) are summarized in Fig.3.19 and all follow the Slater-Pauling rule (Eq.3.5) precisely. All the other magnetic/nonmagnetic metals are marked out in the purple and yellow areas.

The five half-metals CrScAs, CrScSb, CrTiAs, MnVAs, and MnVSb have band gaps in the majority-spin channel since $N_V < 18$, while the band gaps of the half-metals with $N_V > 18$ are in the minority-spin channel. Two half-metals, MnCrAs and CrMnAs, have $N_V = 18$, and in this case the choice of the majority/minority spin channel is arbitrary. However, the channels are different and in both cases the gap occurs in the channel for which the atom on the X-site has more electrons. In other words, if Mn has a positive moment in MnCrAs then the gap is in the majority channel. If Cr has a positive moment in CrMnAs, then the gap is in the majority channel.

In order to analyze the magnetic configurations of the half-metallic half-Heusler compounds, we also list in Table 3.5 the local magnetic moments within spheres of radius 1.45 Å centered at the X-,

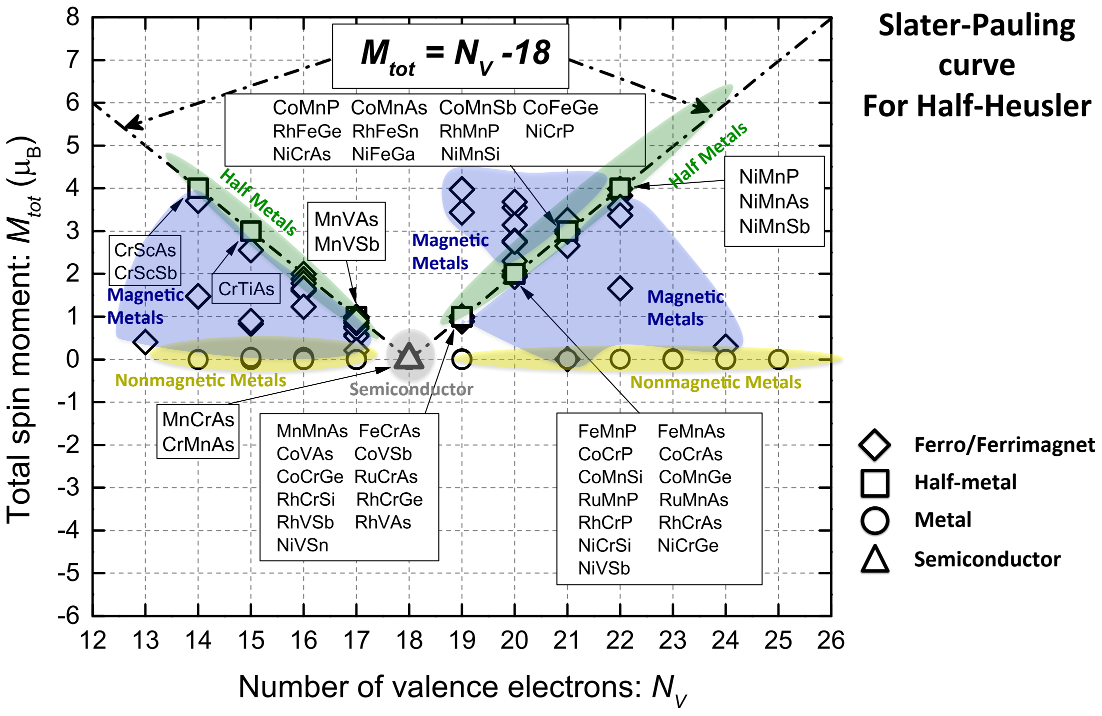

Figure 3.19: Calculated total magnetic moment M_{tot} as a function of the total number of valence electrons N_V per formula unit for the 203 half-Heusler compounds with negative formation energies. The dash-dot line represents the Slater-Pauling rule $M_{tot} = N_V - 18$, and all the 45 half-metals and 26 semiconductors follow this rule precisely. Diamond, square, circle, and triangle symbols indicate ferro/ferrimagnets, half-metals, metals, and semiconductors, respectively. We also use different color shapes to mark off half-metals, semiconductors, and magnetic/nonmagnetic metals. To avoid confusion about the signs of magnetic moments, we uniformly use the absolute values of magnetic moments in this diagram.

Y-, and Z-sites. We find that the magnetic configurations can be divided into several categories by the number of valence electrons N_V. The three half-metals with $N_V < 17$ (CrScAs, CrScSb, CrTiAs) have relatively large moments on the X sublattice with much smaller ferromagnetically aligned moments on the Y sublattice. The small moments on Y are due to the difficulty in magnetically polarizing Sc and Ti atoms. Perhaps the unusual (for a Slater-Pauling half-metal) tetragonal distortions result in additional space for the magnetic atom on the X-site.

For half-Heusler compounds with $N_V = 17$, the half-metals are ferrimagnetic with large moments on X- and smaller antiparallel moments on Y-sites. For compounds with $N_V = 18$, the net magnetic moment is zero: the X and Y sublattices have approximately equal but antiparallel spin moments. For half-Heuslers with $19 \leq N_V \leq 20$, most of the spin moment is on the Y sublattice, while the X sublattice has a moment that is small and usually opposite to that of the Y sublattice. For compounds with $21 \leq N_V \leq 22$, the half-metals tend to be ferromagnetic with large localized moments on the Y sublattice, and small spin moments on the Z sublattice.

We found no $C1_b$ half-metals with $M_{tot} > 4$. This limit can be understood if one makes the approximation that the local moment on the non-transition metal atom (the Z sublattice) is zero and that the number of majority spin electrons on either of the transition metal atoms is less than 5.5. This limit arises from the fact that there are only 5 d-states per spin channel per transition metal atom. Transition metal atoms have approximately one $s-$electron more or less degenerate with the $d-$states, shared between majority and minority. This leads to the $s-d$ bands holding 5.5 or fewer electrons per transition metal atom per spin channel. The requirement that $N^{\uparrow}_{V,X} + N^{\uparrow}_{V,Y} < 11$, together with the requirements that $N^{\uparrow}_{V,Z} = N^{tot}_{V,Z}/2$ and $M_{tot} = N^{tot}_{V,X} + N^{tot}_{V,Y} + N^{tot}_{V,Z} - 18$, leads to the limit $M_{tot} < 2 + N^{tot}_{V,Z}/2$. Since the largest value of $N^{tot}_{V,Z}$ that we considered was 5 and since M_{tot} must be an integer for half-metals, we obtain $M_{tot} \leq 4$. Thus, although one might imagine obtaining a large moment half-metal by choosing a system with large N_V, e.g. NiNiP ($N_V = 25$), a Slater-Pauling state with $M_{tot} = 7$ cannot be obtained because achieving large moments on Ni is not possible. Note that this limit does not apply for very small values of N_V, e.g., $C1_b$ CrTiIn ($N_V = 13$) is predicted to be a Slater-Pauling half-metal with $M_{tot} = 5$. Unfortunately, from the point of view of synthesizing high-moment half-Heusler half-metals, it is also predicted to have a large positive formation energy.

We analyzed the electronic structure – density of electronic states (DOS) and band dispersion – for each half-Heusler compound considered in this work. The size of the bandgap for each half-metal is listed in Table 3.5. All $C1_b$ half-metals with a negative formation energy have indirect band gaps. The valence band maximum is at Γ or L or occasionally at W in the Brillouin zone. The conduction band minimum is uniformly at X. Two half-metals that are tetragonally distorted, CrTiAs and CrScAs, have direct gaps at Γ. It should be noted that in MnVSb and RuMnAs (both counted as half-metals and listed in Table 3.5), and in CoCrSi (listed as a near half-metal in Table 3.7) the Fermi level just touches the band edge but their total magnetic moment still follows the Slater-Pauling rule. The precise location of the Fermi energy in these compounds might be further refined by future calculations.

Fig. 3.20 shows the total and atom-resolved DOS for six half-Heusler half-metals with X or $Y =$

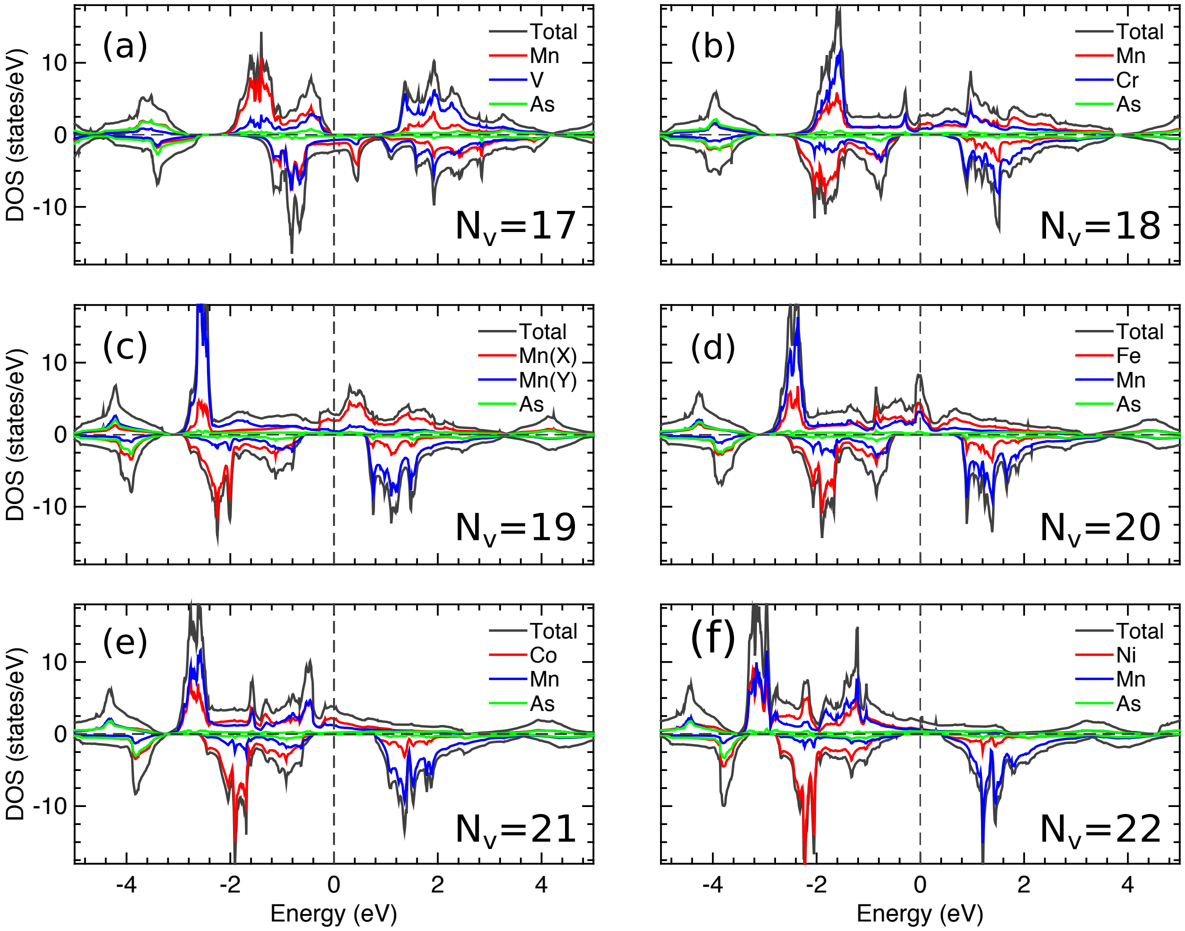

Figure 3.20: Calculated total and atom-resolved densities of electronic states for MnVAs, MnCrAs, MnMnAs, FeMnAs, CoMnAs and NiMnAs. In each subplot, the upper (lower) panel shows the majority (minority) spin channel. The number of valence electrons per f.u. N_V is also indicated for each system. Zero energy corresponds to the Fermi level.

Mn, all with negative formation energy, ordered by the number of valence electrons. In accordance with the Slater-Pauling rule (see Eq. 3.5), the states in one spin channel are filled to the Fermi level located in the band gap separating the filled and unfilled states. There are precisely 3 electrons per atom in this spin channel, and it can be seen that the gapped channel appears very similar for all the 6 compounds. There are 9 total electrons in the gapped channel for all the 6 compounds, and the remaining electrons accumulate in the other spin channel. Compounds with different number of total electrons will have different number of electrons in the metallic channel, implying changes in the energy levels of the transition metal orbitals. It can be seen in Fig. 3.20(a)–(f) that the energy levels and DOS shift downwards in energy in the metallic channel as the number of valence electrons per f.u. increases.

From Table 3.5, we see that the formation energy of the half-metallic half-Heuslers ranges from -0.44 eV/atom to barely negative. The 30 half-Heusler half-metals with positive formation energy are not shown in the table, but the calculated data is available online at `heusleralloys.mint.ua.edu` [83]. Although there is a wide range of formation energies for both, the half-Heusler half-metals are typically less stable than the half-Heusler semiconductors. This difference may be due to the former having a gap in only one spin channel while the latter have a gap in both spin channel (see Figs. 4.8–4.9, and the corresponding discussion in Sec. 3.4).

Using our calculated $C1_b$ formation energies, and the formation energies of all the other phases in the OQMD database, we calculate the hull distance ΔE_{HD} for all the half-metallic half-Heusler compounds (listed in Table 3.5. Of the 45 $C1_b$ half-metals with negative formation energy, our calculations predict 3 (CoVAs, CoMnAs, and NiMnSb) to lie on the convex hull of the respective systems. However, the *Pnma* phase has been observed experimentally for CoVAs and CoMnAs. Since the two *Pnma* phases are not in the OQMD, we calculated their formation energies and found them to be indeed lower than that of the respective $C1_b$ phase by 0.479 and 0.073 eV/atom for CoVAs and CoMnAs, respectively. We also verified that the $C1_b$ phase of NiMnSb is more stable than the *Pnma* phase by 0.172 eV/atom. On the other hand, we found experimental reports indicating that three systems in Table 3.5 (CoVSb, NiVSb, and CoMnSb) have been observed in the $C1_b$ structure, yet all three compounds are predicted to lie above the convex hull, with a linear combination of other phases predicted to be lower in energy:

(a) CoVSb: is predicted to lie near the convex hull with a mixture of phases $\mathrm{CoSb_3}$–$\mathrm{VCo_3}$–$\mathrm{V_3Co}$ lower in energy by $\Delta E_{\mathrm{HD}} = 0.011$ eV/atom. In fact, CoVSb has been synthesized and studied extensively [126,137,138,170–174], and the $C1_b$ phase seems to be well established, but the compound is a weak itinerant ferromagnet rather than a half-metal. It is possible that the spin fluctuations associated with this type of magnetism help to stabilize the phase.

(b) NiVSb: a linear combination of binary phases NiSb–$\mathrm{V_3Sb}$–$\mathrm{Ni_2V}$ is predicted to be lower in energy than the ternary $C1_b$ phase by $\Delta E_{\mathrm{HD}} = 0.130$ eV/atom. NiVSb was reported in the $C1_b$ structure in 1963 [123], but more recent studies of the Ni–V–Sb system, not only report failure in

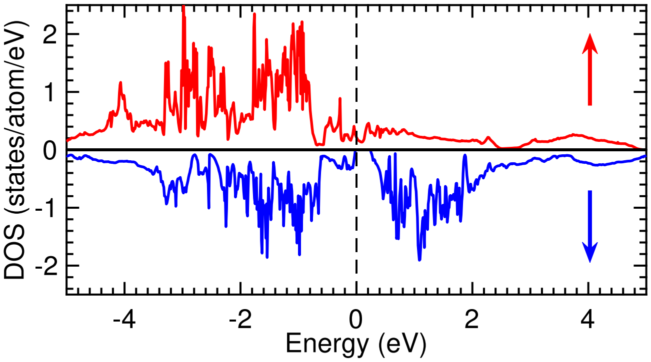

Figure 3.21: Calculated density of electronic states (DOS) of CoMnSb in the Co_2MnSb-MnSb superstructure reported in Ref. [3]. Zero energy corresponds to the Fermi level.

synthesizing the $C1_b$ NiVSb phase but also find a mixture of three binary phases (NiSb, V_3Sb, and VSb) coexisting at the equiatomic composition [175], in qualitative agreement with our calculations.

(c) CoMnSb: has been reported in the $C1_b$ structure [151, 157], but recent work [3] has shown its structure to be more complicated – a superstructure consisting of alternating layers of Co_2MnSb and MnSb. Its observed magnetic moment is substantially larger than the Slater-Pauling value of 3 μ_B/f.u. Our calculations confirm the lower energy of the Co_2MnSb-MnSb superstructure (by 0.012 eV/atom), but in contrast to those in Ref. [3], they indicate that that the superstructure is a non-Slater-Pauling half-metal with a moment of 3.75 μ_B/f.u. (30 μ_B for a 24-atom supercell). The minority channel is predicted to have 2.875 rather than 3 electrons/atom. Our calculated density of electronic states for the Co_2MnSb-MnSb superstructure is shown in Fig. 3.21.

Further, we find that 8 $C1_b$ half-Heusler compounds in Table 3.5 lie close to the convex hull with $\Delta E_{\text{HD}} \leq\sim$0.1 eV/atom. In almost all such cases, we find experimental reports of other non-$C1_b$ compounds at the composition (space group of the structure(s) experimentally reported, and hull distance ΔE_{HD} of the $C1_b$ half-Heusler compound in eV/atom): FeCrAs ($P\overline{6}2m$, 0.005), NiMnAs ($P\overline{6}2m$, $Pnma$, 0.017), MnMnAs ($P\overline{6}2m$, $P4/nmm$, 0.055), MnCrAs ($P4/nmm$, 0.083), RhVAs ($Pnma$, 0.099), CoCrAs ($P\overline{6}2m$, 0.101), RhVSb (none, 0.103), MnVAs ($P4/nmm$, 0.107). Attempts to synthesize some of the above compounds in the half-Heusler structure using non-equilibrium processing techniques may be merited. In addition, we found no experimental reports of phases for a dozen of the potential half-metallic half-Heuslers in Table 3.5. However, our calculated formation energies for these 12 compounds indicate that they all lie above the convex hull of the respective system, with $\Delta E_{\mathrm{HD}} > 0.1$ eV/atom.

We list in Table 3.7 the 34 XYZ half-Heusler phases with negative formation energy which our calculations predict to be "near half-metals", i.e., they have a gap in one of the spin channels at 3 electrons/atom and the Fermi energy falls just above or just below the gap. We also tabulate the calculated properties for the above phases – lattice constant, magnetic moments, formation energy, hull distance, spin polarization at Fermi energy, compounds reported experimentally at each composition, and reports of corresponding X_2YZ full-Heusler phases. These near half-metallic half-Heusler systems may be of interest for spintronic applications, especially if the position of the Fermi energy can be adjusted, e.g., by alloying or by applied electrical bias. It can be seen from Table 3.7 that there is one tetragonal near-half-metal – CrScP (see Table 3.6 and relevant discussion). All other compounds prefer the cubic $C1_b$ cell to a tetragonal distortion of that cell.

The total magnetic moments/f.u. calculated for all the 34 near half-metallic half-Heusler compounds in Table 3.7 are approximately integers. The difference between the total moment and an integer can be used to estimate how far the Fermi energy falls from the band gap in the gapped channel. For example, MnTiAs has 16 valence electrons and is calculated to have a moment of -1.9946 μ_B/f.u. Thus $N^{\uparrow} + N^{\downarrow} = 16$ and $N^{\uparrow} - N^{\downarrow} = 1.9946$ which implies that $N^{\uparrow} = 8.9973$ and $N^{\downarrow} = 7.0027$. There are therefore 0.0027 unfilled states below the gap in the majority channel which occurs at the Slater-Pauling value of 9 electrons/f.u.

Since Ti and Sc are hard to magnetically polarize, for most of the near-half-metals with $N_V \leq 17$, their magnetic moments are mainly localized on X, and there are smaller parallel magnetic moments on Y, resulting in ferromagnetic states. Interestingly, three CoTiZ (Z = Si, Ge, and Sn) compounds behave differently with approximately equal spin moments on Co and Ti. We also found an 18-electron ferrimagnetic near-half-metal, CrMnP, with small total magnetic moment of 0.0016 μ_B/f.u. As the number of valence electrons increases to 19, most of the near-half-metals are ferrimagnets whose spin moments are mainly localized on Y, while three NiVZ (Z = Si, Ge, and Sn) compounds prefer to be ferromagnets. The near-half-metals with $N_V \geq 20$, tend to be ferromagnets with large spin moments remaining on the atom in the Y-site.

Of the 34 compounds in Table 3.7, we find reports of experimental observation of the $C1_b$ phase for only two systems, FeTiSb and CoTiSn. Our calculations predict both the $C1_b$ phases to lie close to the convex hull with hull distances of $\Delta E_{\mathrm{HD}} = 0.034$ and 0.070 eV/atom, respectively. Both of these systems merit further discussion:

(a) FeTiSb: has been reported to exist in the $C1_b$ phase, however, recent experimental and theoretical studies [203] indicate that the composition of this phase is actually intermediate between the half- and full-Heusler compositions, close to $\mathrm{Fe_{1.5}TiSb}$. DFT calculations showed that several layered systems consisting of equal amounts of FeTiSb and $\mathrm{Fe_2TiSb}$ would generate semiconducting $\mathrm{Fe_{1.5}TiSb}$ compounds with formation energy per atom lower than a linear combination of FeTiSb + $\mathrm{Fe_2TiSb}$. The system with the lowest calculated formation energy was shown to be a non-magnetic semiconductor $\mathrm{Fe_{1.5}TiSb}$ phase with primitive unit cells of FeTiSb and $\mathrm{Fe_2TiSb}$ alternatingly layered in the [111] direction.

(b) CoTiSn: both the $C1_b$ XYZ and the $L2_1$ X_2YZ phases have been reported in the system. However, more recent experimental studies [204] have shown its composition also to be closer to $\mathrm{Co_{1.5}TiSn}$. Similar to the case of FeTiSb, a system consisting of alternating layers of $C1_b$ CoTiSn and $L2_1$ $\mathrm{Co_2TiSn}$ primitive cells layered along [111] was calculated to have a formation energy per atom lower than a combination of $C1_b$ CoTiSn + $L2_1$ $\mathrm{Co_2TiSn}$ [205], and was predicted to be a Slater-Pauling half-metal.

Further, we find 6 of the near half-metallic half-Heusler compounds with negative formation energy to lie close to the convex hull, i.e., with hull distances $\Delta E_{\mathrm{HD}} \leq \sim 0.1$ eV/atom. In most of the cases, we find experimental reports of other non-$C1_b$ compounds at the composition (space group of the structure(s) experimentally reported, and hull distance ΔE_{HD} of the $C1_b$ half-Heusler compound in eV/atom): FeFeAs ($P4/nmm$, 0.071), CoFeAs ($P\overline{6}2m$, 0.076), FeTiP ($Pnma$, 0.091), CoFeSb (none, 0.093), CoVP (none, 0.096), RhMnAs ($P\overline{6}2m$, 0.105). In particular, we did not find any compounds experimentally reported at the composition for CoVP and CoFeSb, which merit experimental synthesis efforts. In the case of all the other XYZ compositions for which we did not find any experimental reports of compounds (11 additional XYZ compositions), the calculated formation energies of the $C1_b$ phases predict them to lie farther away ($\Delta E_{\mathrm{HD}} > 0.1$ eV/atom) from the convex hull.

3.8 Summary of Contributions

In this chapter, using density functional calculations, we studied the thermodynamic and structural stability, electronic structure, and magnetism of 378 XYZ half-Heusler compounds (X = Cr, Mn, Fe, Co, Ni, Ru, Rh; Y = Ti, V, Cr, Mn, Fe, Ni; Z = Al, Ga, In, Si, Ge, Sn, P, As, Sb), and an additional 6 compounds with X = Ni, Cr, Y = Sc, and Z = P, As, Sb. We find that almost all of the 384 systems we studied exhibit a Slater-Pauling gap or a pseudogap in at least one of the spin channels, for some value of the lattice parameter. We find that having a gap at the Fermi energy in one or both spin channels contribute significantly to the stability of a half-Heusler compound relative to other possible phases.

We calculated the formation energy of all 384 XYZ compounds, and systematically compared their formation energy against all other phases or linear combination of phases at that composition in the Open Quantum Materials Database (OQMD). We represent the phase stability of each compound using its distance from the convex hull – the farther away a compound is from the convex hull, the less thermodynamically stable it is – and assert that the calculated hull distance of the compound is a good measure of the likelihood of its experimental synthesis. We find low formation energies and (mostly) correspondingly low hull distances for compounds with X = Co, Rh or Ni, Y = Ti or V, and Z = P, As, Sb, or Si.

Of the 384 half-Heuslers considered, we find 26 18-electron Slater-Pauling semiconductors with negative formation energy. In these systems a gap exists at the Fermi energy in both spin channels. Overall the agreement between theory and experiment was found to be good, i.e., most of the 18-electron XYZ compounds were correctly predicted to be in the $C1_b$ or the competing $Pnma$ structures, and all the experimentally reported compounds were found to lie on or close to (i.e., within ~0.1 eV/atom) the convex hull. Our calculations predict CoVGe and FeVAs in the $C1_b$ structure to be sufficiently lower in energy than the experimentally reported $Pnma$ structure that efforts to fabricate the $C1_b$ are justified. Further, our calculations predict semiconducting RuVAs phase (in the $C1_b$ structure), NiScAs, RuVP, RhTiP phases (all in the $Pnma$ structure) to lie on the convex hull (i.e., thermodynamically stable), and CoVSn, RhVGe phases (in the $C1_b$ structure) to lie close to the convex hull of phases. We found no experimental reports of any compounds at these compositions, and thus these compounds present opportunities for experimental exploration.

We find two particularly interesting compounds, CrMnAs and MnCrAs, with 18 electrons/f.u. that are predicted to be zero-moment half-metals rather than semiconductors, and have negative formation energy. Both are calculated to lie above the convex hull, however, and non-equilibrium processing techniques may be necessary to synthesize them.

Further, we find 45 half-Heusler half-metals with negative formation energy. In these systems the Fermi energy falls in the Slater-Pauling gap for only one of the spin channels. We also find 34 half-Heusler near half-metals with negative formation energy. In these systems, there is a Slater-Pauling gap, but the Fermi energy falls very near but not quite in the gap. Our calculations predict a half-metal RhVSb, and two near half-metals, CoFeSb and CoVP, to lie within ~0.1 eV/atom of the convex hull. The lack of experimental reports of any compound at the three compositions merits efforts to synthesize them.

Overall, our calculations correctly predict a large number of experimentally-reported half-Heusler compounds to be thermodynamically stable. In addition, they also predict a number of semiconducting, half-metallic, and near half-metallic half-Heusler compounds to lie above but close to the convex hull. Such compounds may be experimentally realized using suitable (non-equilibrium) synthesis conditions.

Table 3.4: 33 18-electron half-Heuslers with Y = Cr, Mn, or Fe. Successive columns present: calculated lattice constant a, formation energy ΔE_f, electronic ground state, total spin moment M_{tot}, local moments for atoms on X, Y, and Z-sites: $m(X)$, $m(Y)$, and $m(Z)$, gap type, and magnetic lattice constant a_{mag}. ([Legend] Electronic ground state: NMM = non-magnetic metal, HM = half-metal, FiM = ferrimagnetic metal, MM = magnetic metal. Gap type: P = pseudo gap, M/m = gap in the major/minor spin channel.)

XYZ	a	ΔE_f	Electronic	M_{tot}	$m(X)$	$m(Y)$	$m(Z)$	Gap type	a_{mag}
	(Å)	(eV/atom)	ground state		(μ_B/f.u.)				(Å)
CoCrAl	5.45	0.033	NMM	0.000	0.000	0.000	0.000	P	5.90
CoCrGa	5.45	0.078	NMM	0.000	0.000	0.000	0.000	P	5.80
CoCrIn	5.76	0.465	NMM	0.000	0.000	0.000	0.000	P	5.85
RhCrAl	5.73	−0.075	NMM	0.000	0.000	0.000	0.000	P	6.35
RhCrGa	5.74	0.065	NMM	0.000	0.000	0.000	0.000	P	6.25
RhCrIn	6.19	0.207	MM	−3.704	0.020	−3.461	−0.009	m (1.2 eV)	6.25
FeCrSi	5.33	−0.231	NMM	0.000	0.000	0.000	0.000	P	5.65
FeCrGe	5.45	−0.025	NMM	0.000	0.000	0.000	0.000	P	5.60
FeCrSn	5.85	0.274	HM	0.000	1.827	−1.861	0.066	M	5.80
RuCrSi	5.61	−0.115	NMM	0.000	0.000	0.000	0.000	P	6.40
RuCrGe	5.71	0.059	NMM	0.000	0.000	0.000	0.000	P	6.30
RuCrSn	5.99	0.246	NMM	0.000	0.000	0.000	0.000	P	6.40
MnCrP	5.30	−0.460	NMM	0.000	0.000	0.000	0.000	P	5.40
MnCrAs	5.51	−0.101	HM	0.000	1.487	−1.478	0.033	M	5.45
MnCrSb	5.95	0.097	near HM	−0.014	2.709	−2.711	0.046	M (0.07 eV)	5.55
FeMnAl	5.42	0.157	NMM	0.000	0.000	0.000	0.000	P	5.50
FeMnGa	5.49	0.214	near HM	−0.012	1.414	−1.482	0.078	M (0.08 eV)	5.40
FeMnIn	5.95	0.523	near HM	−0.546	2.451	−3.116	0.078	M (0.26 eV)	5.50
RuMnAl	5.67	0.128	NMM	0.000	0.000	0.000	0.000	P	5.80
RuMnGa	5.69	0.236	FiM	0.110	0.105	−0.236	0.200	P	5.70
RuMnIn	6.15	0.421	non-SP HM	4.000	−0.114	−3.741	−0.013	M	5.70
MnMnSi	5.37	−0.098	weakly MM	0.007	1.315	−1.329	0.064	P	5.20
MnMnGe	5.58	0.047	HM	0.000	2.273	−2.317	0.068	M	5.20
MnMnSn	6.05	0.184	near HM	0.174	3.111	−3.348	0.036	M (0.17 eV)	5.20
CrMnP	5.42	−0.264	near HM	0.000	1.725	−1.758	0.066	M (0.01 eV)	5.20
CrMnAs	5.79	−0.009	HM	0.000	2.620	−2.676	0.038	M	5.20
CrMnSb	6.10	0.151	near HM	0.194	3.086	−3.371	−0.007	M (0.18 eV)	5.15
MnFeAl	5.52	0.292	FiM	0.001	1.534	−1.556	0.053	P	5.30
MnFeGa	5.56	0.299	FiM	0.007	1.999	−2.032	0.041	P	5.20
MnFeIn	5.96	0.589	HM	0.000	2.676	−2.708	0.003	M	5.30
CrFeSi	5.45	0.141	FiM	0.050	1.300	−1.385	0.056	P	5.40
CrFeGe	5.65	0.249	HM	0.000	2.129	−2.164	0.021	M	5.35
CrFeSn	6.01	0.417	HM	0.000	2.596	−2.664	−0.014	M	5.50

Table 3.5: DFT-calculated properties of 45 half-metallic XYZ half-Heusler compounds with negative formation energy. Successive columns present: number of valence electrons per formula unit N_V, calculated lattice constant a, total spin moment M_{tot} per f.u., local moments for atoms on the X-, Y-, and Z-sites: $m(X)$, $m(Y)$, and $m(Z)$, formation energy ΔE_f, distance from the convex hull ΔE_{HD}, band gap E_g, experimental reports of compounds with composition XYZ, and experimental reports of corresponding X_2YZ full-Heusler compounds, if any. All half-Heusler compounds listed exhibit an indirect band gap, with the exception of CrScAs and CrTiAs, both of which exhibit a direct gap.

XYZ	N_V	a (Å)	M_{tot}	$m(X)$	$m(Y)$	$m(Z)$	ΔE_f	ΔE_{HD}	E_g (eV)	Experimental reports	X_2YZ reports
			(μ_B)				(eV/atom)				
CrScAs	14	6.11(6.13)	−4	−3.276	−0.445	0.044	−0.128	0.790	0.73		
CrScSb	14	6.43	−4	−3.330	−0.335	0.059	−0.106	0.522	0.99		
CrTiAs	15	5.52(6.66)	−3	−2.458	−0.376	0.011	−0.009	0.623	0.69	$P\bar{6}2m$ [128]	
MnVAs	17	5.59	−1	−1.574	0.625	−0.039	−0.243	0.107	0.87	$P4/nmm$ [98]	
MnVSb	17	5.92	−1	−2.157	1.180	−0.027	−0.034	0.156	0.94	$P6_3/mmc$ [129]	
CrMnAs	18	5.71	0	−2.618	2.671	−0.036	−0.009	0.175	0.98	$P4/nmm$ [130]	
MnCrAs	18	5.51	0	−1.474	1.464	−0.031	−0.101	0.083	0.73	$P4/nmm$ [130]	
MnMnAs	19	5.63	1	−2.068	2.995	0.023	−0.131	0.055	1.11	$P\bar{6}2m$ [131], $P4/nmm$ [132, 133]	
FeCrAs	19	5.48	1	−0.652	1.640	−0.036	−0.137	0.005	0.96	$P\bar{6}2m$ [130, 134]	
RuCrAs	19	5.74	1	−0.316	1.357	−0.064	−0.030	0.168	0.58	$Pnma$ [114, 135]	
CoCrGe	19	5.47	1	−0.339	1.391	−0.078	−0.035	0.124	0.96	$P6_3/mmc$ [136], $Cmcm$ [136]	
CoVAs	19	5.53	1	−0.123	1.092	−0.028	−0.363	0	1.22	$Pnma$ [128]	
CoVSb	19	5.81	1	−0.246	1.217	−0.041	−0.182	0.011	0.90	$F\bar{4}3m$ [126, 137], $P6_3/mmc$ [138]	
RhCrSi	19	5.65	1	−0.148	1.230	−0.093	−0.183	0.407	0.57		
RhCrGe	19	5.75	1	−0.191	1.293	−0.098	−0.056	0.314	0.67		
RhVAs	19	5.81	1	−0.156	1.165	−0.061	−0.377	0.099	0.88	$Pnma$ [114, 139]	
RhVSb	19	6.06	1	−0.166	1.189	−0.062	−0.312	0.103	0.80		
NiVSn	19	5.87	1	0.004	1.017	−0.056	−0.079	0.148	0.48		[140, 141]
FeMnP	20	5.32	2	−0.401	2.380	−0.040	−0.424	0.149	0.83	$Pnma$ [142], $P\bar{6}2m$ [143]	
FeMnAs	20	5.51	2	−0.708	2.690	−0.041	−0.134	0.075	1.08	$P4/nmm$ [134], $P\bar{6}2m$ [144]	
RuMnP	20	5.59	2	−0.313	2.350	−0.072	−0.280	0.261	0.65		
RuMnAs	20	5.76	2	−0.410	2.489	−0.087	−0.053	0.158	0.78	$P\bar{6}2m$ [114, 145]	
CoCrP	20	5.32	2	−0.036	2.054	−0.077	−0.362	0.193	1.34	$Pnma$ [130]	
CoCrAs	20	5.52	2	−0.276	2.305	−0.090	−0.104	0.101	1.07	$P\bar{6}2m$ [130]	
CoMnSi	20	5.36	2	−0.037	2.169	−0.162	−0.209	0.257	0.78	$Pnma$ [146], $P6_3/mmc$ [147]	[119, 148, 149]
CoMnGe	20	5.49	2	−0.254	2.394	−0.152	−0.057	0.150	0.99	$Pnma$ [150], $P6_3/mmc$ [147]	[151–153]
RhCrP	20	5.65	2	−0.234	2.297	−0.121	−0.293	0.377	0.91		
RhCrAs	20	5.81	2	−0.291	2.384	−0.135	−0.121	0.209	0.95	$P\bar{6}2m$ [135, 154]	
NiCrSi	20	5.44	2	0.067	2.040	−0.158	−0.116	0.345	0.85	$Pnma$ [103]	
NiCrGe	20	5.54	2	−0.022	2.150	−0.163	−0.001	0.237	0.64		
NiVSb	20	5.89	2	0.070	1.878	−0.078	−0.122	0.129	0.41	$F\bar{4}3m$ [123]	
CoMnP	21	5.34	3	0.078	2.947	−0.108	−0.443	0.290	1.29	$Pnma$ [155, 156]	
CoMnAs	21	5.53	3	−0.092	3.130	−0.109	−0.211	0	1.16	$Pnma$ [128, 142]	
CoMnSb	21	5.82	3	−0.178	3.262	−0.111	−0.108	0.012	0.89	$F\bar{4}3m$ [151, 157], $Fd\bar{3}m$ [158] $Fm\bar{3}m$ [3, 160]	[151, 159]
CoFeGe	21	5.50	3	0.507	2.601	−0.131	−0.061	0.126	0.44	$P6_3/mmc$ [151]	
RhMnP	21	5.67	3	−0.136	3.229	−0.153	−0.404	0.318	0.89	$P\bar{6}2m$ [135, 161]	
RhFeGe	21	5.78	3	0.201	2.908	−0.102	−0.139	0.231	0.49		
RhFeSn	21	6.05	3	0.192	2.978	−0.094	−0.121	0.225	0.48		
NiCrP	21	5.42	3	0.152	2.854	−0.121	−0.254	0.335	0.77	$Pnma$ [130, 162], $P\bar{6}2m$ [162]	
NiCrAs	21	5.62	3	0.037	2.991	−0.146	−0.079	0.153	0.56	$P\bar{6}2m$ [130, 154]	
NiMnSi	21	5.45	3	0.120	3.028	−0.207	−0.251	0.242	0.85	$P6_3/mmc$ [147], $Pnma$ [103, 163]	
NiFeGa	21	5.56	3	0.332	2.792	−0.132	−0.017	0.266	0.59		[164]
NiMnP	22	5.46	4	0.333	3.607	−0.062	−0.400	0.237	0.87	$P\bar{6}2m$ [142, 165], $Pnma$ [130]	
NiMnAs	22	5.64	4	0.278	3.688	−0.082	−0.250	0.017	0.69	$P\bar{6}2m$ [166], $Pnma$ [130]	
NiMnSb	22	5.91	4	0.222	3.764	−0.081	−0.217	0	0.48	$F\bar{4}3m$ [151, 160, 167]	[151, 168, 169]

Table 3.6: Lattice constants and total magnetic moments per f.u. corresponding to the different energy minima, and the energy difference between the minima, for CrSc5 and CrTi5 compounds. The compounds with integer moments are predicted to be half-metals.

XYZ	Min. (1) (a_1, c_1)	$M_{tot}^{(1)}$ (μ_B)	Min. (2) (a_2, c_2)	$M_{tot}^{(2)}$ (μ_B)	$\Delta E_{(1)-(2)}$ (eV/f.u.)
CrScP	(5.64, 6.65)	−3.9999	(5.96, 5.90)	−4	−0.002
CrScAs	(5.95, 6.48)	−4	(6.11, 6.13)	−4	0.002
CrScSb	—	—	(6.43, 6.42)	−4	—
CrTiP	(5.24, 6.67)	−2.5301	(5.78, 5.50)	−2.983	−0.094
CrTiAs	(5.52, 6.66)	−3	(5.97, 5.67)	−3	−0.052
CrTiSb	—	—	(6.19, 6.15)	−3	—

Table 3.7: DFT-calculated properties of 34 near half-metallic XYZ half-Heusler compounds with negative formation energy. Successive columns present: number of valence electrons per formula unit N_V, calculated lattice constant a, total spin moment M_{tot} per f.u., local moments for atoms on the X-, Y-, and Z-sites: $m(X)$, $m(Y)$, and $m(Z)$, formation energy ΔE_f, distance from the convex hull ΔE_{HD}, spin polarization at Fermi energy $\mathcal{P}(E_F)$, experimental reports of compounds with composition XYZ, and experimental reports of corresponding X_2YZ full-Heusler compounds.

XYZ	N_V	a (Å)	M_{tot}	$m(X)$	$m(Y)$	$m(Z)$	ΔE_f	ΔE_{HD}	$\mathcal{P}(E_F)$	Experimental reports	X_2YZ reports
			(μ_B)				(eV/atom)				
CrScP	14	5.64 (6.65)	−3.9999	−3.271	−0.464	0.021	−0.241	0.838	0.9900		
MnTiAs	16	5.74	−1.9946	−1.848	−0.027	−0.036	−0.298	0.334	0.8902	$P\bar{6}2m$ [128]	
FeTiP	17	5.45	−0.8837	−0.621	−0.180	−0.055	−0.802	0.091	0.6074	$Pnma$ [110, 176]	
FeTiAs	17	5.65	−0.9896	−1.080	0.141	−0.042	−0.550	0.145	0.8895	$P\bar{6}2m$ [128]	
FeTiSb	17	5.95	−0.9550	−1.301	0.356	−0.023	−0.382	0.034	0.6670	$F\bar{4}3m$ [123]	
FeVGe	17	5.56	−1	−1.136	0.202	−0.052	−0.157	0.137	0.6487		
CoTiSi	17	5.58	−0.9998	−0.407	−0.430	−0.102	−0.590	0.222	0.7874	$Pnma$ [120, 177, 178], $P\bar{6}2m$ [179]	[121, 180, 181]
CoTiGe	17	5.64	−0.9734	−0.415	−0.401	−0.078	−0.498	0.117	0.5117	$P\bar{6}2m$ [179]	[121, 181]
CoTiSn	17	5.93	−0.9647	−0.383	−0.416	−0.048	−0.360	0.070	0.7131	$F\bar{4}3m$ [108, 182]	[109, 182, 183]
NiTiIn	17	5.99	−0.9996	−0.078	−0.668	−0.068	−0.168	0.280	0.9664		
MnVP	17	5.40	−0.8574	−1.057	0.268	−0.047	−0.539	0.190	0.2099		
CrMnP	18	5.42	0.0016	−1.715	1.744	−0.064	−0.264	0.282	0.9959		
MnMnP	19	5.33	1	−0.964	1.916	0.002	−0.419	0.178	0.9914	$P\bar{6}2m$ [184, 185]	
FeCrP	19	5.29	0.9978	−0.346	1.298	−0.023	−0.465	0.180	0.8754	$Pnma$ [186–188]	
FeMnSi	19	5.32	0.9718	−0.306	1.295	−0.056	−0.155	0.257	0.9228		
RuCrP	19	5.58	0.9958	−0.240	1.249	−0.052	−0.281	0.215	0.9019		
CoVP	19	5.36	0.9949	−0.022	0.974	−0.010	−0.643	0.096	0.9265		
CoCrSi	19	5.36	1	−0.214	1.254	−0.069	−0.203	0.251	0.9960	$Pnma$ [103]	
RhVP	19	5.66	0.9998	−0.124	1.116	−0.048	−0.567	0.286	0.9587		
NiVSi	19	5.47	0.9582	0.097	0.841	−0.040	−0.316	0.259	0.9097	$Pnma$ [103, 120]	
NiVGe	19	5.58	0.9917	0.042	0.944	−0.052	−0.203	0.127	0.9655	$Pnma$ [120]	
NiVP	20	5.45	1.9054	0.168	1.656	−0.035	−0.403	0.324	0.7368	$Pnma$ [189]	
NiVAs	20	5.62	1.9956	0.127	1.802	−0.063	−0.200	0.182	0.5758	$Pnma$ [98, 128]	
FeFeP	21	5.31	2.9346	0.469	2.447	−0.047	−0.350	0.199	0.5125	$P\bar{6}2m$ [190, 191], $Pnma$ [192] $P321$ [193], $Imm2$ [194]	
FeFeAs	21	5.49	2.9999	0.459	2.547	−0.053	−0.071	0.071	0.9376	$P4/nmm$ [185, 195]	
RuFeAs	21	5.76	2.8648	0.131	2.723	−0.028	−0.012	0.186	0.0665		
CoFeSi	21	5.36	2.9966	0.573	2.514	−0.143	−0.204	0.254	0.8636	$Pnma$ [103]	[151, 196, 197]
RhMnAs	21	5.83	3.0289	−0.182	3.346	−0.160	−0.256	0.105	0.6134	$P\bar{6}2m$ [168, 198]	
RhFeSi	21	5.68	2.9903	0.220	2.860	−0.104	−0.240	0.335	0.7374		
NiMnGe	21	5.57	3.0076	0.032	3.147	−0.203	−0.153	0.111	0.6038	$P6_3/mmc$ [147] $Pnma$ [200–202], $Cmcm$ [201]	[199]
NiFeAl	21	5.56	2.9978	0.361	2.760	−0.137	−0.069	0.377	0.8543		
CoFeP	22	5.35	3.8481	0.920	2.854	−0.021	−0.348	0.236	0.1231	$Pnma$ [142, 165]	
CoFeAs	22	5.53	3.9795	0.982	2.944	−0.024	−0.130	0.076	0.6560	$P\bar{6}2m$ [130]	
CoFeSb	22	5.81	3.9793	0.995	2.982	−0.033	−0.033	0.093	0.5237		

Chapter 4

Screening for Novel Inverse-Heusler Compounds

4.1 Introduction

Heusler-like compounds, sometimes called “inverse-Heuslers” (IH) which are described below can have electronic structures similar to those of the full-Heusler and half-Heusler compounds, in the sense that they may be half-metallic or semiconducting. In addition, the IH compounds can have an electronic structure that has been described as a “spin-gapless semiconductor(SGS)” [206], *i.e.* a large gap at the Fermi energy for one spin channel and a very small gap at the Fermi energy for the other channel.

In this chapter, we describe the results of calculations of the properties of IH compounds with particular emphasis on those IH compounds that may be of use for spintronics applications and which may have a reasonable probability of being synthesized.

A universal feature of the electronic structure of Heusler compounds that we consider is the existence of a relatively broad $s-$band followed at higher energy by bands that are primarily derived from $d-$states (Fig. 4.1). One particular feature of the electronic structure of the IH compounds is especially interesting. The half-Heusler and full-Heusler families often have band gaps after 3 states per atom counting from and including the just mentioned s-band. We call this type of gap a Slater-Pauling gap because Slater and Pauling, but especially Slater, noticed that many bcc based

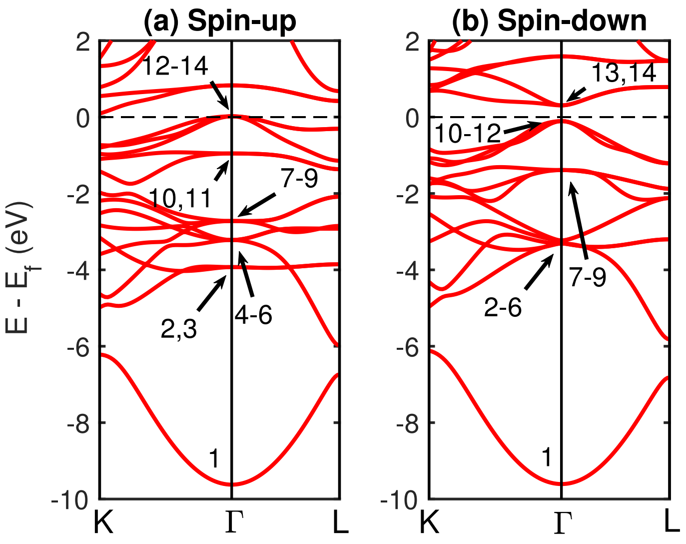

Figure 4.1: The band structures of Mn_2CoAl in (a) spin-up and (b) spin-down channels are shown. Bands from 1 to 14 are labeled in (a) and (b). The zero of the energy axis corresponds to the Fermi level.

alloys have approximately 3 states per atom in the minority spin channel [84, 207, 208]. Furthermore, Slater and Koster showed that for a nearest-neighbor tight-binding model for a B2 alloy (see figure 1.2) with only d-states, a gap forms in the center of the d-band [84].

The "Slater-Pauling" state for bcc alloys has been ascribed to a minimum in the electronic DOS near the center of the $s-d$ band. This minimum becomes an actual gap after 3 states per atom in one of the spin-channels in some Heusler compounds. In contrast, although many IH compounds show Slater-Pauling gaps at 3 states per atom, some have gaps after a number of states per atom that differs from three.

Thus IH compounds often have gaps after 9, 12, and 14 states per formula unit in the gapped channel. The gap after 12 states corresponds to the Slater-Pauling gap. The gaps after 9 states and 14 states are additional gaps allowed by the reduced symmetry of the inverse-Heusler compared to the full-Heusler. Semiconducting states are possible with half-Heuslers and full-Heuslers, but these typically occur when both spin channels have Slater-Pauling gaps, and both spin-channels are identical implying no magnetic moments on any of the atoms. In contrast, the multiple gaps of the IH compounds allows the possibility of a magnetic semiconductor, *e.g.* when the minority channel has a gap after 12 filled states and the majority has a gap after 14 filled states. The multiple gap possibilities and the possibility of a magnetic semiconductor is illustrated by the partial band structures of Mn_2CoAl shown in Fig. 4.1. Here it can be seen that the down spin channel has a gap after 12 states per formula unit and the up spin channel has potential gaps after 9 and after 14 states per formula unit. The effect of reduced symmetry on the potential up spin gap after 9 states can be seen in the avoided crossing of bands 9 and 10. For some systems this avoided crossing leaves only a tiny gap. A full explanation of possible band gaps requires an analysis of the band ordering at symmetry points and the symmetry dependent band compatibility relations.

We note that other authors [32, 39, 41, 209] use the term "Slater-Pauling gap" to refer to any gap that can create a half-metal in a Heusler compound. We prefer to reserve the term for gaps after 3 states per atom. We apologize for any confusion our attempt to refine nomenclature may cause.

The reduced-symmetry-derived gaps after 9 and 14 states are often quite narrow so that a state called a spin gapless semiconductor (SGS), a special type of semiconductor in which the Fermi level falls into a relatively large gap in the minority spin-channel (after 12 states) and within a narrow gap for the majority (after 14 states) [209, 210]. This band structure allows both electrons and holes to be excited simultaneously carrying 100% spin polarized current, potentially with high mobility. Recently, the existence of some IH compounds has been confirmed by experiment [211–213]. Additionally, it has been experimentally verified that Mn_2CoAl is an SGS with high Curie temperature [206].

Interestingly, the half-Heusler $C1_b$ phase has the same space group as the inverse-Heusler XA phase and is also prone to gaps after 9 and 14 states per formula unit in a spin-channel. However, in this case 9 states per formula unit coincides with the Slater-Pauling gap after 3 states/atom.

We anticipate that a large and complete database of consistently calculated properties of IH compounds will allow the testing of hypotheses that may explain the occurrence and size of Slater-Pauling band gaps as well as the gaps that occur in some IH compounds after 9 and 14 states per formula unit.

Although a large number of IH compounds have been analyzed by first-principles calculations [41, 42, 209, 214–216], a comprehensive study of the structural, electronic and magnetic properties of the IH family is useful, because it is not clear how many of the IH half-metals and semiconductors that can be imagined are thermodynamically stable in the XA structure. Thus, a systematic study of the structural stability of the IH family can provide guidance for future work.

In Sec. 4.2 we describe the details of our computational approach. Sec. 4.2.1 describes the DFT calculations. In Sec. 4.2.2, we discuss how the equilibrium structures for each compound were determined and the possibility of multiple solutions in energy and magnetic configuration for some specific compounds. Our approach to estimating the stability of the IH compounds is described in Sec. 4.2.3.

Section 4.2.3 and 4.2.3 describes the formation energies that we calculated for the IH compounds and how these formation energies compare to those of competing phases. Section 4.3.1 describes a study of the calculated formation energies and stability of those IH phases that have been observed experimentally. The relationship between stability and composition is discussed in Sections 4.3.2. Section 4.3.3 describes our calculated results for the formation energy and stability of the 405 IH compounds that we studied, including an investigation of the relation between gaps at the Fermi energy and stability. Section 4.4 and covers the calculated electronic structure of the IH compounds with particular emphasis on those that form semiconductors. In Sec. 4.5, IH half-metals and near-half-metals with negative formation energy are listed and discussed in terms of their electronic structure and structural stability. Sec. 4.6 is a summary of our results and conclusions.

4.2 Computational Details and Structure Determination

In this chapter, (a) X is one of 9 elements – Sc, Ti, V, Cr, Mn, Fe, Co, Ni or Cu, (b) Y is one of 9 elements – Ti, V, Cr, Mn, Fe, Co, Ni, Cu, or Zn, and (c) Z is one of 9 elements – Al, Ga, In, Si, Ge, Sn, P, As or Sb. In summary, we calculated the 405 inverse-Heusler compounds for which the valence (or atomic number since X and Y are both assumed to be $3d$) of Y is larger than that of X. For each of these 405 potential IH compounds, we calculated its electronic and magnetic structure, stability against structural distortion, and formation energy. We also compared its formation energy to those of all phases and combinations of phases in the Open Quantum Materials Database (OQMD) [87,88].

4.2.1 Density Functional Theory Calculations

All calculations were performed using density-functional theory (DFT) as implemented in the Vienna Ab-initio Simulation Package (VASP) [86] with a plane wave basis set and projector-augmented wave (PAW) potentials [66]. The set of PAW potentials for all elements and the plane wave energy cutoff of 520 eV for all calculations were both chosen for consistency with the OQMD [87,88]. The

Perdew-Burke-Ernzerhof (PBE) version of the generalized gradient approximation (GGA) to the exchange-correlation functional of DFT was adopted [89]. The integrations over the irreducible Brillouin zone (IBZ) used the automatic mesh generation scheme within VASP with the mesh parameter (the number of k-points per Å^{-1} along each reciprocal lattice vector) set to 50, which usually generated a $15 \times 15 \times 15$ Γ-centered Monkhorst-Pack grid [90], resulting in 288 k-points in the IBZ. The integrations employed the linear tetrahedron method with Blöchl corrections [91]. Finally, All the crystal structures are fully relaxed until the energy change in two successive ionic steps is less than 1×10^{-5} eV.

The total magnetic moment of each compound is calculated by integrating the spin-polarized charge density over the calculation cell. The division of the total magnetic moment among the atoms in the cell is somewhat ambiguous in VASP. The magnetic moment for a particular atom presented in this paper is evaluated within a sphere of 1.45 Å radius centered on the atomic site. It should be noted that the sum of the atomic moments defined this way is not exactly equal to the total cell moment.

4.2.2 Determination of the Relaxed Structure

We explain our procedure for obtaining the relaxed structures in some detail in order to make clear that there are many possible structures (in addition to the XA structure) that an X_2YZ compound can assume and that the determination of the ground state can be complicated by the additional degrees of freedom associated with the possible formation of magnetic moments of varying magnitude and relative orientation and by possible distortions of the cell.

We calculated the electronic structure of each compound in the XA phase by minimizing the energy with respect to the lattice constant. For each system and each lattice constant, we found it to be important to initiate the calculation with multiple initial configurations of the magnetic moments. We considered four kinds of initial moment configurations: (1) moments on the 3 transition metal atoms are parallel; (2) moment on the Y site is antiparallel to the moments on the X_1 and X_2; (3) moment on the X_1 site is antiparallel with the moments on the X_2 site and Y; (4) moment on the X_2 site is antiparallel with the moments on the X_1 and Y. After the lattice constant and magnetic configuration that determined the minimum energy for the XA structure was determined we compared this energy to the minimum energy determined in a similar way for the $L2_1$ structure.

Competition between XA and $L2_1$

Comparing the calculated energies of the XA and $L2_1$ phases of the 405 compounds that we considered, we found that 277 have lower energy in the $L2_1$ phase. The remaining 128 have lower energy in the XA phase. This result may be compared to the conclusion in references [41,42,217–222] that the XA structure is energetically preferred to the $L2_1$ structure when the atomic number of the Y element is the larger than the atomic number of X. Although this hypothesis is consistent with some experimental observations [42, 212, 213, 223, 224], it does not seem to be generally valid because more than two thirds of the systems in our data set (all of which satisfy $N_Y > N_X$) have lower calculated energy as $L2_1$.

Test for tetragonal distortions via ionic relaxation

After determination of the cubic lattice constant and magnetic configuration in our initial survey, all of the 405 compounds in our survey, both $L2_1$ and XA were tested for stability against tetragonal distortions using an 8 atom tetragonal cell and full ionic relaxation. For both XA and $L2_1$ we considered the structure to be cubic if $|c/a - 1| < 0.01$. All relaxations started from the XA structure or $L2_1$ structure adapted to an 8 atom tetragonal cell.

Of the 277 compounds that preferred the $L2_1$ structure, 136 remained in the $L2_1$ structure while 141 relaxed to a tetragonal '$L2_1$' structure. We notice that few systems with X=Sc, Ti, or V are calculated to be stable as XA. None of the 81 considered compounds with X=Sc were found to be XA. 10 relaxed into the tetragonal '$L2_1$' phase, 63 preferred the $L2_1$ phase and the remaining 8 became tetragonal 'XA' phase. Among the 72 compounds with X=Ti, only 4 compounds preferred XA phase, while 37 relaxed into the tetragonal '$L2_1$' phase, 29 preferred the $L2_1$ phase and 2 distorted to be tetragonal 'XA' phase. Among the 63 compounds with X=V, 43 compounds distorted into tetragonal '$L2_1$' phase, 2 preferred the $L2_1$ phase and 2 distorted to be tetragonal 'XA' phase.

When the 128 compounds that were more stable as XA than $L2_1$ were tested for susceptibility to tetragonal distortion, 95 were found to remain in the XA structure while 33 relaxed to a tetragonal 'XA' phase. In contrast to the half-Heuslers which are prone to trigonal distortions [225], we find that the full-Heuslers and IH compounds tend to retain tetragonal or cubic symmetry during this type of relaxation. The susceptibility of the half-Heuslers to trigonal distortions is likely related to the vacant site in the cell.

If we ignore the competition between XA and $L2_1$ phases, of the 405 potential XA compounds that we considered, 141 were unstable with respect to a tetragonal distortion and the remaining 264 compounds have lower energy in XA phase.

Competition between magnetic configurations

For some compounds, we found multiple solutions to the DFT equations at the same or similar lattice constants with different magnetic configurations. These can be categorized into 6 groups: in the $L2_1$ structure; (1) the moments of the X atoms (which are identical by assumption for $L2_1$) are parallel to those for Y ($L2_1$ ferromagnetic), or (2) the moments of X are anti-parallel to those for Y($L2_1$ ferrimagnetic); in the XA structure, (3) the moments for Y are parallel with those for X_1 but anti-parallel with those for X_2 (XA ferrimagnetic A1), or (4) the moments for Y are parallel with those for X_2 but anti-parallel with those for X_1 (XA ferrimagnetic A2), or (5) the moments for X_1 and X_2 are parallel with each other but anti-parallel with those for Y (XA ferrimagnetic), or (6) the moments for X_1, X_2 and Y are parallel (XA ferromagnetic). Magnetic transitions, in both magnitude and orientation as a function of lattice constant are clearly possible and often observed in our calculations. We did not consider the possibility of non-collinear moments [226], and because the calculations did not include spin-orbit coupling, we did not obtain information about the orientation of the moments relative to the crystal axes.

Example Mn_2ZnP

Mn_2ZnP provides an example of competition between different magnetic states for both the $L2_1$ and XA structures as shown in Fig. 4.2. In this case, the $L2_1$ phases have lower energy. In addition to a nonmagnetic phase with a lattice constant of 5.645Å, two energy minima were found for magnetic phases. These occur at $a = 5.69$ Å and $a = 5.88$ Å. For the solution at $a = 5.69$ Å the total moment per cell is 2.53 μ_B while the moments within a sphere of radius 1.45 Å surrounding each atom are 1.32 for Mn, -0.01 for Zn and -0.10 for P. For the solution at $a = 5.88$ Å the compound has a total magnetic moment of 5.37 μ_B per unit cell, and the moments within the 1.45 Å spheres in this case are 2.75, -0.03, and -0.13 μ_B for Mn, Zn and P, respectively. The solution at $a = 5.88$ Å has higher energy than the solution at 5.69 Å by $\Delta E = 0.230$ eV per formula unit.

There are also multiple XA magnetic phases. The two shown are both ferrimagnetic in the sense that the two Mn moments have opposite signs. The phase with larger lattice constant actually has smaller net moment because of the closer approximate cancellation of the Mn moments.

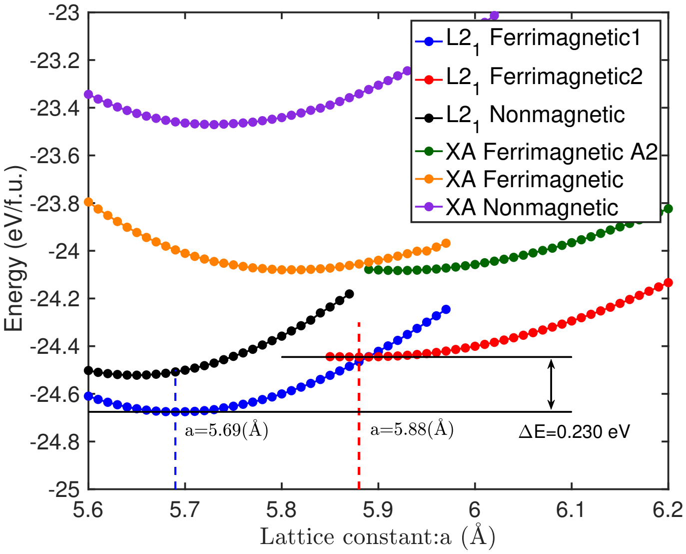

Figure 4.2: Calculated total energies of Mn_2ZnP with full-Heusler $L2_1$ structure and inverse-Heusler XA structure as a function of the lattice constant a in ferrimagnetic, ferromagnetic and nonmagnetic states.

To be clear, the energy comparisons of the preceding paragraph only consider the XA and $L2_1$ phases and their possible tetragonal distortions. Phase stability is discussed more generally in Section 4.2.3.

Competition between ordered and disordered phases

For a few systems, we considered the energy difference between ordered and disordered phases. As will be discussed in detail in Sec.4.3, some Mn_2CoZ and Mn_2RuZ XA compounds, (especially when Z is a larger atom, *e.g.* In, Sn, or Sb,) seem to have disorder in the occupation of the Mn_1 and Y sublattice sites. To approximate this disorder in the XA Mn_2CoZ (Z=In, Sn, and Sb) and Mn_2RuSn, special quasi-random structures (SQS) as described by Zunger *et al.* [227] were generated. The SQS are designed to best represent the targeted disordered alloy by a periodic system of a given size.

Our SQS comprised 32 atom cells for the case of completely random (50%/50%) occupation of the X_1 and Y sites, and 64 atom cells for the case in which the X_1 (Y) site occupation was 75%/25% (25%/75%). The SQS was generated using the Monte Carlo algorithm of Van de Walle *et al.* [228] as implemented in the Alloy Theoretic Automated Toolkit (ATAT) [229]. The cluster correlations used to define the SQS were specified using a distance-based cutoff of all 2-, 3-, and

4-body clusters with a maximum distance of 5-6 Å. We did not consider the case with smaller X/Y ratios because much larger unit cells would have been required. More detailed results will be discussed in Sec.4.3.

4.2.3 phase stability

Formation energy

We further investigated the structural stability of the 405 potential IH compounds by calculating their formation energies. The formation energy of an IH compound X_2YZ is defined as

$$\Delta E_f\left(X_2YZ\right) = E\left(X_2YZ\right) - \frac{1}{4}\left(2\mu_X + \mu_Y + \mu_Z\right) \tag{4.1}$$

where $E\left(X_2YZ\right)$ is the total energy per atom of the IH compound, and μ_i is the reference chemical potential of element i, chosen to be consistent with those used in the OQMD database. Typically the reference energy is the total energy per atom in the elemental phase (see Refs. [87,88] for details). A negative value of ΔE_f indicates that at zero temperature, the compound is more stable than its constituent elements. It is a *necessary but not sufficient* condition for ground state thermodynamic stability. It does not, for example, guarantee the stability of an inverse-Heusler (IH) phase over another competing phase or mixture of phases. For that, we must determine the convex hull.

Convex Hull Distance

Here the convex hull distance definition and calculation is the same with our discussion in 3.3.3. A compound can be thermodynamically stable only if it lies *on* the convex hull of formation energies of all phases in the respective chemical space. Every phase on the convex hull has a formation energy lower than any other phase or linear combination of phases in the chemical space at that composition. Thus, any phase on the convex hull is, by definition, thermodynamically stable at 0K. Conversely, any phase that does not lie on the convex hull is thermodynamically unstable; *i.e.* there is another phase or combination of phases on the convex hull that is lower in energy.

The distance from the convex hull ΔE_{HD} for a phase with formation energy ΔE_f can be calculated as

$$\Delta E_{\text{HD}} = \Delta E_f - E_{hull} \tag{4.2}$$

where E_{hull} is the energy of the convex hull at the composition of the phase. The energy of the convex hull at any composition is given by a linear combination of energies of stable phases. Thus the determination of E_{hull} from a database of formation energies is a linear composition-constrained energy minimization problem [92, 93], and is available as a look-up feature called "grand canonical linear programming"(GCLP) on the OQMD website (http://oqmd.org/analysis/gclp). Obviously, if the hull distance ΔE_{HD} for a phase on the convex hull is 0, there is no other phase or linear combination of phases lower in energy than the phase at that composition. The distance of the formation energy of a phase from the convex hull is an indicator of its thermodynamic stability and the likelihood of it being fabricated because the greater the distance from the convex hull, the higher is the thermodynamic driving force for transformation into another phase or decomposition into a combination of phases.

We note that the distance of a phase from the calculated convex hull depends on the completeness of the set of phases considered in the construction of the convex hull. Ideally, to calculate the convex hull of a system, X-Y-Z, one would calculate the energies of all possible compounds that can be formed from elements X, Y, and Z. Unfortunately, such a comprehensive study is not currently feasible.

A practical approach is to construct the convex hull using all the currently reported compounds in the X-Y-Z phase space. Here, we have limited our set of considered phases to those in the OQMD, which includes many ternary phases that have been reported in the ICSD [230, 231], and $\sim$ 500,000 hypothetical compounds based on common crystal structures. Thus the calculated formation energy of each X_2YZ IH compound is compared against the calculated formation energies of all phases and all linear combinations of phases with total composition X_2YZ in the OQMD.

A phase that we calculate to be above the convex hull may still be realized experimentally for three reasons: (a) There may be errors in the calculation of the energies of the IH compound or in the reference compounds. These errors may be intrinsic to PBE-DFT or due to insufficient precision in the calculation or inability to distinguish the ground state. We have applied considerable effort to reduce or eliminate the latter two possibilities so far as possible. (b) The compounds are usually synthesized at temperatures well above 0K. Because entropic effects will differ for different phases, the phase with lowest free energy at the synthesis temperature may be different from the phase with lowest energy at 0K and this high temperature phase may persist to low temperature due to slow kinetics at laboratory time scales. (c) Non-equilibrium processing techniques can sometimes be used to fabricate non-equilibrium metastable phases.

Conversely, an IH phase that we calculate to be on the calculated convex hull may nevertheless be difficult or impossible to fabricate because of reasons (a) or (b) or because the database used to generate the convex hull does not contain all phases so that the true convex hull lies below the calculated one.

Finally, we remark that our stability investigations are most directly pertinent to bulk phases. The growth of alloy films is a sophisticated art. Phases that are stable in bulk can be difficult to grow as films. Conversely, clever use of substrates, surface energies and kinetics can stabilize film structures different from the equilibrium bulk phase. Even for films, however, the hull distances provided here may provide useful guidance concerning the likelihood that a phase or structure may be stabilized.

4.3 Energetics: Formation Energy and Distance from the Convex Hull

4.3.1 Formation Energy and Convex Hull Distance

In this section, we systematically investigate the formation energy and thermodynamic stability of the 405 IH compounds considered in this paper. The formation energies at 0 K were evaluated by using Eq. (4.1) and the convex hull distances were calculated using Eq. (4.2). We first explored the relationship between formation energy and convex hull distance for the known synthesized IH compounds, including those collected in the Inorganic Crystal Structure Database (ICSD).

We compiled a list of the reported IH compounds by extracting IH compounds from the ICSD and literature including all elements as potential X, Y or Z atoms. From this list we removed the compounds with partially occupied sites. Some of the ICSD entries were from DFT calculations. These were included except for those with a higher DFT energy than the corresponding full Heusler which were obviously included in the ICSD by mistake. Finally, we tabulated the formation energy and convex hull distance as calculated in the OQMD.

A total of 48 distinct IH compounds are reported in ICSD. Of these, 36 have been synthesized experimentally. References to six additional synthesized IH compounds, not included in ICSD, (Fe_2CoGa, Fe_2CoSi, Fe_2CoGe, Fe_2NiGa, Mn_2NiGa, and Fe_2RuSi) were found in recent literature [232, 233]. These can be used for cross validation of our method. Although Mn_2NiSn was synthesized by Luo *et al.* [234], a more recent study shows that it has atomic disorder on the transition metal sites [233] and our DFT calculation show it is 103 meV/atom above the convex hull.

These data from ICSD and the recent literature are displayed in Fig. 4.3, from which it can be seen that most of the synthesized IH compounds are within 52 meV/atom of the convex hull. The green diamonds represent the IH compounds that have not been synthesized but have been sourced into the ICSD by DFT predictions.

Overall, we find most of the experimentally reported IH compounds (38 of 42) have a convex hull distance less than 52 meV/atom. Thus, the convex hull distance of the DFT-calculated formation energy at 0K appears to be a good indicator of the likelihood of synthesis of an IH compound and 52 meV/atom is a reasonable empirical threshold separating the compounds likely to be synthesized by equilibrium processing from those unlikely to be so synthesized.

The empirical 52 meV threshold assumed here may be contrasted with the 100 meV threshold that seemed appropriate for the half-Heusler compounds [225]. We speculate that the more open structure of the half-Heusler phase is associated with a high density of states for low frequency phonons which reduces the free energy of the half-Heusler phase relative to competing phases at temperatures used for synthesis.

Before proceeding it is important to note that several Mn_2YZ compounds (Mn_2CoSn, Mn_2CoSb, Mn_2CoIn, and Mn_2RuSn) appear to significantly violate our empirical hull distance threshold. They also have vanishing or positive formation energy! A discussion of our rationale for *not* extending our hull distance threshold to include these systems follows:

(a) Mn_2CoSn: Our calculations predict that XA phase Mn_2CoSn lies well above the convex hull. A mixture of phases, CoSn-Mn is predicted to be lower in energy by $\Delta E_{\mathrm{HD}} = 0.107$ eV/atom. However, there are reasons to believe that the experimentally reported phase may not be pure XA.

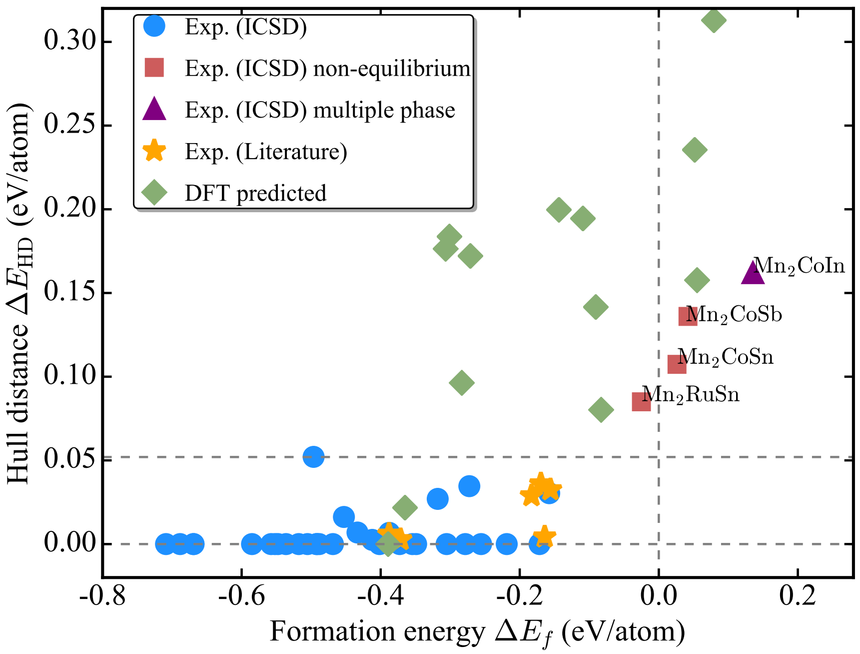

Figure 4.3: DFT-calculated formation energy vs. convex hull distance of inverse Heuslers reported in ICSD and in recent experimental studies. A hull distance ΔE_{HD}=0 (on the convex hull) indicates the compound is thermodynamically stable at 0K. Blue circles and red squares represent experimentally synthesized IH through equilibrium and non-equilibrium process, respectively. Purple triangle is synthesized IH coexisting with other phase. Yellow stars represent synthesized compounds reported in literature but not in ICSD. Green diamonds represent IH compounds predicted using DFT.

The ICSD entry for Mn_2CoSn is based on the work of Liu *et al.* who described synthesis via melt-spinning as well as calculations that employed the FLAPW technique [42]. They found that the non-equilibrium melt-spinning technique generated a material with a “clean” XRD pattern consistent with the XA phase. The measured magnetic moment of 2.98 μ_B per formula unit was consistent with their calculated value of 2.99 and with their calculated DOS, which indicates that this material may be a Slater-Pauling near-half-metal.

Subsequently, Winterlik *et al.* synthesized this compound by the quenching from 1073K of annealed arc-melted samples [213]. They obtained similar XRD results to Liu *et al.*, but with a small admixture of a tetragonal $MnSn_2$ phase. They also concluded that the experimental moment was near the Slater-Pauling half-metal value of 3 μ_B per formula unit. However, their calculations for XA-phase Mn_2CoSn which also employed FLAPW found, in addition to the near-half-metallic phase found by Liu *et al.*, a different magnetic structure with lower energy.

Our calculations using VASP confirm the Winterlik *et al.* results. The PBE-DFT-predicted phase for XA Mn_2CoSn has a magnetic moment around 1.53 μ_B rather far from the value of 3 μ_B necessary to place the Fermi energy into the Slater-Pauling gap after 12 states per atom in the minority channel. There is an interesting competition between two very similar ferrimagnetic states that plays out in many of the 26 and 27 electron Mn_2CoZ systems. The Mn_2 and Co moments are aligned and are partially compensated by the Mn_1 moment. For smaller lattice constants, the compensation yields the correct moment for a half-metal or near-half-metal (i.e., for Mn_2Co(Al,Ga,Si,Ge)), but as the lattice constant increases, (*i.e.,* for Mn_2Co(In,Sn)), the Mn_1 moment becomes too large in magnitude and the partial compensation fails to yield a half-metal.

Winterlik *et al.* conclude from XRD, NMR and Mössbauer studies that their quenched samples of Mn_2CoSn are actually disordered on the MnCo layers. They modeled this disorder using the KKR-CPA approach and obtained values of the moments in reasonable agreement with magnetometry and XMCD. They argued that their model with Mn and Co randomly occupying the sites on alternate (001) layers separated by ordered Mn-Sn layers agreed with XRD as well as the XA model because Mn and Co scatter X-rays similarly. This disordered $L2_1B$ structure has both Mn and Co at the $\left(\frac{1}{4}, \frac{1}{4}, \frac{1}{4}\right)$ and the $\left(\frac{3}{4}, \frac{3}{4}, \frac{3}{4}\right)$ site, whereas the XA structure has only Co at $\left(\frac{1}{4}, \frac{1}{4}, \frac{1}{4}\right)$ and only Mn at $\left(\frac{3}{4}, \frac{3}{4}, \frac{3}{4}\right)$ site.

We investigated the Winterlik *et al.* hypothesis by comparing the energy of a few cubic 16 atom supercells with differing equiatomic occupations of the MnCo layers to the energy of the XA occupation. The energies of these different site occupations were all lower than the XA energy, and most of them were half-metallic or near-half-metallic. The decrease in energy for the non-XA site occupations ranged from 8 meV/atom to 33 meV/atom. These should be considered lower bound estimates of the decrease since we did not optimize the geometries of the model "disordered" structures. We also performed calculations for an SQS designed to mimic a system with disorder on the MnCo layers. Our calculation indicates that the SQS with 25% Mn/Co mixing is 31 meV/atom lower in energy than the XA phase. The net magnetic moment of this SQS is about 1.28 μ_B per f.u., which is lower than that of XA phase (1.53 μ_B) due to the atom disordering.

We propose the following hypothesis and rationale for omitting Mn_2CoSn from the estimate for the hull energy distance threshold: During synthesis at high temperature, Mn_2CoSn is thermodynamically stable in a phase with substantial configurational disorder on the MnCo planes. The configurational disorder on these sites may also decrease the free energy of the compound. A simple mean-field estimate of the configurational entropy (S) of disorder gives a $-TS$ contribution of -32 meV/atom at 1073K. If we add this entropic contribution to the approximately 30 meV/atom difference in total energy between the ordered and disordered systems, we can estimate a decrease in the relative free energy of formation by approximately 60 meV/atom due to disorder. This would yield a negative free energy and a hull distance less than our empirical 52 meV threshold.

(b) Mn_2CoSb: Mn_2CoSb is predicted to lie above the convex hull with a mixture of phases CoMnSb-Mn lower in energy by $\Delta E_{\mathrm{HD}} = 0.133$ eV/atom. This phase also entered the ICSD database from the paper of Liu *et al.* who generated their sample by melt-spinning and also provided FLAPW calculations that predicted XA Mn_2CoSb to be a half-metal with a Slater-Pauling moment of 4 μ_B per formula unit, consistent with their measured value.

Unlike some Mn_2CoZ compounds with smaller Z atoms, synthesis of single XA phase Mn_2CoSb is difficult via arc-melting and a high temperature annealing step. Prior X-ray diffraction investigations [42] revealed a multi-phase Mn_2CoSb in arc-melt samples. Our synthesis supports this finding [235]. On the other hand, a melt-spinning treatment of arc-melt Mn_2CoSb ingots is reported to produce a pure cubic structure [42, 236].

We consider it likely that Mn_2CoSb is similar to Mn_2CoSn. A study by Xin *et al.* found that "disordered" Mn_2CoSb (apparently modeled by replacing the (001) MnCo layers by layers of pure Mn and pure Co alternating with the MnSb layers) was lower in energy than XA by 21 meV/atom [214]. Our SQS calculations show that the 50% Mn/Co mixture within one rock-salt lattice is 60 meV/atom lower in energy than the XA phases. Again, our assertion is that the free energy reduction due to configurational entropy together with the lower energy of the disordered configurations may be sufficient to stabilize the $L2_1B$ phase as it is rapidly quenched from the melt.

(c) Mn_2CoIn: According to Liu *et al.* [42], Mn_2CoIn appears to be multi-phase in samples prepared by arc-melting. Apart from the cubic phase identified as inverse-Heusler, a second phase described as fcc is also apparent. Liu *et al.* also report FLAPW calculations performed at a much smaller lattice constant (5.8 Å) than the experimentally derived lattice constant (6.14 Å). These calculations yielded a moment of 1.95 μ_B in reasonable agreement with experimental value of 1.90 μ_B. A subsequent calculation by Meinert *et al.* found a lattice constant of 6.04 Å and a moment of

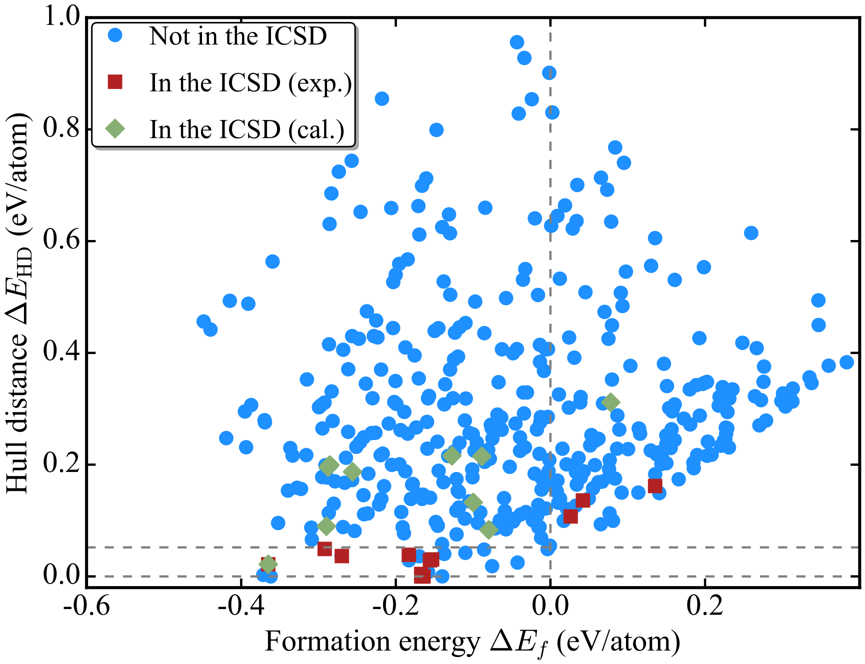

Figure 4.4: DFT-calculated formation energy vs convex hull distance of all IH considered in this paper. A hull distance ΔE_{HD}=0 (on the convex hull) indicates the compound is thermodynamically stable at 0K. Red diamonds and green squares represent IH compounds sourced into ICSD by synthesis and DFT computation, respectively. Blue circles represent the IH compounds calculated in this work.

1.95 μ_B [219].

Our calculations for the XA phase yielded a lattice constant of 6.10 Å, much closer to the experimental value and a moment of 1.74 μ_B. We also found a surprising and unusual sensitivity of our results to the number of plane waves. We performed SQS calculations which indicated that the disordered phase is essentially degenerate in energy with the XA phase. The magnetic moment of SQS is about 1.01 μ_B per f.u..

Given the significant amount of second phase in the experimental sample which would affect the composition of the phase identified as XA, together with the possibility of disorder on the MnCo layers we tentatively conclude that it is reasonable to discount the large calculated formation energy and hull distance in setting our threshold for likely fabricability of XA phases . Additional studies of this putative phase are probably advisable.

(d) Mn_2RuSn: Mn_2RuSn is predicted to lie above the convex hull with a mixture of phases MnSnRu+Mn+Sn_7Ru_3 by ΔE_{HD} = 0.085 eV/atom. The first reports of fabrication by Endo *et* *al.* [237], were unable to distinguish between the XA and $L2_1B$ phases. A later study by Kreiner *et al.* seemed to confidently conclude from powder XRD studies that their sample prepared by alloying through inductive heating had the $L2_1B$ structure [233]. Our calculation of the energy of a SQS for Mn_2RuSn with 25% Mn/Ru mixing gave an energy of the model disordered alloy 18 meV lower than XA. The calculated magnetic moment of the SQS is about 0.24 μ_B per f.u.. A study by Yang *et al.* using the KKR -CPA approach estimated 11% anti-site Mn based on a comparison of the calculated moment to the experimental one [238].

We tentatively conclude that the four experimental systems in the ICSD with anomalously large calculated hull distances and formation energies are probably not XA phase and exclude them from consideration in determining the threshold for estimating which XA phases are likely to be fabricated by equilibrium approaches. We also remind that an additional potential inverse-Heusler, Mn_2NiSn, was excluded from our database of experimental XA phases, because of experimental evidence of similar disorder to that observed in the Mn_2CoZ phases.

We recommend additional studies of the competition between XA and $L2_1B$ phases, especially for compounds which have large Z atoms. Such studies may require careful experimental analysis because of the similarities of the the XRD patterns of the two phases. Theoretical studies may also be difficult because of the need to accurately calculate the formation energy of the disordered $L2_1B$ phase.

We extended the comparison of formation energy and convex hull distance to all the 405 IH compounds considered in this work as shown in Figure 4.4. It can be seen from Fig. 4.4 that the calculated formation energies span a range from -0.45 to 0.38 eV/atom. This may be compared with a range of -1.1 to 0.7 eV/atom that was observed for half-Heuslers [225]. 248 of the IH have negative formation energy, indicating thermal stability against decomposition into the constituent elements at 0 K. The calculated hull distances vary from 0 to nearly 1 eV/atom. It is clear from the lack of correlation between formation energy and hull distance in Figure 4.4 that the formation energy is not a reliable indicator of stability.

The IH compounds considered in this work that are included in ICSD are indicated by red squares in Figure 4.4. These all lie within 0.052 eV/atom of the convex hull except for three compounds mentioned previously (Mn_2CoSn, Mn_2CoIn and Mn_2CoSb) that were synthesized by non-equilibrium processing and are likely $L2_1B$ rather than XA phase. Our calculations predict 13 (out of 405) IH compounds to be within 52 meV/atom of the convex hull. The “success rate”, i.e. the number of predicted potentially stable compounds versus total number of systems investigated is lower for IH (13/405) than for half-Heusler (50/378) [225], but this result is affected by the different hull distance thresholds and the different choices of potential compounds.

4.3.2 Stability and Composition

We systematically investigated the formation energies of the 405 IH compounds in the XA phase. We found that many of these potential IH phases actually have lower energy in other phases, *e.g.* $L2_1$(136), tetragonal ‘$L2_1$’ phase (141), or tetragonal ‘XA(33). Here, however, since we are interested in gaining insight into the systematics of the stability of the XA phase, we compare formation energies as if all 405 compounds remained in the XA phase. To better illustrate the relation between structural stability and composition, we arranged the formation energy data according to X, Y and Z element respectively in Fig. 4.5-4.7.

Figure 4.5 shows the calculated formation energies and hull distances of the 405 calculated X_2YZ compounds arranged by X species, then by Y and finally by Z. From Fig. 4.5, we can see that Sc, Ti, and V generate more negative formation energy XA compounds as X elements. In terms of the fraction with negative formation energy, we found 75/81 with X=Sc, 60/72 with X=Ti, 25/45 with X=Mn and 20/36 with X=Fe, and 15/18 with X=Ni.

Figure 4.6 presents the calculated formation energies and hull distances arranged first by Y, then by X and finally by Z. From Fig. 4.6, it can be seen that when Y is Fe, Co or Ni many XA compounds with negative formation energies result. However, when one considers the fraction of negative formation energy compounds with a given Y in our database, the highest are 9/9 for Y=Ti, 17/18 for Y=V and 24/27 for Y=Cr.

When the compounds are ordered by Z element as presented in Fig. 4.7, we can see that the smaller atoms within a given group (*i.e.* Z=Al, Si, In) tend to have a larger fraction of negative energy XA phases. The large number of $\Delta E_f < 0$ compounds with Z=Al is striking in Fig.4.7, but only 14 compounds have negative formation energy for Z=Sb. Although the number of negative formation energy compounds with Z=Al is greatest, the number among them with formation energies less than -0.2 eV (13) is less than for compounds with Z=Si (25) and Z=P (24).

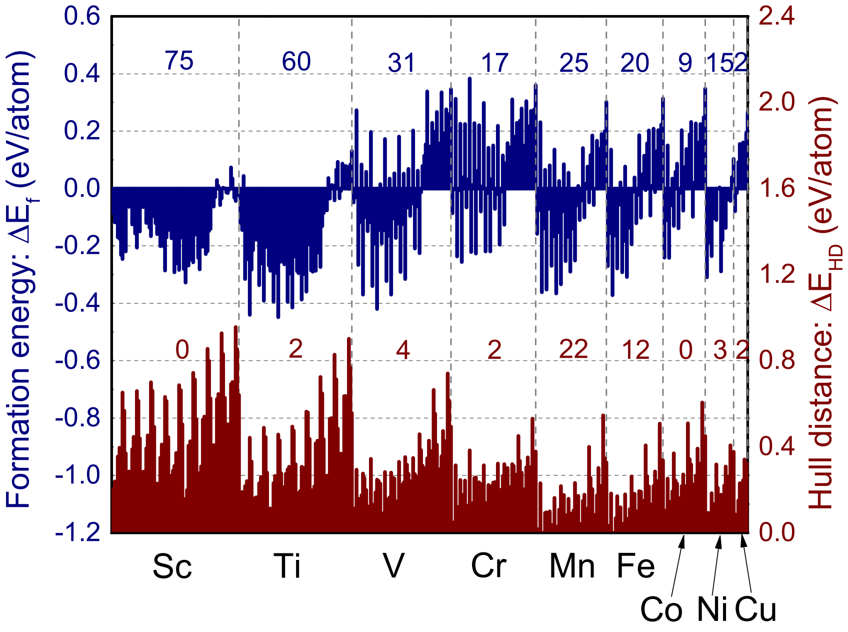

Figure 4.5: DFT formation energies and hull distances for potential inverse-Heusler compounds grouped by the element on the X-site. The numbers near the top (in blue) and center (in brown) of each column denote the number of compounds with negative formation energy ΔE_f and hull distance $\Delta E_{\mathrm{HD}} \leq 0.1$ eV/atom, respectively, in the corresponding Z-element group. Within a given X-element column, the compounds are ordered first by the element on the Y-site (same order as in Fig. 4.6) and then by the element on the Z-site (same order as in Fig. 4.7), i.e., Z varies more rapidly than Y.

It is interesting to contrast the trends in formation energy to those observed by considering the OQMD hull distance. Although Sc, and Ti tend to generate negative formation energies as X atoms in XA phase X_2YZ compounds, the picture is opposite for the hull distances. Very few of these compounds have a hull distance near the empirical 0.052 eV/atom range which is indicative of a potentially synthesizable phase. Using a larger hull distance of 0.1 eV as an (arbitrary) stability threshold we find no X=Sc phases that meet the criterion and only 2 of 72 X=Ti phases. Sc and Ti are “active” elements that form numerous low energy phases. Hull distances tend to be lower when the X atom is Mn or Fe with 22 of 45 X=Mn and 12 of 36 X=Fe meeting the criterion of hull distance less than 0.1eV/atom.

While 9/9 Y=Ti and 17/18 Y=V IH compounds have negative formation energy, none of them meet the relaxed hull distance threshold of 0.1eV/atom. However, relatively large fractions of Y=Fe (10/45), Y=Co (11/45) and Y=Ni (8/63) meet the criterion. Thus, there is better correlation between low formation energy and low hull distance when the XA compounds are grouped by Y

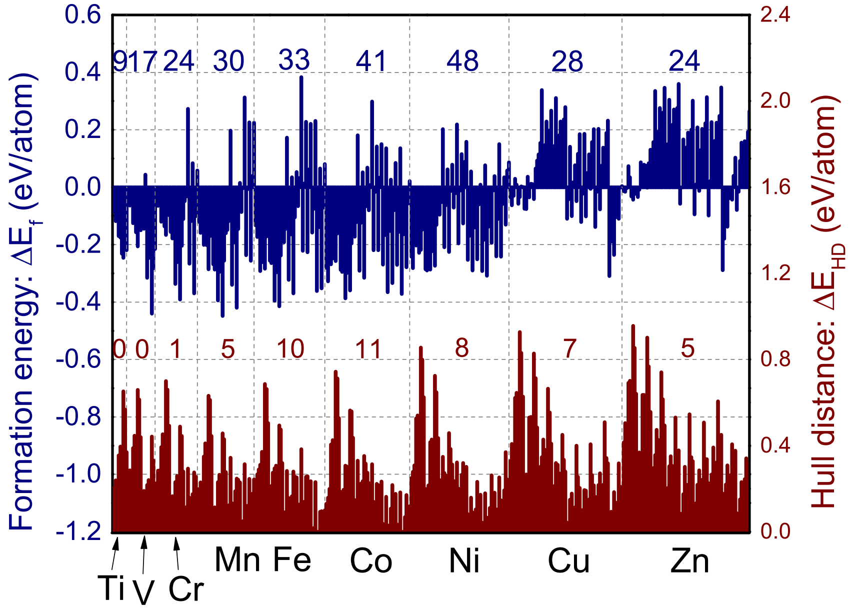

Figure 4.6: DFT formation energies and hull distances for potential inverse-Heusler compounds grouped by the element on the Y-site. The numbers near the top (in blue) and center (in brown) of each column denote the number of compounds with negative formation energy ΔE_f and hull distance $\Delta E_{\text{HD}} \leq 0.1$ eV/atom, respectively, in the corresponding Y-element group. Within a given Y-element column, the compounds are ordered first by the element on the X-site (same order as in Fig. 4.5) and then by the element on the Z-site (same order as in Fig. 4.7), i.e., Z varies more rapidly than X.

element. By both measures, Y=Ni, Co or Fe tend to generate more stable compounds.

The trends in stability with Z atom are also somewhat similar when viewed from the perspectives of hull distance and formation energy. Al, Ga, Si and Ge as Z atom are associated with compounds having relatively low hull distances and negative formation energies. One big difference, however, is Z=P which tends to generate numerous XA compounds with low formation energy, but none with very low hull distances.

4.3.3 Stability and Gaps near the Fermi Energy

We calculated the electronic structure of each compound and obtained its spin polarization at the Fermi level, E_F. The spin polarization P at E_F is defined as:

$$P(E_F) = \frac{N_\uparrow(E_F) - N_\downarrow(E_F)}{N_\uparrow(E_F) + N_\downarrow(E_F)} \tag{4.3}$$

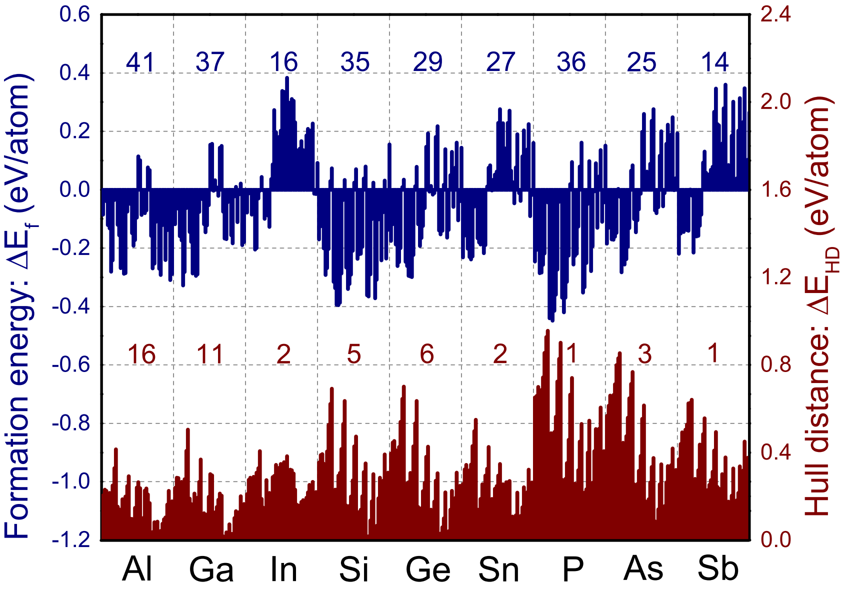

Figure 4.7: DFT formation energies and hull distances for potential inverse-Heusler compounds grouped by the element on the Z-site. The numbers near the top (in blue) and center (in brown) of each column denote the number of compounds with negative formation energy ΔE_f and hull distance $\Delta E_{\mathrm{HD}} \leq 0.1$ eV/atom, respectively, in the corresponding Z-element group. Within a given Z-element column, the compounds are ordered first by the element on the X-site (same order as in Fig. 4.5) and then by the element on the Y-site (same order as in Fig. 4.6), i.e., Y varies more rapidly than X.

where $N_\uparrow$ and $N_\downarrow$ are the densities of states for majority (spin-up) and minority (spin-down) electrons, respectively. We define the compounds with 100% spin polarization ($P(E_F) = 1$) to be half-metals in this paper.

In a study of the half-Heusler compounds gaps at the Fermi energy in one or both spin channels appeared to be associated with low formation energies and low hull distances [225]. Figure 4.8 shows how the number of IH compounds with positive and negative formation energy varies with spin-polarization. It can be seen that for semiconductors and half-metals the ratio of the number of negative formation energy compounds to positive formation energy compounds is particularly high.

Figure 4.9 shows the number of IH compounds with positive and negative hull distances less than and greater than 0.1 eV/atom versus spin polarization. In contrast to the case of the half-Heuslers, the plot of hull distance versus spin-polarization does not present an obvious case for a correlation between gaps near the Fermi energy and stability. As will be discussed in Section 4.4 and 4.5, this is due to the large number of X=Sc and X=Ti compounds in our database that are semi-conductors

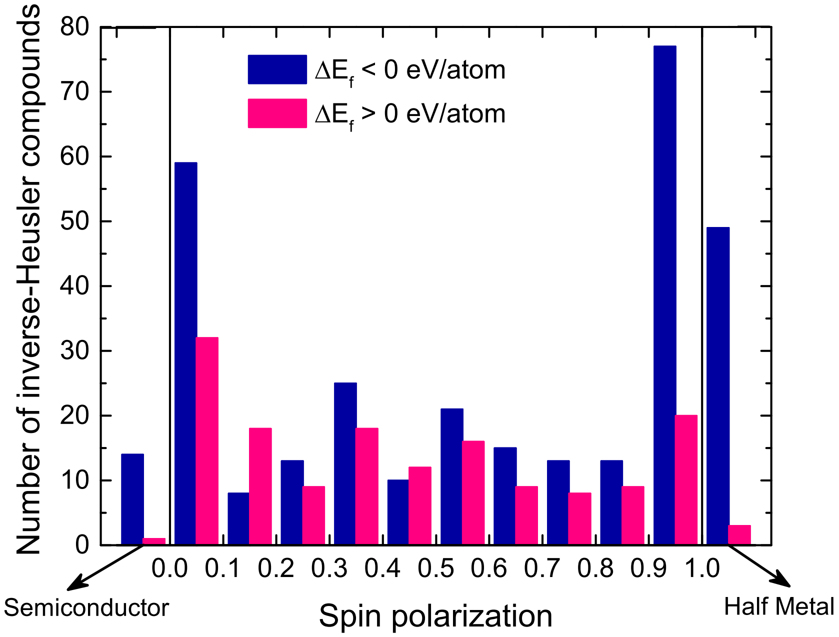

Figure 4.8: The distribution of the 405 potential inverse-Heusler compounds with negative ($\Delta E_f < 0$ eV/atom) and positive ($\Delta E_f > 0$ eV/atom) formation energies as a function of spin polarization $P(E_F)$ (given by Eq. 4.3). In the central region, we show the number of inverse-Heusler compounds grouped by 10 percentage points of spin polarization. In an additional region to the left, we show the 15 semiconductors, including 14 compounds with a negative formation energy and 1 with a positive formation energy. In the additional region on the right, we show 52 half-metals, including 51 with negative formation energy and 1 with positive formation energy.

or half-metals and although they tend to have negative formation energies, they tend to be less stable than competing compounds. On the other hand, as will be discussed in Sec. 4.3.1, only 20 of the IH compounds in our database systems met our 0.052 eV/atom hull distance stability criterion. Half of these are half-metals or near-half-metals. We consider this to be strong support for the notion that gaps in or near the Fermi energy in one or both spin channels contribute to stability.

4.4 Inverse Heusler Semiconductors

The 14 XA semiconductors with negative formation energy that we found are listed in Table 4.1 where the DFT-calculated properties (*i.e.* lattice constant, band gap, gap type, local moments, formation energy, hull distance) are presented. Remarkably, all of these 14 systems are 18 electron *non-Slater-Pauling* semiconductors with gaps after nine electrons per formula unit (2.25 per atom)

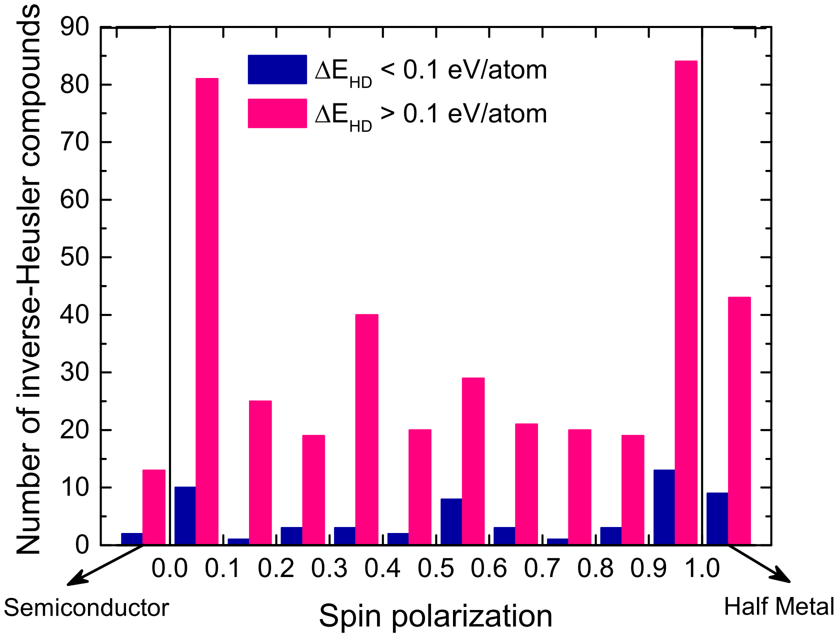

Figure 4.9: The distribution of the 405 potential inverse-Heusler compounds that lie near ($\Delta E_{\mathrm{HD}} <$ 0.1 eV/atom) or far ($\Delta E_{\mathrm{HD}} >$ 0.1 eV/atom) from the convex hull, as a function of spin polarization $P(E_F)$ (given by Eq. 4.3). In the central region, the number of inverse-Heusler compounds grouped by 10 percentage points of spin polarization is shown. In the additional region on the left are shown 15 semiconductors (of which 2 compounds have $E_{\mathrm{HD}} <$ 0.1 eV/atom). On the right are shown the 52 half-metals (of which 9 compounds have $E_{\mathrm{HD}} <$ 0.1 eV/atom).

per spin channel. Recall that *Slater-Pauling* gaps (at least according to the nomenclature we prefer) occur after 3 electrons per atom per spin.

From Table 4.1, it can be seen that all of these semiconductors have either Sc or Ti as X atoms. This is not surprising (given that they all have 18 electrons per formula unit) because the choice of systems that comprise our database (see section 4.2.1) implies that if the number of valence electrons on an X atom exceeds 4, the total number of electrons per formula unit will exceed 18.

Of the 9 XA compounds with X=Sc in our database, 7 are calculated to be non-magnetic semiconductors. The two that are not semiconductors are Sc_2MnAs and Sc_2MnSb. The former is non-magnetic with a very low DOS pseudogap at the Fermi energy.

The absence of a gap in Sc_2MnAs can be traced to a reordering of the states at Γ. Between Sc_2MnP and Sc_2MnAs, a singly degenerate A_1 state (band 7) switches places with a triply degenerate T_2 state (bands 8,9 and 10), as shown in Fig. 4.11. This A_1 state (composed of s-contributions from all 4 atoms) decreases in energy relative to the d-states as the lattice expands from Sc_2MnP to

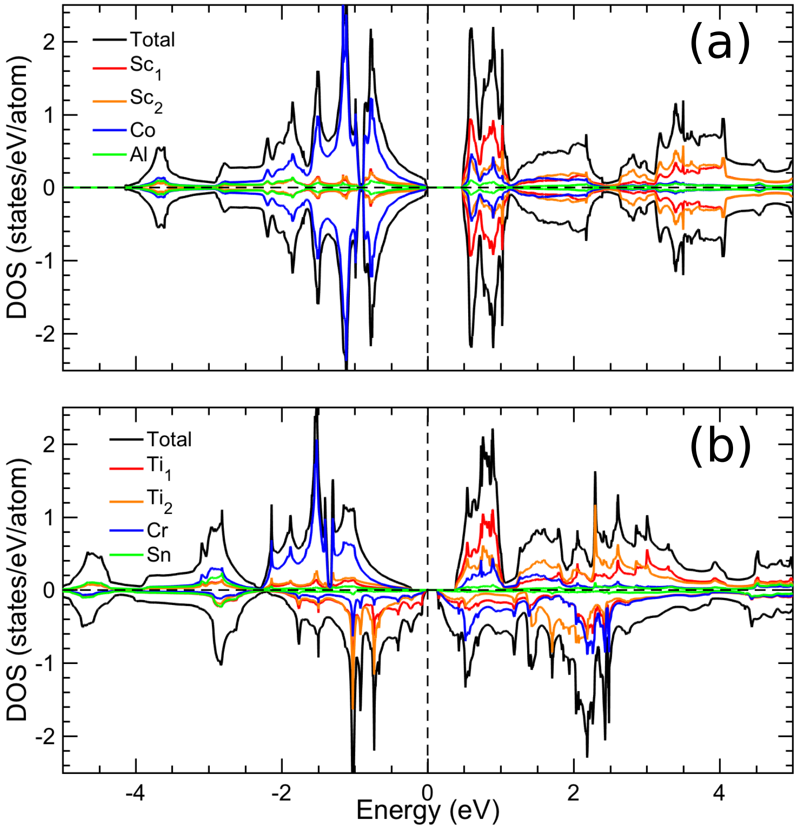

Figure 4.10: Density of states curves for the 18-electron semiconductor (a) Sc_2CoAl and (b) Ti_2CrSn. The curve presents the total DOS (black) and the projected-DOS contributed by Sc_1 (Ti_1) (red), Sc_2 (Ti_2) (orange), Co (Cr) (blue) and Al (Sn) (green). Zero energy corresponds to the Fermi level.

Sc_2MnAs to Sc_2MnSb. However, Sc_2MnSb becomes magnetic as the lattice is expanded before this reordering occurs so it is predicted to be a magnetic near-half-metal with a tiny moment (see Table 4.3).

The reason Sc_2MnSb is magnetic while Sc_2MnP and Sc_2MnAs are not is almost certainly due to the larger lattice constant induced by the larger atom (Sb). For lattice constants less than approximately 6.50 Å, Sc_2MnSb is predicted to be a non-magnetic semiconductor similar to Sc_2MnP.

The DOS of the non-magnetic Sc-based semiconductors in Table 4.1 can be understood by referring to Figure 4.10a which shows the site decomposed DOS for Sc_2CoAl. Because Sc is an early transition metal compared to Co, its *d*-states must lie higher. Thus, the ordering of the states is Al-*s* (in this case forming a narrow band well below the Fermi level and not shown in the figure.) followed by Al-*p*, followed by Co-*d* and finally Sc_1-*d* and Sc_2-*d*. The gap after 9 electrons per spin channel occurs from the hybridization of the Co-*d* and Sc-*d* states, or, more generally, between the

Table 4.1: For each of the 14 18-electron X_2YZ inverse-Heusler compounds that are non-Slater-Pauling semiconductors with negative formation energy, we list the calculated lattice constant a, band gap in two spin channels $E_g^{\uparrow}$, $E_g^{\downarrow}$ within DFT, local moments for atoms on the X, Y and Z sites:$m(X_1)$, $m(X_2)$, $m(Y)$ and $m(Z)$, the formation energy of the compound in the XA and $L2_1$ structures, distance from the convex hull for the XA phase $\Delta E_{\mathrm{HD}}^{XA}$, previous experimental reports.

X_2YZ	a	$E_g^{\uparrow}$	$E_g^{\downarrow}$	$m(X_1)$	$m(X_2)$	$m(Y)$	$m(Z)$	ΔE_f^{XA}	$\Delta E_f^{L2_1}$	$\Delta E_{\mathrm{HD}}^{XA}$
	(Å)	(eV)	(eV)	(μ_B)				(eV/atom)		
Sc_2MnP	6.18	0.052	0.052	0	0	0	0	-0.286	-0.471	0.631
Sc_2FeSi	6.255	0.347	0.347	0	0	0	0	-0.292	-0.416	0.311
Sc_2FeGe	6.33	0.356	0.356	0	0	0	0	-0.262	-0.435	0.371
Sc_2FeSn	6.60	0.337	0.337	0	0	0	0	-0.230	-0.358	0.319
Sc_2CoAl	6.42	0.475	0.475	0	0	0	0	-0.280	-0.350	0.130
Sc_2CoGa	6.36	0.532	0.532	0	0	0	0	-0.328	-0.454	0.159
Sc_2CoIn	6.61	0.470	0.470	0	0	0	0	-0.205	-0.281	0.200
Ti_2VSb	6.47	0.427	0.119	-1.236	-0.521	1.881	-0.009	-0.215	-0.208	0.162
Ti_2CrSi	6.11	0.475	0.086	-1.157	-0.787	2.129	-0.036	-0.337	-0.385	0.230
Ti_2CrGe	6.20	0.522	0.104	-1.254	-0.883	2.348	-0.022	-0.262	-0.305	0.259
Ti_2CrSn	6.47	0.579	0.133	-1.396	-1.018	2.727	-0.016	-0.181	-0.154	0.139
Ti_2MnAl	6.23	0.561	0.043	-1.202	-1.067	2.606	-0.043	-0.268	-0.302	0.088
Ti_2MnGa	6.20	0.603	0.034	-1.201	-1.115	2.611	-0.020	-0.287	-0.341	0.114
Ti_2MnIn	6.47	0.394	0.042	-1.336	-1.266	3.043	-0.020	-0.100	-0.05	0.092

Y-d and X-d states.

Thus, bonding in these systems appears to have a considerable ionic component with transfer of electrons to the Al and Co atoms from the Sc atoms.It can be seen from Table 4.1 that all of the X=Sc 18-electron semiconductors are predicted to be substantially more stable in the $L2_1$ phase than in the XA phase. In addition, the XA hull distances all exceed our 0.052 eV threshold for potentially being stable in equilibrium.

Of the nine 18 electron compounds in our database with X=Ti, seven are predicted to be semiconductors and are included in Table 4.1. One, Ti_2VP is predicted to be a near-half-metal (see Table 4.3) with a tiny moment. The final compound, Ti_2VAs, is predicted to be a magnetic semiconductor similar to Ti_2VSb, but its formation energy is greater than zero and so is omitted from Table 4.1.

In contrast to the non-magnetic 18 electron semiconductors with X=Sc, the systems with X=Ti develop magnetic moments and have gaps of different size in the majority and minority spin-channels. The net moment per formula unit is predicted to be zero for the semiconductors, with the Ti moments having the same sign and being balanced by a larger moment of opposite sign

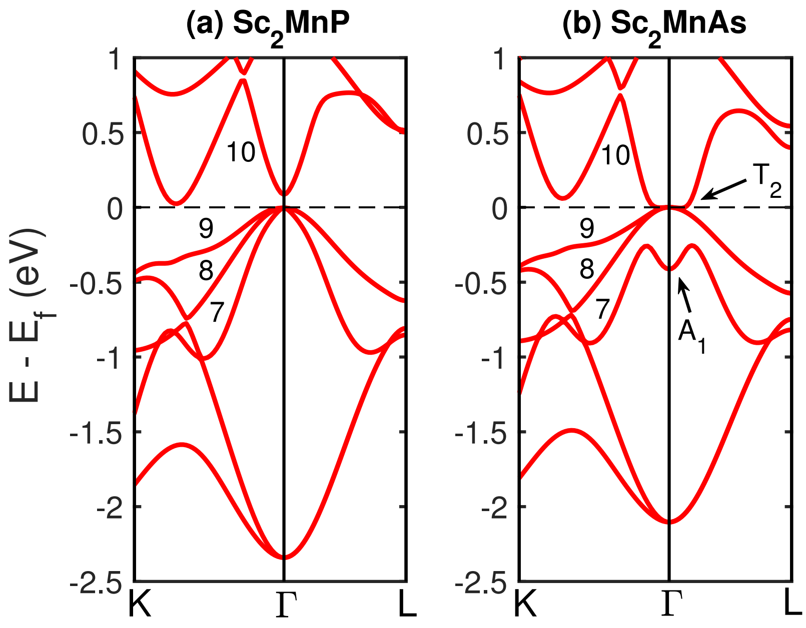

Figure 4.11: The band structures of (a) Sc_2MnP and (b) Sc_2MnAs are shown. The singly degenerate A_1 state and triply degenerate T_2 state are labeled in (b). Bands 7, 8, 9 and 10 are labeled in (a) and (b). The zero of the energy axis corresponds to the Fermi level.

on the Y site. If the sign of the moment on the Y atom is taken to be positive, then the larger gaps are in the majority channel while the smaller gaps are in the minority channel, becoming slightly negative for Ti_2VP.

The larger gap (in the majority channel in Table 4.1) for the Ti_2YZ magnetic semiconductors is very similar to the gaps in both channels for the Sc_2YZ non-magnetic semiconductors. The positive moment on the Y atom shifts its majority d-level down while negative moments on the Ti atoms shift their majority d-levels up, the larger moment on the Ti_1 giving it a slightly larger upward shift. As a consequence, the state ordering in the majority channel is Z-s, Z-p, Y-d, Ti_2-d, Ti_1-d so that the majority gap after 9 states per formula unit arises from hybridization between Y-d and X_2-d and X_1-d similar to the case for both channels in the Sc_2YZ 18 electron semiconductors.

The persistence of the very small gaps after 9 states per formula unit in the minority channel is surprising and seems to be aided by avoided band crossings along Γ to K and along L to W. We find these small gaps to be common when the d-levels of the three transition metals are similar. The avoided crossings and hence the gaps are likely symmetry related since the non-magnetic compound V_2VGa has several allowed band crossings that are avoided when the symmetry between X_1, X_2

and Y atoms is broken. These avoided band crossings lead to the small gap after 9 states and are quite common when X_1, X_2 and Y are similar, but not identical in one of the spin channels. For example, simple electron counting ignoring charge transfer and using the calculated moments yields for Ti_2MnGa, that the number of electrons for the minority channel on each atom are approximately 2.6 for X_1 and X_2 and 2.2 for Y. The corresponding minority gap is tiny, 0.034 eV.

The atom-projected DOS of Ti_2CrSn is presented in Fig. 4.10. The energy ordering of the atomic orbitals is Sn-s (in this case forming a narrow band more than 10 eV below the Fermi level and not shown in the figure.) followed by Sn-p, followed in the majority channel by Cr-d and then the closely spaced Ti_2-d and Ti_1-d. In the minority channel the ordering of the d-states is different, Ti_1-d, Ti_2-d, followed by Cr-d. In the majority channel, the hybridization between the lower-lying Cr-d and the higher Ti-d states produces a relatively large gap (0.579 eV), while in the minority channel, the relatively closely spaced Cr-d and Ti-d states creates a smaller gap (0.133 eV).

Ti_2CrSn might have interesting spin-dependent transport and tunneling properties if it can be synthesized. The calculated hull distance for the compound is 0.139 eV/atom meaning that the OQMD contains phases or a combination of phases (in this case a mixture of binaries) that is lower in energy than our 0.052 eV/atom empirical threshold.

We found no 24-electron Slater-Pauling semiconductors among the XA compounds that we investigated. Of the 405 XA compounds that we studied, 24 had a valence electron count of 24. None were semiconducting, though 6 were half-metallic with zero moment or near-half-metallic with a very small moment. The reason for the absence of 24-electron XA semiconductors is relatively simple. As we shall discuss in the next section, the Slater-Pauling gap in the XA phase requires formation of significant magnetic moments to create a significant difference between the $d-$onsite energies of the two X atoms. When moments form, the two spin channels will generally be different and a semiconductor becomes unlikely. The interesting exception to this rule are the 18-electron semiconductors with moments, but zero net moment in which even very small differences between the $d-$onsite energies of the X atoms can effectuate a small gap. All of the semiconductors in Table 4.1, have hull distances that exceed our stability threshold criterion of 0.052 eV/atom.

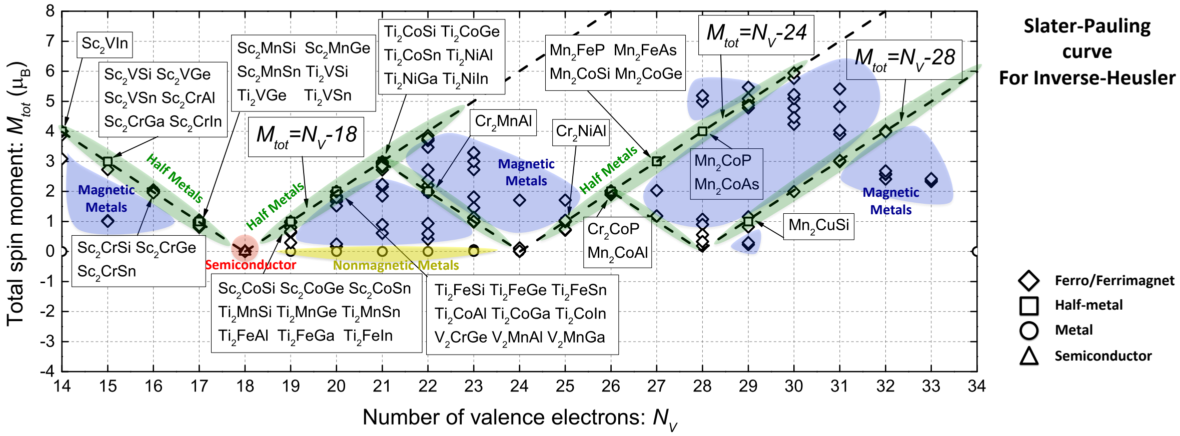

Figure 4.12: Calculated total magnetic moment per unit cell as a function of the total valence electron number per unit cell for 254 XA compounds with negative formation energies. The orange dashed line represents $|M_{tot}| = N_V - 18$, the blie dashed line represents the Slater-Pauling rule, $|M_{tot}| = N_V - 24$ and the light green dashed line represents $|M_{tot}| = N_V - 28$. The compounds from Table 4.2 are listed in the boxes. All of these compounds follow the rules precisely. Diamond, square, circle and triangle symbols indicate ferromagnets/ferrimagnets, half-metals, metals and semiconductors, respectively. We also use different color shapes to mark off half-metals, semiconductors, and magnetic/nonmagnetic metals. To avoid confusion about the signs of magnetic moments, we uniformly use the absolute values of magnetic moments in this diagrams.

4.5 Half-metals and “Near” Half-metals

Although a large number of XA phase half-metals have been predicted based on theoretical simulations [41], we found that most of them do not remain in the XA phase after relaxation, or they have lower energies in the $L2_1$ or the tetragonal ‘$L2_1$’ phase phase. However, in order to better understand the XA phase, we have listed in Tables 4.2 and 4.3 all of the half-metals and near-half-metals found in our survey of 405 XA systems for which the calculated formation energy was negative. Our definition of a “near-half-metal” is given in Appendix. A.

Both tables are divided into three sections according to whether the gap leading to half-metallicity is located after 9, 12 or 14 states. The tables give, N_V, the number of valence electrons per formula unit, a, the lattice constant, the total magnetic moment per formula unit as well as the individual moments on each atom evaluated within atom centered spheres of 1.45 Å radius.

For almost all of the half-metals and near-half-metals that follow the Slater-Pauling rule (gap after 12 states), the spin moments on the X_1 atoms are antiparallel to those on X_2 atoms. If one uses the local moments given in Table 4.2 to estimate the number of majority and minority s-d

electrons on the transition metal sites one finds that for the Slater-Pauling half-metals with minority gap, there are approximately 4 minority electrons on the X_1 and Y sites and approximately 2 on the X_2 sites. This implies that the transition metal nearest neighbors always differ in number of electrons by approximately 2. The implied contrast in the positions of the d-states of these neighbors leads to the hybridization gap in the minority channel. Since the average of 4 and 2 is 3, the gap should fall after 3 states per atom [85].

The tables also give the formation energy, ΔE_f, and the hull distance calculated within the OQMD, ΔE_{HD} (see Sec 4.5.2) as well as the formation energy of the $L2_1$ phase, $E_f(L2_1)$. The final three columns show the calculated energy gap, references to experimental reports of the XA phase and references to experimental reports of the $L2_1$ phase for Y_2XZ. The presence of these phases indicates that it may be difficult to distinguish a mixture of X_2YZ in the XA phase and Y_2XZ in the $L2_1$ phase. Since they have the same XRD reflection peaks, it is difficult to distinguish the composition from the XRD patterns, which may lead to a wrong conclusion about the composition of the sample.

4.5.1 Moment vs. Electron Count

Figure 4.12 shows the total spin magnetic moment per formula unit (M_{tot}) plotted versus the total valence electron number per formula unit (N_V) for 254 XA compounds with negative formation energy. In this plot, the half-metallic phases fall along one of the lines, $M_{tot} = |N_V - 18|$, $M_{tot} = |N_V - 24|$, or $M_{tot} = |N_V - 28|$ depending on whether the system is placing the Fermi energy in a gap after 9, 12, or 14 states respectively. The half-metals are listed in Table 4.2 along with their calculated properties. Table 4.3 is a similar list of the near-half-metals.

The half-metals and near-half-metals found along the $M_{tot} = |N_V - 18|$ line with a gap after 9 states per formula unit in one of the spin channels primarily have X=Sc, or Ti, while those found along the $M_{tot} = |N_V - 24|$ lines generally have X=Cr or Mn. Systems with X=V also fall mainly along the $M_{tot} = |N_V - 18|$ line, but there is one near-half-metal, (V_2CoSi) that uses the gap after 12 states. We find only one half-metal (Mn_2CuSi) and one near-half-metal (Mn_2CuP) along the $M_{tot} = |N_V - 28|$ line. The systems that appear to be on that line at $N_V = 30$ and $N_V = 31$ have pseudogaps rather than gaps near the Fermi energy.

Table 4.2: DFT-calculated properties of 51 half-metals in the inverse-Heusler phase that have negative formation energy. Successive columns present: number of valence electrons per formula unit, N_V, calculated lattice constant, a, total spin moment per f.u., M_{tot}, local moments for atoms on the X_1, X_2, Y, and Z sites: $m(X_1)$, $m(X_2)$, $m(Y)$ and $m(Z)$, formation energy ΔE_f, distance from the convex hull ΔE_{HD}, formation energy in $L2_1$ phase $\Delta E_f(L2_1)$, band gap E_g, gap type, experimental reports of compounds with composition X_2YZ, and experimental reports of corresponding Y_2XZ full-Heusler compounds, if any.

X_2YZ	N_V	a	M_{tot}	$m(X_1)$	$m(X_2)$	$m(Y)$	$m(Z)$	ΔE_f	ΔE_{HD}	$\Delta E_f(L2_1)$	E_g	Experimental reports	Y_2XZ reports
		(Å)		(μ_B)				(eV/atom)			(eV)		
Sc_2VIn	14	6.938	-4	-0.072	-0.509	-2.675	0.041	-0.013	0.276	-0.100	0.504		
Sc_2VSi	15	6.53	-3	0.058	-0.452	-2.228	0.073	-0.125	0.388	-0.196	0.499		
Sc_2VGe	15	6.61	-3	0.084	-0.424	-2.274	0.070	-0.118	0.446	-0.203	0.480		
Sc_2VSn	15	6.87	-3	0.144	-0.327	-2.388	0.058	-0.157	0.323	-0.210	0.518		
Sc_2CrAl	15	6.67	-3	0.295	-0.064	-3.133	0.082	-0.039	0.225	-0.096	0.684		
Sc_2CrGa	15	6.62	-3	0.284	-0.050	-3.121	0.067	-0.065	0.283	-0.158	0.684		
Sc_2CrIn	15	6.86	-3	0.337	0.056	-3.302	0.049	-0.003	0.286	-0.069	0.646		
Sc_2CrSi	16	6.43	-2	0.380	0.020	-2.454	0.079	-0.120	0.393	-0.161	0.632		
Sc_2CrGe	16	6.52	-2	0.429	0.112	-2.613	0.065	-0.110	0.453	-0.184	0.646		
Sc_2CrSn	16	6.79	-2	0.505	0.234	-2.878	0.051	-0.136	0.344	-0.180	0.631		
Sc_2MnSi	17	6.37	-1	0.465	0.443	-2.218	0.062	-0.200	0.350	-0.285	0.518		
Sc_2MnGe	17	6.461	-1	0.536	0.554	-2.455	0.041	-0.188	0.410	-0.314	0.428		
Sc_2MnSn	17	6.75	-1	0.628	0.654	-2.833	0.031	-0.202	0.312	-0.287	0.266		
Ti_2VSi	17	6.173	-1	0.575	-0.028	-1.476	0.007	-0.316	0.217	-0.379	0.219		
Ti_2VGe	17	6.262	-1	0.688	0.094	-1.706	0.008	-0.246	0.240	-0.316	0.285		
Ti_2VSn	17	6.523	-1	0.879	0.257	-2.052	0.004	-0.166	0.139	-0.189	0.423		
Sc_2CoSi	19	6.28	1	0.426	0.173	0.220	0.053	-0.268	0.406	-0.506	0.67		
Sc_2CoGe	19	6.367	1	0.432	0.221	0.165	0.029	-0.248	0.425	-0.521	0.591		
Sc_2CoSn	19	6.627	1	0.421	0.206	0.182	0.010	-0.239	0.345	-0.421	0.594		
Ti_2MnSi	19	6.024	1	1.055	0.652	-0.920	0.043	-0.394	0.231	-0.409	0.461		
Ti_2MnGe	19	6.123	1	1.204	0.844	-1.314	0.024	-0.295	0.265	-0.346	0.517		
Ti_2MnSn	19	6.39	1	1.41	1.106	-1.916	0.017	-0.188	0.188	-0.178	0.593		
Ti_2FeAl	19	6.12	1	1.013	0.709	-0.964	0.031	-0.256	0.187	-0.279	0.536		
Ti_2FeGa	19	6.122	1	1.005	0.757	-0.966	0.009	-0.265	0.212	-0.344	0.57		
Ti_2FeIn	19	6.37	1	1.208	1.064	-1.673	0.004	-0.045	0.274	-0.072	0.532		
Ti_2FeSi	20	5.99	2	1.257	0.621	-0.101	0.041	-0.395	0.295	-0.447	0.628		
Ti_2FeGe	20	6.07	2	1.282	0.677	-0.186	0.011	-0.297	0.307	-0.394	0.622		
Ti_2FeSn	20	6.339	2	1.356	0.801	-0.509	0.001	-0.185	0.256	-0.227	0.617		
Ti_2CoAl	20	6.13	2	1.252	0.705	-0.204	0.020	-0.287	0.185	-0.293	0.684		
Ti_2CoGa	20	6.11	2	1.230	0.773	-0.211	-0.005	-0.295	0.178	-0.363	0.689		
Ti_2CoIn	20	6.351	2	1.245	0.837	-0.381	-0.009	-0.089	0.195	-0.086	0.613		
V_2CrGe	20	5.94	2	1.167	-0.415	1.158	0.003	-0.118	0.151	-0.120	0.086		
V_2MnAl	20	5.922	2	1.354	-0.309	0.870	0.016	-0.148	0.097	-0.072	0.142		[239]
V_2MnGa	20	5.924	2	1.229	-0.416	1.138	-0.007	-0.118	0.123	-0.070	0.124		[240]
Ti_2CoSi	21	6.02	3	1.528	0.789	0.394	0.059	-0.387	0.307	-0.437	0.798		
Ti_2CoGe	21	6.10	3	1.518	0.812	0.396	0.018	-0.299	0.303	-0.384	0.779		
Ti_2CoSn	21	6.35	3	1.495	0.802	0.373	-0.004	-0.217	0.220	-0.197	0.727		
Ti_2NiAl	21	6.19	3	1.524	0.982	0.149	0.028	-0.285	0.200	-0.277	0.46		
Ti_2NiGa	21	6.17	3	1.491	1.056	0.158	-0.003	-0.289	0.193	-0.364	0.522		
Ti_2NiIn	21	6.4	3	1.452	1.058	0.135	-0.013	-0.127	0.216	-0.096	0.418		
Cr_2MnAl	22	5.831	−2	-1.835	1.536	-1.678	-0.021	-0.086	0.048	0.002	0.204		
Cr_2NiAl	25	5.7	1	-1.239	1.828	0.452	-0.057	-0.071	0.236	0.148	0.142		[151]
Cr_2CoP	26	5.619	2	-0.794	1.912	0.854	-0.012	-0.22	0.217	-0.159	0.48		
Mn_2CoAl	26	5.735	2	-1.617	2.701	0.958	-0.061	-0.27	0.036	-0.141	0.38	XA [42, 206]	[241]
Mn_2FeP	27	5.558	3	-0.452	2.632	0.733	0.024	-0.352	0.096	-0.292	0.252		
Mn_2FeAs	27	5.72	3	-0.732	2.772	0.885	0.022	-0.071	0.086	0.014	0.337		
Mn_2CoSi	27	5.621	3	-0.548	2.670	0.849	-0.012	-0.365	0.018	-0.177	0.513		[242–244]
Mn_2CoGe	27	5.75	3	-0.804	2.863	0.903	0.005	-0.153	0.03	-0.011	0.323	XA [42]	[245]
Mn_2CoP	28	5.581	4	0.091	2.793	1.017	0.032	-0.333	0.216	-0.232	0.508		
Mn_2CoAs	28	5.738	4	-0.007	2.916	1.013	0.025	-0.085	0.08	0.081	0.295		
Mn_2CoSb	28	5.985	4	-0.041	3.093	0.938	-0.003	0.042	0.133	0.193	0.499	XA [42, 236]	[151, 246]
Mn_2CuSi	29	5.762	1	-1.876	2.838	0.003	0.018	-0.101	0.177	-0.091	0.318		

Table 4.3: DFT-calculated properties of 50 near-half-metallic X_2YZ inverse-Heusler compounds with negative formation energy. Successive columns present: number of valence electrons per formula unit N_V, calculated lattice constant (a_{calc}), total spin moment (M_{tot}) per f.u., local moments for atoms on the X_1, X_2, Y and Z sites: $m(X_1)$, $m(X_2)$, $m(Y)$ and $m(Z)$, formation energy (ΔE_f), distance from the convex hull ΔE_{HD}, formation energy in $L2_1$ phase $\Delta E_f(L2_1)$, experimental reports of compounds with composition X_2YZ, and experimental reports of corresponding Y_2XZ full-Heusler compounds.

X_2YZ	N_V	a_{calc}	M_{tot}	$m(X_1)$	$m(X_2)$	$m(Y)$	$m(Z)$	ΔE_f	ΔE_{HD}	$\Delta E_f(L2_1)$	Experimental records	Rep. Y_2XZ
		(Å)	(μ_B)					(eV/atom)				
Sc_2VAl	14	6.756	-3.8779	-0.077	-0.508	-2.588	0.040	-0.033	0.231	-0.134		
Sc_2VGa	14	6.708	-3.9989	-0.114	-0.579	-2.613	0.050	-0.064	0.285	-0.184		
Sc_2MnAl	16	6.59	-1.9983	0.429	0.231	-2.903	0.074	-0.122	0.174	-0.160		
Sc_2MnGa	16	6.54	-1.9999	0.425	0.285	-2.919	0.052	-0.159	0.229	-0.243		
Sc_2MnIn	16	6.80	-1.9969	0.489	0.398	-3.203	0.038	-0.085	0.221	-0.138		
Sc_2VSb	16	6.78	-2.0011	0.319	-0.188	-1.949	0.049	-0.150	0.439	-0.173		
Ti_2VAl	16	6.32	-1.9633	0.380	-0.579	-1.541	0.016	-0.120	0.153	-0.179		
Ti_2VGa	16	6.27	-1.9529	0.314	-0.567	-1.499	0.022	-0.145	0.189	-0.219		
Sc_2CrP	17	6.303	-1.0043	0.491	0.349	-2.051	0.063	-0.166	0.699	-0.296		
Sc_2CrSb	17	6.74	-1.0001	0.660	0.526	-2.598	0.046	-0.097	0.492	-0.178		
Sc_2FeAl	17	6.47	-0.9071	0.248	0.216	-1.539	0.029	-0.1323	0.216	-0.244		
Sc_2FeGa	17	6.43	-0.9488	0.264	0.277	-1.656	0.015	-0.1735	0.267	-0.345		
Sc_2FeIn	17	6.69	-0.9714	0.344	0.412	-2.042	0.013	-0.069	0.290	-0.189		
Ti_2CrAl	17	6.297	-0.8021	1.032	0.775	-2.723	0.019	-0.1556	0.141	-0.197		
Ti_2CrGa	17	6.266	-0.8659	1.008	0.785	-2.747	0.011	-0.1781	0.166	-0.245		
Ti_2CrIn	17	6.51	-0.8538	1.141	0.939	-3.078	0.005	-0.002	0.149	0.022		
Sc_2MnSb	18	6.685	0.0047	-0.656	-0.712	1.984	0.018	-0.1449	0.444	-0.296		
Ti_2VP	18	6.06	0.0033	-0.941	-0.365	1.371	-0.013	-0.4397	0.442	-0.495		
Sc_2NiAl	19	6.502	0.9649	0.413	0.217	0.120	0.031	-0.2413	0.249	-0.425		
Sc_2NiGa	19	6.453	0.9738	0.423	0.272	0.081	0.015	-0.2817	0.278	-0.544		
Sc_2NiIn	19	6.69	0.9839	0.414	0.271	0.078	0.006	-0.1993	0.309	-0.375		
Ti_2CrAs	19	6.11	0.8077	1.015	0.535	-0.941	0.023	-0.2035	0.444	-0.255		
Ti_2CrSb	19	6.38	0.965	1.301	0.775	-1.441	0.019	-0.111	0.279	-0.084		
Sc_2CoSb	20	6.64	1.9999	0.656	0.299	0.664	0.055	-0.138	0.528	-0.394		
Sc_2NiSi	20	6.38	1.8015	0.689	0.459	0.220	0.093	-0.203	0.527	-0.591		
Sc_2NiGe	20	6.46	1.8123	0.691	0.517	0.184	0.050	-0.200	0.540	-0.621		
Sc_2NiSn	20	6.72	1.8438	0.690	0.523	0.164	0.019	-0.228	0.430	-0.516		
Ti_2MnSb	20	6.323	1.9891	1.318	0.564	-0.231	0.009	-0.1596	0.277	-0.181		
Ti_2FeAs	21	6.07	2.9395	1.424	0.469	0.780	0.036	-0.2374	0.475	-0.391		
V_2FeGa	21	5.91	2.8487	1.803	-0.231	1.200	-0.001	-0.146	0.091	-0.047		[151]
Ti_2NiSn	22	6.427	3.8602	1.604	1.307	0.451	0.001	-0.189	0.294	-0.236		
Ti_2FeSb	21	6.31	2.9885	1.449	0.441	0.802	0.009	-0.1583	0.319	-0.209		
V_2FeAl	21	5.914	2.911	1.862	-0.197	1.132	0.026	-0.191	0.088	-0.023		[247]
V_2MnGe	21	5.92	-2.8136	-1.627	0.516	-1.610	0.005	-0.193	0.115	-0.110		
V_2MnSn	21	6.20	-2.9604	-1.690	0.944	-2.148	0.014	-0.002	0.188	0.179		
V_2FeGe	22	5.891	-1.9779	-1.415	0.434	-0.944	-0.004	-0.165	0.146	-0.129		
Cr_2MnGa	22	5.832	-1.993	-1.880	1.614	-1.716	-0.003	-0.004	0.049	0.038		
Cr_2MnGe	23	5.8	-0.9919	-1.478	1.610	- 1.147	0.010	-0.007	0.122	-0.008		
V_2CoSi	23	5.78	-0.997	-0.754	0.182	-0.374	-0.029	-0.291	0.199	-0.193		
Cr_2CoAl	24	5.79	0.0095	1.892	-1.698	-0.307	0.086	-0.08	0.227	0.126		[121]
Cr_2CoSi	25	5.657	1.0086	-0.949	1.440	0.547	0.053	-0.2187	0.139	-0.022		
Cr_2CoGe	25	5.792	1.0225	-1.593	2.034	0.619	0.043	-0.0171	0.109	0.155		
Mn_2FeAl	25	5.75	1.0009	-1.856	2.714	0.142	-0.025	-0.158	0.008	-0.086		[240]
Mn_2FeGa	25	5.79	1.0386	-2.185	2.888	0.315	-0.004	-0.075	0.018	-0.038		
Cr_2NiSi	26	5.705	1.8915	-0.857	2.130	0.573	-0.023	-0.195	0.201	-0.035		
Cr_2NiGe	26	5.82	1.9414	-1.132	2.434	0.573	-0.008	-0.012	0.176	0.124		
Mn_2CoGa	26	5.76	2.0045	-1.820	2.879	0.955	-0.030	-0.167	0	-0.087	XA [42]	[248]
Mn_2FeSi	26	5.6006	2.0077	-0.798	2.407	0.371	-0.015	-0.362	0	-0.259		[151]
Mn_2FeGe	26	5.72	2.0135	-1.243	2.667	0.556	-0.004	-0.14	0	-0.035		
Mn_2CuP	30	5.716	1.9946	-1.242	3.042	0.057	0.083	-0.048	0.399	-0.091		

Some systems appear on or near two lines. Systems with $N_V = 21$ can in principle have gaps after both 9 states and 12 states. Ti_2CoSi is a half-metal with the Fermi energy in the minority gap after 9 states, but the Fermi energy also falls in a pseudogap at 12 states in majority. The near-half-metals $Ti_2Fe(P,As,Sb)$ all have gaps after 9 states in minority and after 12 states in majority, however the moment is not large enough to place the Ferni energy in the gaps. In each case it falls just above the minority gap and just below the majority gap by an equal number of states. Similarly, for $N_V = 26$ one can have systems on both the $M_{tot} = |N_V - 24|$ and the $M_{tot} = |N_V - 28|$ lines. Thus Mn_2CoAl has a minority gap after 12 states and a pseudogap at 14 majority states.

Although we predicted that Mn_2CoSb would have a positive formation energy (0.042 eV), we found references indicating that it can be fabricated in the XA phase [42, 236] using melt-spinning. For this reason Mn_2CoSb was included in Fig. 4.12 and Table 4.2. As discussed in Sec. 4.3.1, we speculate that the experimental samples may be $L2_1B$ phase rather than XA.

4.5.2 Hull Distances

Using our calculated XA formation energies, and the formation energies of all the other phases in the OQMD, we calculated the hull distance ΔE_{HD} for the negative formation energy half-metallic inverse-Heusler compounds listed in Table 4.2 and the near-half-metals listed in Table 4.3. Our calculations predict all the Sc, Ti-, and V-based half-metals lie significantly above the convex hull and have a ΔE_{HD} that exceeds our empirical criterion of $\Delta E_{\mathrm{HD}} \leq 0.052$eV/atom for having a reasonable probability of synthesizability. We predict 4 half-metals (Cr_2MnAl, Mn_2CoAl, Mn_2CoSi, Mn_2CoGe) to lie close enough to the convex hull to meet our criterion. Two of these compounds Mn_2CoAl [42, 206] and Mn_2CoGe [42] have been experimentally observed by X-ray diffraction (XRD) measurements to exist in the XA phase. We also found 6 near-half-metals (Cr_2MnGa, Mn_2FeAl, Mn_2FeGa, Mn_2FeSi, Mn_2FeGe, Mn_2CoGa) that meet our criterion for stability, three of these (Mn_2FeGa, Mn_2FeSi, Mn_2FeGe) have a calculated hull distance of zero meaning that no phase or combination of phases in the OQMD had lower energy.

4.6 Summary of Contributions

In this chapter, we have performed extensive first-principles calculations on 405 inverse-Heusler compounds X_2YZ, where X=Sc, Ti, V, Cr, Mn, Fe, Co, Ni, or Cu; Y=Ti, V, Cr, Mn, Fe, Co, Ni, Cu, or Zn; and Z=Al, Ga, In, Si, Ge, Sn, P, As, or Sb with a goal of identifying materials of interest for spintronic applications. We identified 14 semiconductors with negative formation energy. These are listed in Table 4.1. We identified many half-metals and near-half-metals. Those half-metals and near-half-metals that we identified and that have negative formation energy are listed in Tables 4.2 and 4.3. respectively.

We have identified four half-metals and six near-half-metals that meet a criterion for stability that we estimated based on a study of the hull distances of known XA phases. Seven of these ten predicted phases have not (to our knowledge) been observed experimentally.

In establishing our stability criterion, we analyzed the experimental and theoretical data for several reported XA phases (Mn_2CoIn, Mn_2CoSb, Mn_2CoSn, Mn_2RuSn) and tentatively concluded that they are not XA but are more likely a disordered phase such as $L2_1B$. We recommend more extensive studies of these materials.

The ten half-metallic or near-half-metallic phases that we identified as reasonably likely to be stable, are all Slater-Pauling phases, *i.e.* they have a gap in the density of states after three states per atom in one of the two spin channels, and the Fermi energy is in or near this gap. Many half-metallic and near-half-metallic phases based on a gap after 9 states per formula unit (2.25 states per atom) were identified, but we estimate that other phases or combination of phases are likely to be more stable in equilibrium.

Chapter 5

Half-Heusler/MgO Magnetic Tunnel Junctions

5.1 Introduction

Spin Transfer Torque Random Access Memory (STT-RAM) has been attracting a great deal of attention due to its potential to combine the speed of SRAM, the density of DRAM, and the non-volatility of Flash, all while providing excellent scalability and outstanding endurance [249]. The magnetic tunneling junction(MTJ) inside a STT-RAM cell stores information with relative magnetization of electrode layers, with STT switching resulting in magnetization reversal. In order to fabricate a practical STT-RAM, a robust MTJ with optimized and matched interfaces between barriers and electrodes is necessary [250]. This requires a novel magnetic material with high spin polarization, low saturation magnetization, low magnetic damping and perpendicular magnetic anisotropy(PMA) [251]. If the materials can be compatible with MgO in crystal interfaces, it will be more promising in current spintronics application.

Half-metals(HM) have been regarded as the most ideal electrode materials in spintronics field. They have a gap at the Fermi level for minority spin-channel, while show metallic for the majority, creating the opportunity to generate a fully spin-polarized current in principle. The first half-metal, half-Heusler alloy NiMnSb, was recognized by de Groot and collaborators in 1983 [30]. Since then, there is a series of Heusler alloys have been discovered as half-metals and near-half-metals theoretically [32,35,36,39,41,252]. In order to do a systematical research for Heusler alloy family, we created a Heusler alloy database including electronic structures, magnetism and structure stability of 378 half-Heusler alloys [253]. From half-Heusler database, we have identified 45 half-metals and 34 near-half-metals with negative formation energy, that follow the Slater-Pauling rule of three electrons per atom.

But most of these half-metals and near-half-metals are not compatible well with MgO in lattice constants. And another drawback of half-Heusler alloys with $C1_b$ crystal structure for application as a MTJ electrode layer is that because of their cubic symmetry, they do not have uniaxial magnetocrystalline anisotropy (MCA). In this work, we select out six half-metals and near-half-metals with less than 1% lattice mismatch with MgO, and calculate the electronic structure of their heterostructures by using ab-initio simulations.

5.2 structure and computational method

Calculations have been performed for periodic Heusler-MgO junction superlattices consisting of five layers of MgO(B1 structure, a=5.95 Å) and five layers of the half-Heusler alloys, using density-functional theory(DFT) as implemented in the Vienna Ab-initio Simulation Package(VASP) [86] which uses a plane wave basis set and the projector augmented wave (PAW) method [91]. A uniform cut-off energy of 520 eV was implemented for all calculations. The Perdew-Buker-Ernzerhof(PBE) version of the generalized gradient approximation(GGA) to the exchange-correlation functional of DFT was adopted [89]. To achieve a higher accuracy with respect to the magnetic moment, the interpolation formula form Vosko, Wilk, and Nusair [61] was used in all calculations. In order to take into account all degrees of freedom for the Heusler-MgO interfaces, we have performed full structural optimizations for the superlattice parameters and internal coordinates. The convergence criterion of the total energy change is set to 10^{-5}eV. The k-point mesh is taken as $12 \times 12 \times 2$ for (100) interfaces.

The half-Heusler alloy XYZ crystallizes in the face-centered cubic $C1_b$ structure ($F\bar{4}3m$) with one formula unit per unit cell. It consists of four sublattices: X at the ($\frac{1}{4}$, $\frac{1}{4}$, $\frac{1}{4}$), Y at the ($\frac{1}{2}$, $\frac{1}{2}$, $\frac{1}{2}$), Z at the (0,0,0), and the vacancies at the ($\frac{3}{4}$, $\frac{3}{4}$, $\frac{3}{4}$) sites. The six half-Heusler alloys we studied here are CrScAs, MnVSb, FeTiSb, CoTiSn, NiTiIn and NiMnSb, and all of them are hypothetical except

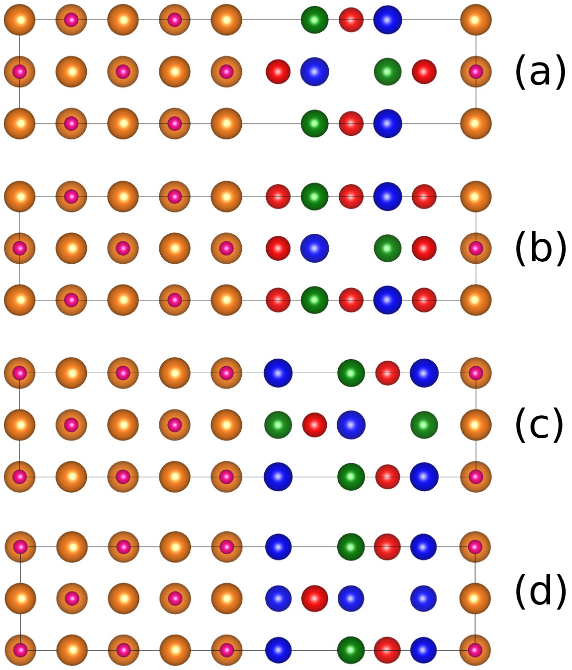

Figure 5.1: Side views of the superlattices of the half-Heusler(110)/MgO junctions: (a) X/OMg-terminated interface, (b) XX/OMg-terminated interface, (c) YZ/OMg-terminated interface,and (d) YY/OMg-terminated interface. Color note: X(red), Y(blue), Z(green), Mg(orange), O(pink).

for NiMnSb [151]. The calculated lattice constant of NiMnSb (5.91 Å) is within 1% accuracy to the experimental result (5.92 Å) [151], indicating the reliability for our simulations. The [100] direction of these alloys and [110] direction of MgO present a nearly perfect lattice matching.

At the MgO interface as shown in FIG 5.1, there are four kinds of Heusler terminations could be touched: X (three layers of X and two layers of YZ in total), XX (two layers of XX, one layer of X and two layers of YZ in total), YZ (two layers of X and three layers of YZ in total) and YY (two layers of YY, one layer of YZ and two layers of X in total) terminals. The XX termination means that the vacancies in the bulk are occupied by X atoms at the interfaces, but the X layers inside the bulk still keep the vacancies empty. The YY terminations means that the Z atoms in YZ termination are replaced by Y atoms. More structural details will be discussed in the following section.

5.3 Interface binding energy and half-metallicity

We performed full ionic relaxations for the six supercells in FIG 5.1 to obtain equilibrium structures. The bond types and lengths at the different interfaces are illustrated in TABLE 5.1. For example, Cr/OMg interface is composed of a layer containing only Cr atoms and a layer containing both O and Mg atoms with direct Cr-O bonds. We notice that the length of bonds is found to be the shortest at the X/OMg terminated interfaces in all Heusler-MgO junctions, while the optimized Y/Z-O bonds are the longest at the YZ/OMg interfaces.

We also analyzed the bonding strength of the interfaces by calculating their binding energies W:

$$W = E_{\mathrm{XYZ/MgO}} - E_{\mathrm{XYZ}} - E_{\mathrm{MgO}} \tag{5.1}$$

where $E_{\mathrm{XYZ/MgO}}$ is the total energies of optimized Heusler-MgO junctions, and $E_{\mathrm{XYZ}}(E_{\mathrm{MgO}})$ is the total energy of the Heusler(MgO) slab surrounded by vacuum in supercell. The lattice parameters of slab supercells are the same with those of optimized Heusler-MgO junctions, and no further relaxation is performed for slab supercells. We found that the YY/OMg interfaces present the lowest binding energies for most Heusler-MgO junctions except CrScAs-MgO, which indicates that metal-O bonds not only have stronger bond strength, but also energetically favor more Y-rich interfaces to form more stable Heusler-MgO junctions. Previous investigation also predicted full-Heusler alloys also tend to stabilize in pure XX or YY layers [254] due to the strong oxidation.

Table 5.2 lists the geometric and magnetic properties of Heusler-MgO junctions. a_r is the lattice parameter obtained from the layer parallel with the interface after relaxation, while c_r is the average lattice parameter of the four "internal" spacings in five Heusler layers. If the $\mathrm{c}_r/\mathrm{a}_r$ value is larger than 1.01, we consider that this Heusler layer has been distorted to be a tetragonal structure. The Table 5.2 also lists the induced anisotropy ($\perp$ K), the saturation magnetization (M_S), and whether the supercell still remains half-metallicity (HM) or near-half-metallicity (NHM). A positive anisotropy K suggests that the magnetization prefers to be perpendicular to the Heusler layers, while a negative one implies that the magnetization tends to lie in-plane.

Although the uniaxial anisotropy is induced by the tetragonal distortion in the Heusler layers, its value and easy axis direction are not determined by $\mathrm{c}_r/\mathrm{a}_r$. The value of uniaxial anisotropy

Table 5.1: Bond lengths and binding energy W for the half-Heusler(100)/MgO interfaces

Interface terminal	Bond type	Bond length (Å)	W (eV)
Cr	Cr-O	2.06	-2.69
CrCr	Cr-O	2.10	-3.83
ScAs	Sc-O/As-O	2.30/3.11	-1.74
ScSc	Sc-O	2.32	-3.74
Mn	Mn-O	2.03	-2.34
MnMn	Mn-O	2.13	-2.92
VSb	V-O/Sb-O	2.32/2.88	-1.51
VV	V-O	2.10	-4.26
Fe	Fe-O	1.98	-2.47
FeFe	Fe-O	2.05	-3.99
TiSb	Ti-O/Sb-O	2.34/2.92	-1.64
TiTi	Ti-O	2.18	-4.35
Co	Co-O	1.96	-2.47
CoCo	Co-O	2.02	-4.21
TiSn	Ti-O/Sn-O	2.29/2.74	-2.00
TiTi	Ti-O	2.18	-4.23
Ni	Ni-O	2.00	-2.05
NiNi	Ni-O	2.07	-3.21
TiIn	Ti-O/In-O	2.26/2.57	-2.39
TiTi	Ti-O	2.18	-4.35
Ni	Ni-O	2.01	-2.06
NiNi	Ni-O	2.08	-3.22
MnSb	Mn-O/Sb-O	2.46/3.01	-1.84
MnMn	Mn-O	2.18	-3.65

is significantly conditioned by the atoms at the Heusler layer interface. For example, the TiSb interface layers in FeTiSb/MgO junction, anisotropy is in-plane, while Fe and FeFe interface layers generate significant perpendicular anisotropy.

As we said before, not only an enough PMA, the half-metallicity of the Heusler layers is also expected to be retained. This property is very difficult to be kept in supercells and governed by the interface types. It is very interesting that the systems with YY interface layers tend to remain near half-metallic and half-metallic, as seen in FIG. 5.2 and 5.3, while other interfaces lose their half-metallicity. One might argue that the in-plane distortion of a_r also influences on half-metallicity, such as that the MnVSb/MgO junction with VV interface layer remains as the bulk system with near-half-metallicity, while other systems are metals. However, in the case of NiMnSb, the amount of in-plane distortions is the same when the interface layers are NiNi and MnMn, but the Heusler layer loses its half-metallicity for NiNi interface layer. It has been verified experimentally by spin-resolved

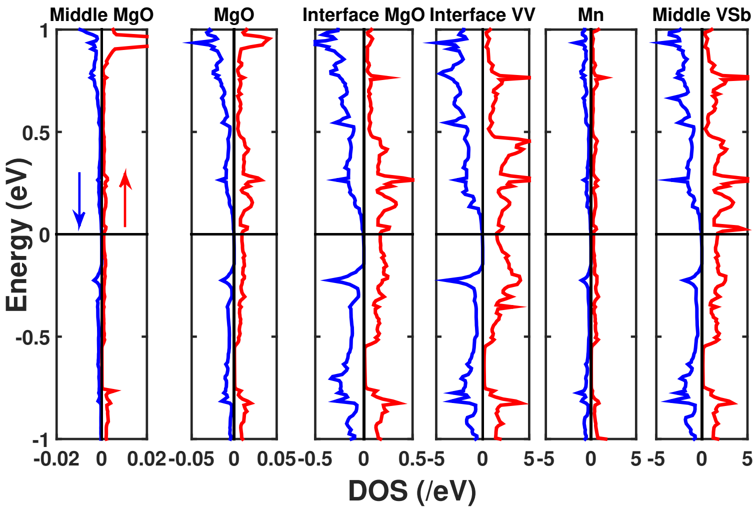

Figure 5.2: Local density of states for a MnVSb-MgO periodic supercell with VV/OMg interface. The supercell stays NHM (Band gap is opened in the spin-down channel).

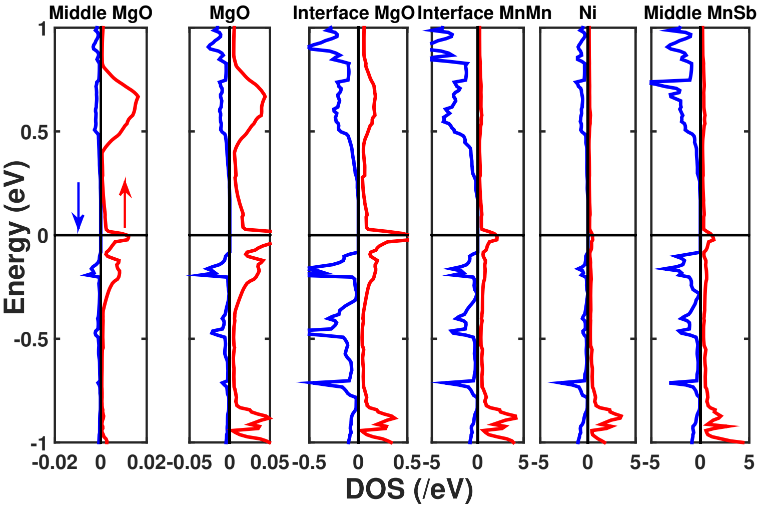

Figure 5.3: Local density of states for a NiMnSb-MgO periodic supercell with MnMn/OMg interface. The supercell stay HM (Band gap is opened in the spin-down channel).

X-ray photoemission spectroscopy(SR-XPS) of a NiMnSb/MgO(100) junction that a Mn interface layer can be achieved and some oxidization of Mn exists when a MgO(001) epitaxial barrier was grown on top of NiMnSb using molecular beam epitaxy(MBE) [255, 256]. However, the half-metallicity and high TMR ratio of NiMnSb-MgO junction is not yet been observed in experiments due to a decrease of the Mn magnetization at the interface with MgO [255, 257]. Hence, similar with the case of anisotropy, interface layer is a more important factor in governing half-metallicity rather than in-plane distortion. We also need to point out that although the induced PMA is predicted

Table 5.2: Summary of the geometric and magnetic properties of various half-Heusler-MgO junctions.

XYZ	a (Å)	a_r (Å)	interface	δa_r	c_r/a_r	M_S (emu/cm^3)	K $\times 10^6$ (erg/cm^3)	Half metallic?
CrScAs(HM)	5.92,6.54	ScAs	5.87	-0.79	1.1684	618	-0.89	No
		Cr	5.92	0.01	1.1693	896	-2.40	No
		CrCr	6.03	0.19	1.0428	747	-0.31	No
		ScSc	6.15	3.8	0.9889	475	0.78	No
MnVSb(HM)	5.92	VSb	5.90	-0.27	1.0371	59	6.75	No
		Mn	5.96	0.64	1.0116	372	-1.17	No
		MnMn	6.00	1.30	1.0156	737	0.66	No
		VV	5.92	0	0.9345	381	-1.31	NHM
NiTiIn(NHM)	5.99	TiIn	5.97	-0.26	0.9846	70	0.24	No
		Ni	5.92	-1.19	1.0295	0.01	-2.25	No
		NiNi	5.94	-0.85	1.0375	13	-1.79	No
		TiTi	6.00	0.17	0.96	248	0.06	NHM
FeTiSb(NHM)	5.95	TiSb	5.89	-0.94	1.0063	72	-1.68	No
		Fe	5.92	-0.44	1.0055	208	5.27	No
		FeFe	5.98	0.45	0.9882	421	5.09	No
		TiTi	5.98	0.55	0.9431	0	0	No
CoTiSn(NHM)	5.93	TiSn	5.91	-0.30	1.0028	0	0	No
		Co	5.90	-0.43	1.0049	14	1.19	No
		CoCo	5.96	0.51	0.9805	0.90	-0.00017	No
		TiTi	5.98	0.89	0.9461	160	1.28	NHM
NiMnSb(HM)	5.91	MnSb	5.89	-0.42	0.9802	1130	8.10	No
		Ni	5.93	0.27	0.9757	811	0.02	No
		NiNi	5.96	0.79	0.9791	796	-2.83	No
		MnMn	5.96	0.79	0.9327	1881	2.15	HM

in NiMnSb/MgO junction with pure MnMn interface, the large saturation magnetization M_S of NiMnSb will hence the magnetization to lie in-plane. It is the same with other near half-metallic Heusler-MgO junctions.

5.4 I-V characteristics of Half-Heusler-MgO MTJs

The transport calculations are performed in SMEAGOL [258], which employs nonequilibrium Green's-function method combined with density-functional theory (DFT) in on a pseudo-atomic orbit basis [259]. Double η is used for all orbitals and the generalised gradient approximation (GGA) with PerdewBurkeErnzerhof (PBE) functional are adopted throughout all calculations. The electronic temperature is set at 300K. The spin dependent current is calculated from:

$$I^{\sigma}(V) = \frac{e}{h}\int T^{\sigma}(E;V)(f_L - f_R)dE\ , \tag{5.2}$$

$$T^{\sigma}(E;V) = \mathrm{Tr}\left[\Gamma^{\sigma}_{L}G^{\sigma}\Gamma^{\sigma}_{R}G^{\sigma\dagger}\right]. \tag{5.3}$$

where $T^{\sigma}(E;V)$ is the bias dependent transmission, $f_{L,R}$ are the fermi-dirac distribution for the left/right heusler contact respectively. The transmission is calculated through NEGF [260] where $\Gamma^{\sigma}_{L,R}$ are self-energies from left/right contact and G^{σ} is the retarded green's function. At equilibrium, a 5×5 $\mathbf{k}_{\perp}$-point mesh is used to converge the charge density. A 20×20 $\mathbf{k}_{\perp}$-point mesh is used to calculate the spin dependent current. At finite bias, a constant potential is added to heusler contacts and a linear potential is added in the MgO. This approximation is appropriate for magnetic tunnel junction where voltage drops mostly in the high resistant MgO [261]. It reduces the computational cost for self-consistent calculations.

Fig. 5.4 shows the I-V characteristics of the six MTJs. Among them NiMnSb shows the highest current density ($\sim 10^8$ A/cm^2) than the rest ($\sim 10^5$ A/cm^2). The reason for the big difference in current amplitude is because for NiMnSb, the fermi energy in the conducting spin channel lies in the middle of the s band, which has the lowest decaying rate in MgO due to the same symmetry as the Δ_1 band in MgO. For other systems, the conducting spin channel has fermi energy lie in non Δ_1 symmetry bands [262]. It could also be due to the different work functions of the electrode materials. Therefore the energy barrier heights between MgO and the electrodes are different, resulting in different tunneling probabilities. Some systems show negative differential resistance (NDR) at low bias which will be explained later.

MTJs are widely used in read units where the tunnel magnetoresistance (TMR) ratio is a key metric. The TMR can be calculated from the currents in parallel and anti-parallel configuration:

$$\mathrm{TMR} = \frac{I_p - I_{ap}}{I_{ap}} \tag{5.4}$$

Fig. 5.5 shows the TMR ratio as a function of the voltage for the six MTJs. Out of the six junctions, four of them show high TMR at low bias. It is worth mentioning that the specific value of the TMR ratio for a single junction is not important because our current calculations assume full ballistic

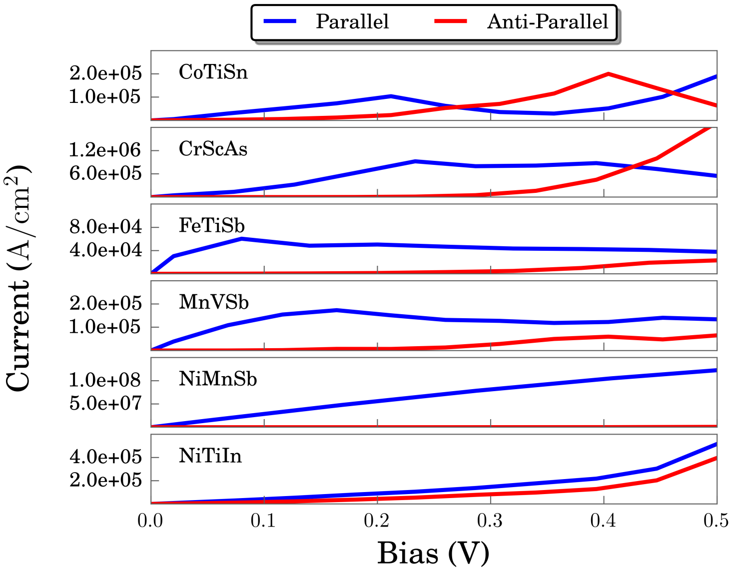

Figure 5.4: IVs of Half-heusler/MgO/Half-heusler junction.

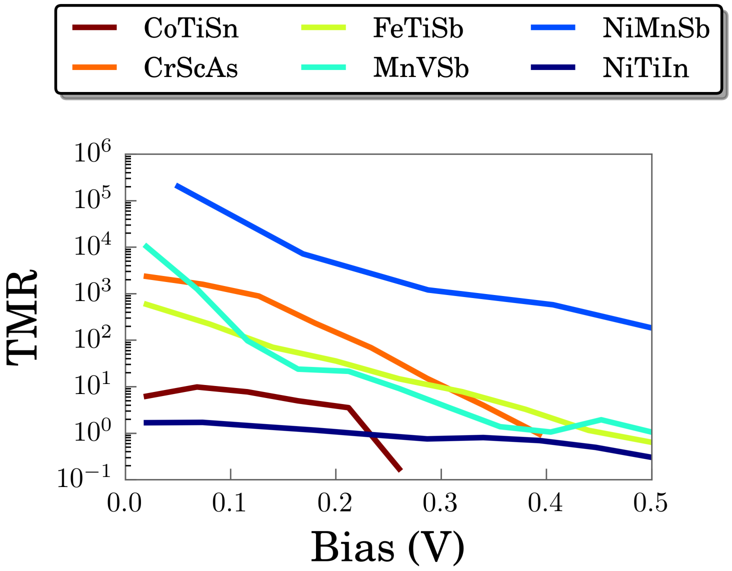

Figure 5.5: The tunnel magnetoresistance of half-heusler/MgO magnetic tunnel junctions.

transport without any spin scattering mechanism. Since the denominator I_{ap} is a very small number, any spin scattering can alter the TMR greatly. Depending on the specific mechanism, the TMR can vary with temperature [263] or magnetic impurity concentration. Still, comparing the TMRs from different junctions can create a reference on which material might perform better in terms of read operation in MgO based MTJs.

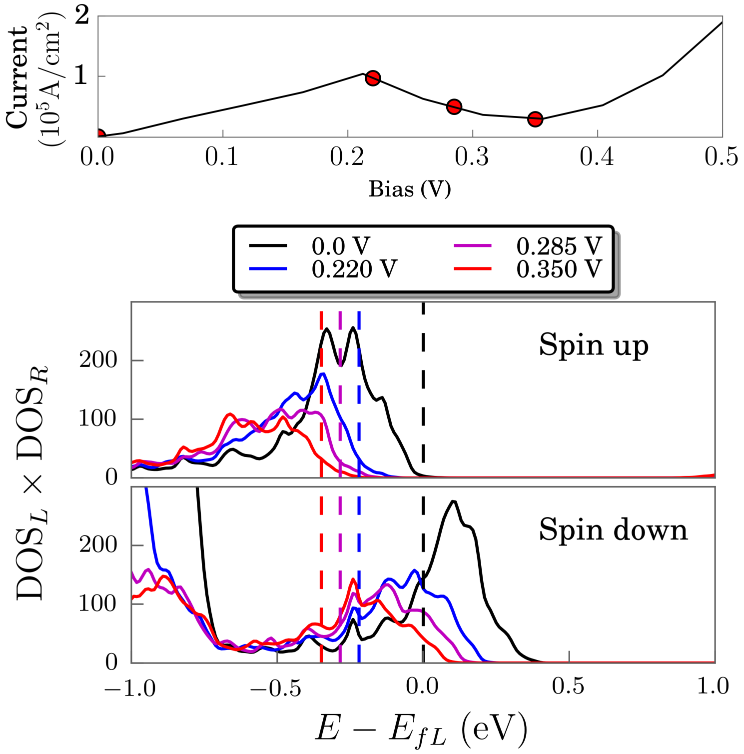

Figure 5.6: Top. IV of CoTiSn/MgO/CoTiSn in parallel configuration. Bottom. The product of the DOS from left and right electrode at finite bias.

Some systems show NDR effects in our calculations. We argue that it is due to two factors. We will analyze one of the systems CoTiSn to illustrate the point. The first factor is that the energy window between the fermi energies of the left/right electrode opens up as voltage increases, allowing more electronic states to contribute to the current. This contributes to the increase of current at the beginning (between 0 V to 0.22 V). The second factor is that as the voltage increases, the energy shift of the left and right electrode will change the transmission inside the bias window. Here we employ a simple model to see this effect. Assuming the transmission is proportional to the product of the density of states from left/right electrode. Since the left/right electrode are the same material, their DOS match at zeros bias (peak to peak). Using left electrode as a reference, as the voltage increases, the DOS from the right will shift. Some energy levels will have higher transmission as the peak of the right DOS pass by while other energies will have lower transmission if the DOS peak moves out. In the bottom plot of Fig. 5.6, it is clear that from 0.22 V to 0.35 V the DOS product in the bias window keeps dropping for both spin channels. Therefore even though the bias windows is expanding, the transmission amplitude is decreasing near the fermi energy. The combined effects cause the NDR in the IV. But we want to emphasize that in reality, the NDR is hard to observe due to imperfect interface between electrode and MgO. It can be easily washed out by impurities and defects.

5.5 Summary of Contributions

In this chapter, we have proven that it is possible to obtain uniaxial anisotropy and keep half-metallicity in a Heusler-MgO junction. Our results may promote further discovery of half-Heusler alloys as potential candidates as electrode layers in STT-RAM devices. There is an obvious relation between the interface layer and two properties, PMA and HM. To understand the physics underneath the relation, further theoretical work is necessary to be done in the future.

Chapter 6

Inverse Heusler for Ultrasmall and Fast skymion

6.1 Magnetic Skyrmions in Thin Films

6.1.1 Magnetic Skyrmions as Information Carrier

Magnetic skyrmions have topological spin textures that are stabilized by the antisymmetric exchange or Dzyaloshinskii-Moriya interaction (DMI). Their vortex-like spin configurations were predicted to exist stably at the nanometer scale in bulk non-centrosymmetric materials as well as thin film heterostructures [264,265]. Substantial progress has been made in observing skyrmions and skyrmion lattices in multiple systems by means of neutron scattering, Lorentz transmision electron microscopy, scanning tunneling microscopy and X-ray holography. Reported material systems supporting skyrmions include the B20 family (such as MnSi [266,267], FeGe [268], $Fe_{0.5}Co_{0.5}Si$ [269]), multiferroic materials [270], tetragonal inverse heuslers [271], thin film Fe/Ir [272,273], FeCoB/Pt [274], and amorphous ferrimagnets such as $Gd_{44}Co_{56}$ [275]. These exciting results bring up possible applications of skyrmions in reliable high density information processing and storage, such as racetrack memory, where information is stored in magnetic domains and driven by a current, as has been demonstrated in magnetic nanowires [276].One of the challenges with racetrack memory is the pinning of domain wall at defect sites. Skyrmions can be manipulated by spin transfer torque or spin-orbit torque much like the magnetic domains, with the added advantages of smaller size and some amount of topological protection, reducing the threshold current for activation around defects [277]. However, the reported skyrmions are either too big ($\sim 100\,\mathrm{nm}$) or exist only at low temperatures [273]. Another issue is that the magnus force (from the chiral spin structure of skyrmion) swivels the skyrmions away from a linear trajectory towards the device edges for potential annihilation.

6.1.2 Skyrmion Type

The antisymmetric Dzyaloshinskii-Moriya interaction has the following general form (in the continuous limit) [278]:

$$M_i \frac{\partial M_j}{\partial \xi} - M_j \frac{\partial M_i}{\partial \xi} \tag{6.1}$$

where $M_{i,j}$ are the components of the magnetic moment $\mathbf{M} = (M_x, M_y, M_z)$ and ξ is a spacial coordinate (x, y, z). With different crystal symmetries, various kinds of magnetic skyrmions can be stablized (Neel skyrmion, Bloch skyrmion, and Antiskyrmion).

$$\begin{aligned}
E_{\mathrm{dm}}^{\mathrm{Neel}} &= D\mathbf{m} \cdot [(\hat{\mathbf{z}} \times \vec{\nabla}) \times \mathbf{m})] = \left(m_x \frac{\partial m_z}{\partial x} - m_z \frac{\partial m_x}{\partial x} \right) + \left(m_y \frac{\partial m_z}{\partial y} - m_z \frac{\partial m_y}{\partial y} \right) \\
E_{\mathrm{dm}}^{\mathrm{Bloch}} &= \left(m_z \frac{\partial m_y}{\partial x} - m_y \frac{\partial m_z}{\partial x} \right) + \left(m_x \frac{\partial m_z}{\partial y} - m_z \frac{\partial m_x}{\partial y} \right) + \left(m_y \frac{\partial m_x}{\partial z} - m_x \frac{\partial m_y}{\partial z} \right) \\
E_{\mathrm{dm}}^{\mathrm{Anti}} &= m_z \frac{\partial m_x}{\partial y} - m_x \frac{\partial m_z}{\partial y} + m_z \frac{\partial m_y}{\partial x} - m_y \frac{\partial m_z}{\partial x}
\end{aligned}$$

Fig. 6.1 shows the spin textures of those three types of skyrmions. Neel type skyrmions commonly exist from the broken inversion symmetry at the interface in heterostructures consisting of a thin magnetic film and a heavy metal over/under-layer. Bloch type skyrmions exist in non-centrosymmetric bulk materials such as B20 compounds (MnSi, FeGe, MnGe, and etc.). Antiskyrmions exist in systems with D_{2d} symmetry e.g. tetragonal inverse heuslers [271]. Our studies focus on the Neel type skyrmion in thin films.

6.2 Small and Stable Skyrmion in Inverse-Heusler

Based on Yunkun's analytical work [279], the conditions for hosting small and fast skyrmion has inspired us to look for ferrimagnetics/antiferromagnets in the Heusler family. The selection criteria include ferrimagnetic order (exists in Inverse Heusler) with small saturation magnetization, high

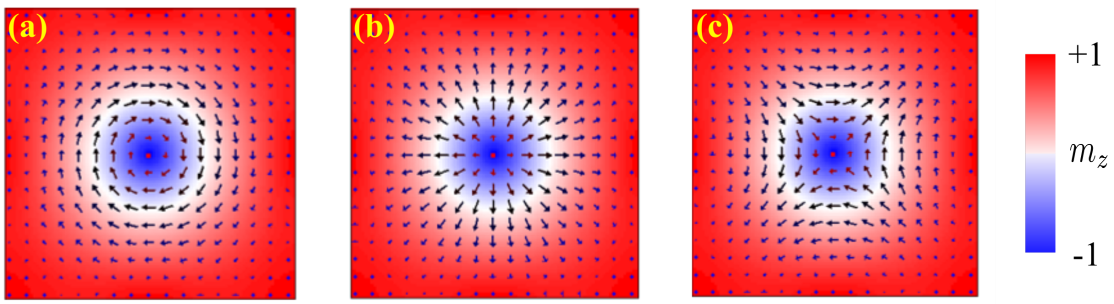

Figure 6.1: Different types of magnetic skyrmion spin texture (top view). The arrows show local spin direction and the color shows the z component of the spin. (a) Bloch type skyrmions. (b) Neel type (Hedgehog) skyrmion. (c) Anti-skyrmions. The figures are generated with public code OOMMF [4].

Neel temperature, anisotropy and potentially half-metallic bandstructures. Half-metals are known to have low magnetic damping due to the lack of electron states in one spin channel [280,281]. In the remainder of this chapter, we present half-metallic and near half-metallic ferrimagnets from previous high-throughput studies on the inverse Heuslers in chapter 4, along with detailed calculations of their magnetic properties.

6.2.1 Crystal structure

The Inverse-Heusler X_2YZ has a face-centered cubic structure with four atoms per cubic unit cell. Its crystal structure can be viewed as four interpenetrating FCC sublattices, occupied by the two X, Y and Z elements, respectively as shown in Fig. 6.2(a). We use X_1 and X_2 to distinguish these two X atoms sitting at the two nonequivalent sites. The tetragonal inverse-Heusler structure can be obtained by stretching or compressing the parent cubic structure along the z axis. We can define the tetragonality as c/a. The lattice constant a_c of the cubic structure can be obtained from a as $a_c = \sqrt{2}a$.

6.2.2 Computational Details

Fundamental electronic and magnetic properties of the Inverse Heusler familiy are investigated using the Vienna *Ab Initio* Simulation Package (VASP) [63,64] in our previous work [282]. Here we extend the investigations to include the exchange coupling and Gilbert damping via the framework of the Korringa-Kohn-Rostoker Greens function formalism, as implemented in the Munich spin-

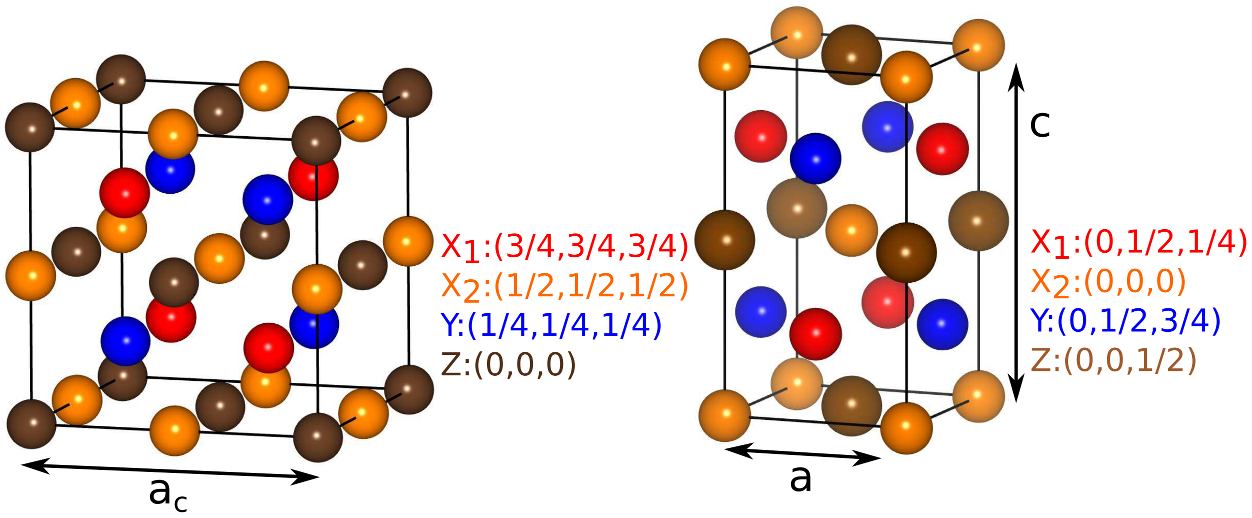

Figure 6.2: Schematic representation of (a) cubic Inverse-Heusler structure and (b) tetragonal Inverse-Heusler structure. X_1 and X_2 are the same transition metal element but they have different environments and magnetic moments. The tetragonal unit cell is rotated 45° around the z axis relative to the parent cubic structure.

polarized relativistic Korringa-Kohn-Rostoker (SPR-KKR) package [283]. Relativistic effects were taken into account by solving the Dirac equation for the electronic states, and the atomic sphere approximation (ASA) was employed for the shape of potentials. An angular momentum cutoff of $l_{max} = 3$ (corresponding to f-wave symmetry) was used in the multiple-scattering expansion. A k-point grid consisting of ∼1000 points in the irreducible Brillouin zone was employed in the self-consistent calculation, while a substantially denser grid of ∼300000 points was employed for the Gilbert damping calculation. To achieve convergence, we used the BROYDEN2 algorithm with the exchange-correlation potential of Vosko-Wilk-Nusair (VWN) [61].

6.2.3 Exchange interactions and Curie temperatures

Our previous studies on Inverse Heusler (chapter 3) and Half Heusler compounds (chapter 4) have predicted a series of experimentally feasible half-metals and near-half-metals, determined by the short distance to their respective convex hull of stable phases (less than 0.052 eV/atom for Inverse Heusler, less than 0.1 eV/atom for Half Heusler) [282,285]. In Table 6.1, we selected 9 Inverse Heusler candidates with hull distance less than 0.052 eV/atom. All of those compounds are ferrimagnets (with MnCrAs being antiferromagnet). Mn_2CoAl, Mn_2CoSi, and Mn_2CoGe are predicted half-metals.

Table 6.1: Structural and magnetic properties of Heusler compounds with low hull distance. Successive columns present: composition, calculated lattice constant, a_{Cal}, experiment lattice constant, a_{Exp}, saturation magnetization, M_S, formation energy ΔE_f, distance from the convex hull ΔE_{HD}, experiment Neel temperature, T_N(Exp), calculated Neel temperature T_N(Cal), calculated Gilbert damping at room temperature, α, and electronic ground state (Electronic ground state: M = nonmagnetic metal, HM = half-metal, NHM = Near half-metal). The last two columns show their potential tetragonal phase structure and energy difference from their cubic phase $\Delta E = E_{\text{cubic}} - E_{\text{tetragonal}}$.

	Cubic phase								Tetragonal phase	
XYZ	a_{Cal} (Å)	a_{Exp}	M_S (emu/cc)	ΔE_{HD} (eV/atom)	T_N(Exp) (K)	T_N(Cal)	α (10^{-3})	Electronic ground state	a, c (Å)	ΔE (eV/atom)
Mn_2CoAl	5.735	5.798 [206]	393.5	0.036	720 [206]	845	4.04	HM	3.76, 6.68	-0.05
Mn_2CoGa	5.76	5.86 [42]	389.1	0	740 [284]	770	2.18	NHM	3.71, 7.13	-0.0103
Mn_2CoSi	5.621		627.3	0.018		460	3.01	HM		
Mn_2CoGe	5.75	5.80 [42]	590.6	0.03		471	4.97	HM	3.75, 6.84	0.0144
Mn_2FeAl	5.75		195.3	0.008		380	8.14	NHM	3.67, 7.28	0.0026
Mn_2FeGa	5.79		198.5	0.018		496	7.37	NHM	3.68, 7.29	0.0331
Mn_2FeSi	5.60		424	0		71	3.98	NHM	3.56, 7.26	-0.071
Mn_2FeGe	5.72		399.1	0		210	3.04	NHM	3.62, 7.45	-0.0164
Mn_2CuAl	5.89		33.4	0.042		1145	1.84	Metal		
Mn_2CuGa	5.937		57.86	0.0208		1242	1.59	Metal		

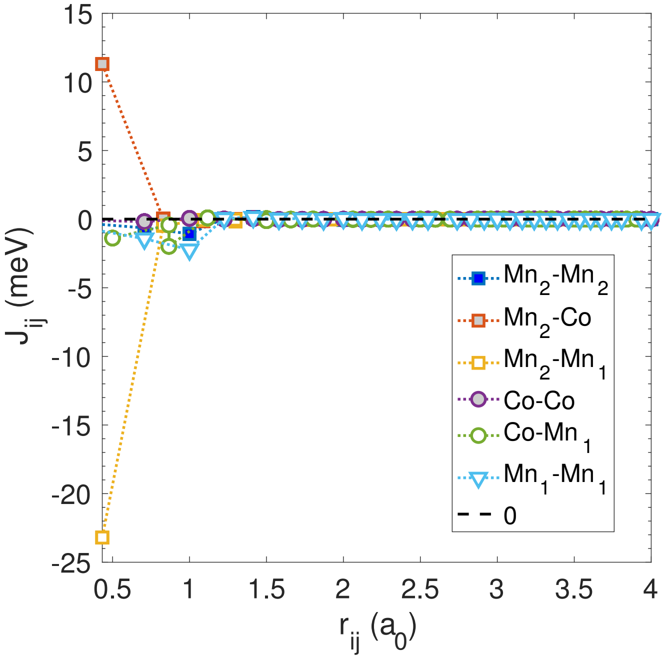

Figure 6.3: Intersublattice/intrasublattice Heisenberg exchange parameter as a function of renormalized interatomic distance for Mn_2CoGa. Different colors represents the coupling between different atomic sites.The subscript in the element denotes the site position same notations in Fig.6.2

Mn_2CoGa, Mn_2FeAl, Mn_2FeGa, Mn_2FeSi, Mn_2FeGe are predicted near-half-metals with real gap around the Fermi level. Mn_2CuAl and Mn_2CuGa are metals with pseudogap.

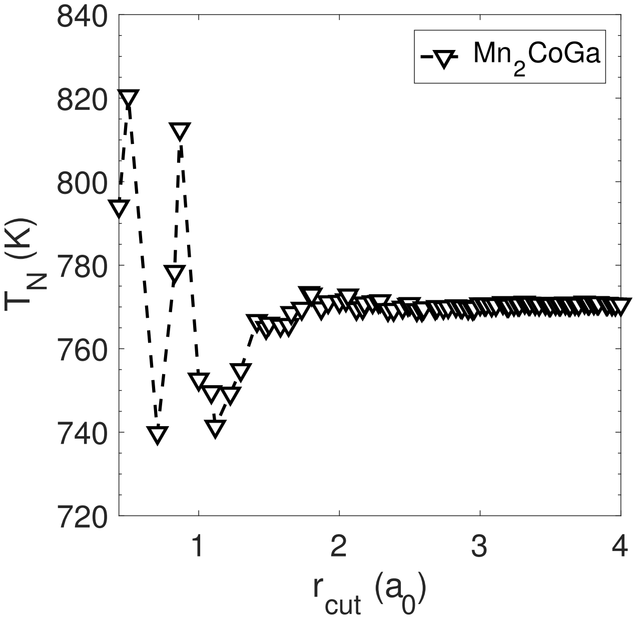

Figure 6.4: Neel temperature T_N as a function of the cluster radius taken into account.

Here we use Mn_2CoGa as example to describe the magnetic exchange coupling details (Fig.6.3). The magnetic exchange parameters decay very rapidly with the interatomic distance, r_{ij}, which is attributed to the existence of the spin gap in the minority-channel [286,287]. We can observe that the first nearest-neighbor interactions, Mn_1-Mn_2 and Mn_2-Co, are dominating, where the Mn_1-Mn_2 coupling is the stronger one. The second nearest-neighbor interactions Mn_1-Co is much weaker in comparison. In this figure, we omit the interaction with Z element, due to its tiny spin moment. The Mn_2 and Co couple antiferromagnetically to Mn_1, whereas Co and Mn_2 couple ferromagnetically. Thus, the antiparallel alignment of the Mn_1 moment is stable with respect to Mn_2 and Co. However, we also can observe that the exchange couplings beyond the second nearest neighbor site still do contribute to the system. We need to take all the J_{ij} in the plot into account for Neel temperature.

In Fig. 6.4 we show the calculated Neel Temperature in dependence on the cluster radius taken into account in Eq.2.54. As expected from the exchange-coupling plot in Fig. 6.3, T_N is not only determined by the first and second nearest neighbor interactions in compound. The temperature variation are observed with increasing cluster radius and it is finally converged around $r = 1.7a_0$. The final Neel Temperature is converged to be 770K, quite closed to the experimented $T_N = 740$ [284].

The other inverse-Heusler compounds also show similar behavior of J_{ij} with increasing interaction

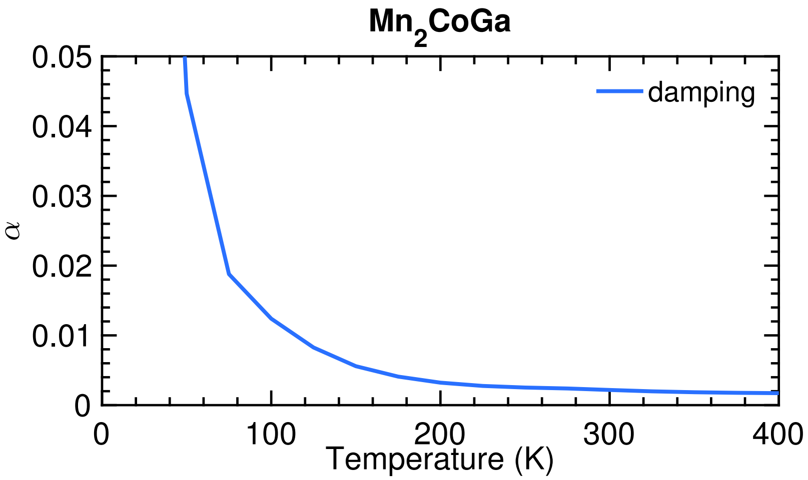

Figure 6.5: The temperature dependence of the calculated damping parameter α is shown for Mn$_2$CoGa

distance. The the first nearest-neighbor interactions, X_1-X_2 and X_2-Y, are dominating among all the interactions. But the difference in coupling strength results in the different Neel temperatures as shown in Table. 6.1. Mn$_2$CoAl, Mn$_2$CoGa, Mn$_2$CuAl, and Mn$_2$CuGa have Neel temperature much larger than the room temperature and two of those compounds have been confirmed with high Neel temperature in experiments [206, 284]. It is obvious that our mean field calculations seem to overestimate the Neel temperature compared to experimental values.

6.2.4 Gilbert damping

Based on my colleague Yunkun's calculation, ultra-small damping is also a important parameter to increase the current-driven skyrmion mobility. We further use SPRKKR to calculate the damping parameters for each inverse-Heusler compound.

We still use Mn$_2$CoGa as the example. Fig. 6.5 visualizes the dependency of the α with increasing temperature in detail. We can observe that the α steeply decreases in the low-temperature region initially. As the temperature keeps increasing, a regime with a weak variation of α with temperature is reached. This variation behavior is commonly explained as a transition from *conductivity-like* to *resistivity-like* behavior [288].

The breathing Fermi surface model of Kambersky offers a qualitative explanation for conductive-itylike contribution to damping in the low temperature region [289, 290]. The damping determined by conductiveity-like term increases linearly with the electron lifetime τ. Since the electron lifetime decreases with the increasing temperature, the damping is expected to diminishes. The physics driving the resistivity-like term is captured by Kambersky's torque-correlation model [291]. In this model, the interband spin-flip scattering is responsible for high-temperature dissipation and give the resistivity-like contribution, resulting the raising of α with increasing temperature. In the half-metallic Heusler compound, the proximity of the Fermi energy to the energy gap in the minority spin channel limits the interband spin-flip scattering at high temperature region. Besides, the intraband spin-flip contributions are limited at high temperature. The limited spin-flip scattering results in a small damping coefficient $10^{-4} \sim 10^{-3}$. Furthermore, the unoccupied minority band at E_F contributes to a lowered total density $D(E_F)$ can also reduce the damping from the equation $\alpha\xi^2 D(E_F)$ (ξ is the spinorbit coupling interaction) [292]. Similar low damping simulations and experimental results have been verified for the full-Heusler half-metal $\mathrm{Co_2MnSi}$ [293] and $\mathrm{Co_2MnGe}$ [294]. In table 6.1, we can see that all the candidates have relative low damping parameter in the order of 10^{-3} at the room temperature. This also enhances their potential for generating ultra-fast skyrmion.

Finally, we also calculated the tetragonal distorted structure for the 9 inverse-Heusler candidates, in order to look for intrinsic crystal anisotropy. Seven of them have local energy minima in the tetragonal phase. The energy differences between the cubic and the tetragonal phases are listed in table 6.1. Positive ΔE indicates the tetragonal phase is the global energy minima. It is worth mentioning that $\mathrm{Mn_2CoGa}$ has enhanced Neel temperature ($770\,\mathrm{K} \rightarrow 975\,\mathrm{K}$(tetragonal)) and a much reduced saturation magnetization ($389.1\,\mathrm{emu/cc} \rightarrow 27.6\,\mathrm{emu/cc}$(tetragonal)) in the tetragonal phase compared to its cubic phase, which makes it the most promising candidate among those in the table. For the cubic phase, an interface-induced anisotropy (or external field) is needed to achieve perpendicular magnetization.

6.3 Summary of Contribution

In this chapter, we we have scanned through the Heusler database and identified 9 promising candidates within the Inverse-Heusler family with desirable properties, i.e. low M_s ferrimagnet, low damping and high Neel temperature for hosting small skyrmions. We find that the first nearest neighbor exchange interactions between X_1-X_2 and X_2-Y dominate among all the interatomic interactions. But we still need to include all the exchange interactions within large cluster radius to achieve accurate the Neel temperature. We analyze the dependency of Gilbert damping with increasing temperature and find all the inverse-Heusler candidates have relative small damping around the room temperature.

Chapter 7

Conclusions and Future work

7.1 Conclusions

The work presented in this dissertation focuses on two major aspects. First, to predict which Heusler compounds can be stable to be synthesized as semiconductor, half-metal or near half-metal by using first-principle method. We demonstrate that the half-Heusler compound is easier to stabilize as a semiconductor and we suggest some novel candidates (CoVGe, FeVAs, RuVAs, CoVSn, RhVGe) for future experiments. However, only one experiment reported NiMnSb as a stable as half-metal in the database. So half-Heusler half-metal is expected to be synthesized difficultly. In comparison, we find a series of novel semiconductors in inverse-Heusler compounds, but they have quite large hull distance to be unstable. But we uncover five novel near-half-metals (Cr_2MnGa, Mn_2FeAl, Mn_2FeGa, Mn_2FeSi, Mn_2FeGe) that meet our criterion for stability. The inverse-Heusler can tend to be more stable as half-metal or near-half-metal in conclusion. We demonstrated the new possibility to fabricate novel electrode materials for tunneling magnetic junction with high TMR ratio. We give clear direction guidance for the future experimental work, and some experimentalists is try to fabricate our predicted candidates and some of them have been verified [203]. If Heusler-based MTJ can be verified with TMR ratio ¿ 300% at the room temperature, the performance of MRAM and hard disk drive would be improved significantly.

Second, try to identify the ideal candidate for further spintronics device application. The NiMnSb/MgO superlattice demonstrate the possibility to retain the half-metallicity and create interface anisotropy. The ballistic I-V curves show the resulting high TMR ratio in the Heusler MTJ.

But we need to realize the interface defect and impurity diffusion can prevent the half-metallicity in reality. The 9 stable ferrimagnetic inverse-Heusler candidates may open new opportunity to hosting ultrasmall and fast skyrmion, due to their low magnetization, high Neel temperature and low damping. It also gives a new opportunity and clear direction for experimentalist to fabricate novel skyrmion devices with low power, high information density and high speed. We can conclude that a further understanding and exploiting of Heusler compounds is much needed and this dissertation is just a starting point.

7.2 Future Work

There are numerous challenges in exploring new materials and developing new necessary technique to study them. The challenge we faced in our previous studies also point out the possible directions in the future. Here is an incomplete list of possible extension of work:

Symmetry analysis for Full Heusler compounds

The full-Heusler is also the important member in Heusler family. We need to finish up the structural stability discovery for the rest 576 full-Heusler compounds. Since full-Heusler compounds are easier to stabilize as ferromagnet, identifying more stable full-Heusler half-metals would be more significant for future MTJ structure. Until now, the group symmetry analysis for different bandstructure for inverse-Heusler and full-Heusler are still lacking. One can study the different behavior of d-orbitals for different elements between $L2_1$ and XA phase in the first-principle framework.

Magnetic Weyl semimetal in the Heusler compensated ferrimagnet

Weyl semimetals are recently discovered topological states in condensed matter physics that have attracted extensive interest due to their novel properties and potential applications in spintronics [295, 296]. Shi *et al.* predict a magnetic Weyl semimetal in the inverse Heusler Ti2MnAl, a compensated ferrimagnet with a vanishing net magnetic moment and a Curie temperature of over 650 K [297]. It demonstrates a new opportunity and direction to study the inverse-Heusler family. One can utilize the high-throughput method in our previous work to screen out the stable Weyl semimetals with a wider range of element choice.

Temperature dependent polarization of Half-metal based MTJs

Half-metals, with its theoretically 100% spin polarization, make perfect magnetic electrodes for the MTJs and our zero-temperature simulations seem to suggest the same. However, there are experimental evidence that shows the TMR reduces more dramatically with temperature in half-metal based MTJs. One possible explanation is the tilt of magnetic moment at the interface between the half-metallic layer and the tunnel barrier. The tilted moment destroys the half-metallicity by mixing spin-up/down channels. Exactly how much does this affect the performance of an MTJ and whether it is universal in all half-metal based MTJs are unknown. One can study this effect in the first-principle NEGF framework: e.g. by tilting the magnetic moment at the interface from its equilibrium position and calculates the TMR and STT. These calculations can reveal how much degradation we can expect from the room temperature environment.

DMI calculation for interface between Heusler compounds and heavy transition metal substrate

The Dzyaloshinskii-Moriya interaction (DMI) plays a crucial role in the generation of magnetic skyrmions in thin films. Although we have identified the ideal Heusler candidates for small and fast skyrmion in bulk cubic phase, it is necessary to estimate the interface DMI behavior for these candidates in the thin film structures, e.g. Mn2.5Ga/Pt. One can study the main features and microscopic mechanisms of DMI in Heusler/Pt bilayers via first principles calculations. It is important to figure out the thickness dependence of DMI variation to guide the further skyrmion manipulation experiment.

Appendices

Appendix A

Electronic Structure of Each Inverse-Heusler Compound

In this appendix we will briefly discuss each of the 405 XA compounds discussing gaps in their DOS, and whether they are half-metals or near-half-metals. The designation of half-metal is binary. If the Fermi energy lies in a gap for one of the spin-channels, but not for the other, then it is a half-metal. There may be other important quantitative questions such as the distances between the Fermi energy and the band edges, but the calculated band structure either corresponds to a half-metal or it does not. It should be noted that the determination of whether a given inverse-Heusler has a gap is not always trivial if the gap is small because the Brilliouin zone is sampled at a finite number of points. We used both the DOS calculated using the linear tetrahedron method and an examination of the bands along symmetry directions to decide difficult cases.

In contrast to the binary choice between half-metal or not, the designation of a "near-half-metal" is more qualitative. There are a couple of ways a calculated DOS could be "almost" half-metallic; (a) the Fermi energy could fall at an energy for which the DOS for one of the spin channels is very small, i.e. a pseudogap, (b) the DOS could have a gap in one of the spin channels with the Fermi energy lying slightly outside the gap. If we choose criterion (a) we must choose a threshold for "very small" and if we choose (b) we must choose a threshold for "slightly". Criterion (a) is difficult to implement because there are an infinite number of ways the DOS can vary near a pseudogap, e.g. a pseudogap may be wide and only fairly small or it might be narrow but extremely small or some combination. Another issue with criterion (a) is that a low density of states is often associated with a highly dispersive band that leads to a large conductivity. For these reasons, we choose criterion (b), i.e. we require that there be an actual gap and that the Fermi energy fall "near" this gap. The (arbitrary) criterion we choose for "near" is 0.2 electron states per formula unit. Other criteria could be used, e.g. the distance from the Fermi energy to the nearest band edge. Our choice of using the number of states has the advantage of being easily related to the magnetic moment. It has the disadvantage that occasionally a system with a highly dispersive band above or below the Fermi energy with a very small density of states can lead to a situation in which we label a system near-half-metallic when the Fermi energy is as much as 0.3 eV into the band.

For each of the systems, we note the gaps in the DOS, typically after 9, 12 or 14 states per formula unit per spin channel and whether the Fermi energy falls in one or more of the gaps or close enough to the gap (0.2 states) to be designated a near-half-metal. Simple state and electron counting dictates that to make a half-metal by taking advantage of a gap after N_s states when there are N electrons per formula unit, the magnetic moment per formula unit must be $N - 2N_s$.

13 electron systems: Our dataset contained 3 systems with 13 valence electrons, Sc_2Ti(Al,Ga,In). All three were magnetic metals with small gaps after 9 states per spin channel in both channels (except for Sc_2TiIn minority). However, the moments were not large enough (a total moment of 5 μ_B per formula unit would have been needed) to move the majority Fermi energy into the gap.

14 electrons systems: Our dataset contained 6 systems with 14 valence electrons, Sc_2Ti(Si,Ge,Sn) and Sc_2V(Al,Ga,In). These systems require a moment of 4 μ_B to place the Fermi energy in a majority gap after 9 electrons per spin channel.

Sc_2Ti(Si,Ge,Sn): Sc_2TiSi and Sc_2TiGe are predicted to be non-magnetic metals and to have small gaps after 9 states in both spin channels. Sc_2TiSn is predicted to be magnetic and to have a majority gap after 9 states, but its moment closer to 3 than 4 μ_B.

Sc_2V(Al,Ga,In): These all have relatively large gaps after 9 states in the majority channel. The position of the Fermi energy rises relative to the gap as the atomic size of the Z atom increases the lattice constant, facilitating the formation of large moments on V and even small moments on Sc. For Sc_2VAl and Sc_2VGa, the moment is not quite large enough to place the Fermi energy in the gap making them near-half-metals (Table 3.7). However, the lattice constant of Sc_2VIn *is* large enough to support a moment large enough to move the Fermi energy into the gap so it is a half-metal (Table 3.5).

15 electron systems: Our dataset contained 9 systems with 15 valence electrons, $Sc_2Ti(P,As,Sb)$, $Sc_2V(Si,Ge,Sn)$ and $Sc_2Cr(Al,Ga,In)$. A moment of 3 μ_B is needed to place the Fermi energy in a majority gap after 9 states.

$Sc_2Ti(P,As,Sb)$: These systems do not have gaps after 9 states per atom in either channel because of a reordering of the states at Γ. A singly degenerate state, usually band 10 at Γ, interchanges with a triply degenerate T_2 state so that bands 8, 9, and 10 are associated with the triply degenerate T_2 state, precluding a gap.

$Sc_2V(Si,Ge,Sn)$: These systems have majority gaps after 9 states. The Fermi energy is in the gap and they are classified as half-metals as described in Table 3.5.

$Sc_2Cr(Al,Ga,In)$: These systems all have large gaps after 9 states in majority and small gaps or pseudogaps near 9 states in minority. The Fermi energy falls in the majority gap for all three so they are classified as half-metals and described in Table 3.5.

16 electron systems: Our dataset contained 12 systems with 16 valence electrons per formula unit, $Sc_2V(P,As,Sb)$, $Sc_2Cr(Si,Ge,Sn)$, $Sc_2Mn(Al,Ga,In)$, and $Ti_2V(Al,Ga,In)$. For 16 valence electrons per formula unit and a gap after 9 states in the majority spin channel, a moment of 2 μ_B is needed to place the Fermi energy in the gap to make a half-metal.

$Sc_2V(P,As,Sb)$: Sc_2VP and Sc_2VAs have a region with an extremely low but non-zero DOS at the Fermi energy. These pseudogaps can be be traced to a band reordering similar to that mentioned previously in which a singly degenerate state at Γ drops below a triply degenerate state so that the triply degenerate state connects to bands 8, 9 and 10, thus precluding a gap. In the case of Sc_2VSb, the singly degenerate state is a few hundredths of an eV above the triply degenerate state so it is a near-half-metal with a tiny gap.

$Sc_2Cr(Si,Ge,Sn)$: These systems have large majority gaps after 9 states. They generated half-metals as described in Table 3.5.

$Sc_2Mn(Al,Ga,In)$: The three systems with X=Sc and Y=Mn have large majority and tiny minority gaps after 9 states. Their moments are very slightly less than 2 μ_B so they generated near-half-metals as described in Table 3.7 by placing the Fermi energy at the valence edge of the majority gap.

Ti_2V(Al,Ga,In): These systems have tiny majority and minority gaps after 9 states per spin channel. All take advantage of the majority gap to generate near-half-metals as shown in Table 3.7. Ti_2VIn is not included in the table because it has a positive formation energy.

17 electron systems: Our dataset contained 15 systems that had 17 electrons per formula unit, Sc_2Cr(P,As,Sb), Sc_2Mn(Si,Ge,Sn), Sc_2Fe(Al,Ga,In), Ti_2V(Si,Ge,Sn), and Ti_2Cr(Al,Ga,In). Systems with 17 electrons per formula unit can generate half-metals by taking advantage of a gap after 9 states in majority if their magnetic moment per formula unit is 1 μ_B.

Sc_2Cr(P,As,Sb): Sc_2CrP and Sc_2CrAs both have majority pseudogaps at the Fermi energy. The gap after 9 electrons per formula unit is converted into a pseudogap by a band reordering at Γ similar to that occurring for Sc_2V(P,As) and Sc_2Ti(P,As,Sb). Sc_2CrSb has a "normal" band ordering at Γ and is a near-half-metal similar to Sc_2VSb, but with a much larger gap.

Sc_2Mn(Si,Ge,Sn): These systems have majority gaps after 9 states and are all half-metals as described in Table 3.5. In addition to the majority gap Sc_2MnSi has a gap after 9 states in minority. A pseudogap near 9 states in minority for Sc_2MnSi can also be identified.

Sc_2Fe(Al,Ga,In): These systems have gaps after 9 states in both majority and minority channels. All three take advantage of the majority gap to generate near-half-metals as described in Table 3.7. Sc_2FeAl also has a minority pseudogap near 12 states and a majority pseudogap near 14 states.

Ti_2V(Si,Ge,Sn): These all have gaps after 9 states in both majority and minority with the majority gap being larger. All three compounds utilize the majority gap to form half-metals as described in Table 3.5.

Ti_2Cr(Al,Ga,In): These have gaps after 9 states in both spin channels. They are all near-half-metals (Table 3.7), having moments just large enough to satisfy our criterion. The large moment on the Cr atom opens a large gap in the majority channel (hybridization between Cr and Ti-d and with the Cr d-onsite energy well below that of the Ti atoms). The gap in minority is smaller and is dependent on the difference between the two Ti potentials and avoided band crossings.

18 electron systems: Our dataset contained 18 systems with 18 valence electrons. These were described in Section 4.4.

19 electron systems: Our dataset contained 21 systems with 19 valence electrons per formula unit, Sc_2Fe(P,As,Sb), Sc_2Co(Si,Ge,Sn), Sc_2Ni(Al,Ga,In), Ti_2Cr(P,As,Sb), Ti_2Mn(Si,Ge,Sn),

Ti_2Fe(Al,Ga,In), and V_2Cr(Al,Ga,In). Systems with 19 valence electrons need a moment of 1 μ_B to place the Fermi energy in a gap after 9 states in the minority channel.

Sc_2Fe(P,As,Sb): Sc_2FeP is non-magnetic with gaps after 9 states in both spin channels. Sc_2FeAs is also non-magnetic, but the gaps after 9 states are converted to pseudogaps by the inversion of singly and triply degenerate states at Γ similar to Sc_2CrP and Sc_2CrAs. The larger lattice constant of Sc_2FeSb allows it to develop a moment. There are sizeable gaps after 9 states in both the minority and majority channels, but the moment is not quite large enough (0.79 μ_B) to meet our criterion for calling it a near-half-metal.

Sc_2Co(Si,Ge,Sn): All three of these are half-metals with sizable gaps after 9 states in both spin channels (Table 4.2). The Fermi energy falls near the top of the gap, in all three cases but especially for Ge.

Sc_2Ni(Al,Ga,In): All three have sizable gaps after 9 states in both spin channels and moments as given in Table 4.3 that qualify them as near-half-metals.

Ti_2Cr(P,As,Sb): All three compounds have gaps in the minority channel after 9 states, but only and Ti_2CrAs and Ti_2CrSb have sufficiently large moments to be classified as near-half-metals. (Ti_2CrAs only barely made the cut-off.) Ti_2CrSb also has a tiny gap after 9 states in majority.

Ti_2Mn(Si,Ge,Sn): All three of these compounds have sizable gaps after 9 states in minority and much smaller gaps in majority. They also have pseudogaps near 12 states in minority. For all three, the Fermi energy falls in the gap so they are are included in Table 4.3.

Ti_2Fe(Al,Ga,In): All three of these compounds have gaps after 9 states in both channels and peseudogaps in both channels after 12 states. The gaps after 9 states are much smaller in majority than in minority. The Fermi energy for each of the three falls in the minority gap creating three half-metals as described in Table 4.2.

V_2Cr(Al,Ga,In): All three of these systems have gaps after 9 states in both spin channels. In all cases, however, the magnetic moment is not large enough to meet our criterion for a near-half-metal. The formation energy is small and negative for V_2CrAl and V_2CrGa. It is positive for V_2CrIn.

20 electron systems: Our dataset contained 24 compounds with 20 electrons per formula unit, Sc_2Co(P, As, Sb), Sc_2Ni(Si, Ge, Sn), Sc_2Cu(Al, Ga, In), Ti_2Mn(P, As, Sb), Ti_2Fe(Si, Ge, Sn), Ti_2Co(Al,Ga,As), V_2Cr(Si, Ge, Sn) and V_2Mn(Al, Ga, In).

Sc_2Co(P,As,Sb): Sc_2CoP and Sc_2CoAs both have gaps after 9 states per formula unit in both spin channels, but in both cases the net magnetic moment is much too small to pull the Fermi energy into one of the gaps. Sc_2CoSb, on the other hand, due to its larger lattice constant supports a moment sufficiently large (1.999 μ_B) that the Fermi energy falls at the top edge of the minority gap. We classify it as a near-half-metal (Table 4.3).

Sc_2Ni(Si,Ge,Sn): The compounds, Sc_2Ni(Si,Ge,Sn), all have gaps after 9 electrons in both spin channels. However, the total moment (1.80 μ_B, 1.81 μ_B, 1.84 μ_B respectively) does not reach the value (2.00 μ_B) needed to place the Fermi energy in the gap. Even when the lattice is expanded the magnetic moment of these Sc_2Ni(Si,Ge,Sn) compounds hardly increases because the d-bands of Ni are filled so that Ni only supports a very small moment in these materials. Nevertheless, these compounds meet (barely) our threshold to be called near-half-metals (Table 4.3).

Sc_2Cu(Al,Ga,In): The systems Sc_2Cu(Al,Ga,In) all have pseudogaps after 9 states in both spin channels.

Ti_2Mn(P,As,Sb):All three of these compounds have gaps after 9 electrons in both spin-channels. However only Ti_2MnSb (due to its larger lattice constant) has a moment (1.989 μ_B) close enough to 2 μ_B to be classified a "near-half-metal". Ti_2MnAs (1.7967 μ_B) barely misses the cut-off to be included in Table 4.3.

Ti_2Fe(Si, Ge, Sn): The compounds Ti_2Fe(Si,Ge,Sn) all have gaps in both channels after 9 states and pseudogaps after 12 states. The Fermi energy falls within the gap in all three cases so they are predicted to be half-metals as described in Table 4.2.

Ti_2Co(Al,Ga,As): The compounds Ti_2Co(Al,Ga,In) have large minority gaps after 9 states and somewhat smaller gaps after 9 states in majority. The Fermi energy falls within the minority gap in all three cases so they are are predicted to be half-metals as described in Table 4.2.

V_2Cr(Si,Ge,Sn):V_2CrSi has small gaps after 9 states in both spin channels, but is not magnetic. V_2CrGe is magnetic with a moment of 2 μ_B. The Fermi energy falls very close to the top of the gap, but V_2CrGe is predicted to be a half-metal as described in Table 4.2. V_2CrSn has a gap after 9 states in the majority channel which is not useful for generating a half-metal. There is no gap in minority.

V_2Mn(Al, Ga, In): V_2MnAl has a tiny majority gap and a sizable minority gap after 9 states. It also has pseudogaps after 12 states in majority and 14 states in minority. It takes advantage of the minority gap after 9 states to become a half-metal. The DOS for V_2MnGa is similar. It is also a half-metal. Both compounds are included in Table 4.2. V_2MnIn has a gap after 9 states in the majority, but only a pseudogap after 9 states in minority. Its large moment, in excess of $3\mu_B$, places the Fermi energy well below this pseudogap.

21 electron systems: Our database contains 27 systems with 21 valence electrons, Sc_2Ni(P,As,Sb), Sc_2Cu(Si,Ge,Sn), Sc_2Zn(Al,Ga,In), Ti_2Fe(P,As,Sb), Ti_2Co(Si,Ge,Sn), Ti_2Ni(Al,Ga,In), V_2Cr(P,As,Sb), V_2Mn(Si,Ge,Sn), V_2Fe(Al,Ga,In). Systems with 21 valence electrons are interesting because they can, in principle, place the Fermi energy in a gap after 9 electrons or a gap after 12 electrons or both. If a majority gap present after 12 states is present as well as a minority gap after 9 states, a moment of 3 μ_B would yield a magnetic semiconductor.

Sc_2Ni(P,As,Sb): Sc_2NiP has tiny gaps in both spin channels after 9 states while Sc_2NiAs has pseudogaps after 9 states in both spin channels. Both have very small moments. Sc_2NiSb has gaps after 9 states in both spin channels, but its moment (2.15 μ_B) is too small to place the Fermi energy in or near the gap.

Sc_2Cu(Si,Ge,Sn): All three of these compounds have gaps after 9 states in minority and much smaller gaps in majority. However their moments are too small to place the Fermi energy in the minority gap.

Sc_2Zn(Al,Ga,In): These three non-magnetic compounds only have pseudogaps after 9 states in both spin channels because of a highly dispersive band 10 which drops below band 9 along Γ to X.

None of the 21-electron systems with X=Sc generate half-metals or near-half-metals because a moment of 3 μ_B would be necessary to take advantage of a gap after 9 states per spin per formula unit or to take advantage of a gap after 12 states per spin per formula unit. The compounds are not able to do this because Sc is difficult to polarize and Ni, Cu and Zn cannot support a large moment because their d-bands are filled or (in the case of Ni) nearly filled.

Ti_2Fe(P,As,Sb): These three compounds have large gaps after 9 states in the minority channel and smaller gaps in the majority channel after 9 states. Ti_2FeP and Ti_2FeAs have pseudogaps after 12 states in the maority which becomes a very small real gap for Ti_2FeSb. The moments for the three are $2.72\mu_B$, $2.94\mu_B$ and $2.99\mu_B$ respectively. Ti_2FeAs and Ti_2FeSb meet our criterion for near-half-metallicity. If the moment for Ti_2FeSb were very slightly larger, we would predict it to be a magnetic semiconductor with a large minority gap and a tiny majority gap, i.e. a 9/12 magnetic semiconductor. The present prediction is for a magnetic semi-metal that has a pocket of down-spin electrons along Γ to K and a Γ-centered pocket of up-spin holes.

Ti_2Co(Si,Ge,Sn): These three compounds all have gaps in both spin channels after 9 states, with the minority gap being larger. Ti_2CoSi also has a majority pseudogap after 12 states. For all three, the Fermi energy falls within the minority gap giving each a moment of 3 μ_B and making them half-metals (Table 4.2). For Ti_2CoSi the current at zero K would be carried by up-spin holes at Γ and up-spin electrons at X.

Ti_2Ni(Al,Ga,In): These three compounds all have gaps after 9 states in both spin channels. The Fermi energy falls well inside the minority gaps yielding half-metals with moments of 3 μ_B in each case (Table 4.2).

V_2Cr(P,As,Sb): V_2CrP has gaps after 9 states in both spin channels, but is non-magnetic. V_2CrP has a gap in the minority channel after 9 states and a pseudogap after 9 states in the majority channel. Its moment is too small (1.85 μ_B) for it to be classified as a near-half-metal. V_2CrSb has a pseudogap after 9 states in the majority channel and a sizable gap after 12 states also in majority chanel. Its moment is large enough (2.89 μ_B) that we would classify it as a near-half-metal. However, its formation energy is positive so it is not included in Table 4.3.

V_2Mn(Si,Ge,Sn): V_2MnSi has pseudogaps after 9 states in both spin channels and is non-magnetic. V_2MnGe has gaps after 9 states in both spin channels and a pseudogap after 12 states in majority. Its moment of 2.81 μ_B qualifies it (barely) for inclusion with the near-half-metals in Table 4.3. V_2MnSn has majority gaps after 9 and 12 states and a pseudogap after 9 states in minority. It's moment of 2.96 μ_B qualifies it for inclusion in Table 4.3 as a Slater-Pauling near-half-metal.

V_2Fe(Al,Ga,In): V_2FeAl has gaps after 9 and 14 states in minority and after 12 states in majority. Its moment of 2.91 μ_B qualifies it as a "double near-half-metal" since its Fermi energy is near gaps after 9 states in minority and 12 states in majority. V_2FeGa has a gap after 9 states in minority and a pseudogap after 12 states in majority. Its moment of 2.85 μ_B meets the threshold for inclusion in Table 4.3 as a near-half-metal. V_2FeIn has gaps in both spin channels after 9 states and a pseudogap after 12 states in majority. Its moment is large enough for inclusion for inclusion in Table 4.3, but its formation energy is positive.

22 electron systems: Our database contains 27 systems with 22 electrons, Sc_2Cu(P,As,Sb), Sc_2Zn(Si,Ge,Sn), Ti_2Co(P,As,Sb), Ti_2Ni(Si,Ge,Sn), Ti_2Cu(Al,Ga,In), V_2Mn(P,As,Sb), V_2Fe(Si,Ge,Sn),

V_2Co(Al,Ga,As), and Cr_2Mn(Al,Ga,In). These systems would need a moment of 4 μ_B to place the Fermi energy into a gap after 9 states in the minority channel or a moment of 2 μ_B to place the Fermi energy into a gap after 12 states in the majority channel.

Sc_2Cu(P,As,Sb): The systems with X=Sc and Y=Cu generate only small moments (0.40, 0.62 and 0.79)μ_B for Z=P, As, and Sb respectively. They have gaps in both channels after 9 states and no gaps after 12 states.

Sc_2Zn(Si,Ge,Sn): The systems with X=Sc and Y=Zn also generate moments that are too small (0.55, 0.92 and 0.93 μ_B for Si, Ge, and Sn respectively). These systems have pseudogaps after 9 states in both spin channels, but no gaps after 12 states.

Ti_2Co(P,As,Sb): These three systems have gaps after 9 states in both spin channels, but their moments (2.20, 2.38, and 2.73)μ_B are much smaller than the 4 μ_B needed to place the Fermi energy in the minority gap.

Ti_2Ni(Si,Ge,Sn): These three systems have gaps after 9 states in both spin channels. Their moments are larger than those of the Ti_2Co(P,As,Sb) systems (3.47, 3.69 and 3.86μ_B) for Si, Ge and Sn respectively. Thus, Ti_2NiSn meets our threshold for inclusion in Table 4.3 as a near-half-metal.

Ti_2Cu(Al,Ga,In): Ti_2CuAl has gaps after 9 states in both spin channels, but its moment is too low (3.72 μ_B) to meet our criterion for near-half-metal status. Ti_2CuGa and Ti_2CuIn have gaps after 9 states in majority, but only pseduogaps after 9 states in minority.

The 22 electron systems with X=Ti and Y=Co, Ni or Cu tend to have gaps after 9 states per spin channel per formula unit in both spin channels. They do not have gaps after 12 states per spin channel, presumably because insufficient contrast can be generated between the d-onsite energies of the two Ti atoms. In most cases the moments are too small to place the Fermi energy in the minority gap after 9 states. The moments are largely on the Ti atoms and the moments tend to increase with the atomic number of the Y atom, increasing from Co to Ni to Cu, and with the size of the Z atom.

V_2Mn(P,As,Sb): V_2MnP has gaps after 9 states in both spin channels but a very small moment (0.59 μ_B) so it cannot take advantage of the minority gap to make a half-metal. V_2MnAs also has gaps after 9 states in both channels and a pseudogap after 12 states in the majority. Its moment of 1.97 μ_B places the Fermi energy close to the majority pseudogap after 12 states, but the absence of a real gap precludes its designation as a near-half-metal. V_2MnSb has a majority gap after 9 states, a minority pseudogap after 9 states and a majority gap after 12 states. Its moment of 1.9987 μ_B places the Fermi energy just below the majority gap after 12 states. Only its positive formation energy precludes its inclusion in Table 4.3.

V_2Fe(Si,Ge,Sn): All three compounds have gaps after 9 states in both spin channels. V_2FeGe also has a majority gap after 12 states and V_2FeSn has a pseudogap after 12 states in the majority channel. The moment of V_2FeGe (1.98 μ_B) places its Fermi energy quite close to the majority gap so it is a near-half-metal as described in Table 4.3.

V_2Co(Al,Ga,As): All three of these compounds have gaps in both channels after 9 states with the minority gap being much larger than the small majority gap. All three also have pseudogaps after 12 states in the majority. The pseudogap for V_2CoAl is particularly pronounced. The moment is slightly less than 2 μ_B for all three compounds, but according to our definition, they are not near-half-metals.

Cr_2Mn(Al,Ga,In):Cr_2MnAl and Cr_2MnGa both have gaps after 12 states in the majority channel. Cr_2MnIn only has a pseudogap there. Cr_2MnAl is a half-metal as described in Table 4.2 and Cr_2MnGa is a near-half-metal as described in Table 4.3. All three of these compounds are predicted to have ferrimagnetic states in which the moments of Cr_1 and Mn are aligned, and the moment of Cr_2 is opposite.

23 electron systems: Our database contains 27 systems with 23 electrons, Sc_2Zn(P,As,Sb), Ti_2Ni(P,As,Sb), Ti_2Cu(Si,Ge,Sn), Ti_2Zn(Al,Ga,In), V_2Fe(P,As,Sb), V_2Co(Si,Ge,Sn), V_2Ni(Al,Ga,In), Cr_2Mn(Si,Ge,Sn), and Cr_2Fe(Al,Ga,In). These compounds can take advantage of a gap after 9 states in minority to make a half-metal, but a moment of 5 μ_B would be needed. Alternatively, they could take advantage of a gap after 12 states in majority which would only require a moment of 1 μ_B. A few of these systems have pseudogaps after 14 states. In principle, one could have a 23 electron inverse-Heusler magnetic semiconductor with a moment of 5 μ_B that uses gaps after 9 states in minority and 14 states in majority; however such solutions did not appear in our database.

Sc_2Zn(P,As,Sb): The three systems Sc_2Zn(P,As,Sb) have pseudogaps after 9 states in both channels. They are all non-magnetic and have no gaps after 12 sates.

Ti_2Ni(P,As,Sb): These compounds all have gaps after 9 states in both spin-channels, but their moments are much too small to make half-metals or near-half-metals.

Ti_2Cu(Si,Ge,Sn): The three systems Ti_2Cu(Si,Ge,Sn) have gaps in both channels after 9 and pseudogaps in majority after 14 states. Their moments, however (3.00, 3.16, and 3.33)μ_B are much less than the 5 μ_B that would be needed to place the Fermi energy in the minority gap.

Ti_2Zn(Al,Ga,In): These compounds all have pseudogaps near 9 states per formula unit in the minority channel but no gaps at 9 or 12 states nor is the Fermi energy near the pseudogap. Ti_2ZnAl and Ti_2ZnGa also have majority gaps after 9 states and Ti_2ZnAl also has a pseudogap after 14 states in majority.

V_2Fe(P,As,Sb): These compounds have gaps in both spin channels after 9 states. V_2FeP and V_2FeAs have pseudogaps in the majority channel after 12 states. V_2FeSb, however does have a majority gap after 12 states and the magnetic moment (0.9996 μ_B) places the Fermi energy at the lower edge of this gap. V_2FeSb is not included in Table 4.3 because it has a positive formation energy.

V_2Co(Si,Ge,Sn): These compounds have gaps after 9 states in both channels, but only pseudogaps after 12 states except for V_2CoSi which has a tiny gap after 12 states. The Fermi energy falls just below this gap (moment = 0.997 μ_B). (See Table 4.3.)

V_2Ni(Al,Ga,In): These compounds have sizable gaps after 9 states in both spin channels, but the moments are small ($\approx 1\mu_B$) and there are no gaps after 12 states in the majority channel, hence no half-metals or near-half-metals.

Cr_2Mn(Si,Ge,Sn): Cr_2MnSi has a gap after 9 states in the majority channel and a pseudogap after 9 states in minority. Cr_2MnGe has a pseudogap after 9 states in majority and a sizable gap after 12 states in majority. Its moment of 0.99 μ_B allows it to use this gap to become a near-half-metal (Table 4.3). Cr_2MnSn also has a majority gap after 12 states and a moment of approximately 1.00 μ_B so it is a near-half-metal, but it is not included in Table 4.3 because its formation energy is positive.

Cr_2Fe(Al,Ga,In): Cr_2FeAl has minority gaps after 9 states and 14 states, and a majority pseudogap near 12 states. Its moment of approximately 1.00 μ_B places the Fermi energy into this peseudogap. Cr_2FeGa has a minority pseudogap after 9 states and a majority gap after 12 states. Its moment of 0.98 μ_B makes it a near-half-metal, but it is not included in Table 4.3 because its formation energy is positive. Cr_2FeGa has a majority pseudogap near 12 states.

24 electron systems: Our database contained 24 systems with 24 valence electrons, Ti_2Cu(P,As,Sb), Ti_2Zn(Si,Ge,Sn), V_2Co(P,As,Sb), V_2Ni(Si,Ge,Sn), V_2Cu(Al,Ga,In), Cr_2(P,As,Sb), Cr_2Fe(Si,Ge,Sn), Cr_2Co(Al,Ga,In). Based on electron count alone, these systems would offer the opportunity for non-magnetic semiconductors or zero net moment half-metals arising from Slater-Pauling gaps after 12 states per formula unit in one or both spin-channels. In practice, we find that only four of the 24 systems display Slater-Pauling gaps (and only in one spin-channel). In all four of these systems the Fermi energy falls at the edge of the gap but just outside so that they would be classified as near-half-metals. Three of these four near-half-metals have positive formation energy.

The gaps after 9 states, on the other hand, seem to be more robust. Only Cr_2MnSb failed to show a gap or a pseudogap after 9 states in at least one of the spin channels. Most systems showed gaps after 9 states in both spin channels. However, none of the systems were able to generate a moment of 6 μ_B that would have been necessary to use one of the gaps after 9 states to generate a half-metal.

Ti_2Cu(P,As,Sb): These systems showed gaps in both channels after 9 states, but their moments were much too small to place the Fermi energy near the minority gap.

Ti_2Zn(Si,Ge,Sn): These systems showed pseudogaps in both channels near 9 states per formula unit. The gaps were converted to pseudopgaps by a highly dispersive band 10 along Γ to X dropping down below the maximum of bands 7-9 at Γ.

The 9 systems in our database with X=V all showed gaps after 9 states in both spin channels. In all cases, the moments were quite small so that the Fermi energy could not fall into these gaps. Six of the 9 systems, V_2Co(P,As,Sb) and V_2Ni(Si,Ge,Sn) have pseudogaps around 12 states per atom in at least one spin channel.

V_2Co(P,As,Sb): These systems show gaps after 9 states and pseudogaps after 12 states in both spin channels. The moments are too small (V_2CoSb) or zero precluding half-metals.

V_2Ni(Si,Ge,Sn): V_2NiSi has gaps in both spin channels after 9 states and pseudogaps after both spin channels after 12 states. V_2NiGe has gaps in both spin channels after 9 states and a marginal pseudogap after 12 states in majority. V_2NiSn has gaps after 9 states in both spin channels and pseudogaps after 12 states in minority and after 14 states in majority. The lack of real gaps after 12 states and their very small moments preclude half-metals.

V_2Cu(Al,Ga,In): These compounds have gaps after 9 states in both spin channels and minority gaps after 14 states. V_2CuIn also has a majority gap after 14 states while V_2CuAl and V_2CuGa have pseudogaps in majority near 14 states. Their small moments and the absence of gaps after 12 states preclude half-metals.

Cr_2Mn(P,As,Sb): In the minority channel, Cr_2MnP has a gap after 9 states and a pseudogap near 12 states. It also has a pseudogap near 9 states in majority. It has a small moment placing the Fermi energy in the minority pseudogap near 12 states. Cr_2MnAs has minority gaps after 9 and 12 states. The very small moment (0.005 μ_B)places the Fermi energy just below the gap at 12 states. Thus Cr_2MnAs is a near-half-metal, but it is not included in Table 3.7 because its calculated formation energy is positive. Cr_2MnSb has a minority gap after 12 states. Its tiny moment (0.0002 μ_B) makes it a near-half-metal, but it is not included in Table 3.7 because its formation energy is positive.

Cr_2Fe(Si,Ge,Sn): Cr_2FeSi is non-magnetic and has gaps after 9 states in both channels. Cr_2FeGe has gaps in both spin channels after 9 states and a minority gap after 12 states. Its small moment makes it a near-half-metal, but we do not list it in Table 4.3 because of its positive formation energy. Cr_2FeSn has a majority gap after 9 states and a minority gap after 12 states. Its small moment places the Fermi energy somewhat below this gap yielding a near-half-metal. It is not listed in Table 4.3 because of its positive formation energy.

Cr_2Co(Al,Ga,In): These systems all have gaps after nine states in the majority channel and all have gaps (Al,Ga) or pseudogaps (In) in the minority channel after 12 states. All three have tiny moments. Cr_2CoAl and Cr_2CoGa are near-half-metals, but only the former has a negative formation energy. Cr_2CoAl is the only Slater-Pauling 24 electron near-half-metal with negative formation energy in Table 4.3.

25 electron systems: Ti_2Zn(P,As,Sb), V_2Ni(P,As,Sb), V_2Cu(Si,Ge,Sn) V_2Zn(Al,Ga,In), Cr_2Fe(P,As,Sb), Cr_2Co(Si,Ge,Sn), Cr_2Ni(Al,Ga,As), Mn_2Fe(Al,Ga,As). Many of the 25 electron inverse-Heusler systems show gaps after 9 states per formula in one or both spin-channels. None of these systems, however, are able to take advantage of these gaps to make a half-metal or near-half-metal by moving the Fermi energy to the gap, because that would require a relatively large moment (7 μ_B per formula unit). This large moment would be difficult to produce in systems whose transition metal elements come from the early or late part of the transition metal series, e.g. X=Ti or V and Y=Ni, Cu or Zn. The systems that could produce such large moments, e.g. X=Cr or Mn and Y=Fe or Co seem to prefer smaller net moments closer to 1 μ_B which allows them to take advantage of gaps and pseudogaps after 12 states per formula unit. Several systems show gaps after 14 states, but none of these have the correct moment (3 μ_B) to make a half-metal.

Ti_2Zn(P,As,Sb): All three compounds have gaps after 9 states in both spin channels, but their moments are too small to move the Fermi energy near these gaps.

V_2Ni(P,As,Sb): All three compounds have gaps after 9 states in both spin channels, but their moments are too small to move the Fermi energy near these gaps.

V_2Cu(Si,Ge,Sn): All three compounds have gaps after 9 states in both spin channels. V_2CuSn also has gaps after 14 electrons in both spin channels. In all three cases, the moments are too small to move the Fermi energy near the minority gap after 9 states or the majority gap after 14 states.

V_2Zn(Al,Ga,Sb): V_2ZnAl has a gap after 14 states in majority and a pseudogap after 14 states in minority. V_2ZnGa has a pseudogap after 14 states in majority and a gap after 14 states in minority. V_2ZnIn has a gap in both spin channels after 14 states. Their small moments preclude half-metals or near-half-metals.

Cr_2Fe(P,As,Sb): Cr_2FeP has gaps in both spin channels after 9 states and a pseudogap in minority after 12 states. Cr_2FeAs has gaps in both spin channels after 9 states and a sizable gap in minority after 12 states. Cr_2FeSb has a gap after 9 states in majority and a pseudogap after 9 states in minority. It also has a gap after 12 states in minority. All three have moments of approximately 1.01 μ_B which places the Fermi energy near the gap or pseudogap at 12 states. Cr_2FeAs and Cr_2FeSb are near-half-metals, but are not included in Table 4.3 because of their positive formation energies.

Cr_2Co(Si,Ge,Sn): Cr_2CoSi has gaps in both spin channels after 9 states and a minority gap after 12. Cr_2CoGe has a majority gap after 9 states and a minority gap after 12 states. Both of these systems are predicted to be near-half-metals as described in Table 4.3. Cr_2CoSn has a majority gap after 9 states and a pseudogap in minority near 12 states.

Cr_2Ni(Al,Ga,In): Cr_2NiAl has gaps after 9 and 14 states in majority and after 12 states in minority. It uses the gap after 12 states in minority to generate a half-metal as described in Table 4.2. Cr_2NiGa has gaps after 9 states in majority and after 14 states in minority. It also has a pseudogap near 12 states in minority. Cr_2NiIn has a gap after 9 states in majority and a pseudogap near 12 states in minority.

Mn2Fe(Al,Ga,In): Mn_2FeAl and Mn_2FeGa both have gaps after 9 states in majority and after 12 states in minority. Both place the Fermi energy slightly below the minority gap to generate near-half-metals as described in Table 4.3. In Mn_2FeIn, the minority gap after 12 states becomes a pseudogap. It also has minority gaps after 9 states and after 14 states.

26 electron systems: V_2Cu(P,As,Sb), V_2Zn(Si,GeSn), Cr_2Co(P,As,Sb), Cr_2Ni(Si,Ge,Sn), Cr_2Cu(Al,Ga,In), Mn_2Fe(Si,GeSn), Mn_2Co(Al,Ga,As). Many of the 26 electron systems show gaps after 9 states, some show gaps after 12 states and a few show gaps after 14 states. None of these systems can generate the 8 μ_B moment needed to generate a half-metal using the gap after 9 states. Several, however, can generate the moment of 2 μ_B needed to generate a half-metal or near-half-metal by using a minority gap after 12 states. A moment of 2 μ_B would also be consistent with a half-metal taking advantage of a a majority gap after 14 states. In principle, a majority gap after 14 states and a minority gap after 12 combined with a moment of 2 μ_B could lead to a magnetic semiconductor. Mn_2CoAl comes close to this situation.

V_2Cu(P,As,Sb) have gaps in both spin channels after 9 states and are non-magnetic. V_2CuSb also has pseudogaps in both spin-channels after 14 states.

V_2Zn(Si,Ge,Sn) have only pseudogaps near 9 states and are also non-magnetic. None of the 26 electron systems with X=V are predicted to be half-metals or near-half-metals.

Cr_2Co(P,As,Sb) have majority gaps after 9 states and minority gaps after 12 states. Cr_2CoP also has a small minority gap after 9 states that becomes a pseudopgap for Cr_2CoAs and Cr_2CoSb. Cr_2CoP is a half-metal with a moment of 2 μ_B. Cr_2CoAs and Cr_2CoSb are near-half-metals with moments of 2.0047 and 2.0016 μ_B respectively, however they are omitted from Table 4.3 because of their positive formation energy.

Cr_2Ni(Si,Ge,Sn) are remarkable for the large gaps after 9 states in the majority channel. Cr_2NiSi and Cr_2NiGe also have smaller gaps after 9 states in the minority channel. Cr_2NiSi and Cr_2NiGe also have gaps after 12 states in minority. The Fermi energy falls just above these gaps after 12 states giving moments of 1.89 and 1.94 μ_B respectively. Cr_2NiGe also has a minority gap after 14 states. Cr_2NiSn has a single gap after 9 states in the majority channel and a relatively small moment (0.83 μ_B). Cr_2NiSi and Cr_2NiGe satisfy our criteria for near-half-metals and are listed in Table 4.3.

Cr_2Cu(Al,Ga,In) all show gaps after 9 states in both spin channels. In addition Cr_2CuAl has gaps after 14 states in both channels while Cr_2CuGa has gaps after 14 states in the minority channel. For all cases, however, the net moments are too small to place the Fermi energy near any of the gaps. These three systems are ferrimagnets with relatively large anti-aligned moments on the two Cr atoms.

Mn_2Fe(Si,Ge,Sn)all have minority gaps after 12 states. Mn_2FeSi and Mn_2FeSn also have pseudogaps after 9 states in majority while Mn_2FeGe has a gap after 9 states in minority. The moments (2.008 μ_B, 2.016 μ_B and 1.999 μ_B) are the right size to make all three of these systems near-half-metals (Table 4.3); however the formation of Mn_2FeSn is positive.

Mn_2Co(Al,Ga,In) tend to have minority gaps (Al,Ga) or pseudogaps (In) after 12 states and their net moments tend to be large enough to take advantage of these gaps to make near-half-metals. Thus Mn_2CoAl is a half-metal (Table 4.2) and Mn_2CoGa is a near-half-metal(Table 4.3).

In addition to the gap in the minority channel after 12 states that Mn_2CoAl utilizes to make itself a half-metal, it also has a slightly negative gap in the majority channel, *i.e.* a very slight overlap between bands 14 and 15. The maximum of band 14 at the Γ point is only slightly higher than the minimum of band 15 at the X point. This situation has led some to refer this system as a "spin-gapless semiconductor" [209, 298]. In our calculation and also that of Ouardi *et al.* [206] it is a semi-metal rather than a semiconductor.

27 electron systems: The 21 systems in our database comprise: V_2Zn(P,As,Sb), Cr_2Ni(P,As,Sb), Cr_2Cu(Si,Ge,Sn), Cr_2Zn(Al,Ga,In), Mn_2Fe(P,As,Sb), Mn_2Co(Si,Ge,Sn), Mn_2Ni(Al,Ga,As). A system with 27 electrons could take advantage of a minority gap after 12 states to make a half-metal with a moment of 3 μ_B or a majority gap after 14 states to to make a half-metal with a moment of 1 μ_B.

V_2Zn(P,As,Sb): All three have gaps after 9 states in both spin channels. V_2ZnP is non-magnetic while V_2ZnAs and V_2ZnSb have relatively small moments on the V sites with ferrimagnetic alignment.Because their moments are small and there are no gaps after 12 or 14 states, these systems are very far from being half-metals.

Cr_2Ni(P,As,Sb): These three systems all generate large gaps after 9 states in the majority channel, and gaps after 12 states and after 14 states in the minority channel. The gaps after 14 states cannot be used to generate a half-metal because they are in the minority channel. The gaps after 12 states could be used to make half-metals or near-half-metals but the net moments are too small (2.03 μ_B, 1.69 μ_B and 1.29 μ_B respectively) for the Fermi energy to be near the gap.

Cr_2Cu(Si,Ge,Sn): These three systems generate gaps after 9 states in both channels and gaps (Si and Ge) or pseudogaps (Sn) after 14 states in the minority channel . There are no gaps after 12 states. The moments are too small to take advantage of the gaps after 9 states and the gaps after 14 states are in the wrong channel to be useful for making half-metals.

Cr_2Zn(Al,Ga,In): These systems only generate gaps after 14 states; Cr_2ZnAl in both channels, Cr_2ZnGa in the minority and for Cr_2ZnIn there are no gaps. The one opportunity for making a half-metal is the majority channel of Cr_2ZnAl, but the net moment is somewhat smaller (0.706 μ_B) than the 1.0 μ_B needed to make a half-metal. Pseudogaps near 9 states can be identified in both majority and minority of all three.

Mn_2Fe(P,As,Sb): These systems all generate gaps after 12 states in the minority channel and the moments have the correct value (3 μ_B)to generate half-metals (Table 4.2). The predicted half-metal, Mn_2FeSb is omitted from Table 3.5 because it is predicted to have positive formation energy. These systems are also predicted to have pseudogaps around 9 states in both majority and minority. Mn_2FeP has a small gap after 9 states in minority.

Mn_2Co(Si,Ge,Sn): These systems all generate gaps after 12 states in the minority channel. For Mn_2CoSi and Mn_2CoGe the moment is large enough (3 μ_B)to generate a half-metal (Table 4.2). The moment of Mn_2CoSn is too small to generate a gap. There are also gaps after 9 states in majority for Mn_2CoSi and Mn_2CoGe. This gap becomes a pseudogap for Mn_2CoSn.

Mn_2Ni(Al,Ga,As): No gaps are predicted for these three systems. Mn_2NiAl and Mn_2NiGa have pseudogaps around 14 states.

28 electron systems: The 18 systems with 28 valence electrons in our dataset comprise: Cr_2Cu(P,As,Sb), Cr_2Zn(Si,Ge,Sn), Mn_2Co(P,As,Sb), Mn_2Ni(Si,Ge,Sb), Mn_2Cu(Al,Ga,In), and Fe_2Co(Al,Ga,In). In principle, these systems could take advantage of gaps after 14 electrons to make zero moment half-metals or semiconductors, however we found no examples of such an electronic structure in a system with negative formation energy. They can also take advantage of a minority gap after 12 states to make half-metals with moments of 4 μ_B per formula unit. We found three examples of this type of electronic structure.

Two systems Cr_2Cu(P,As,Sb): These systems all have sizable gaps in majority after 9 states and smaller gaps in minority after 9 states. Cr_2CuP has a pseudogap after 14 states in minority and Cr_2CuSb has a minority pseudogap after 14 states. The moments are small.

Cr_2Zn(Si,Ge,Sn): These systems have pseudogaps near 9 states per formula unit in both spin channels. Cr_2ZnSi and Cr_2ZnGe have gaps after 14 electrons. Cr_2ZnSi has gaps in both channels so that it is predicted to be a ferrimagnetic semiconductor with zero net moment and two different gap widths. The smaller gap is a direct gap at the L point and is on the order of 0.02 eV so that XA phase Cr_2ZnSi could be called a "spin gapless semiconductor". Cr_2ZnGe only has a gap after 14 states in one spin channel. Its net moment is almost zero (0.0004 μ_B) so that it is predicted to be a near-half-metal. Unfortunately, both of these interesting systems are predicted to have positive formation energy and hull distances in excess of 0.3 eV/atom.

Mn_2Co(P,As,Sb): Mn_2CoP and Mn_2CoAs have gaps in both channels after 9 states. All three systems have gaps after 12 states in minority. All three have the requisite moment (4 μ_B) to generate half-metals and are listed in Table 4.2. We include details about the calculated Mn_2CoSb XA-phase in Table 4.2 even though its calculated formation energy is positive because of the controversy over the experimentally observed phase as discussed in Section 4.3.1.

Mn_2Ni(Si,Ge,Sb): These systems all have minority gaps after 12 states. Mn_2NiSi and Mn_2NiGe also have majority pseudogaps near 9 states. The moments on these systems are all too small to take advantage of the minority gap after 12 states.

Mn_2Cu(Al,Ga,In): One can identify pseudogaps near 9 states in majority in Mn_2CuAl and Mn_2CuGa along with a tiny gap after 9 states in minority in Mn_2CuGa. One can also identify pseudogaps near 14 states in both majority and minority in Mn_2CuAl.

Fe_2Co(Al,Ga,In): These systems have minority gaps after 9 states. Pseudogaps near 12 minority states can also be identified above the Fermi energy in all three systems. Even if there were a minority gap after 12 states, the moments in these systems would be too large to take advantage of it.

29 electron systems: Our database contained 18 systems with 29 valence electrons per formula unit: Cr_2Zn(P,As,Sb), Mn_2Ni(P,As,Sb), Mn_2Cu(Si,Ge,Sn), Mn_2Zn(Al,Ga,In), Fe_2Co(Si,Ge,Sn), and

Fe_2Ni(Al,Ga,In). In principle, a system with 29 electrons per formula unit could utilize a minority gap after 9, 12, or 14 states together with moments of 9 μ_B, 5 μ_B, or 1 μ_B respectively, to make a half-metal. In practice we only find one 29 electron half-metal, Mn_2CuSi, with a moment of 1 μ_B.

Cr_2Zn(P,As,Sb): These systems all showed gaps after 9 states and 15 states in the minority channel. Cr_2ZnP also has a gap after 9 states in the majority channel and a pseudogap after 14 states in minority. Cr_2ZnAs also has a pseudogap near 9 states and a gap after 14 states in majority. In principle the gap after 14 states in the majority could be utilized to make a half-metal, but the moment is too small (0.47 μ_B). Cr_2ZnSb has in addition to the minority gaps after 9 and 15 states, a pseudogap near 9 states in majority. The gap after 15 states observed in the minority channel of Cr_2Zn(P,As,Sb) is unusual and can be traced to a singly degenerate state at Γ that is usually band 15 or band 17 dropping below a triply degenerate state.

Mn_2Ni(P,As,Sb): These three systems have gaps (Mn_2NiP) or pseudogaps (Mn_2Ni(As,Sb)) near 12 states in the minority channel, but the moments are all much less than the 5 μ_B that would be necessary to make a half-metal. In addition, pseudogaps near 9 states in majority and 14 states in minority can be identified for Mn_2NiP.

Mn_2Cu(Si,Ge,Sn): all have gaps after 9 states in both the majority and minority channels. Mn_2CuSi also has a minority pseudogap near 12 states and a minority gap after 14 states. The system uses the minority gap after 14 states to make a half-metal (Table 4.2).

Mn_2Zn(Al,Ga,In): all have small moments and no gaps. Pseudogaps in both channels near 9 states can be identified.

Fe_2Co(Si,Ge,Sn): all have moments near 5 μ_B. However instead of gaps after 12 states in minority there are pseudogaps. All three have gaps after 9 states in minority. Fe_2CoSi also has a pseudogap near 9 states in majority.

Fe_2Ni(Al,Ga,In): also all have moments near 5 μ_B, but the only gaps are after 9 states in the minority channel. Fe_2NiAl has a minority pseudogap near 12 states and majority pseudogaps near 14 and 16 states. Fe_2NiGa has majority pseudogaps near 9 states and 16 states.

30 electron systems: The 15 systems in our database with 30 electrons are: Mn_2Cu(P,As,Sb), Mn_2Zn(Si,Ge,Sn), Fe_2Co(P,As,Sb), Fe_2Ni(Si,Ge,Sn), and Fe_2Cu(Al,Ga,In). In principle gaps after 14, 12, or 9 states could be used to make half-metals with moments of 2 μ_B , 6 μ_B or 12 μ_B

respectively. In practice we find one negative-formation-energy near-half-metal with a moment near 2 μ_B.

Mn_2Cu(P,As,Sb): These all have gaps after 9 states in both majority and minority. Mn_2CuP also has a gap after 14 states in the minority channel. The moment is nearly 2 μ_B which makes it a near-half-metal.

Mn_2Zn(Si,Ge,Sn): These systems have pseudogaps in both spin channels near 9 states. Mn_2ZnSi also has a gap after 14 electrons in the minority channel and a spin moment of exactly 2 μ_B which makes it a half-metal. Unfortunately, its calculated formation energy is positive. Mn_2ZnGe and Mn_2ZnSn do not have gaps in the DOS at the experimental lattice constant. If, however, their lattices are significantly contracted, the gap after 14 states reappears and the Fermi energy falls into the gap.

Fe_2Co(P,As,Sb): These all have gaps after 9 electrons in the minority channel and pseudogaps near 12 states also in the minority channel. The moments are large enough (5.76 μ_B, 5.95 μ_B, 5.93 μ_B respectively) to place the Fermi energy in the vicinity of the 12 state pseudogap, but because there is not really a gap, these are not near-half-metals.

Fe_2Ni(Si,Ge,Sn): These all have gaps after 9 states in the minority. Fe_2NiSi and Fe_2NiGe also have majority gaps after 9 states. Fe_2NiSi also has a minority gap after 12 states while Fe_2NiGe has a minority pseudogap after 12 states. The moments are relatively large (4.78 μ_B, 5.09 μ_B, 5.23 μ_B respectively) but not large enough (6 μ_B would have been required) to make them half-metals or near-half-metals.

Fe_2Cu(Al,Ga,In): These all have relatively large minority gaps after 9 states and small majority gaps after 14 states (Fe_2CuAl and Fe_2CuGa) or after 16 states (Fe_2CuIn). Fe_2CuIn also has a pseudogap after 14 states in the majority. The majority gaps after 14 states cannot be used to make a half-metal and although the majority gap after 16 could be used, the moment is too large, 4.84μ_B rather than 2μ_B.

31 electron systems: The 15 systems in our database with 31 electrons comprise Mn_2Zn(P,As,Sb), Fe_2Ni(P,As,Sb), Fe_2Cu(Si,Ge,Sn), Fe_2Zn(Al,Ga,In) and Co_2Ni(Al,Ga,In). Compounds with 31 electrons could, in principle, take advantage of a minority gap after 14, 12 or 9 states with a moment of 3μ_B, 7μ_B, or 13μ_B respectively. In addition, we find one example of a gap after 15 states which would allow a half-metal with a moment of 1 μ_B. In practice, we find no 31-electron half-metals or near-half-metals with negative formation energy.

Mn_2Zn(P,As,Sb): All three systems have gaps after 9 states in minority. Mn_2ZnP also has a gap after 9 states in majority while Mn_2ZnAs has a pseudogap near 9 states in majority. Mn_2ZnP has a pseudogap near 14 states in minority. Mn_2ZnAs has a tiny minority gap after 15 states and a moment (1.001 μ_B) that places the Fermi energy very near this gap. Unfortunately, its formation energy is positive. Mn_2ZnSb has a similar electronic structure and moment, but the tiny gap in Mn_2ZnAs is replaced by a pseudogap in Mn_2ZnSb.

Fe_2Ni(P,As,Sb): These all have minority gaps after 9 states. Fe_2NiP also has a minority gap after 12 states while Fe_2NiAs and Fe_2NiSb have pseudogaps after 12 states. The moments are too small to take advantage of the gap or pseudogaps after 12 states.

Fe_2Cu(Si,Ge,Sn): These all have gaps after 9 states in both spin channels, with the minority gap being larger than the majority gap. In addition, Fe_2CuSi and Fe_2CuSn have narrow gaps after 14 states in the majority. None of these gaps are near the Fermi energy.

Fe_2Zn(Al,Ga,In): These systems have gaps (Al) or pseudogaps (Ga,In) at 14 states in minority. The moments are to large to place the Fermi energy near these gaps or pseudogaps.

Co_2Ni(Al,Ga,In): These systems have numerous gaps and pseudogaps. All three have narrow, deep, pseudogaps near 14 states in minority and have moments (2.99, 3.02, 3.13)μ_B that place the Fermi energy in the pseudogaps. They are not "near-half-metals" according to our definition. In addition, all three have minority pseudogaps near 12 states. They all also have gaps after 9 states in minority. Co_2NiAl has a gap after 14 states in majority. Co_2NiGa has a gap after 9 states in majority and pseudogaps near 14 and 16 states in majority.

32 electron systems: The 12 systems with 32 electrons in our database include Fe_2Cu(P,As,Sb), Fe_2Zn(Si,Ge,Sn), Co_2Ni(Si,Ge,Sn), and Co_2Cu(Al,Ga,In).

Fe_2Cu(P,As,Sb): These systems all have gaps after 9 states in both spin channels and pseudogaps after 14 states in the minority channel. Their moments are all greater than 4 μ_B, and the moment of Fe_2CuP is 4.018 μ_B, quite close the the value of 4 needed to generate a half-metal. Unfortunately, the Fermi energy is on the edge of a pseudogap rather than a gap.

Fe_2Zn(Si,Ge,Sn): The 31 electron Fe_2ZnZ XA compounds have pseudogaps rather than gaps near 9 states in both spin channels, but similar to the 31-electron Fe_2CuZ systems, they have pseudogaps near 14 states in the minority channel. The pseudogap near 14 states in Fe_2ZnSi is remarkable in that the DOS plots appear to show a gap after 14 states. Its moment (3.982 μ_B) is close enough to 4 that we would classify Fe_2ZnSi as a near-half-metal and include it in Table 4.3 because it also has a negative formation energy. However, bands 14 and 15 cross between X and W, spoiling the gap.

Co_2Ni(Si,Ge,Sn): These all have gaps after nine states in both spin channels and pseudogaps near 12 states in minority. Their moments are too small (2.51 μ_B, 2.56 μ_B, 2.70 μ_B) to place the Fermi energy near the pseudogaps. None are half-metals or near-half-metals.

Co_2Cu(Al,Ga,In) These all have gaps after 9 states in the minority channel. None are half-metals or near-half-metals.

33 electron systems: The 12 systems with 33 electrons in our database include Fe_2Zn(P,As,Sb), Co_2Ni(P,As,Sb), Co_2Cu(Si,Ge,Sn), and Co_2Zn(Al,Ga,In). These systems would need a moment of 5 μ_B to utilize a gap after 14 states to make a half-metal. They have neither the gaps nor the moment.

Fe_2Zn(P,As,Sb): These systems have either gaps (P,As) or pseudogaps after 9 states in both spin channels.

Co_2Ni(P,As,Sb): These systems all have gaps after 9 states in both spin channels. Pseudogaps near 12 states in minority can also be identified for all three systems.

Co_2Cu(Si,Ge,Sn): These systems also have gaps after 9 states in both channels. Two (Si,Ge) have pseudogaps after 12 states in both spin channels.

Co_2Zn(Al,Ga,In): No gaps or convincing pseudogaps were observed in these systems.

34 electron systems: The 9 systems in our database with 34 electrons include Co_2Cu(P,As,Sb), Co_2Zn(Si,Ge,Sn) and Ni_2Cu(Al,Ga,In).

Co_2Cu(P,As,Sb): These systems have gaps after 9 states in both channels. Co_2CuP also has a majority gap after 12 states which becomes a pseudogap for the other two compounds. The moments are not nearly large enough to place the Fermi energy near the gaps or pseudogaps.

Co_2Zn(Si,Ge,Sn): These systems all have pseudogaps near 9 states in both spin channels and also a pseudogap near 12 states in the minority channel.

Ni_2Cu(Al,Ga,In): These systems are non-magnetic and have no gaps. Ni_2CuAl and Ni_2CuGa have pseudogaps near 12 states in both channels. Ni_2CuGa and Ni_2CuIn have pseudogaps after 9 states in both channels.

35 electron systems: The 9 systems in our database with 35 electrons include Co_2Zn(P,As,Sb), Ni_2Cu(Si,Ge,Sn) and Ni_2Zn(Al,Ga,In). A system with 35 electrons would need a moment of 7 μ_B to take advantage of a gap after 14 states in minority. Such moments would be unlikely in these systems because the d-bands are nearly filled for Co and especially for Ni.

Co_2Zn(P,As,Sb): These systems are magnetic with moments relatively small moments, (2.4 μ_B, 2.5 μ_B, and 2.7 μ_B). Co_2ZnP and Co_2ZnAs have gaps after 9 states in both spin channels while Co_2ZnSb has pseudogaps near 9 states in both spin channels. Pseudogaps near 14 states can be identified in all three systems.

Ni_2Cu(Si,Ge,Sn): These are all non-magnetic and have gaps after 9 states in each of the identical spin channels. Pseudogaps near 12 states can be identified in all three as well as near 14 states in Ni_2CuSn.

36 electron systems: The 6 systems in our database with 36 electrons include Ni_2Cu(P,As,Sb) and Ni_2Zn(Si,Ge,Sn). None of these systems are magnetic.

Ni_2Cu(P,As,Sb): These have gaps after 9 states and pseudogaps near 12 states and 14 states.

Ni_2Zn(Si,Ge,Sn): These have pseudogaps near 14 states.

37 electron systems: The 6 systems in our database with 37 electrons are Ni_2Zn(P,As,Sb) and Cu_2Zn(Al,Ga,In). None of these 6 systems has a magnetic moment and therefore cannot be half-metals.

Ni_2Zn(P,As,Sb): Ni_2ZnP and Ni_2ZnAs have gaps after 9 states. Ni_2ZnSb has a pseudogap near 9 states. Pseudogaps after 14 states can be identified for all three.

Cu_2Zn(Al,Ga,In): These systems have no gaps.

38 electron systems: The three systems in our database with 38 electrons are Cu_2Zn(Si,Ge,Sn). They have neither moments nor gaps.

39 electron systems: The three systems in our database with 39 electrons are Cu_2Zn(P,As,Sb). They have neither moments nor gaps.

Appendix B

Publications

B.1 Journals

1. Xie, Yunkun, Jianhua Ma, Hamed Vakilitaleghani, Yaohua Tan, and Avik W. Ghosh. "Computational search for ultrasmall and fast skyrmions in the Inverse Heusler family." *preprint arXiv*:1901.09446 (2019).

2. Ma, Jianhua, Puhan Zhang, Yaohua Tan, Avik W. Ghosh, and Gia-Wei Chern. "Machine learning electron correlation in a disordered medium." *Physical Review B* 99, no. 8 (2019): 085118.

3. Yan, Yongke, Liwei D. Geng, Yaohua Tan, Jianhua Ma, Lujie Zhang, Mohan Sanghadasa, Khai Ngo, Avik W. Ghosh, Yu U. Wang, and Shashank Priya. "Colossal tunability in high frequency magnetoelectric voltage tunable inductors." *Nature communications* 9, no. 1 (2018): 4998.

4. Ma, Jianhua, Vinay I. Hegde, Kamaram Munira, Yunkun Xie, Sahar Keshavarz, David T. Mildebrath, C. Wolverton, Avik W. Ghosh, and W. H. Butler. "Computational investigation of inverse-Heusler compounds for spintronics applications." *Physical Review B* 98, no. 9 (2018): 094410.

5. Xie, Yunkun, Jianhua Ma, Samiran Ganguly, and Avik W. Ghosh. “From materials to systems: a multiscale analysis of nanomagnetic switching.” *Journal of Computational Electronics* 16, no. 4 (2017): 1201-1226.

6. Ma, Jianhua, Vinay I. Hegde, Kamaram Munira, Yunkun Xie, Sahar Keshavarz, David T. Mildebrath, C. Wolverton, Avik W. Ghosh, and W. H. Butler. ”Computational investigation of half-Heusler compounds for spintronics applications.” *Physical Review B* 95, no. 2 (2017): 024411.

7. Ma, Jianhua, Yunkun Xie, Kamaram Munira, Avik W. Ghosh and W. H. Butler. ”Computational Investigation of Half-Heusler/MgO Magnetic Tunnel Junctions” *In preparation*

8. Naghibolashrafi, N., S. Keshavarz, Vinay I. Hegde, A. Gupta, W. H. Butler, J. Romero, K. Munira, P. LeClair, D. Mazumdar, J. Ma, A. W. Ghosh, C. Wolverton. ”Synthesis and characterization of Fe-Ti-Sb intermetallic compounds: Discovery of a new Slater-Pauling phase.” *Physical Review B* 93, no. 10 (2016): 104424.

9. Azadani, Javad G., Kamaram Munira, Jonathon Romero, Jianhua Ma, Chockalingam Sivakumar, Avik W. Ghosh, and William H. Butler. ”Anisotropy in layered half-metallic Heusler alloy superlattices.” *Journal of Applied Physics* 119, no. 4 (2016): 043904.

Bibliography

[1] Yasuo Ando. Spintronics technology and device development. Japanese Journal of Applied Physics, 54(7):070101, 2015.

[2] Koichi Momma and Fujio Izumi. *VESTA3* for three-dimensional visualization of crystal, volumetric and morphology data. Journal of Applied Crystallography, 44(6):1272–1276, Dec 2011.

[3] Vadim Ksenofontov, Gennadiy Melnyk, Marek Wojcik, Sabine Wurmehl, Kristian Kroth, Sergey Reiman, Peter Blaha, and Claudia Felser. Structure and properties of comnsb in the context of half-metallic ferromagnetism. Phys. Rev. B, 74:134426, Oct 2006.

[4] Michael J Donahue. Oommf user's guide, version 1.0. Technical report, 1999.

[5] Jan M Rabaey, Anantha P Chandrakasan, and Borivoje Nikolic. Digital integrated circuits, volume 2. Prentice hall Englewood Cliffs, 2002.

[6] H. Iwai. Roadmap for 22 nm and beyond (invited paper). Microelectronic Engineering, 86(79):1520 – 1528, 2009. {INFOS} 2009.

[7] Michael F. L. De Volder, Sameh H. Tawfick, Ray H. Baughman, and A. John Hart. Carbon nanotubes: Present and future commercial applications. Science, 339(6119):535–539, 2013.

[8] Ankur Gupta, Tamilselvan Sakthivel, and Sudipta Seal. Recent development in 2d materials beyond graphene. Progress in Materials Science, 73:44 – 126, 2015.

[9] Gianluca Fiori, Francesco Bonaccorso, Giuseppe Iannaccone, Tomas Palacios, Daniel Neumaier, Alan Seabaugh, Sanjay K. Banerjee, and Luigi Colombo. Electronics based on two-dimensional materials. Nat Nano, 9(10):768–779, October 2014.

[10] M. N. Baibich, J. M. Broto, A. Fert, F. Nguyen Van Dau, F. Petroff, P. Etienne, G. Creuzet, A. Friederich, and J. Chazelas. Giant magnetoresistance of (001)fe/(001)cr magnetic superlattices. Phys. Rev. Lett., 61:2472–2475, Nov 1988.

[11] Roger Wood. Future hard disk drive systems. Journal of Magnetism and Magnetic Materials, 321(6):555 – 561, 2009. Current Perspectives: Perpendicular Recording.

[12] W. H. Butler, X.-G. Zhang, T. C. Schulthess, and J. M. MacLaren. Spin-dependent tunneling conductance of Fe|MgO|Fe sandwiches. Phys. Rev. B, 63:054416, Jan 2001.

[13] Stuart S. P. Parkin, Christian Kaiser, Alex Panchula, Philip M. Rice, Brian Hughes, Mahesh Samant, and See-Hun Yang. Giant tunnelling magnetoresistance at room temperature with mgo (100) tunnel barriers. Nat Mater, 3(12):862–867, December 2004.

[14] X. Fong, Y. Kim, K. Yogendra, D. Fan, A. Sengupta, A. Raghunathan, and K. Roy. Spin-transfer torque devices for logic and memory: Prospects and perspectives. IEEE Transactions on Computer-Aided Design of Integrated Circuits and Systems, 35(1):1–22, Jan 2016.

[15] Li Su, Youguang Zhang, Jacques-Olivier Klein, Yue Zhang, Arnaud Bournel, Albert Fert, and Weisheng Zhao. Current-limiting challenges for all-spin logic devices. Scientific Reports, 5:14905, September 2015.

[16] G. Schmidt, D. Ferrand, L. W. Molenkamp, A. T. Filip, and B. J. van Wees. Fundamental obstacle for electrical spin injection from a ferromagnetic metal into a diffusive semiconductor. Phys. Rev. B, 62:R4790–R4793, Aug 2000.

[17] M Bowen, A Barthlmy, M Bibes, E Jacquet, J P Contour, A Fert, D Wortmann, and S Blgel. Half-metallicity proven using fully spin-polarized tunnelling. Journal of Physics: Condensed Matter, 17(41):L407, 2005.

[18] R. J. Soulen, J. M. Byers, M. S. Osofsky, B. Nadgorny, T. Ambrose, S. F. Cheng, P. R. Broussard, C. T. Tanaka, J. Nowak, J. S. Moodera, A. Barry, and J. M. D. Coey. Measuring the spin polarization of a metal with a superconducting point contact. Science, 282(5386):85–88, 1998.

[19] H. Kato, T. Okuda, Y. Okimoto, Y. Tomioka, K. Oikawa, T. Kamiyama, and Y. Tokura. Structural and electronic properties of the ordered double perovskites $A_2m\mathrm{reo}_6$ (a=sr,ca; m=mg,sc,cr,mn,fe,co,ni,zn). Phys. Rev. B, 69:184412, May 2004.

[20] Tatsuya Shishidou, A. J. Freeman, and Ryoji Asahi. Effect of gga on the half-metallicity of the itinerant ferromagnet cos_2. Phys. Rev. B, 64:180401, Oct 2001.

[21] Wen-Hui Xie, Ya-Qiong Xu, Bang-Gui Liu, and D. G. Pettifor. Half-metallic ferromagnetism and structural stability of zincblende phases of the transition-metal chalcogenides. Phys. Rev. Lett., 91:037204, Jul 2003.

[22] H. Yamada, K. Fukamichi, and T. Goto. Itinerant-electron metamagnetism and strong pressure dependence of the curie temperature. Phys. Rev. B, 65:024413, Dec 2001.

[23] D P Kozlenko, I N Goncharenko, B N Savenko, and V I Voronin. High pressure effects on the crystal and magnetic structure of la 0.7 sr 0.3 mno 3. Journal of Physics: Condensed Matter, 16(37):6755, 2004.

[24] Ichiro Tsubokawa. The magnetic properties of single crystals of chromium selenide. Journal of the Physical Society of Japan, 15(12):2243–2247, 1960.

[25] L. Ranno, A. Barry, and J. M. D. Coey. Production and magnetotransport properties of cro2 films. Journal of Applied Physics, 81(8):5774–5776, 1997.

[26] Tanja Graf, Claudia Felser, and Stuart S.P. Parkin. Simple rules for the understanding of heusler compounds. Progress in Solid State Chemistry, 39(1):1 – 50, 2011.

[27] A. Hirohata, M. Kikuchi, N. Tezuka, K. Inomata, J.S. Claydon, Y.B. Xu, and G. van der Laan. Heusler alloy/semiconductor hybrid structures. Current Opinion in Solid State and Materials Science, 10(2):93 – 107, 2006.

[28] PJ Webster and KRA Ziebeck. Alloys and compounds of d-elements with main group elements. Part, 2:75–184, 1988.

[29] Claudia Felser and Atsufumi Hirohata. Heusler Alloys: Properties, Growth, Applications, volume 222. Springer, 2015.

[30] R. A. de Groot, F. M. Mueller, P. G. van Engen, and K. H. J. Buschow. New class of materials: Half-metallic ferromagnets. Phys. Rev. Lett., 50:2024–2027, Jun 1983.

[31] Delia Ristoiu, J. P. Nozires, C. N. Borca, B. Borca, and P. A. Dowben. Manganese surface segregation in nimnsb. Applied Physics Letters, 76(17):2349–2351, 2000.

[32] I. Galanakis, P. H. Dederichs, and N. Papanikolaou. Origin and properties of the gap in the half-ferromagnetic heusler alloys. Phys. Rev. B, 66:134428, Oct 2002.

[33] S. J. Youn and B. I. Min. Effects of the spin-orbit interaction in heusler compounds: Electronic structures and fermi surfaces of nimnsb and ptmnsb. Phys. Rev. B, 51:10436–10442, Apr 1995.

[34] Janusz Toboła and Jacques Pierre. Electronic phase diagram of the xtz (x=fe, co, ni; t=ti, v, zr, nb, mn; z=sn, sb) semi-heusler compounds. Journal of Alloys and Compounds, 296(1-2):243 – 252, 2000.

[35] Hem Chandra Kandpal, Claudia Felser, and Ram Seshadri. Covalent bonding and the nature of band gaps in some half-heusler compounds. Journal of Physics D: Applied Physics, 39(5):776, 2006.

[36] I Galanakis, Ph Mavropoulos, and P H Dederichs. Electronic structure and slater-pauling behaviour in half-metallic heusler alloys calculated from first principles. Journal of Physics D: Applied Physics, 39(5):765, 2006.

[37] Luo Hongzhi, Zhu Zhiyong, Ma Li, Xu Shifeng, Liu Heyan, Qu Jingping, Li Yangxian, and Wu Guangheng. Electronic structure and magnetic properties of fe 2 ysi (y = cr, mn, fe, co, ni) heusler alloys: a theoretical and experimental study. Journal of Physics D: Applied Physics, 40(22):7121, 2007.

[38] Hem C Kandpal, Gerhard H Fecher, and Claudia Felser. Calculated electronic and magnetic properties of the half-metallic, transition metal based heusler compounds. Journal of Physics D: Applied Physics, 40(6):1507, 2007.

[39] I. Galanakis, P. H. Dederichs, and N. Papanikolaou. Slater-pauling behavior and origin of the half-metallicity of the full-heusler alloys. Phys. Rev. B, 66:174429, Nov 2002.

[40] Lukas Wollmann, Stanislav Chadov, Jürgen Kübler, and Claudia Felser. Magnetism in cubic manganese-rich heusler compounds. Phys. Rev. B, 90:214420, Dec 2014.

[41] S. Skaftouros, K. Özdoğan, E. Şaşıoğlu, and I. Galanakis. Generalized slater-pauling rule for the inverse heusler compounds. Phys. Rev. B, 87:024420, Jan 2013.

[42] G. D. Liu, X. F. Dai, H. Y. Liu, J. L. Chen, Y. X. Li, Gang Xiao, and G. H. Wu. $\mathrm{mn}_2\mathrm{Co}z$ ($z = \mathrm{Al}, \mathrm{Ga}, \mathrm{In}, \mathrm{Si}, \mathrm{Ge}, \mathrm{Sn}, \mathrm{Sb}$) compounds: Structural, electronic, and magnetic properties. Phys. Rev. B, 77:014424, Jan 2008.

[43] K. E. H. M. Hanssen and P. E. Mijnarends. Positron-annihilation study of the half-metallic ferromagnet nimnsb: Theory. Phys. Rev. B, 34:5009–5016, Oct 1986.

[44] K. E. H. M. Hanssen, P. E. Mijnarends, L. P. L. M. Rabou, and K. H. J. Buschow. Positron-annihilation study of the half-metallic ferromagnet nimnsb: Experiment. Phys. Rev. B, 42:1533–1540, Jul 1990.

[45] M. M. Kirillova, A. A. Makhnev, E. I. Shreder, V. P. Dyakina, and N. B. Gorina. Interband optical absorption and plasma effects in half-metallic xmny ferromagnets. physica status solidi (b), 187(1):231–240, 1995.

[46] U Geiersbach, A Bergmann, and K Westerholt. Preparation and structural properties of thin films and multilayers of the heusler compounds cu2mnal, co2mnsn, co2mnsi and co2mnge. Thin Solid Films, 425(12):225 – 232, 2003.

[47] Silvia Picozzi and Arthur J Freeman. Polarization reduction in half-metallic heusler alloys: the effect of point defects and interfaces with semiconductors. Journal of Physics: Condensed Matter, 19(31):315215, 2007.

[48] M. Jourdan, J. Minr, J. Braun, A. Kronenberg, S. Chadov, B. Balke, A. Gloskovskii, M. Kolbe, H. J. Elmers, G. Schnhense, H. Ebert, C. Felser, and M. Klui. Direct observation of half-metallicity in the heusler compound co2mnsi. Nature Communications, 5:3974, May 2014.

[49] J. Braun, M. Jourdan, A. Kronenberg, S. Chadov, B. Balke, M. Kolbe, A. Gloskovskii, H. J. Elmers, G. Schönhense, C. Felser, M. Kläui, H. Ebert, and J. Minár. Monitoring surface resonances on $\mathrm{co}_2\mathrm{MnSi}(100)$ by spin-resolved photoelectron spectroscopy. Phys. Rev. B, 91:195128, May 2015.

[50] Hong xi Liu, Takeshi Kawami, Kidist Moges, Tetsuya Uemura, Masafumi Yamamoto, Fengyuan Shi, and Paul M Voyles. Influence of film composition in quaternary heusler alloy co 2 (mn,fe)si thin films on tunnelling magnetoresistance of co 2 (mn,fe)si/mgo-based magnetic tunnel junctions. Journal of Physics D: Applied Physics, 48(16):164001, 2015.

[51] Wenhong Wang, Hiroaki Sukegawa, and Koichiro Inomata. Temperature dependence of tunneling magnetoresistance in epitaxial magnetic tunnel junctions using a co_2feal heusler alloy electrode. Phys. Rev. B, 82:092402, Sep 2010.

[52] Hong xi Liu, Yusuke Honda, Ken ichi Matsuda, Masashi Arita, Tetsuya Uemura, and Masafumi Yamamoto. Highly spin-polarized tunneling in epitaxial magnetic tunnel junctions with a co 2 mnsi electrode and a mgo barrier with improved interfacial structural properties. Japanese Journal of Applied Physics, 51(9R):093004, 2012.

[53] Hong xi Liu, Yusuke Honda, Ken ichi Matsuda, Masashi Arita, Tetsuya Uemura, and Masafumi Yamamoto. Highly spin-polarized tunneling in epitaxial magnetic tunnel junctions with a co 2 mnsi electrode and a mgo barrier with improved interfacial structural properties. Japanese Journal of Applied Physics, 51(9R):093004, 2012.

[54] W. Kohn. Nobel lecture: Electronic structure of matter¯wave functions and density functionals. Rev. Mod. Phys., 71:1253–1266, Oct 1999.

[55] P. Hohenberg and W. Kohn. Inhomogeneous electron gas. Phys. Rev., 136:B864–B871, Nov 1964.

[56] W. Kohn and L. J. Sham. Self-consistent equations including exchange and correlation effects. Phys. Rev., 140:A1133–A1138, Nov 1965.

[57] O. Gunnarsson and B. I. Lundqvist. Exchange and correlation in atoms, molecules, and solids by the spin-density-functional formalism. Phys. Rev. B, 13:4274–4298, May 1976.

[58] U von Barth and L Hedin. A local exchange-correlation potential for the spin polarized case. i. Journal of Physics C: Solid State Physics, 5(13):1629, 1972.

[59] D. M. Ceperley and B. J. Alder. Ground state of the electron gas by a stochastic method. Phys. Rev. Lett., 45:566–569, Aug 1980.

[60] Klaus Capelle. A bird's-eye view of density-functional theory. Brazilian Journal of Physics, 36:1318 – 1343, 12 2006.

[61] S. H. Vosko, L. Wilk, and M. Nusair. Accurate spin-dependent electron liquid correlation energies for local spin density calculations: a critical analysis. Canadian Journal of Physics, 58(8):1200–1211, 1980.

[62] John P. Perdew, Kieron Burke, and Matthias Ernzerhof. Generalized gradient approximation made simple. Phys. Rev. Lett., 77:3865–3868, Oct 1996.

[63] G. Kresse and J. Furthmüller. Efficient iterative schemes for ab initio total-energy calculations using a plane-wave basis set. Phys. Rev. B, 54:11169–11186, Oct 1996.

[64] G. Kresse and D. Joubert. From ultrasoft pseudopotentials to the projector augmented-wave method. Phys. Rev. B, 59:1758–1775, Jan 1999.

[65] H Ebert, D Kdderitzsch, and J Minr. Calculating condensed matter properties using the kkr-green's function methodrecent developments and applications. Reports on Progress in Physics, 74(9):096501, 2011.

[66] P. E. Blöchl. Projector augmented-wave method. Phys. Rev. B, 50:17953–17979, Dec 1994.

[67] Peter E. Blöchl, Clemens J. Först, and Johannes Schimpl. Projector augmented wave method:ab initio molecular dynamics with full wave functions. Bulletin of Materials Science, 26(1):33–41, Jan 2003.

[68] J Korringa. On the calculation of the energy of a bloch wave in a metal. Physica, 13(6):392 – 400, 1947.

[69] W. Kohn and N. Rostoker. Solution of the schrödinger equation in periodic lattices with an application to metallic lithium. Phys. Rev., 94:1111–1120, Jun 1954.

[70] Phivos Mavropoulos and Nikos Papanikolaou. The korringa-kohn-rostoker (kkr) green function method i. electronic structure of periodic systems. Computational Nanoscience: Do It Yourself, 31:131–158, 2006.

[71] P. Lloyd and P.V. Smith. Multiple scattering theory in condensed materials. Advances in Physics, 21(89):69–142, 1972.

[72] A.I. Liechtenstein, M.I. Katsnelson, V.P. Antropov, and V.A. Gubanov. Local spin density functional approach to the theory of exchange interactions in ferromagnetic metals and alloys. Journal of Magnetism and Magnetic Materials, 67(1):65 – 74, 1987.

[73] Larry Engelhardt, Marshall Luban, and Christian Schröder. Finite quantum heisenberg spin models and their approach to the classical limit. Phys. Rev. B, 74:054413, Aug 2006.

[74] Allan R Mackintosh and OK Andersen. The electronic structure of transition metals. Electrons at the Fermi Surface,, pages 149–224, 1980.

[75] E aioglu, L M Sandratskii, and P Bruno. First-principles study of exchange interactions and curie temperatures of half-metallic ferrimagnetic full heusler alloys mn 2 v z (z = al, ge). Journal of Physics: Condensed Matter, 17(6):995, 2005.

[76] Philip W Anderson. Theory of magnetic exchange interactions: exchange in insulators and semiconductors. Solid state physics, 14:99–214, 1963.

[77] H. Ebert, S. Mankovsky, D. Ködderitzsch, and P. J. Kelly. Ab initio calculation of the gilbert damping parameter via the linear response formalism. Phys. Rev. Lett., 107:066603, Aug 2011.

[78] S. Mankovsky, D. Ködderitzsch, G. Woltersdorf, and H. Ebert. First-principles calculation of the gilbert damping parameter via the linear response formalism with application to magnetic transition metals and alloys. Phys. Rev. B, 87:014430, Jan 2013.

[79] H. Ebert and S. Mankovsky. Anisotropic exchange coupling in diluted magnetic semiconductors: Ab initio spin-density functional theory. Phys. Rev. B, 79:045209, Jan 2009.

[80] H. Ebert, S. Mankovsky, D. Ködderitzsch, and P. J. Kelly. Ab initio calculation of the gilbert damping parameter via the linear response formalism. Phys. Rev. Lett., 107:066603, Aug 2011.

[81] W. H. Butler. Theory of electronic transport in random alloys: Korringa-kohn-rostoker coherent-potential approximation. Phys. Rev. B, 31:3260–3277, Mar 1985.

[82] H. Ebert, S. Mankovsky, K. Chadova, S. Polesya, J. Minár, and D. Ködderitzsch. Calculating linear-response functions for finite temperatures on the basis of the alloy analogy model. Phys. Rev. B, 91:165132, Apr 2015.

[83] William H Butler et al. Heuslers home. `http://heusleralloys.mint.ua.edu/`, 2016.

[84] J. C. Slater and G. F. Koster. Simplified lcao method for the periodic potential problem. Phys. Rev., 94:1498–1524, Jun 1954.

[85] William H Butler, Claudia KA Mewes, Chunsheng Liu, and Tianyi Xu. Rational design of half-metallic heterostructures. arXiv preprint arXiv:1103.3855, 2011.

[86] G. Kresse and J. Furthmüller. Efficiency of ab-initio total energy calculations for metals and semiconductors using a plane-wave basis set. Computational Materials Science, 6(1):15 – 50, 1996.

[87] JamesE. Saal, Scott Kirklin, Muratahan Aykol, Bryce Meredig, and C. Wolverton. Materials design and discovery with high-throughput density functional theory: The open quantum materials database (oqmd). JOM, 65(11):1501–1509, 2013.

[88] Scott Kirklin, James E Saal, Bryce Meredig, Alex Thompson, Jeff W Doak, Muratahan Aykol, Stephan Rühl, and Chris Wolverton. The open quantum materials database (oqmd): assessing the accuracy of dft formation energies. npj Computational Materials, 1:15010, 2015.

[89] John P. Perdew, Kieron Burke, and Matthias Ernzerhof. Generalized gradient approximation made simple. Phys. Rev. Lett., 77:3865–3868, Oct 1996.

[90] Hendrik J. Monkhorst and James D. Pack. Special points for brillouin-zone integrations. Phys. Rev. B, 13:5188–5192, Jun 1976.

[91] Peter E. Blöchl, O. Jepsen, and O. K. Andersen. Improved tetrahedron method for brillouin-zone integrations. Phys. Rev. B, 49:16223–16233, Jun 1994.

[92] A. R. Akbarzadeh, V. Ozoli, and C. Wolverton. First-principles determination of multicomponent hydride phase diagrams: Application to the li-mg-n-h system. Advanced Materials, 19(20):3233–3239, 2007.

[93] Scott Kirklin, Bryce Meredig, and Chris Wolverton. High-throughput computational screening of new li-ion battery anode materials. Advanced Energy Materials, 3(2):252–262, 2013.

[94] R. Guerin, M. Sergent, and J. Prigent. Influence de 'electronegativite sur l'apparition de l'ordere dans les phases m m'p et m m'as des metaux de transition. Annales de Chimie (Paris), 4:411 – 417, 1979.

[95] C. Djega-Mariadassou, , E. Both, and G. Trumpy. Influence de 'electronegativite sur l'apparition de l'ordere dans les phases m m'p et m m'as des metaux de transition. Annales de Chimie (Paris), pages 505 – 516, 1970.

[96] E. A. Vasilev and V. A. Virchenko. Solid solutions in the $(\mathrm{Fe1.22Sb})_{1-x}(\mathrm{Fe1.68Sn})_x$ system. physica status solidi (a), 70:K141–K143, 1982.

[97] Vancliff Johnson. Ternary transition metal germanides and arsenides. Materials Research Bulletin, 8:1067 – 1072, 1973.

[98] Mme Roy-Montreuil, B. Deyris, A. Michel, A. Rouault, P. l'Héritier, A. Nylund, J.P. Sénateur, and R. Fruchart. Nouveaux composes ternaires mm'p et mm'as interactions metalliques et structures. Materials Research Bulletin, 7(8):813 – 826, 1972.

[99] Wolfgang G. Zeier, Jennifer Schmitt, Geoffroy Hautier, Umut Aydemir, Zachary M. Gibbs, Claudia Felser, and G. Jeffrey Snyder. Engineering half-heusler thermoelectric materials using zintl chemistry. Nature Reviews Materials, 1:1 – 10, 2016.

[100] Holger Kleinke and Hugo F. Franzen. Sc-sc bonding in the new ternary phosphide scnip. Journal of Solid State Chemistry, 137(2):218 – 222, 1998.

[101] VK Pecharskii, YUK Pankevich, and OI Bodak. Crystal structures of the compounds rnisb with various rare earth elements. Sov. Phys. Crystallogr., 28(1):97–98, 1983.

[102] A.E. Dwight, J.M. Haschke, and H.A. Eick. Crystal structure of DyNiSb, DyPtSb and related compounds. Technical Report CONF-741002--P2, Northern Illinois Univ., DeKalb; Michigan State Univ., East Lansing (USA), 1974.

[103] Gregory A. Landrum, Roald Hoffmann, Jürgen Evers, and Hans Boysen. The tinisi family of compounds: structure and bonding. Inorganic Chemistry, 37(22):5754–5763, 1998.

[104] C. B. Shoemaker and D. P. Shoemaker. A ternary alloy with pbcl$_2$-type structure: Tinisi(e). Acta Crystallographica, 18(5):900–905, 1965.

[105] W. Bazela and A. Szytula. Crystal and magnetic structure of the nimn1-ttitge system. physica status solidi (a), 66(1):45–52, 1981.

[106] Yu. Stadnyk, A. Horyn', V.V. Romaka, Yu. Gorelenko, L.P. Romaka, E.K. Hlil, and D. Fruchart. Crystal, electronic structure and electronic transport properties of the ti1-xvxnisn solid solutions. Journal of Solid State Chemistry, 183(12):3023 – 3028, 2010.

[107] W. Jeitschko. Transition metal stannides with mgagas and mncu2al type structure. Metallurgical Transactions, 1(11):3159–3162, 1970.

[108] J. Pierre, R.V. Skolozdra, Yu.K. Gorelenko, and M. Kouacou. From nonmagnetic semiconductor to itinerant ferromagnet in the tinisn-ticosn series. Journal of Magnetism and Magnetic Materials, 134(1):95 – 105, 1994.

[109] P.G. van Engen, K.H.J. Buschow, and M. Erman. Magnetic properties and magneto-optical spectroscopy of heusler alloys based on transition metals and sn. Journal of Magnetism and Magnetic Materials, 30(3):374 – 382, 1983.

[110] STIG Rundqvist and PICHET CHANTRA Nawapong. The crystal structure of zrfep and related compounds. Acta Chemica Scandinavica, 20:2250–2254, 1966.

[111] S. Rundqvist and P. Transuriwongs. Ternary transition metal arsenides with the anti-pbcl2 structure. Acta Chemica Scandinavica, 21:813–814, 1967.

[112] I. Skovsen, L. Bjerg, M. Christensen, E. Nishibori, B. Balke, C. Felser, and B. B. Iversen. Multi-temperature synchrotron pxrd and physical properties study of half-heusler ticosb. Dalton Trans., 39:10154–10159, 2010.

[113] Z Szytula, Z Tomkowicz, and M Turowski. Crystal structure and magnetic properties of heusler-type alloys mtisb(m= ni, co, fe) and fe 2 tisn. Acta Phys. Polon., (1):147–149, 1973.

[114] B Deyris, J Roy-Montreuil, A Rouault, A Krumbuegel-Nylund, JP Senateur, R Fruchart, and A Michel. Structural characteristics of 9 new ternary compounds mmas (m= ru, rh, pd)(m= transition element 3d). Comptes Rendus Hebdomadaires Des Seances De L Academie Des Sciences Serie C, 278(4):237–239, 1974.

[115] A.E. Dwight. Alloying behavior of zirconium, hafnium and the actinides in several series of isostructural compounds. Journal of the Less Common Metals, 34(2):279 – 284, 1974.

[116] R. Marazza, R. Ferro, and G. Rambaldi. Some phases in ternary alloys of titanium, zirconium, and hafnium, with a mgagas or alcu2mn type structure. Journal of the Less Common Metals, 39(2):341 – 345, 1975.

[117] V.Y. Markiv, E.I. Gladyshevskii, and Y.B. Kuz'ma. New ternary compounds with a structure of the mncu2al type. Dopovidi Akademii Nauk Ukrains'koi RSR, pages 1329–1331, 1962.

[118] M Conrad, B Herrmann, and B Harbrecht. Refinement of the crystal structure of monovanadium monocobalt monosilicide, vcosi. Zeitschrift für Kristallographie-New Crystal Structures, 220(3):319–320, 2005.

[119] E. I. Gladyshevskii. Crystal structure of compounds and phase equilibria in ternary systems of two transition metals and silicon. Soviet Powder Metallurgy and Metal Ceramics, 1(4):262–265, 1962.

[120] W Jeitschko, AG Jordan, and Paul A Beck. V and e phase in ternary systems with transition metals and silicon or germanium. Trans Met Soc AIME, 245(2):335–339, 1969.

[121] A.W. Carbonari, R.N. Saxena, W. Pendl Jr., J. Mestnik Filho, R.N. Attili, M. Olzon-Dionysio, and S.D. de Souza. Magnetic hyperfine field in the heusler alloys co2yz (y = v, nb, ta, cr; z = al, ga). Journal of Magnetism and Magnetic Materials, 163(3):313 – 321, 1996.

[122] J.C. Suits. Structural instability in new magnetic heusler compounds. Solid State Communications, 18(3):423 – 425, 1976.

[123] PI Kripyakevich and V Ya Markiv. Crystal structures of ternary compounds in the systems ti (v)–fe (co, ni)–sn (sb). Dopovidi Akademii Nauk Ukrains'koi RSR, 12:1606–1608, 1963.

[124] Yu. Stadnyk, A. Horyn, V. Sechovsky, L. Romaka, Ya. Mudryk, J. Tobola, T. Stopa, S. Kaprzyk, and A. Kolomiets. Crystal structure, electrical transport properties and electronic structure of the vfe1-xcuxsb solid solution. Journal of Alloys and Compounds, 402(1-2):30 – 35, 2005.

[125] Bo Kong, Bo Zhu, Yan Cheng, Lin Zhang, Qi-Xian Zeng, and Xiao-Wei Sun. Structural, mechanical, thermodynamics properties and phase transition of fevsb. Physica B: Condensed Matter, 406(15-16):3003 – 3010, 2011.

[126] Christoph B.H. Evers, Carolin G. Richter, Klaus Hartjes, and Wolfgang Jeitschko. Ternary transition metal antimonides and bismuthides with mgagas-type and filled nias-type structure. Journal of Alloys and Compounds, 252(12):93 – 97, 1997.

[127] W. H. Butler, T. Mewes, C. K. A. Mewes, P. B. Visscher, W. H. Rippard, S. E. Russek, and R. Heindl. Switching distributions for perpendicular spin-torque devices within the macrospin approximation. IEEE Transactions on Magnetics, 48(12):4684–4700, Dec 2012.

[128] Vancliff Johnson. Ternary transition metal germanides and arsenides. Materials Research Bulletin, 8(9):1067 – 1072, 1973.

[129] Y. Noda, M. Shimada, and M. Koizumi. High-pressure synthesis and magnetic properties of mmnsb (m = ti, v, cr) with nickel-indium (ni2in) type structures. Inorganic Chemistry, 23(5):628–630, 1984.

[130] Melle A. Nylund, M.M.A. Roger, J.P. Sénateur, and R. Fruchart. Evolution structurale des phosphures, arséniures et arséniophosphures m2p, m2as et m2(p1-xasx). Journal of Solid State Chemistry, 4(1):115 – 122, 1972.

[131] W. Jeitschko and V. Johnson. High pressure Mn_2As with Fe_2P-type structure. Acta Crystallographica Section B, 28(6):1971–1973, Jun 1972.

[132] Motoyoshi Yuzuri and Motohiko Yamada. On the magnetic properties of the compound mn2as. Journal of the Physical Society of Japan, 15(10):1845–1850, 1960.

[133] WB Pearson. The cu2sb and related structures. Zeitschrift für Kristallographie-Crystalline Materials, 171(1-4):23–40, 1985.

[134] Laszlo Hollan. Etude structurale et magnétique d'arséniures mixtes m2as. Annales de Chimie, pages 437–448, 1966.

[135] T. Kanomata, T. Kawashima, H. Utsugi, T. Goto, H. Hasegawa, and T. Kaneko. Magnetic properties of the intermetallic compounds mmx (m= cr, mn, m= ru, rh, pd, and x= p, as). Journal of Applied Physics, 69(8):4639–4641, 1991.

[136] J Wirringa, R Wartchow, and M Binnewies. Crystal structure of cobalt chromium germanium, cocrge. Zeitschrift für Kristallographie-New Crystal Structures, 215(2):197–198, 2000.

[137] Michiko Terada, Keizo Endo, Yūkō Fujita, Tetuo Ohoyama, and Ren'iti Kimura. Magnetic susceptibilities of clb compounds covsb and cotisb. Journal of the Physical Society of Japan, 29(4):1091–1091, 1970.

[138] Yukio Noda, Masahiko Shimada, and Mitsue Koizumi. Synthesis of high-pressure phases of vanadium-cobalt-antimony (vcosb) and vanadium-iron-antimony (vfesb) with a dinickel-indium (ni2in) (b82) type structure. Inorganic Chemistry, 18(11):3244–3246, 1979.

[139] J Roy-Montreuil, P Chaudouet, A Rouault, D Boursier, JP Senateur, and R Fruchart. Analyse de l'ordre dans les arséniures mm'as. Annales de chimie, 9:579–586, 1984.

[140] C. C. M. Campbell and C. V. Stager. Magnetization studies of the heusler alloys. Canadian Journal of Physics, 54(21):2197–2203, 1976.

[141] Y. Fujita, K. Endo, M. Terada, and R. Kimura. Magnetic properties of heusler type alloys m2xsn (m = fe, co or ni, x = ti or v). Journal of Physics and Chemistry of Solids, 33(7):1443 – 1446, 1972.

[142] Anna Nylund, A. Roger, J.P. Senateur, and R. Fruchart. Strukturelle übergänge zwischen phosphiden, arseniden und arsenophosphiden der zusammensetzungm 2p, m 2as undm 2 (p1xasx). Monatshefte für Chemie / Chemical Monthly, 102(5):1631–1642, 1971.

[143] B. Chenevier, J.L. Soubeyroux, M. Bacmann, D. Fruchart, and R. Fruchart. The high temperature orthorhombic hexagonal phase transformation of femnp. Solid State Communications, 64(1):57 – 61, 1987.

[144] Janusz Toboła, Madeleine Bacmann, Daniel Fruchart, Pierre Wolfers, Stanislaw Kaprzyk, and Abdel-Azziz Koumina. Structure and magnetism in the polymorphous mnfeas. Journal of Alloys and Compounds, 317-318(0):274 – 279, 2001.

[145] B. Deyris, J. Roy-Montreuil, A. Michel, J.P. Sénateur, A. Rouault, A. Krumbugel-Nylund, and R. Fruchart. Etude cristallographique et magnetique de la solution solide (fe1-xrux) mnas. Materials Research Bulletin, 10(7):603 – 606, 1975.

[146] H. Biczycka, A. Szytua, J. Todorovi, T. Zaleski, and A. Ziba. Metamagnetism of comnsi. physica status solidi (a), 35(1):K69–K72, 1976.

[147] V. Johnson. Diffusionless orthorhombic to hexagonal transitions in ternary silicides and germanides. Inorganic Chemistry, 14(5):1117–1120, 1975.

[148] Shinpei Fujii, Shoji Ishida, and Setsuro Asano. Electronic and magnetic properties of x2mn1-xvxsi (x=fe and co). Journal of the Physical Society of Japan, 63(5):1881–1888, 1994.

[149] Rudolf Sobczak. Magnetic measurements on heusler alloys co2xy x=ti, zr, hf, v, nb, cr, mn and fe; y=al, ga, si, ge and snx=ti, zr, hf, v, nb, cr, mn und fe;y=al, ga, si, ge und sn. Monatshefte für Chemie / Chemical Monthly, 107(4):977–983, 1976.

[150] S Nizioł, A Bombik, W Bazela, A Szytuła, and D Fruchart. Crystal and magnetic structure of coxni1-xmnge system. Journal of Magnetism and Magnetic Materials, 27(3):281 – 292, 1982.

[151] K.H.J. Buschow, P.G. van Engen, and R. Jongebreur. Magneto-optical properties of metallic ferromagnetic materials. Journal of Magnetism and Magnetic Materials, 38(1):1 – 22, 1983.

[152] H Ido and S Yasuda. Magnetic properties of co-heusler and related mixed alloys. J. Phys. Colloques, 49:C8–141–C8–142, 1988.

[153] M. Kogachi, T. Fujiwara, and S. Kikuchi. Atomic disorder and magnetic property in co-based heusler alloys co2mnz (z = si, ge, sn). Journal of Alloys and Compounds, 475(12):723 – 729, 2009.

[154] Satoru Ohta, Takejiro Kaneko, Hajime Yoshida, Takeshi Kanomata, and Hiroshi Yamauchi. Pressure effect on the magnetic transition temperatures and thermal expansion in chromium ternary pnictides crmas (m = ni, rh). Journal of Magnetism and Magnetic Materials, 150(2):157 – 164, 1995.

[155] D. Fruchart, M. Backmann, and P. Chaudouet. Structure du phosphure de cobalt et de manganèse. Acta Crystallographica Section B, 36(11):2759–2761, Nov 1980.

[156] D. Fruchart, C. Martin-Farrugia, A. Rouault, and J. P. Sénateur. Etude structurale et magnétique de comnp3). physica status solidi (a), 57(2):675–682, 1980.

[157] M.J. Otto, H. Feil, R.A.M. Van Woerden, J. Wijngaard, P.J. Van Der Valk, C.F. Van Bruggen, and C. Haas. Electronic structure and magnetic, electrical and optical properties of ferromagnetic heusler alloys. Journal of Magnetism and Magnetic Materials, 70(1-3):33 – 38, 1987.

[158] J.P. Senateur, A. Rouault, R. Fruchart, and D. Fruchart. Etude cristallographique de comnsb. relation avec la structure de type c1b. Journal of Solid State Chemistry, 5(2):226 – 228, 1972.

[159] Moti R. Paudel, Christopher S. Wolfe, Heather Patton, Igor Dubenko, Naushad Ali, Joseph A. Christodoulides, and Shane Stadler. Magnetic and transport properties of heusler alloys. Journal of Applied Physics, 105(1), 2009.

[160] A Szytuła, Ž Dimitrijević, J Todorović, A Kołodziejczyk, J Szelag, and A Wanic. Atomic and magnetic structure of the heusler alloys nimnsb and comnsb. physica status solidi (a), 9(1):97–103, 1972.

[161] N. Suzuki, T. Kanomata, T. Suzuki, K. Sato, T. Kaneko, M. Yamagishi, and S. Endo. Thermal expansion of mnrhp. Journal of Alloys and Compounds, 281(2):77 – 80, 1998.

[162] SV Orishchin and Yu B Kuz'ma. Cr(w)-ni-p ternary systems. Izv Akad Nauk SSSR, Neorg Mater, 20(3):425–430, 1984.

[163] V. Johnson and C. G. Frederick. Magnetic and crystallographic properties of ternary manganese silicides with ordered co2p structure. physica status solidi (a), 20(1):331–335, 1973.

[164] K.H.J. Buschow and P.G. van Engen. Magnetic and magneto-optical properties of heusler alloys based on aluminium and gallium. Journal of Magnetism and Magnetic Materials, 25(1):90 – 96, 1981.

[165] R. Fruchart, A. Roger, and J. P. Senateur. Crystallographic and magnetic properties of solid solutions of the phosphides m2p, m = cr, mn, fe, co, and ni. Journal of Applied Physics, 40(3):1250–1257, 1969.

[166] P. Chaudouet, J. Roy Montreuil, J.P. Snateur, D. Boursier, A. Rouault, and R. Fruchart. New compounds mm'as and mm'p involving a 3d and a 4d element. In Seventh International Conference on Solid Compounds of Transition Elements, volume IIIA4 of Collected Abstracts, Grenoble, France, 1982.

[167] P.P.J. van Engelen, D.B. de Mooij, J.H. Wijngaard, and K.H.J. Buschow. Magneto-optical and magnetic properties of some solid solutions of c1b-heusler compounds. Journal of Magnetism and Magnetic Materials, 130:247 – 254, 1994.

[168] T. Kanomata, K. Shirakawa, H. Yasui, and T. Kaneko. Effect of hydrostatic pressure on the magnetic transition temperatures of mnrhas. Journal of Magnetism and Magnetic Materials, 68(3):286 – 290, 1987.

[169] P.J. Webster and R.M. Mankikar. Chemical order and magnetic properties of the system. Journal of Magnetism and Magnetic Materials, 42(3):300–308, 1984.

[170] Bo Kong, Xiang-Rong Chen, Jing-Xin Yu, and Cang-Ling Cai. Structural, elastic properties and pressure-induced phase transition of half-heusler alloy covsb. Journal of Alloys and Compounds, 509(5):2611 – 2616, 2011.

[171] Michiko Terada, Keizo Endo, Yūkō Fujita, and Ren'iti Kimura. Magnetic properties of clb compounds; covsb, cotisb and nitisb. Journal of the Physical Society of Japan, 32(1):91–94, 1972.

[172] L Heyne, T Igarashi, T Kanomata, K-U Neumann, B Ouladdiaf, and K R A Ziebeck. Atomic and magnetic order in the weak ferromagnet covsb: is it a half-metallic ferromagnet? Journal of Physics: Condensed Matter, 17(33):4991, 2005.

[173] K Kaczmarska, J Pierre, J Beille, J Tobola, R.V Skolozdra, and G.A Melnik. Physical properties of the weak itinerant ferromagnet covsb and related semi-heusler compounds. Journal of Magnetism and Magnetic Materials, 187(2):210 – 220, 1998.

[174] J. Pierre, R.V. Skolozdra, J. Tobola, S. Kaprzyk, C. Hordequin, M.A. Kouacou, I. Karla, R. Currat, and E. Lelivre-Berna. Proceedings of the twelfth international conference on solid compounds of transition elements properties on request in semi-heusler phases. Journal of Alloys and Compounds, 262:101 – 107, 1997.

[175] Ya. F. Lomnytska and O. P. Pavliv. Phase equilibria in the v-ni-sb system. Inorganic Materials, 43(6):608–613, 2007.

[176] Andrei V Ivanov, Michael E Zolensky, Akihiro Saito, Kazumasa Ohsumi, S Vincent Yang, Nataliya N Kononkova, and Takashi Mikouchi. Florenskyite, fetip, a new phosphide from the kaidun meteorite. American Mineralogist, 85(7-8):1082–1086, 2000.

[177] W. Bażela-Wróbel, A. Szytula, and J. Leciejewicz. Magnetic properties of rhmnsi and cotisi. physica status solidi (a), 82(1):195–200, 1984.

[178] A Szytuła, W Bażla, and S Radenković. Crystal and magnetic structure of the comn1- xtixsi system. Journal of Magnetism and Magnetic Materials, 38(1):99 – 104, 1983.

[179] W. Jeitschko. The crystal structure of TiFeSi and related compounds. Acta Crystallographica Section B, 26(6):815–822, 1970.

[180] Natalja Krendelsberger, Franz Weitzer, Julius C. Schuster, and Frank Stein. Constitution of the ternary system cositi. Intermetallics, 38:92–101, 2013.

[181] P.J. Webster and K.R.A. Ziebeck. Magnetic and chemical order in heusler alloys containing cobalt and titanium. Journal of Physics and Chemistry of Solids, 34(10):1647 – 1654, 1973.

[182] J. Pierre, R.V. Skolozdra, and Yu.V. Stadnyk. Influence of cobalt vacancies and nickel substitution on the magnetic properties of tico2sn heusler-type compound. Journal of Magnetism and Magnetic Materials, 128(1-2):93 – 100, 1993.

[183] E.A. Grlich, K. atka, A. Szytua, D. Wagner, R. Kmie, and K. Ruebenbauer. Magnetic ordering in the system co2-xnix tisn studied by 119sn-mssbauer spectroscopy and magnetization measurements. Solid State Communications, 25(9):661 – 663, 1978.

[184] Stig Rundqvist. X-ray investigations of mn3p, mn2p and ni2p. Acta Chemica Scandinavica, 16:992–998, 1962.

[185] L. Häggström, J. Sjöström, and T. Ericsson. A 57fe mössbauer study of mn2p. Journal of Magnetism and Magnetic Materials, 60(2-3):171 – 174, 1986.

[186] Sudhish Kumar, Anjali Krishnamurthy, BipinK. Srivastava, A. Das, and S.K. Paranjpe. Magnetization and neutron diffraction studies on fecrp. Pramana, 63(2):199–205, 2004.

[187] Michael Zolensky, Matthieu Gounelle, Takashi Mikouchi, Kazumasa Ohsumi, Loan Le, Kenji Hagiya, and Osamu Tachikawa. Andreyivanovite: A second new phosphide from the kaidun meteorite. American Mineralogist, 93(8-9):1295–1299, 2008.

[188] Roland Guérin and Marcel Sergent. Nouveaux arseniures et phosphures ternaires de molybdene ou de tungstene et d'elements 3d, de formule: M2-xmexx (m= lment 3d; me= mo, w; x= as, p). Materials Research Bulletin, 12(4):381 – 388, 1977.

[189] Ya F Palfij and Yu B Kuz'ma. Vnip compound crystal structure. Vyisnik L'vyivs'kij Derzhavnij Unyiversitet imeni I Franka, 21, 1979.

[190] Hironobu Fujii, Shigehiro Komura, Takayoshi Takeda, Tetsuhiko Okamoto, Yuji Ito, and Jun Akimitsu. Polarized neutron diffraction study of fe2p single crystal. Journal of the Physical Society of Japan, 46(5):1616–1621, 1979.

[191] A. Catalano, R.J. Arnott, and A. Wold. Magnetic and crystallographic properties of the system fe2p1-xasx. Journal of Solid State Chemistry, 7(3):262 – 268, 1973.

[192] Sergey N Britvin, Nikolay S Rudashevsky, Sergey V Krivovichev, Peter C Burns, and Yury S Polekhovsky. Allabogdanite,(fe, ni) 2p, a new mineral from the onello meteorite: The occurrence and crystal structure. American Mineralogist, 87(8-9):1245–1249, 2002.

[193] Sterling B Hendricks and Peter R Kosting. Xxxv. the crystal structure of fe2p, fe2n, fe3n and feb. Zeitschrift für Kristallographie-Crystalline Materials, 74(1):511–533, 1930.

[194] E. K. Delczeg-Czirjak, L. Delczeg, M. P. J. Punkkinen, B. Johansson, O. Eriksson, and L. Vitos. *Ab initio* study of structural and magnetic properties of si-doped $\mathrm{fe}_2\mathrm{P}$. Phys. Rev. B, 82:085103, Aug 2010.

[195] Arne Kjekshus and Kjell Erik Skaug. On the Phases Cr2As, Fe2As, Co2As, Rh2As. Acta Chemica Scandinavica, 26:2554–2556, 1972.

[196] V. Niculescu, T.J. Burch, K. Raj, and J.I. Budnick. Properties of heusler-type materials fe2tsi and feco2si. Journal of Magnetism and Magnetic Materials, 5(1):60 – 66, 1977.

[197] Sabine Wurmehl, Gerhard H. Fecher, Hem Chandra Kandpal, Vadim Ksenofontov, Claudia Felser, and Hong-Ji Lin. Investigation of co2fesi: The heusler compound with highest curie temperature and magnetic moment. Applied Physics Letters, 88(3):032503, 2006.

[198] B. Chenevier, D. Fruchart, M. Bacmann, J. P. Senateur, P. Chaudouet, and L. Lundgren. Propriétés magéhtiques de mnrhas. etude de la transition antiferro-ferromagnétique. physica status solidi (a), 84(1):199–206, 1984.

[199] V. A. Oksenenko, L. N. Trofimova, Yu. N. Petrov, Y. V. Kudryavtsev, J. Dubowik, and Y. P. Lee. Structural dependence of some physical properties of the ni2mnge heusler alloy films. Journal of Applied Physics, 99(6), 2006.

[200] W Bazela, A Szytuła, J Todorović, Z Tomkowicz, and A Ziba. Crystal and magnetic structure of nimnge. physica status solidi (a), 38(2):721–729, 1976.

[201] G Mavrodiev, S Koneska, and A Szytuła. Dilatometric and ddc measurements of nimnge1-xsix and nimn1- ttitge systems. physica status solidi (a), 88(2):K105–K109, 1985.

[202] H Fjellvåg and AF Andresen. On the crystal structure and magnetic properties of mnnige. Journal of Magnetism and Magnetic Materials, 50(3):291 – 297, 1985.

[203] N. Naghibolashrafi, S. Keshavarz, Vinay I. Hegde, A. Gupta, W. H. Butler, J. Romero, K. Munira, P. LeClair, D. Mazumdar, J. Ma, A. W. Ghosh, and C. Wolverton. Synthesis and characterization of fe-ti-sb intermetallic compounds: Discovery of a new slater-pauling phase. Phys. Rev. B, 93:104424, Mar 2016.

[204] Tatsuhito Nobata, Go Nakamoto, Makio Kurisu, Yoshikazu Makihara, Kenji Ohoyama, and Masayoshi Ohashi. Neutron diffraction study on the heusler compound co1.50tisn and its nitrogenation products. Journal of Alloys and Compounds, 347(12):86 – 90, 2002.

[205] Vinay I. Hegde. Computational discovery of Heusler-based ternary phases in the Co–Ti–Sn system. unpublished, 2016.

[206] Siham Ouardi, Gerhard H. Fecher, Claudia Felser, and Jürgen Kübler. Realization of spin gapless semiconductors: The heusler compound mn$_2$CoAl. Phys. Rev. Lett., 110:100401, Mar 2013.

[207] J. C. Slater. Electronic structure of alloys. Journal of Applied Physics, 8(6):385–390, 1937.

[208] Linus Pauling. The nature of the interatomic forces in metals. Phys. Rev., 54:899–904, Dec 1938.

[209] S. Skaftouros, K. Özdoğan, E. Şaşıoğlu, and I. Galanakis. Search for spin gapless semiconductors: The case of inverse heusler compounds. Applied Physics Letters, 102(2):–, 2013.

[210] I. Galanakis, K. Özdoğan, E. Şaşıoğlu, and S. Blügel. Conditions for spin-gapless semiconducting behavior in mn2coal inverse heusler compound. Journal of Applied Physics, 115(9):–, 2014.

[211] N. Lakshmi, Anil Pandey, and K. Venugopalan. Hyperfine field distributions in disordered mn2cosn and mn2nisn heusler alloys. Bulletin of Materials Science, 25(4):309–313, 2002.

[212] Markus Meinert, Jan-Michael Schmalhorst, Christoph Klewe, Günter Reiss, Elke Arenholz, Tim Böhnert, and Kornelius Nielsch. Itinerant and localized magnetic moments in ferrimagnetic mn$_2$coga thin films probed by x-ray magnetic linear dichroism: Experiment and *ab initio* theory. Phys. Rev. B, 84:132405, Oct 2011.

[213] Jürgen Winterlik, Gerhard H. Fecher, Benjamin Balke, Tanja Graf, Vajiheh Alijani, Vadim Ksenofontov, Catherine A. Jenkins, Olga Meshcheriakova, Claudia Felser, Guodong Liu, Shigenori Ueda, Keisuke Kobayashi, Tetsuya Nakamura, and Marek Wójcik. Electronic, magnetic, and structural properties of the ferrimagnet mn$_2$cosn. Phys. Rev. B, 83:174448, May 2011.

[214] Yuepeng Xin, Hongyue Hao, Yuexing Ma, Hongzhi Luo, Fanbin Meng, Heyan Liu, Enke Liu, and Guangheng Wu. Competition of {XA} and {L21B} ordering in heusler alloys mn2coz (z=al, ga, si, ge and sb) and its influence on electronic structure. Intermetallics, 80:10 – 15, 2017.

[215] F. Ahmadian and A. Salary. Half-metallicity in the inverse heusler compounds sc2mnz (z=c, si, ge, and sn). Intermetallics, 46:243 – 249, 2014.

[216] A. Jakobsson, P. Mavropoulos, E. Şaşıoğlu, S. Blügel, M. Ležaić, B. Sanyal, and I. Galanakis. First-principles calculations of exchange interactions, spin waves, and temperature dependence of magnetization in inverse-heusler-based spin gapless semiconductors. Phys. Rev. B, 91:174439, May 2015.

[217] K. zdogan and I. Galanakis. First-principles electronic and magnetic properties of the half-metallic antiferromagnet. Journal of Magnetism and Magnetic Materials, 321(15):L34 – L36, 2009.

[218] Hongzhi Luo, Zhiyong Zhu, Li Ma, Shifeng Xu, Xiaoxi Zhu, Chengbao Jiang, Huibin Xu, and Guangheng Wu. Effect of site preference of 3d atoms on the electronic structure and half-metallicity of heusler alloy mn 2 y al. Journal of Physics D: Applied Physics, 41(5):055010, 2008.

[219] Markus Meinert, Jan-Michael Schmalhorst, and Gnter Reiss. Exchange interactions and curie temperatures of mn 2 coz compounds. Journal of Physics: Condensed Matter, 23(11):116005, 2011.

[220] Ben Xu, Ming Zhang, and Hui Yan. First-principles study on half-metallic properties of cuhg2ti-type alloys fev2z (z?=?si, ge, as, sb). physica status solidi b, 248(12):2870–2876, 2011.

[221] Maria Pugaczowa-Michalska. Theoretical prediction of ferrimagnetism in mn2feb, mn2cob and mn2nib. Intermetallics, 24:128 – 134, 2012.

[222] Nazmiye Kervan and Seluk Kervan. Half-metallic properties of ti2fesi full-heusler compound. Journal of Physics and Chemistry of Solids, 72(11):1358 – 1361, 2011.

[223] P. Klaer, C. A. Jenkins, V. Alijani, J. Winterlik, B. Balke, C. Felser, and H. J. Elmers. Disentangling the mn moments on different sublattices in the half-metallic ferrimagnet mn3xcoxga. Applied Physics Letters, 98(21):212510, 2011.

[224] Vajiheh Alijani, Juergen Winterlik, Gerhard H. Fecher, and Claudia Felser. Tuning the magnetism of the heusler alloys mn3xcoxga from soft and half-metallic to hard-magnetic for spin-transfer torque applications. Applied Physics Letters, 99(22):222510, 2011.

[225] Jianhua Ma, Vinay I. Hegde, Kamaram Munira, Yunkun Xie, Sahar Keshavarz, David T. Mildebrath, C. Wolverton, Avik W. Ghosh, and W. H. Butler. Computational investigation of half-heusler compounds for spintronics applications. Phys. Rev. B, 95:024411, Jan 2017.

[226] O. Meshcheriakova, S. Chadov, A. K. Nayak, U. K. Rößler, J. Kübler, G. André, A. A. Tsirlin, J. Kiss, S. Hausdorf, A. Kalache, W. Schnelle, M. Nicklas, and C. Felser. Large noncollinearity and spin reorientation in the novel mn_2RhSn heusler magnet. Phys. Rev. Lett., 113:087203, Aug 2014.

[227] Alex Zunger, S.-H. Wei, L. G. Ferreira, and James E. Bernard. Special quasirandom structures. Phys. Rev. Lett., 65:353–356, Jul 1990.

[228] A Van de Walle, P Tiwary, M De Jong, DL Olmsted, M Asta, A Dick, D Shin, Y Wang, L-Q Chen, and Z-K Liu. Efficient stochastic generation of special quasirandom structures. Calphad, 42:13–18, 2013.

[229] Axel van de Walle. Multicomponent multisublattice alloys, nonconfigurational entropy and other additions to the alloy theoretic automated toolkit. Calphad, 33(2):266–278, 2009.

[230] G. Bergerhoff and I. D. Brown. Crystallographic databases. International Union of Crystallography, Chester, 360:77–95, 1987.

[231] Alec Belsky, Mariette Hellenbrandt, Vicky Lynn Karen, and Peter Luksch. New developments in the Inorganic Crystal Structure Database (ICSD): accessibility in support of materials research and design. Acta Crystallographica Section B, 58(3 Part 1):364–369, Jun 2002.

[232] Ming Yin, Philip Nash, and Song Chen. Enthalpies of formation of selected fe2yz heusler compounds. Intermetallics, 57:34 – 40, 2015.

[233] Guido Kreiner, Adel Kalache, Steffen Hausdorf, Vajiheh Alijani, Jin-Feng Qian, Guangcun Shan, Ulrich Burkhardt, Siham Ouardi, and Claudia Felser. New mn2-based heusler compounds. Zeitschrift fr anorganische und allgemeine Chemie, 640(5):738–752, 2014.

[234] Hongzhi Luo, Guodong Liu, Zhongqiu Feng, Yangxian Li, Li Ma, Guangheng Wu, Xiaoxi Zhu, Chengbao Jiang, and Huibin Xu. Effect of the main-group elements on the electronic structures and magnetic properties of heusler alloys mn2niz (z=in, sn, sb). Journal of Magnetism and Magnetic Materials, 321(24):4063 – 4066, 2009.

[235] Said Bakkar and Dipanjan Mazumdar. unpublished, 2017.

[236] Xuefang Dai, Guodong Liu, Lijie Chen, Jinglan Chen, and Guangheng Wu. Mn2cosb compound: Structural, electronic, transport and magnetic properties. Solid State Communications, 140(1112):533 – 537, 2006.

[237] K. Endo, T. Kanomata, H. Nishihara, and K.R.A. Ziebeck. Magnetic properties of new compounds rumn2sn and rumn2si. Journal of Alloys and Compounds, 510(1):1 – 5, 2012.

[238] Ling Yang, Bohua Liu, Hongzhi Luo, Fanbin Meng, Heyan Liu, Enke Liu, Wenhong Wang, and Guangheng Wu. Investigation of the site preference in mn2rusn using kkr-cpa-lda calculation. Journal of Magnetism and Magnetic Materials, 382:247 – 251, 2015.

[239] Takur Nakamichi and Hiroshi Itoh. On ferromagnetism of ordered alloys in the mn-v-al ternary system. Journal of the Physical Society of Japan, 38(6):1781–1781, 1975.

[240] K.H.J. Buschow and P.G. van Engen. Magnetic and magneto-optical properties of heusler alloys based on aluminium and gallium. Journal of Magnetism and Magnetic Materials, 25(1):90 – 96, 1981.

[241] R. Y. Umetsu, K. Kobayashi, A. Fujita, R. Kainuma, and K. Ishida. Magnetic properties and stability of l21 and b2 phases in the co2mnal heusler alloy. Journal of Applied Physics, 103(7):07D718, 2008.

[242] Shinpei Fujii, Shoji Ishida, and Setsuro Asano. Electronic and magnetic properties of x2mn1-xvxsi (x=fe and co). Journal of the Physical Society of Japan, 63(5):1881–1888, 1994.

[243] K. Miyamoto, A. Kimura, Y. Miura, M. Shirai, M. Ye, Y. Cui, K. Shimada, H. Namatame, M. Taniguchi, Y. Takeda, Y. Saitoh, E. Ikenaga, S. Ueda, K. Kobayashi, and T. Kanomata. Absence of temperature dependence of the valence-band spectrum of co_2MnSi. Phys. Rev. B, 79:100405, Mar 2009.

[244] Muhammad Ariful Islam Nahid, Mikihiko Oogane, Hiroshi Naganuma, and Yasuo Ando. Structural and magnetic properties of co 2 mnsi heusler alloy thin films on si. Japanese Journal of Applied Physics, 48(8R):083002, 2009.

[245] Rudolf Sobczak. Magnetic measurements on heusler alloys co2xy x=ti, zr, hf, v, nb, cr, mn and fe; y=al, ga, si, ge and snx=ti, zr, hf, v, nb, cr, mn und fe;y=al, ga, si, ge und sn. Monatshefte für Chemie / Chemical Monthly, 107(4):977–983, 1976.

[246] Moti R. Paudel, Christopher S. Wolfe, Heather Patton, Igor Dubenko, Naushad Ali, Joseph A. Christodoulides, and Shane Stadler. Magnetic and transport properties of co2mnsnxsb1x heusler alloys. Journal of Applied Physics, 105:013716, 2009.

[247] E Shreder, S V Streltsov, A Svyazhin, A Makhnev, V V Marchenkov, A Lukoyanov, and H W Weber. Evolution of the electronic structure and physical properties of fe 2 meal (me = ti, v, cr) heusler alloys. Journal of Physics: Condensed Matter, 20(4):045212, 2008.

[248] B.S.D.Ch.S. Varaprasad, A. Rajanikanth, Y.K. Takahashi, and K. Hono. Highly spinpolarized co2mnga0.5sn0.5 heusler compound. Acta Materialia, 57(9):2702 – 2709, 2009.

[249] Jian-Gang Zhu. Magnetoresistive random access memory: The path to competitiveness and scalability. Proceedings of the IEEE, 96(11):1786–1798, Nov 2008.

[250] K. Munira, W. H. Butler, and A. W. Ghosh. A quasi-analytical model for energy-delay-reliability tradeoff studies during write operations in a perpendicular stt-ram cell. Electron Devices, IEEE Transactions on, 59(8):2221–2226, Aug 2012.

[251] E. Chen, D. Apalkov, Z. Diao, A. Driskill-Smith, D. Druist, D. Lottis, V. Nikitin, X. Tang, S. Watts, S. Wang, S.A. Wolf, A.W. Ghosh, J.W. Lu, S.J. Poon, M. Stan, W.H. Butler, S. Gupta, C.K.A. Mewes, T. Mewes, and P.B. Visscher. Advances and future prospects of spin-transfer torque random access memory. Magnetics, IEEE Transactions on, 46(6):1873–1878, June 2010.

[252] I Galanakis. Appearance of half-metallicity in the quaternary heusler alloys. Journal of Physics: Condensed Matter, 16(18):3089, 2004.

[253] William H Butler, Avik W Ghosh, et al. Heuslers home. `http://heusleralloys.mint.ua.edu/`, 2016.

[254] Kamaram Munira, Jonathon Romero, and William H. Butler. Achieving perpendicular anisotropy in half-metallic heusler alloys for spin device applications. Journal of Applied Physics, 115(17):–, 2014.

[255] M. Sicot, P. Turban, S. Andrieu, A. Tagliaferri, C. De Nadai, N.B. Brookes, F. Bertran, and F. Fortuna. Spin polarization at the nimnsb/mgo (100) interface. Journal of Magnetism and Magnetic Materials, 303(1):54 – 59, 2006.

[256] P. Turban, S. Andrieu, B. Kierren, E. Snoeck, C. Teodorescu, and A. Traverse. Growth and characterization of single crystalline nimnsb thin films and epitaxial nimnsb/mgo/nimnsb(001) trilayers. Phys. Rev. B, 65:134417, Mar 2002.

[257] P. Turban, S. Andrieu, E. Snoeck, B. Kierren, and C. Teodorescu. Nimnsb/mgo/nimnsb heterostructures grown by {MBE}. Journal of Magnetism and Magnetic Materials, 240(13):427 – 429, 2002. 4th International Symposium on Metallic Multilayers.

[258] A Reily Rocha, Víctor M García-Suárez, S Bailey, C Lambert, J Ferrer, and S Sanvito. Spin and molecular electronics in atomically generated orbital landscapes. Physical Review B, 73(8):085414, 2006.

[259] José M Soler, Emilio Artacho, Julian D Gale, Alberto García, Javier Junquera, Pablo Ordejón, and Daniel Sánchez-Portal. The siesta method for ab initio order-n materials simulation. Journal of Physics: Condensed Matter, 14(11):2745, 2002.

[260] Supriyo Datta. Quantum transport: atom to transistor. Cambridge University Press, 2005.

[261] Yunkun Xie, Ivan Rungger, Kamaram Munira, Maria Stamenova, Stefano Sanvito, and Avik W Ghosh. Spin transfer torque: A multiscale picture. Nanomagnetic and Spintronic Devices for Energy-Efficient Memory and Computing, page 91, 2016.

[262] William H Butler et al. Heuslers home. http://heusleralloys.mint.ua.edu/, 2016.

[263] AH MacDonald, T Jungwirth, and M Kasner. Temperature dependence of itinerant electron junction magnetoresistance. Physical review letters, 81(3):705, 1998.

[264] AN Bogdanov and DA Yablonskii. Thermodynamically stable" vortices" in magnetically ordered crystals. the mixed state of magnets. Zh. Eksp. Teor. Fiz, 95:182, 1989.

[265] AN Bogdanov and UK Rößler. Chiral symmetry breaking in magnetic thin films and multilayers. Physical review letters, 87(3):037203, 2001.

[266] A Neubauer, C Pfleiderer, B Binz, A Rosch, R Ritz, PG Niklowitz, and P Böni. Topological hall effect in the a phase of mnsi. Physical review letters, 102(18):186602, 2009.

[267] C Pappas, E Lelièvre-Berna, P Falus, PM Bentley, E Moskvin, S Grigoriev, P Fouquet, and B Farago. Chiral paramagnetic skyrmion-like phase in mnsi. Physical review letters, 102(19):197202, 2009.

[268] SX Huang and CL Chien. Extended skyrmion phase in epitaxial fege (111) thin films. Physical review letters, 108(26):267201, 2012.

[269] XZ Yu, Yoshinori Onose, Naoya Kanazawa, JH Park, JH Han, Yoshio Matsui, Naoto Nagaosa, and Yoshinori Tokura. Real-space observation of a two-dimensional skyrmion crystal. Nature, 465(7300):901, 2010.

[270] Shinichiro Seki, XZ Yu, S Ishiwata, and Y Tokura. Observation of skyrmions in a multiferroic material. Science, 336(6078):198–201, 2012.

[271] Ajaya K Nayak, Vivek Kumar, Tianping Ma, Peter Werner, Eckhard Pippel, Roshnee Sahoo, Franoise Damay, Ulrich K Rößler, Claudia Felser, and Stuart SP Parkin. Magnetic antiskyrmions above room temperature in tetragonal heusler materials. Nature, 548(7669):561, 2017.

[272] Stefan Heinze, Kirsten Von Bergmann, Matthias Menzel, Jens Brede, André Kubetzka, Roland Wiesendanger, Gustav Bihlmayer, and Stefan Blügel. Spontaneous atomic-scale magnetic skyrmion lattice in two dimensions. Nature Physics, 7(9):713, 2011.

[273] Niklas Romming, Christian Hanneken, Matthias Menzel, Jessica E Bickel, Boris Wolter, Kirsten von Bergmann, André Kubetzka, and Roland Wiesendanger. Writing and deleting single magnetic skyrmions. Science, 341(6146):636–639, 2013.

[274] Seonghoon Woo, Kai Litzius, Benjamin Krüger, Mi-Young Im, Lucas Caretta, Kornel Richter, Maxwell Mann, Andrea Krone, Robert M Reeve, Markus Weigand, et al. Observation of room-temperature magnetic skyrmions and their current-driven dynamics in ultrathin metallic ferromagnets. Nature materials, 15(5):501, 2016.

[275] Lucas Caretta, Maxwell Mann, Felix Büttner, Kohei Ueda, Bastian Pfau, Christian M Günther, Piet Hessing, Alexandra Churikova, Christopher Klose, Michael Schneider, et al. Fast current-driven domain walls and small skyrmions in a compensated ferrimagnet. Nature nanotechnology, page 1, 2018.

[276] Stuart Parkin and See-Hun Yang. Memory on the racetrack. Nature nanotechnology, 10(3):195–198, 2015.

[277] João Sampaio, Vincent Cros, Stanislas Rohart, André Thiaville, and Albert Fert. Nucleation, stability and current-induced motion of isolated magnetic skyrmions in nanostructures. Nature nanotechnology, 8(11):839, 2013.

[278] IE Dzyaloshinskii. Theory of helicoidal structures in antiferromagnets. 1. nonmetals. Sov. Phys. JETP, 19:960–971, 1964.

[279] Yunkun Xie, Jianhua Ma, Hamed Vakilitaleghani, Yaohua Tan, and Avik W Ghosh. Computational search for ultrasmall and fast skyrmions in the inverse heusler family. arXiv preprint arXiv:1901.09446, 2019.

[280] Chunsheng Liu, Claudia KA Mewes, Mairbek Chshiev, Tim Mewes, and William H Butler. Origin of low gilbert damping in half metals. Applied Physics Letters, 95(2):022509, 2009.

[281] Ankit Kumar, Fan Pan, Sajid Husain, Serkan Akansel, Rimantas Brucas, Lars Bergqvist, Sujeet Chaudhary, and Peter Svedlindh. Temperature-dependent gilbert damping of co 2 feal thin films with different degree of atomic order. Physical Review B, 96(22):224425, 2017.

[282] Jianhua Ma, Jiangang He, Dipanjan Mazumdar, Kamaram Munira, Sahar Keshavarz, Tim Lovorn, C Wolverton, Avik W Ghosh, and William H Butler. Computational investigation of inverse heusler compounds for spintronics applications. Physical Review B, 98(9):094410, 2018.

[283] H Ebert, D Kdderitzsch, and J Minr. Calculating condensed matter properties using the kkr-green's function methodrecent developments and applications. Reports on Progress in Physics, 74(9):096501, 2011.

[284] Rie Y. Umetsu and Takeshi Kanomata. Spin stiffness constant of half-metallic ferrimagnet in mn-based heusler alloys. Physics Procedia, 75:890 – 897, 2015. 20th International Conference on Magnetism, ICM 2015.

[285] Jianhua Ma, Vinay I. Hegde, Kamaram Munira, Yunkun Xie, Sahar Keshavarz, David T. Mildebrath, C. Wolverton, Avik W. Ghosh, and W. H. Butler. Computational investigation of half-heusler compounds for spintronics applications. Phys. Rev. B, 95:024411, Jan 2017.

[286] J. Rusz, L. Bergqvist, J. Kudrnovský, and I. Turek. Exchange interactions and curie temperatures in ni$_{2-x}$MnSb alloys: First-principles study. Phys. Rev. B, 73:214412, Jun 2006.

[287] M. Pajda, J. Kudrnovský, I. Turek, V. Drchal, and P. Bruno. Ab initio calculations of exchange interactions, spin-wave stiffness constants, and curie temperatures of fe, co, and ni. Phys. Rev. B, 64:174402, Oct 2001.

[288] K. Gilmore, Y. U. Idzerda, and M. D. Stiles. Identification of the dominant precession-damping mechanism in fe, co, and ni by first-principles calculations. Phys. Rev. Lett., 99:027204, Jul 2007.

[289] V Kamberskỳ. On the landau–lifshitz relaxation in ferromagnetic metals. Canadian Journal of Physics, 48(24):2906–2911, 1970.

[290] J. Kuneš and V. Kamberský. First-principles investigation of the damping of fast magnetization precession in ferromagnetic $3d$ metals. Phys. Rev. B, 65:212411, Jun 2002.

[291] V. Kamberský. On ferromagnetic resonance damping in metals. Czechoslovak Journal of Physics B, 26(12):1366–1383, Dec 1976.

[292] Simon Trudel, Oksana Gaier, Jaroslav Hamrle, and Burkard Hillebrands. Magnetic anisotropy, exchange and damping in cobalt-based full-heusler compounds: an experimental review. Journal of Physics D: Applied Physics, 43(19):193001, apr 2010.

[293] Albrecht Köhler, Lukas Wollmann, Daniel Ebke, Stanislav Chadov, Christian Kaiser, Zhitao Diao, Yuankai Zheng, Qunwen Leng, and Claudia Felser. Tunable damping in the heusler compound $\mathrm{co}_{2-x}\mathrm{ir}_x\mathrm{MnSi}$. Phys. Rev. B, 93:094410, Mar 2016.

[294] Justin M Shaw, Erna K Delczeg-Czirjak, Eric RJ Edwards, Yaroslav Kvashnin, Danny Thonig, Martin AW Schoen, Matt Pufall, Michael L Schneider, Thomas J Silva, Olof Karis, et al. Magnetic damping in sputter-deposited c o 2 mnge heusler compounds with a2, b2, and l21 orders: Experiment and theory. Physical Review B, 97(9):094420, 2018.

[295] Binghai Yan and Claudia Felser. Topological materials: Weyl semimetals. Annual Review of Condensed Matter Physics, 8(1):337–354, 2017.

[296] N. P. Armitage, E. J. Mele, and Ashvin Vishwanath. Weyl and dirac semimetals in three-dimensional solids. Rev. Mod. Phys., 90:015001, Jan 2018.

[297] Wujun Shi, Lukas Muechler, Kaustuv Manna, Yang Zhang, Klaus Koepernik, Roberto Car, Jeroen van den Brink, Claudia Felser, and Yan Sun. Prediction of a magnetic weyl semimetal without spin-orbit coupling and strong anomalous hall effect in the heusler compensated ferrimagnet $\mathrm{ti}_2\mathrm{MnAl}$. Phys. Rev. B, 97:060406, Feb 2018.

[298] X. L. Wang. Proposal for a new class of materials: Spin gapless semiconductors. Phys. Rev. Lett., 100:156404, Apr 2008.

[299] A. R. Akbarzadeh, V. Ozoliņš, and C. Wolverton. First-principles determination of multicomponent hydride phase diagrams: Application to the li-mg-n-h system. Advanced Materials, 19:3233–3239, 2007.

[300] Scott Kirklin, Bryce Meredig, and Chris Wolverton. High-throughput computational screening of new li-ion battery anode materials. Advanced Energy Materials, 3:252–262, 2013.

[301] Van An Dinh, Kazunori Sato, and Hiroshi Katayama-Yoshida. New high-tc half-heusler ferromagnets nimnz (z=si, p, ge, as). Journal of the Physical Society of Japan, 77:014705, 2008.

[302] O. Arstad and H.N. Nowotny. Roentgenographische Untersuchungen im System Mn-P. Zeitschrift fuer Physikalische Chemie, Abteilung B: Chemie der Elementarprozesse, Aufbau der Materie, 38:356–358, 1937.

[303] L Calvert. National research council of canada ottawa, canada., icdd grant-in-aid (1978); guillevic j. Acta Crystallogr, 32, 1976.

[304] Stanislav Chadov, Xiaoliang Qi, Jürgen Kübler, Gerhard H Fecher, Claudia Felser, and Shou Cheng Zhang. Tunable multifunctional topological insulators in ternary heusler compounds. Nature Materials, 9(7):541–545, 2010.

[305] E. Chen, D. Apalkov, A. Driskill-Smith, A. Khvalkovskiy, D. Lottis, K. Moon, V. Nikitin, A. Ong, X. Tang, S. Watts, R. Kawakami, M. Krounbi, S.A. Wolf, S.J. Poon, J.W. Lu, A.W. Ghosh, M. Stan, W. Butler, T. Mewes, S. Gupta, C.K.A. Mewes, P.B. Visscher, and R.A. Lukaszew. Progress and prospects of spin transfer torque random access memory. Magnetics, IEEE Transactions on, 48(11):3025–3030, Nov 2012.

[306] EE Cherkashin, EI Gladyshevskii, Yu B Kuzma, and V Markiv. Crystal structure of some ternary intermetallic titanium compounds. 1966.

[307] EE Cherkashyn, EI Gladyshevskii, and YB Kuzma. X-ray structural study of some systems of the transition metals. Zh Neorg Khim, 3:650–653, 1958.

[308] Vadim Ksenofontov, Gennadiy Melnyk, Marek Wojcik, Sabine Wurmehl, Kristian Kroth, Sergey Reiman, Peter Blaha, and Claudia Felser. Structure and properties of comnsb in the context of half-metallic ferromagnetism. Phys. Rev. B, 74:134426, Oct 2006.

[309] R.A.M. VAN WOERDEN J. WIJNGAARD P.J. VAN DER VALK M.J. OTTO, H. FEIL. Electronic structure and magnetic, electrical and optical properties. Journal of Magnetism and Magnetic Materials, 70:33–38, 1987.

[310] W Jeitschko, AG Jordan, and Paul A Beck. V and e phases in ternary systems with transition metals and silicon or germanium. Trans Met Soc AIME, 245(2):335–339, 1969.

[311] K. Hartjes C. B. H. Evers, C. G. Richter and Wolfgang Jeitschko. Ternary transition metal antimonides and bismuthides with mgagas-type and filled nias-type structure. Journal of Alloys and Compounds, 252:93–97, 1997.

[312] MASAHIKO SHIMADA YUKIO NODA and MITSUE KOIZUMI. Synthesis of high-pressure phases of vcosb and vfesb with a ni21n (b82) type structure. Inorganic Chemistry, 18:3244–3246, 1979.

[313] Y. Fujita T. Ohoyama R. Kimura M. Terada, K. Endo. Magnetic suceptibilities of c1b compounds covsb and cotisb. Journal of Physical Society of Japan, 29:1091, 1970.

[314] C. A. Culbert, M. Williams, M. Chshiev, and W. H. Butler. Half-metallic l21 structures with (001) planar insertions. Journal of Applied Physics, 103(7), 2008.

[315] Claudia Felser, Lukas Wollmann, Stanislav Chadov, Gerhard H. Fecher, and Stuart S. P. Parkin. Basics and prospective of magnetic heusler compounds. APL Materials, 3(4):–, 2015.

[316] I Galanakis and Ph Mavropoulos. Spin-polarization and electronic properties of half-metallic heusler alloys calculated from first principles. Journal of Physics: Condensed Matter, 19(31):315213, 2007.

[317] Tanja Graf, Peter Klaer, Joachim Barth, Benjamin Balke, Hans-Joachim Elmers, and Claudia Felser. Phase separation in the quaternary heusler compound coti(1x)mnxsb a reduction in the thermal conductivity for thermoelectric applications. Scripta Materialia, 63(12):1216 – 1219, 2010.

[318] M. Hakimi, M. Venkatesan, K. Rode, K. Ackland, and J. M. D. Coey. The zero-magnetization heusler ferrimagnet. Journal of Applied Physics, 113(17):–, 2013.

[319] R. B. Helmholdt, R.A. de Groot, F.M. Mueller, P.G. van Engen, and K.H.J. Buschow. Magnetic and crystallographic properties of several c1b type heusler compounds. Journal of Magnetism and Magnetic Materials, 43(3):249 – 255, 1984.

[320] William H. Butler. Heusler database, June 2015.

[321] Kamaram Munira Tim Lovorn Jonathon Romero Chris Lample Leighton Wilson Jianhua Ma Yunkun Xie Sahar Keshavarz David Mildebrath Bill Butler, Avik Ghosh. Heusler database, aug 2015.

[322] L. Häggström, J. Sjöström, and T. Sundqvist. Magnetic order of fecrp. Solid State Communications, 59(4):193 – 194, 1986.

[323] Atsufumi Hirohata, James Sagar, Leonardo Lari, LukeR. Fleet, and VladoK. Lazarov. Heusler-alloy films for spintronic devices. Applied Physics A, 111(2):423–430, 2013.

[324] Atsufumi Hirohata and Koki Takanashi. Future perspectives for spintronic devices. Journal of Physics D: Applied Physics, 47(19):193001, 2014.

[325] C. Hordequin, J.P. Nozieres, and J. Pierre. Half metallic nimnsb-based spin-valve structures. Journal of Magnetism and Magnetic Materials, 183(1-2):225 – 231, 1998.

[326] Hisao Katsuraki and Norio Achiwa. The magnetic structure of fe2as. Journal of the Physical Society of Japan, 21(11):2238–2243, 1966.

[327] T. Kawahara, K. Ito, R. Takemura, and H. Ohno. Spin-transfer torque ram technology: Review and prospect. Microelectronics Reliability, 52(4):613 – 627, 2012. Advances in non-volatile memory technology.

[328] Javad G. Azadani, Kamaram Munira, Jonathon Romero, Jianhua Ma, Chockalingam Sivakumar, Avik W. Ghosh, and William H. Butler. Anisotropy in layered half-metallic heusler alloy superlattices. Journal of Applied Physics, 119(4), 2016.

[329] P Lecocq. Etude magnetique et structurale des solutions solides de germanium dans le fer, dans le cobalt et dans le nickel et des germaniures du type m3ge et m2ge. 1. techniques experimentales. Annales De Chimie France, 8(1-2):86, 1963.

[330] Kazuo Kanematsu, Kō Yasukōchi, and Tetuo Ohoyama. Magnetic properties of (fe, co)1.67ge and (fe, ni)1.67ge. Journal of the Physical Society of Japan, 18(10):1429–1436, 1963.

[331] Hong-xi Liu, Yusuke Honda, Tomoyuki Taira, Ken-ichi Matsuda, Masashi Arita, Tetsuya Uemura, and Masafumi Yamamoto. Giant tunneling magnetoresistance in epitaxial co2mnsi/mgo/co2mnsi magnetic tunnel junctions by half-metallicity of co2mnsi and coherent tunneling. Applied Physics Letters, 101(13):–, 2012.

[332] Y Lomnitskaya. Interaction of components in the titanium– cobalt– phosphorus system. Ukr. Khim. Zh., 47(2):142–146, 1981.

[333] A. Michel, R. Fruchart, J.P. Senateur, B. Deyris, J. Roy-montreuil, and D. Boursier. Influence de lelectronegativite sur lapparition de lordre dans les phases mmas (m=ru, rh, pd; m' = element des transition 3d). Annales de Chimie (Paris), year(9), 1984.

[334] Scott Kirklin, Bryce Meredig, and Chris Wolverton. Oqmd:an open quantum materials database. `http://oqmd.org/`, 2013.

[335] Chris. Wolverton. Oqmd:an open quantum materials database, June 2015.

[336] M. Methfessel and A. T. Paxton. High-precision sampling for brillouin-zone integration in metals. Phys. Rev. B, 40:3616–3621, Aug 1989.

[337] Serdar Öğüt and Karin M. Rabe. Band gap and stability in the ternary intermetallic compounds nisn M (M =ti,zr,hf): A first-principles study. Phys. Rev. B, 51:10443–10453, Apr 1995.

[338] G. Kresse and J. Furthmüller. Efficient iterative schemes for ab initio total-energy calculations using a plane-wave basis set. Phys. Rev. B, 54:11169–11186, Oct 1996.

[339] F. B. Mancoff, B. M. Clemens, E. J. Singley, and D. N. Basov. Infrared probe of the electronic structure and carrier scattering in nimnsb thin films. Phys. Rev. B, 60:R12565–R12568, Nov 1999.

[340] G. A. de Wijs and R. A. de Groot. Towards 100nimnsb/cds interface. Phys. Rev. B, 64:020402, Jun 2001.

[341] J Kübler. Curie temperatures of zinc-blende half-metallic ferromagnets. Phys. Rev. B, 67:220403, Jun 2003.

[342] David Kieven, Reiner Klenk, Shahab Naghavi, Claudia Felser, and Thomas Gruhn. I-ii-v half-heusler compounds for optoelectronics: *Ab initio* calculations. Phys. Rev. B, 81:075208, Feb 2010.

[343] Wanxiang Feng, Di Xiao, Ying Zhang, and Yugui Yao. Half-heusler topological insulators: A first-principles study with the tran-blaha modified becke-johnson density functional. Phys. Rev. B, 82:235121, Dec 2010.

[344] Anindya Roy, Joseph W. Bennett, Karin M. Rabe, and David Vanderbilt. Half-heusler semiconductors as piezoelectrics. Phys. Rev. Lett., 109:037602, Jul 2012.

[345] H. van Leuken and R. A. de Groot. Half-metallic antiferromagnets. Phys. Rev. Lett., 74:1171–1173, Feb 1995.

[346] Delia Ristoiu, J. P. Nozires, C. N. Borca, B. Borca, and P. A. Dowben. Manganese surface segregation in nimnsb. Applied Physics Letters, 76(17):2349–2351, 2000.

[347] J Roy-Montreuil, B Deyris, A Michel, R Fruchart, JP Sénateur, and D Boursier. Influence of electronegativity of transition-metals m and m-'upon crystallographic order in the phosphides mm'p and the arsenides mm'as. In Annales De Chimie-Science Des Materiaux, volume 4, pages 411–417. Masson Editeur 120 Blvd Saint-Germain, 75280 Paris 06, France, 1979.

[348] James E. Saal and C. Wolverton. Thermodynamic stability of mg-based ternary long-period stacking ordered structures. Acta Materialia, 68:325 – 338, 2014.

[349] S. Sakurada and N. Shutoh. Effect of ti substitution on the thermoelectric properties of (zr,hf)nisn half-heusler compounds. Applied Physics Letters, 86(8):082105, 2005.

[350] Joseph R Sootsman, Duck Young Chung, and Mercouri G Kanatzidis. New and old concepts in thermoelectric materials. Angewandte Chemie International Edition, 48(46):8616–8639, 2009.

[351] A Szytuła, AT Pedziwiatr, Z Tomkowicz, and W Bażela. Crystal and magnetic structure of comnge, cofege, femnge and nifege. Journal of Magnetism and Magnetic Materials, 25(2):176 – 186, 1981.

[352] Clifford T. Tanaka, Janusz Nowak, and Jagadeesh S. Moodera. Spin-polarized tunneling in a half-metallic ferromagnet. Journal of Applied Physics, 86(11):6239–6242, 1999.

[353] W. Van Roy, J. De Boeck, B. Brijs, and G. Borghs. Epitaxial nimnsb films on gaas(001). Applied Physics Letters, 77(25):4190–4192, 2000.

[354] Jürgen Winterlik, Stanislav Chadov, Arunava Gupta, Vajiheh Alijani, Teuta Gasi, Kai Filsinger, Benjamin Balke, Gerhard H. Fecher, Catherine A. Jenkins, Frederick Casper, Jürgen Kübler, Guo-Dong Liu, Li Gao, Stuart S. P. Parkin, and Claudia Felser. Design scheme of new tetragonal heusler compounds for spin-transfer torque applications and its experimental realization. Advanced Materials, 24(47):6283–6287, 2012.

[355] Sabine Wurmehl, Hem C Kandpal, Gerhard H Fecher, and Claudia Felser. Valence electron rules for prediction of half-metallic compensated-ferrimagnetic behaviour of heusler compounds with complete spin polarization. Journal of Physics: Condensed Matter, 18(27):6171, 2006.

[356] A. Szytuła, A.T. Pędziwiatr, Z. Tomkowicz, and W. Bażela. Crystal and magnetic structure of comnge, cofege, femnge and nifege. Journal of Magnetism and Magnetic Materials, 25:176 – 186, 1981.

[357] W. Bażla, A. Szytuła, and W. Zając. Magnetic ordering in comnsn studied by neutron diffraction and 119sn mssbauer spectroscopy. Solid State Communications, 38:875 – 877, 1981.

[358] R. Srinivasan. Spintronics. Resonance, 10(9):53–62, 2005.

[359] L. Wang, T. Y. Chen, and C. Leighton. Spin-dependent band structure effects and measurement of the spin polarization in the candidate half-metal cos_2. Phys. Rev. B, 69:094412, Mar 2004.

[360] Tanja Graf, Claudia Felser, and Stuart S.P. Parkin. Simple rules for the understanding of heusler compounds. Progress in Solid State Chemistry, 39(1):1 – 50, 2011.

[361] KRA Ziebeck and KU Neumann. Magnetic properties of metals. Landolt-Boörnstein, New Series, Group III, 32:64–414, 2001.

[362] R. A. de Groot, F. M. Mueller, P. G. van Engen, and K. H. J. Buschow. New class of materials: Half-metallic ferromagnets. Phys. Rev. Lett., 50:2024–2027, Jun 1983.

[363] I. Galanakis, P. H. Dederichs, and N. Papanikolaou. Origin and properties of the gap in the half-ferromagnetic heusler alloys. Phys. Rev. B, 66:134428, Oct 2002.

[364] S. J. Youn and B. I. Min. Effects of the spin-orbit interaction in heusler compounds: Electronic structures and fermi surfaces of nimnsb and ptmnsb. Phys. Rev. B, 51:10436–10442, Apr 1995.

[365] Janusz Toboła and Jacques Pierre. Electronic phase diagram of the xtz (x=fe, co, ni; t=ti, v, zr, nb, mn; z=sn, sb) semi-heusler compounds. Journal of Alloys and Compounds, 296(1-2):243 – 252, 2000.

[366] Hem Chandra Kandpal, Claudia Felser, and Ram Seshadri. Covalent bonding and the nature of band gaps in some half-heusler compounds. Journal of Physics D: Applied Physics, 39(5):776, 2006.

[367] I Galanakis, Ph Mavropoulos, and P H Dederichs. Electronic structure and slater-pauling behaviour in half-metallic heusler alloys calculated from first principles. Journal of Physics D: Applied Physics, 39(5):765, 2006.

[368] Lukas Wollmann, Stanislav Chadov, Jürgen Kübler, and Claudia Felser. Magnetism in cubic manganese-rich heusler compounds. Phys. Rev. B, 90:214420, Dec 2014.

[369] I. Galanakis, P. H. Dederichs, and N. Papanikolaou. Slater-pauling behavior and origin of the half-metallicity of the full-heusler alloys. Phys. Rev. B, 66:174429, Nov 2002.

[370] K. E. H. M. Hanssen, P. E. Mijnarends, L. P. L. M. Rabou, and K. H. J. Buschow. Positron-annihilation study of the half-metallic ferromagnet nimnsb: Experiment. Phys. Rev. B, 42:1533–1540, Jul 1990.

[371] J. C. Slater. Electronic structure of alloys. Journal of Applied Physics, 8(6):385–390, 1937.

[372] Linus Pauling. The nature of the interatomic forces in metals. Phys. Rev., 54:899–904, Dec 1938.

[373] G. Kresse and J. Furthmüller. Efficiency of ab-initio total energy calculations for metals and semiconductors using a plane-wave basis set. Computational Materials Science, 6(1):15 – 50, 1996.

[374] P. E. Blöchl. Projector augmented-wave method. Phys. Rev. B, 50:17953–17979, Dec 1994.

[375] JamesE. Saal, Scott Kirklin, Muratahan Aykol, Bryce Meredig, and C. Wolverton. Materials design and discovery with high-throughput density functional theory: The open quantum materials database (oqmd). JOM, 65(11):1501–1509, 2013.

[376] Scott Kirklin, James E Saal, Bryce Meredig, Alex Thompson, Jeff W Doak, Muratahan Aykol, Stephan Rühl, and Chris Wolverton. The open quantum materials database (oqmd): assessing the accuracy of dft formation energies. npj Computational Materials, 1:15010, 2015.

[377] Hendrik J. Monkhorst and James D. Pack. Special points for brillouin-zone integrations. Phys. Rev. B, 13:5188–5192, Jun 1976.

[378] Peter E. Blöchl, O. Jepsen, and O. K. Andersen. Improved tetrahedron method for brillouin-zone integrations. Phys. Rev. B, 49:16223–16233, Jun 1994.

[379] S. H. Vosko, L. Wilk, and M. Nusair. Accurate spin-dependent electron liquid correlation energies for local spin density calculations: a critical analysis. Canadian Journal of Physics, 58(8):1200–1211, 1980.

[380] A. R. Akbarzadeh, V. Ozoliņš, and C. Wolverton. First-principles determination of multicomponent hydride phase diagrams: Application to the li-mg-n-h system. Advanced Materials, 19:3233–3239, 2007.

[381] C. Felser, V. Alijani, J. Winterlik, S. Chadov, and A. K. Nayak. Tetragonal heusler compounds for spintronics. IEEE Transactions on Magnetics, 49(2):682–685, Feb 2013.

[382] Felix A. Faber, Alexander Lindmaa, O. Anatole von Lilienfeld, and Rickard Armiento. Machine learning energies of 2 million elpasolite (abC_2D_6) crystals. Phys. Rev. Lett., 117:135502, Sep 2016.

[383] J Kübler. Ab initio estimates of the curie temperature for magnetic compounds. Journal of Physics: Condensed Matter, 18(43):9795, 2006.

[384] A Ślebarski, J Goraus, J Deniszczyk, et al. Electronic structure, magnetic properties and electrical resistivity of the fe2v1-xtixal heusler alloys: experiment and calculation. Journal of Physics: Condensed Matter, 18(46):10319, 2006.

[385] Warren E Pickett and Helmut Eschrig. Half metals: from formal theory to real material issues. Journal of Physics: Condensed Matter, 19(31):315203, 2007.

[386] S. Tsunegi, Y. Sakuraba, M. Oogane, Hiroshi Naganuma, K. Takanashi, and Y. Ando. Enhancement in tunnel magnetoresistance effect by inserting cofeb to the tunneling barrier interface in co2mnsi/mgo/cofe magnetic tunnel junctions. Applied Physics Letters, 94(25):–, 2009.

[387] Jo Sato, Mikihiko Oogane, Hiroshi Naganuma, and Yasuo Ando. Large magnetoresistance effect in epitaxial co 2 fe 0.4 mn 0.6 si/ag/co 2 fe 0.4 mn 0.6 si devices. Applied Physics Express, 4(11):113005, 2011.

[388] Yasuo Ando. Spintronics technology and device development. Japanese Journal of Applied Physics, 54(7):070101, 2015.

[389] Claudia Felser, GerhardH. Fecher, and Benjamin Balke. Spintronics: A challenge for materials science and solid-state chemistry. Angewandte Chemie International Edition, 46(5):668–699, 2007.

[390] C. G. F. Blum, C. A. Jenkins, J. Barth, C. Felser, S. Wurmehl, G. Friemel, C. Hess, G. Behr, B. Bchner, A. Reller, S. Riegg, S. G. Ebbinghaus, T. Ellis, P. J. Jacobs, J. T. Kohlhepp, and H. J. M. Swagten. Highly ordered, half-metallic co2fesi single crystals. Applied Physics Letters, 95(16):–, 2009.

[391] EI Gladyshevskiy and GN Shvets. Phase equilibrium diagram of ternary v-fe-si alloys and crystal structure of the compounds. RUSSIAN MET, (2):63–65, 1965.

[392] T. Graf, S. S. P. Parkin, and C. Felser. Heusler compounds-a material class with exceptional properties. IEEE Transactions on Magnetics, 47(2):367–373, Feb 2011.

[393] T. M. Nakatani, T. Furubayashi, S. Kasai, H. Sukegawa, Y. K. Takahashi, S. Mitani, and K. Hono. Bulk and interfacial scatterings in current-perpendicular-to-plane giant magnetoresistance with co2fe(al0.5si0.5) heusler alloy layers and ag spacer. Applied Physics Letters, 96(21):–, 2010.

[394] Y. K. Takahashi, A. Srinivasan, B. Varaprasad, A. Rajanikanth, N. Hase, T. M. Nakatani, S. Kasai, T. Furubayashi, and K. Hono. Large magnetoresistance in current-perpendicular-to-plane pseudospin valve using a co2fe(ge0.5ga0.5) heusler alloy. Applied Physics Letters, 98(15):152501, 2011.

[395] Michelle E. Jamer, Badih A. Assaf, Trithep Devakul, and Don Heiman. Magnetic and transport properties of mn2coal oriented films. Applied Physics Letters, 103(14), 2013.

[396] Q.F. Li, C.H. Yang, and J.L. Su. Effect of doping v on the half-metallic and magnetic properties of mn3al intermetallic compound. Physica B: Condensed Matter, 406(19):3726 – 3730, 2011.

[397] J. Kübler, G. H. Fecher, and C. Felser. Understanding the trend in the curie temperatures of co_2-based heusler compounds: *Ab initio* calculations. Phys. Rev. B, 76:024414, Jul 2007.

[398] Stanislav Chadov, Tanja Graf, Kristina Chadova, Xuefang Dai, Frederick Casper, Gerhard H. Fecher, and Claudia Felser. Efficient spin injector scheme based on heusler materials. Phys. Rev. Lett., 107:047202, Jul 2011.

[399] Igor Žutić, Jaroslav Fabian, and S. Das Sarma. Spintronics: Fundamentals and applications. Rev. Mod. Phys., 76:323–410, Apr 2004.

[400] M. I. Katsnelson, V. Yu. Irkhin, L. Chioncel, A. I. Lichtenstein, and R. A. de Groot. Half-metallic ferromagnets: From band structure to many-body effects. Rev. Mod. Phys., 80:315–378, Apr 2008.

[401] N. Tezuka, N. Ikeda, F. Mitsuhashi, and S. Sugimoto. Improved tunnel magnetoresistance of magnetic tunnel junctions with heusler co2feal0.5si0.5 electrodes fabricated by molecular beam epitaxy. Applied Physics Letters, 94(16):162504, 2009.

[402] Taku Iwase, Yuya Sakuraba, Subrojati Bosu, Kesami Saito, Seiji Mitani, and Koki Takanashi. Large interface spin-asymmetry and magnetoresistance in fully epitaxial co 2 mnsi/ag/co 2 mnsi current-perpendicular-to-plane magnetoresistive devices. Applied Physics Express, 2(6):063003, 2009.

[403] Atsufumi Hirohata and Koki Takanashi. Future perspectives for spintronic devices. Journal of Physics D: Applied Physics, 47(19):193001, 2014.

[404] Xiao-Ping Wei, Jian-Bo Deng, Ge-Yong Mao, Shi-Bin Chu, and Xian-Ru Hu. Half-metallic properties for the ti2yz (y=fe, co, ni, z=al, ga, in) heusler alloys: A first-principles study. Intermetallics, 29:86 – 91, 2012.

[405] Hong-Xi Liu, Yusuke Honda, Tomoyuki Taira, Ken-ichi Matsuda, Masashi Arita, Tetsuya Uemura, and Masafumi Yamamoto. Giant tunneling magnetoresistance in epitaxial co2mnsi/mgo/co2mnsi magnetic tunnel junctions by half-metallicity of co2mnsi and coherent tunneling. Applied Physics Letters, 101(13):132418, 2012.

[406] Hong-Xi Liu, Takeshi Kawami, Kidist Moges, Tetsuya Uemura, Masafumi Yamamoto, Fengyuan Shi, and Paul M Voyles. Influence of film composition in quaternary heusler alloy co 2 (mn,fe)si thin films on tunnelling magnetoresistance of co 2 (mn,fe)si/mgo-based magnetic tunnel junctions. Journal of Physics D: Applied Physics, 48(16):164001, 2015.

[407] Jianhua Ma, Vinay I Hegde, Kamaram Munira, Yunkun Xie, Sahar Keshavarz, David T Mildebrath, C Wolverton, Avik W Ghosh, and WH Butler. Computational investigation of half-heusler compounds for spintronics applications. Physical Review B, 95(2):024411, 2017.

[408] D. C. Worledge and T. H. Geballe. Magnetoresistive double spin filter tunnel junction. Journal of Applied Physics, 88(9):5277–5279, 2000.

[409] P. LeClair, J. K. Ha, H. J. M. Swagten, J. T. Kohlhepp, C. H. van de Vin, and W. J. M. de Jonge. Large magnetoresistance using hybrid spin filter devices. Applied Physics Letters, 80(4):625–627, 2002.

[410] Hongzhi Luo, Fanbin Meng, Zhongqiu Feng, Yangxian Li, Wei Zhu, Guangheng Wu, Xiaoxi Zhu, Chengbao Jiang, and Huibin Xu. Ferromagnetism in the mn-based heusler alloy mn2nisb. Journal of Applied Physics, 105(10):103903, 2009.

[411] N. Naghibolashrafi, S. Keshavarz, Vinay I. Hegde, A. Gupta, W. H. Butler, J. Romero, K. Munira, P. LeClair, D. Mazumdar, J. Ma, A. W. Ghosh, and C. Wolverton. Synthesis and characterization of fe-ti-sb intermetallic compounds: Discovery of a new slater-pauling phase. Phys. Rev. B, 93:104424, Mar 2016.

[412] A. Nelson, P. Kharel, Y. Huh, R. Fuglsby, J. Guenther, W. Zhang, B. Staten, P. Lukashev, S. Valloppilly, and D. J. Sellmyer. Enhancement of curie temperature in mn2rusn by co substitution. Journal of Applied Physics, 117(15):153906, 2015.

[413] Jianguo Chen, Hongzhi Luo, Pengzhong Jia, Fanbin Meng, Guodong Liu, Enke Liu, Wenhong Wang, and Guangheng Wu. Site preference and electronic structure of mn2rusn: A theoretical study. Journal of Magnetism and Magnetic Materials, 365:132 – 137, 2014.

[414] Felix Büttner, Ivan Lemesh, and Geoffrey SD Beach. Theory of isolated magnetic skyrmions: From fundamentals to room temperature applications. Scientific reports, 8(1):4464, 2018.

[415] S Rohart and A Thiaville. Skyrmion confinement in ultrathin film nanostructures in the presence of dzyaloshinskii-moriya interaction. Physical Review B, 88(18):184422, 2013.

[416] AB Butenko, AA Leonov, UK Rößler, and AN Bogdanov. Stabilization of skyrmion textures by uniaxial distortions in noncentrosymmetric cubic helimagnets. Physical Review B, 82(5):052403, 2010.

[417] Stephan von Malottki, Pavel F Bessarab, Soumyajyoti Haldar, Anna Delin, and Stefan Heinze. Skyrmion lifetimes in ultrathin films. arXiv preprint arXiv:1811.12067, 2018.

[418] A Siemens, Y Zhang, J Hagemeister, EY Vedmedenko, and Roland Wiesendanger. Minimal radius of magnetic skyrmions: statics and dynamics. New Journal of Physics, 18(4):045021, 2016.

[419] Kai Litzius, Ivan Lemesh, Benjamin Krüger, Pedram Bassirian, Lucas Caretta, Kornel Richter, Felix Büttner, Koji Sato, Oleg A Tretiakov, Johannes Förster, et al. Skyrmion hall effect revealed by direct time-resolved x-ray microscopy. Nature Physics, 13(2):170, 2017.

[420] Wanjun Jiang, Xichao Zhang, Guoqiang Yu, Wei Zhang, Xiao Wang, M Benjamin Jungfleisch, John E Pearson, Xuemei Cheng, Olle Heinonen, Kang L Wang, et al. Direct observation of the skyrmion hall effect. Nature Physics, 13(2):162, 2017.

[421] AA Thiele. Steady-state motion of magnetic domains. Physical Review Letters, 30(6):230, 1973.

[422] Hiu Tung Fook, Wei Liang Gan, Indra Purnama, and Wen Siang Lew. Mitigation of magnus force in current-induced skyrmion dynamics. IEEE Transactions on Magnetics, 51(11):1–4, 2015.

[423] Se Kwon Kim, Kyung-Jin Lee, and Yaroslav Tserkovnyak. Self-focusing skyrmion racetracks in ferrimagnets. Physical Review B, 95(14):140404, 2017.

[424] Xichao Zhang, Motohiko Ezawa, and Yan Zhou. Thermally stable magnetic skyrmions in multilayer synthetic antiferromagnetic racetracks. Physical Review B, 94(6):064406, 2016.

[425] Xichao Zhang, Yan Zhou, and Motohiko Ezawa. Magnetic bilayer-skyrmions without skyrmion hall effect. Nature communications, 7:10293, 2016.